



NATIONAL TECHNICAL UNIVERSITY OF ATHENS
SCHOOL OF ELECTRICAL AND COMPUTER ENGINEERING
SCHOOL OF MECHANICAL ENGINEERING
Laboratory of Biofluid Mechanics & Biomedical Technology

INTERDISCIPLINARY POSTGRADUATE PROGRAMME
“Translational Engineering in Health and Medicine”

**4D Flow MRI-enabled patient-specific computational
hemodynamics of thoracic aorta: CFD predictions vs. in vivo
imaging data**

Postgraduate Diploma Thesis

Postgraduate student Petrolekas Dimitrios

Supervisor: *Manopoulos Christos, Associate Professor NTUA*

Athens, June 2025



NATIONAL TECHNICAL UNIVERSITY OF ATHENS
SCHOOL OF ELECTRICAL AND COMPUTER ENGINEERING
SCHOOL OF MECHANICAL ENGINEERING
Laboratory of Biofluid Mechanics & Biomedical Technology

INTERDISCIPLINARY POSTGRADUATE PROGRAMME
“Translational Engineering in Health and Medicine”

**4D Flow MRI-enabled patient-specific computational
hemodynamics of thoracic aorta: CFD predictions vs. in vivo
imaging data**

Postgraduate Diploma Thesis

Postgraduate student Petrolekas Dimitrios

Supervisor: *Manopoulos Christos, Associate Professor NTUA*

The postgraduate diploma thesis has been approved by the examination committee
on 25 June 2025

1st member

2nd member

3rd member

*Christos Manopoulos
Associate Professor NTUA*

*Konstantina Nikita
Professor NTUA*

*Georgios Matsopoulos
Professor NTUA*

Athens, June 2025

.....

Petrolekas Dimitrios
Graduate of the Interdisciplinary Postgraduate Programme,
“Translational Engineering in Health and Medicine”,
Master of Science,
School of Electrical and Computer Engineering,
National Technical University of Athens

Copyright © Petrolekas Dimitrios, 2025
All rights reserved.

You may not copy, reproduce, distribute, publish, display, modify, create derivative works, transmit, or in any way exploit this thesis or part of it for commercial purposes. You may reproduce, store or distribute this thesis for non-profit educational or research purposes, provided that the source is cited, and the present copyright notice is retained. Inquiries for commercial use should be addressed to the original author.

The ideas and conclusions presented in this paper are the author’s and do not necessarily reflect the official views of the National Technical University of Athens.

Abstract

The assessment of hemodynamic parameters within the human vasculature is crucial for understanding cardiovascular health and disease progression. This study employs patient-specific 4D Flow MRI data to validate computational fluid dynamics (CFD) simulations of blood flow in the thoracic aorta. Two CFD solvers, SimVascular and CRIMSON, are utilized to simulate hemodynamics using both patient-specific and parabolic inlet velocity profiles. The objective is to evaluate the accuracy of computational predictions in comparison to in vivo imaging data.

The methodology includes 3D reconstruction of the thoracic aorta from MRI data, preprocessing of velocity fields, and numerical simulations incorporating appropriate boundary conditions. A direct comparison between simulated and MRI-derived velocity fields, pressure distributions, and wall shear stress (WSS) is conducted at multiple time points throughout the cardiac cycle. Special emphasis is placed on analyzing flow characteristics in critical regions, including the ascending aorta, aortic arch, and descending aorta.

Results indicate that while both CFD solvers accurately capture global flow trends, differences arise in local flow patterns, particularly in regions with complex hemodynamics. The patient-specific velocity profile demonstrates superior agreement with MRI data, especially in replicating secondary flow structures and WSS distributions. Conversely, the parabolic profile tends to overestimate peak velocities and introduce deviations in flow patterns. The analysis also highlights minor discrepancies between CRIMSON and SimVascular, likely attributed to differences in mesh resolution and numerical techniques.

The findings emphasize the importance of patient-specific boundary conditions in cardiovascular simulations, as they significantly impact flow field accuracy. The study underscores the strengths and limitations of CFD modeling for clinical applications and highlights the potential of 4D Flow MRI as a validation tool for computational hemodynamics. Future work should explore the integration of fluid-structure interaction (FSI) models to enhance simulation realism by incorporating vessel wall compliance.

Keywords: computational fluid dynamics, patient-specific modeling, model validation, in-vivo imaging, computational hemodynamics, biomedical engineering, thoracic aorta, hemodynamic modeling

Acknowledgements

I would like to express my gratitude to my supervisor, Associate Professor Christos Manopoulos, Director of the Biofluid Mechanics and Biomedical Engineering Laboratory in the Department of Mechanical Engineering at NTUA, for entrusting me with this thesis and for his invaluable insights and feedback, which significantly shaped its direction and quality. I am also grateful to Dr. Anastasios Raptis for his consistent guidance and support throughout the course of this work. Additionally, I would like to thank Dr. Efstratios Karavasilis for generously sharing his expertise in 4D Flow MRI, which greatly enhanced my understanding and contributed significantly at various stages of the project.

Moreover, I am deeply grateful to my friends, whose unwavering support helped me navigate the challenges of this thesis. Among my friends, I would especially like to thank Fillipos Katsimalis, Dimitrios Tsogias, Konstantinos Papanikolaou, and Dimitrios Sdrolis for their constant encouragement and for always being there when I faced difficulties. Finally, I owe my heartfelt thanks to my family—my father Panagiotis, my mother Evanthia, and my sister Angeliki—for their unconditional support, trust, and belief in me. Their guidance and encouragement have played a vital role in both my personal and academic development, continually inspiring me to strive for excellence.

Contents

1.	Introduction.....	15
1.1	Cardiovascular System.....	15
1.1.1	Heart.....	16
1.1.2	Blood Vessels.....	18
1.1.3	Aorta.....	19
1.2	Magnetic Resonance Imaging (MRI).....	20
1.2.1	Brief historical overview of Magnetic Resonance Imaging.....	21
1.2.2	Basic principles of Magnetic Resonance Imaging (MRI).....	22
1.2.3	Phase-Contrast Magnetic Resonance Imaging (PC-MRI).....	25
1.2.4	4D Flow Magnetic Resonance Imaging.....	27
1.3	Fluid Mechanics.....	28
1.3.1	Navier-Stokes.....	28
1.3.2	Pipe Flow.....	29
1.3.3	Computational Fluid Dynamics.....	32
1.4	Hemodynamic Models.....	33
1.4.1	Arterial Models.....	33
1.4.2	The Windkessel Models.....	34
2.	Methods.....	40
2.1	Software.....	40
2.1.1	SimVascular.....	40
2.1.2	CRIMSON.....	40
2.1.3	ParaView.....	41
2.2	Procedure Overview.....	42
2.2.1	Data Acquisition and interpretation.....	42
2.2.2	Data preprocessing and 4D velocity array creation.....	43
2.2.3	3D Model Reconstruction.....	45
2.2.4	Exporting, Refining, and Integrating the 3D Model for Simulation in Crimson 49	
2.2.5	Preparing the Mesh and Defining Boundary Conditions.....	51
2.2.6	Solver setup and simulation files creation.....	55
2.2.7	Error Quantification and Comparison with the Original 4D Flow MRI Data..	57
2.3	Patient Specific Velocity Profile Extraction.....	61
3.	Results and Discussion.....	66
3.1	Patient-specific velocity profile.....	68
3.1.1	Pressure Profile.....	68
3.1.2	Flow rate profile and velocity vector field.....	76
3.1.3	Wall shear stress.....	91
3.1.4	Velocity comparison between the CFD data and patient-MRI data.....	97
3.2	Parabolic velocity profile.....	113
3.2.1	Pressure Profile.....	113
3.2.2	Flow rate profile & velocity vector field.....	120
3.2.3	Wall Shear Stress (Parabolic).....	129
3.2.4	Velocity comparison between the CFD data and patient-MRI data (Parabolic Velocity Profile).....	135
3.3	Direct comparison between the patient-specific and parabolic velocity profile.	147
4.	Conclusions.....	160
5.	References.....	163

List of Figures

Figure 1: Simple schematic of the cardiovascular system	15
Figure 2: Internal anatomy of the heart (Hammer, 2010).....	16
Figure 3: Stages of the Cardiac Cycle (Perez, 2016)	17
Figure 4: Comparison between aortic, ventricular and atrial pressure. Comparison between ventricular volume and aortic flow (Herman, 2016).....	17
Figure 5: Simplified overview of the basic blood vessels (Britannica, Online)	18
Figure 6: Aorta geometry, main sections and location in the human body (Cleveland Clinic, Online).....	19
Figure 7: Detailed view of the aortic arch with all its branches visible (Orozco-Sevilla & Coselli, 2023).....	20
Figure 8: Depiction of an MRI structure and scan (NCI, Online).....	21
Figure 9: Example 4D Flow MRI data of the upper part of the aorta. The blood velocity distribution can be seen as well as the respective coordinate axis (Shan et al., 2017)	28
Figure 10: Depiction of the parabolic velocity profile (CV Physiology, Online)	30
Figure 11: Visualization of shear stress profile (AOBL, Online)	31
Figure 12: Description of arterial models (Perez, 2016).....	33
Figure 13: Analogy between Ohm's and Poiseuille's law (GSU Hyperphysics, Online).....	34
Figure 14: Hemodynamic and electrical presentation of the 2-element windkessel model (Westerhof, 2009)	35
Figure 15: Hemodynamic and electrical presentation of the 3-element windkessel model (Westerhof, 2009).....	37
Figure 16: Four-element-series Windkessel model (a), four-element-parallel Windkessel model (b)	38
Figure 17: Sample magnitude image of the data used.....	42
Figure 18: Sample phase image of the data used	43
Figure 19: Sample of the contents of the h5 file used in the analysis.....	44
Figure 20: Spatial Domain Definition of 4D Flow Scan Using SimVascular.....	45
Figure 21: The paths for the aorta, brachiocephalic, left common carotid and subclavian arteries	46
Figure 22: Selection of Path Points and Overview of Path Points Defining the Aorta's Main Body.....	46
Figure 23: Segmentations used for the model reconstructions along with their respective paths.....	47
Figure 24: Example of Segmentation Selection and Overview of All Segmentations	48
Figure 25: The complete 3D model with its respective segmentations	48
Figure 26: Visualization of the VTP model in the ParaView environment, displaying the normal (triangles) of the model.....	49
Figure 27: The test 3D model after the modifications in Meshmixer	50
Figure 28: Test Mesh used in SimVascular (left) and in CRIMSON (right).....	51
Figure 29: Region of Interest (ROI) used during systole phase of the cardiac cycle	52
Figure 30: Flow profiles for all velocity components derived from the 4D Flow MRI data	53
Figure 31: Volumetric flow rate of ascending aorta during one cardiac cycle	53
Figure 32: Representation of the CFD model's geometric reconstruction in the new HDF5 file.	59
Figure 33: Representation of the downsampled CFD model's geometric reconstruction	59
Figure 34: Visualization of the cap's mesh	61
Figure 35: Patient specific velocity profile after spatial interpolation	64
Figure 36: 3D model with patient specific velocity profile applied.....	65

Figure 37: Refined thoracic aorta model 66

Figure 38: Timeline of Key Analysis Timepoints Across the Cardiac Cycle 67

Figure 39: Pressure waveforms for Ascending Aorta 68

Figure 40: Pressure waveforms for Descending Aorta 69

Figure 41: Pressure waveforms for Brachiocephalic Artery 69

Figure 42: Pressure waveforms for Left Common Carotid Artery 70

Figure 43: Pressure waveforms for Left Subclavian Artery 70

Figure 44: Pressure Distribution at start of the systolic phase (SimVascular) 71

Figure 45: Pressure Distribution at start of the systolic phase (Crimson) 71

Figure 46: Pressure Distribution at peak of the systolic phase (SimVascular) 72

Figure 47: Pressure Distribution at peak of the systolic phase (Crimson) 73

Figure 48: Pressure Distribution at the end of the systolic phase (SimVascular) 73

Figure 49: Pressure Distribution at the end of the systolic phase (Crimson) 74

Figure 50: Pressure Distribution during the diastolic phase (SimVascular) 74

Figure 51: Pressure Distribution during diastolic phase (Crimson) 75

Figure 52: Flow rate in ascending aorta (inlet) 76

Figure 53: Flow rate in descending aorta (outlet) 77

Figure 54: Flow rate in brachiocephalic artery (outlet) 78

Figure 55: Flow rate in left common carotid artery (outlet) 79

Figure 56: Flow rate in left subclavian artery (outlet) 79

Figure 57: Patient-specific velocity profile at the start of the systolic phase (SimVascular) ... 82

Figure 58: Patient-specific velocity profile at the start of the systolic phase (CRIMSON) 82

Figure 59: Velocity vector field and streamlines at start of systolic phase (SimVascular) 83

Figure 60: Velocity vector field and streamlines at start of systolic phase (Crimson) 83

Figure 61: Patient-specific velocity profile at the peak of the systolic phase (SimVascular) ... 84

Figure 62: Patient-specific velocity profile at the peak of the systolic phase (Crimson) 84

Figure 63: Velocity vector field and streamlines at peak of systolic phase (SimVascular) 85

Figure 64: Velocity vector field and streamlines at peak of systolic phase (Crimson) 85

Figure 65: Patient-specific velocity profile at the end of the systolic phase (SimVascular) ... 86

Figure 66: Patient-specific velocity profile at the end of the systolic phase (Crimson) 87

Figure 67: Velocity vector field and streamlines at end of systolic phase (SimVascular) 87

Figure 68: Velocity vector field and streamlines at end of systolic phase (Crimson) 88

Figure 69: Patient-specific velocity profile during the diastolic phase (SimVascular) 89

Figure 70: Patient-specific velocity profile during the diastolic phase (Crimson) 89

Figure 71: Velocity vector field and streamlines during the diastolic phase (SimVascular) ... 90

Figure 72: Velocity vector field and streamlines during the diastolic phase (Crimson) 90

Figure 73: Wall shear stress of the aortic wall at the start of the systolic phase (SimVascular) 91

Figure 74: Wall shear stress of the aortic wall at the start of the systolic phase (Crimson) ... 92

Figure 75: Wall shear stress of the aortic wall at the peak of the systolic phase (SimVascular) 92

Figure 76: Wall shear stress of the aortic wall at the peak of the systolic phase (Crimson) ... 93

Figure 77: Wall shear stress of the aortic wall at the end of the systolic phase (SimVascular) 94

Figure 78: Wall shear stress of the aortic wall at the end of the systolic phase (Crimson) 94

Figure 79: Wall shear stress of the aortic wall during the diastolic phase (SimVascular) 95

Figure 80: Wall shear stress of the aortic wall during the diastolic phase (Crimson) 95

Figure 81: Time averaged wall shear stress for one cardiac cycle (SimVascular) 96

Figure 82: Time averaged wall shear stress for one cardiac cycle (Crimson) 96

Figure 83: CFD data in the initial 4D array form 98

Figure 84: CFD data in the downsampled 4D array form 98

Figure 85: Axial slice for the upper descending aorta 99

Figure 86: Graph comparing the u-velocity component in the upper descending aorta 100

Figure 87: Graph comparing the v-velocity component in the upper descending aorta 100

Figure 88: Graph comparing the w-velocity component in the upper descending aorta 101

Figure 89: Graph comparing the velocity magnitude in the upper descending aorta 101

Figure 90: Axial slice for the ascending aorta 102

Figure 91: Graph comparing the u-velocity component before the flow enters the aortic arch
..... 103

Figure 92: Graph comparing the v-velocity component before the flow enters the aortic arch
..... 103

Figure 93: Graph comparing the w-velocity component before the flow enters the aortic arch
..... 104

Figure 94: Graph comparing the velocity magnitude before the flow enters the aortic arch
..... 104

Figure 95: Coronal slice before LCC branch 105

Figure 96: Graph comparing the u-velocity component before the LCC branch of the aortic
arch..... 106

Figure 97: Graph comparing the v-velocity component before the LCC branch of the aortic
arch..... 107

Figure 98: Graph comparing the w-velocity component before the LCC branch of the aortic
arch..... 107

Figure 99: Graph comparing the velocity magnitude before the LCC branch of the aortic arch
..... 108

Figure 100: Coronal slice before LSA branch 108

Figure 101: Graph comparing the u-velocity component before the LSA branch of the aortic
arch..... 110

Figure 102: Graph comparing the v-velocity component before the LSA branch of the aortic
arch..... 110

Figure 103: Graph comparing the w-velocity component before the LSA branch of the aortic
arch..... 111

Figure 104: Graph comparing the w-velocity component before the LSA branch of the aortic
arch..... 111

Figure 105: Pressure waveforms for Ascending Aorta (Parabolic) 113

Figure 106: Pressure waveforms for Descending Aorta (Parabolic) 114

Figure 107: Pressure waveforms for Brachiocephalic Artery (Parabolic)..... 114

Figure 108: Pressure waveforms for Left Common Carotid Artery (Parabolic)..... 115

Figure 109: Pressure waveforms for Left Subclavian Artery (Parabolic)..... 115

Figure 110: Pressure Distribution at start of the systolic phase (Parabolic profile/SimVascular)
..... 116

Figure 111: Pressure Distribution at start of the systolic phase (Parabolic profile/Crimson) 116

Figure 112: Pressure Distribution at the peak of the systolic phase (Parabolic
profile/SimVascular)..... 117

Figure 113: Pressure Distribution at the peak of the systolic phase (Parabolic
profile/Crimson)..... 117

Figure 114: Pressure Distribution at the end of the systolic phase (Parabolic
profile/SimVascular)..... 118

Figure 115: Pressure Distribution at the end of the systolic phase (Parabolic profile/Crimson)
..... 118

Figure 116: Pressure Distribution during the diastolic phase (Parabolic profile/SimVascular)
..... 119

Figure 117: Pressure Distribution during the diastolic phase (Parabolic profile/Crimson) ... 119

Figure 118: Parabolic velocity profile at the start of the systolic phase (SimVascular) 120

Figure 119: Parabolic velocity profile at the start of the systolic phase (Crimson) 121

Figure 120: Velocity vector field and streamlines at the start of systolic phase (SimVascular) 121

Figure 121: Velocity vector field and streamlines at the start of systolic phase (Crimson) .. 122

Figure 122: Parabolic velocity profile at the peak of the systolic phase (SimVascular) 122

Figure 123: Parabolic velocity profile at the peak of the systolic phase (Crimson) 123

Figure 124: Velocity vector field and streamlines at the peak of systolic phase (SimVascular) 123

Figure 125: Velocity vector field and streamlines at the peak of systolic phase (Crimson) .. 124

Figure 126: Parabolic velocity profile at the end of the systolic phase (SimVascular)..... 124

Figure 127: Parabolic velocity profile at the end of the systolic phase (Crimson)..... 125

Figure 128: Velocity vector field and streamlines at the end of systolic phase (SimVascular) 125

Figure 129: Velocity vector field and streamlines at the end of systolic phase (Crimson) ... 126

Figure 130: Parabolic velocity profile during diastolic phase (SimVascular) 126

Figure 131: Parabolic velocity profile during diastolic phase (Crimson) 127

Figure 132: Velocity vector field and streamlines during the diastolic phase (SimVascular) 127

Figure 133: Velocity vector field and streamlines during the diastolic phase (Crimson) 128

Figure 134: Wall shear stress of the aortic wall at the start of systolic phase (Parabolic/SimVascular) 129

Figure 135: Wall shear stress of the aortic wall at the start of the systolic phase (Parabolic/Crimson) 130

Figure 136: Wall shear stress of the aortic wall at the peak of the systolic phase (Parabolic/SimVascular) 130

Figure 137: Wall shear stress of the aortic wall at the peak of the systolic phase (Parabolic/Crimson) 131

Figure 138: Wall shear stress of the aortic wall at the end of systolic phase (Parabolic/SimVascular) 132

Figure 139: Wall shear stress of the aortic wall at the end of systolic phase (Parabolic/Crimson) 132

Figure 140: Wall shear stress of the aortic wall during diastolic phase (Parabolic/SimVascular) 133

Figure 141: Wall shear stress of the aortic wall during diastolic phase (Parabolic/Crimson) 133

Figure 142: Time averaged wall shear stress for one cardiac cycle (Parabolic/SimVascular) 134

Figure 143: Time averaged wall shear stress for one cardiac cycle (Parabolic/Crimson) 134

Figure 144: Graph comparing the u-velocity component at the upper descending aorta.... 136

Figure 145: Graph comparing the v-velocity component at the upper descending aorta 136

Figure 146: Graph comparing the w-velocity component at the upper descending aorta ... 137

Figure 147: Graph comparing the velocity magnitude at the upper descending aorta 137

Figure 148: Graph comparing the u-velocity component before entering the aortic arch... 139

Figure 149: Graph comparing the v-velocity component before the brachiocephalic artery 139

Figure 150: Graph comparing the w-velocity component before the brachiocephalic artery 140

Figure 151: Graph comparing the velocity magnitude before the brachiocephalic artery ... 140

Figure 152: Graph comparing the u-velocity component before the LCC artery 142

Figure 153: Graph comparing the v-velocity component before the LCC artery..... 142

Figure 154: Graph comparing the w-velocity component before the LCC artery..... 143

Figure 155: Graph comparing the velocity magnitude before the LCC artery..... 143
Figure 156: Graph comparing the u-velocity component before the LS artery..... 145
Figure 157: Graph comparing the v-velocity component before the LS artery 145
Figure 158: Graph comparing the w-velocity component before the LS artery 146
Figure 159: Graph comparing the velocity magnitude before the LS artery 146
Figure 160: Graph comparing the u-velocity component at the upper descending aorta 148
Figure 161: Graph comparing the v-velocity component at the upper descending aorta 149
Figure 162: Graph comparing the w-velocity component at the upper descending aorta ... 149
Figure 163: Graph comparing the velocity magnitude at the upper descending aorta 150
Figure 164: Graph comparing the u-velocity component before the aortic arch..... 151
Figure 165: Graph comparing the v-velocity component before the aortic arch 152
Figure 166: Graph comparing the w-velocity component before the aortic arch 152
Figure 167: Graph comparing the velocity magnitude before the aortic arch 153
Figure 168: Graph comparing the u-velocity component before the LCCA 154
Figure 169: Graph comparing the v-velocity component before the LCCA..... 155
Figure 170: Graph comparing the w-velocity component before the LCCA..... 155
Figure 171: Graph comparing the velocity magnitude before the LCCA..... 156
Figure 172: Graph comparing the u-velocity component before the LSA..... 157
Figure 173: Graph comparing the v-velocity component before the LSA 158
Figure 174: Graph comparing the w-velocity component before the LSA 158
Figure 175: Graph comparing the velocity magnitude before the LSA 159

List of Tables

Table 1: Test Mesh properties	51
Table 2: Data used as inflow boundary condition for test simulation	54
Table 3: Initial values used for test simulation (Pirola et al., 2017)	54
Table 4: Solver Parameters used in the software	55
Table 5: BCT File Structure and Description	57
Table 6: Flow Rates at the Inlet and Outlets with Mass Conservation Verification.....	80
Table 7: Location bound to create the 4D velocity arrays.....	97
Table 8: Number slices used in each 4D velocity array	97
Table 9: Reynolds numbers of each cross-section at the peak of the systolic phase	112
Table 10: Reynolds numbers of each cross-section at the peak of the systolic phase (parabolic profile).....	147

1. Introduction

1.1 Cardiovascular System

The cardiovascular system is widely regarded as one of the most vital systems in the human body, playing a fundamental role in sustaining life. It is responsible for the transportation of blood, oxygen, nutrients, hormones, and waste products to and from the cells, tissues, and organs. Without the constant and efficient operation of the circulatory system, the body would be unable to maintain homeostasis. This disruption would lead to oxygen and nutrient deprivation at the cellular level, accumulation of waste products, and ultimately, organ failure and death.

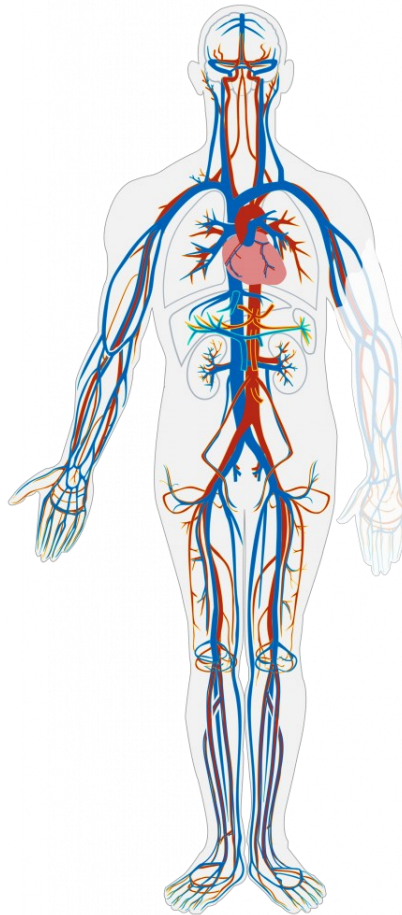


Figure 1: Simple schematic of the cardiovascular system

The cardiovascular system (Figure 1) consists of the heart, a muscular organ that serves as the pump, and a complex network of vessels (arteries, veins, and capillaries) that form a closed circulatory loop. Blood is continually propelled by the heart through these vessels, circulating repeatedly through the body's various circulatory pathways. A key aspect of the cardiovascular system is its role in maintaining homeostasis. It ensures the regulated and uninterrupted flow of blood through an extensive network of capillaries that infiltrate every tissue and reach every cell. Within these microscopic capillaries, blood performs its vital transport function, delivering essential nutrients and substances to the surrounding tissues while simultaneously removing waste products, thereby supporting the overall function of the body. (SEER Training Website, Online)

1.1.1 Heart

The heart's function can be summed up by one word: "pump." Its contractions generate the pressure necessary to propel blood into the major vessels, the aorta and pulmonary trunk, through which blood is then distributed throughout the body. While the term "pump" often evokes images of mechanical devices, the heart is far more intricate; it is a living, dynamic muscle with remarkable capabilities. Throughout this chapter, keep in mind the dual nature of the heart: both a pump and a muscle.

The heart, this relatively small, four-chambered organ, is positioned on the diaphragm, near the center of the thoracic cavity. Its primary role is to maintain continuous blood flow, pumping blood through an extensive network of vessels. To meet the demands of this constant circulation, the heart beats about 100,000 times a day i.e., approximately 2.5 billion beats over an average lifetime (Perez, 2016). As the cornerstone of the cardiovascular system, the heart is essential for sustaining life. It drives blood circulation, delivering oxygen and nutrients to tissues while removing waste products. Without its constant function, the body cannot survive, underscoring the heart's vital role in maintaining overall health and vitality. In Figure 2, a schematic of heart anatomy can be seen.

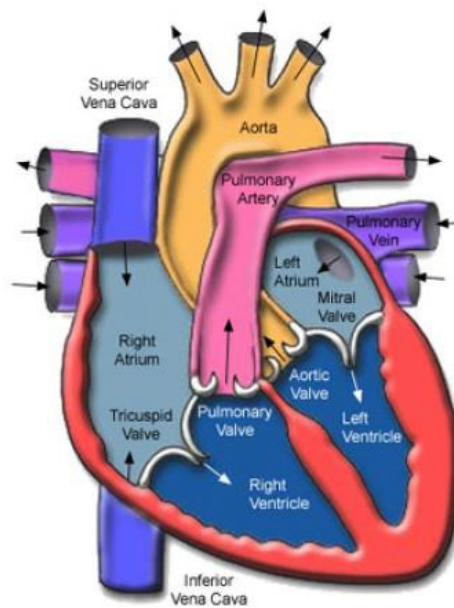


Figure 2: Internal anatomy of the heart (Hammer, 2010)

The heart functions as a pump, driving blood through the circulatory system to sustain life. Circulation occurs in two primary loops: systemic circulation, which delivers oxygen-rich blood to the body, and pulmonary circulation, where carbon dioxide is exchanged for oxygen in the lungs (Betts & Gordon, 2013). Deoxygenated blood from the body returns to the right atrium (RA), passes into the right ventricle (RV), and is pumped to the lungs for oxygenation. Oxygenated blood returns to the left atrium (LA), flows into the left ventricle (LV), and is ejected into the aorta to be distributed throughout the body. From the aorta, blood moves through arteries, arterioles, and capillaries, where nutrient and gas exchange occur before returning to the heart (Perez, 2016).

The heart's pumping action follows a rhythmic sequence known as the cardiac cycle, consisting of alternating contraction and relaxation phases (Figure 3). During systole (ventricular contraction), blood is forced into the aorta and pulmonary arteries. This is followed by diastole, when the ventricles relax and refill blood from the atria. The atria and ventricles function in coordination, when the ventricles contract, the atria relax to collect blood; when the ventricles relax, the atria contract to fill them (Hall, 2011).

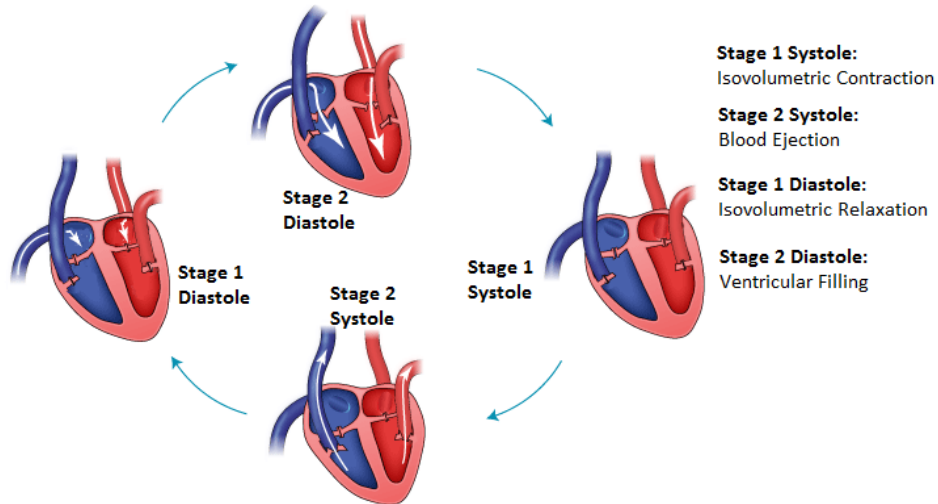


Figure 3: Stages of the Cardiac Cycle (Perez, 2016)

At the start of the cycle, the ventricles relax, allowing blood to flow from the atria through the open mitral and tricuspid valves. Atrial contraction follows, pushing additional blood into the ventricles. As the ventricles begin to contract, rising pressure closes the mitral and tricuspid valves, preventing backflow. When ventricular pressure exceeds that in the aorta and pulmonary arteries, the aortic and pulmonary valves open, ejecting blood from the heart. After ejection, the ventricles relax, the aortic and pulmonary valves close, and the cycle begins again (Hall, 2011).

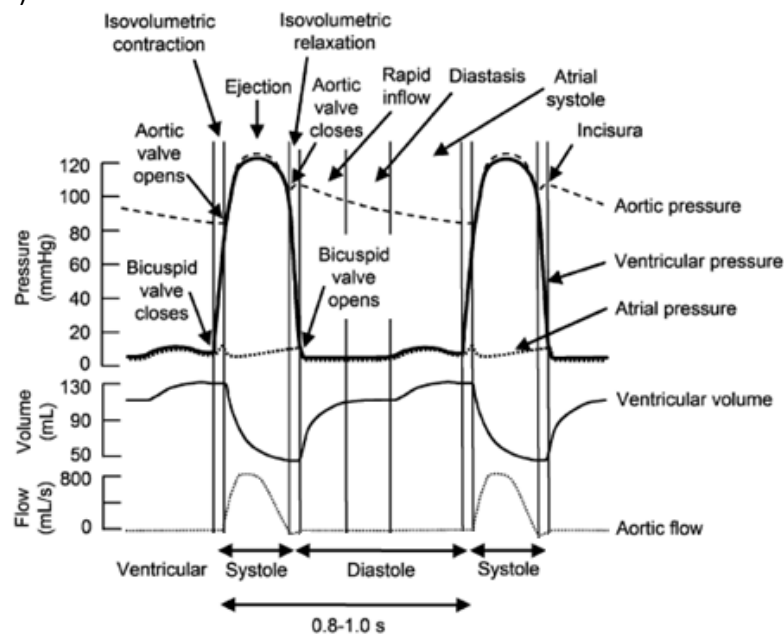


Figure 4: Comparison between aortic, ventricular and atrial pressure. Comparison between ventricular volume and aortic flow (Herman, 2016)

The description of systole and diastole in Figure 4 illustrates the mechanics at the aortic valve. It highlights how changes in ventricular pressure drive the opening and closing of the aortic valve, initiating blood flow through it. This project will focus on pressure and flow measurements just beyond the left ventricle, after the blood has passed through the aortic valve. Figure 4 presents the differences in pressure between the left atrium, ventricle, and aorta, alongside the variations in aortic flow and ventricular volume.

1.1.2 Blood Vessels

Blood vessels are vital tubular structures within the circulatory system, responsible for transporting blood throughout the body (Shea, 2015). Acting as conduits, they deliver oxygen, nutrients, and blood cells to tissues while simultaneously removing carbon dioxide and metabolic waste, while spanning approximately 60,000 miles (Suleman, 2023). The vascular system is categorized into three main types of blood vessels: arteries, veins, and capillaries (Figure 5). Each of them plays a distinct role in circulation, as described below.

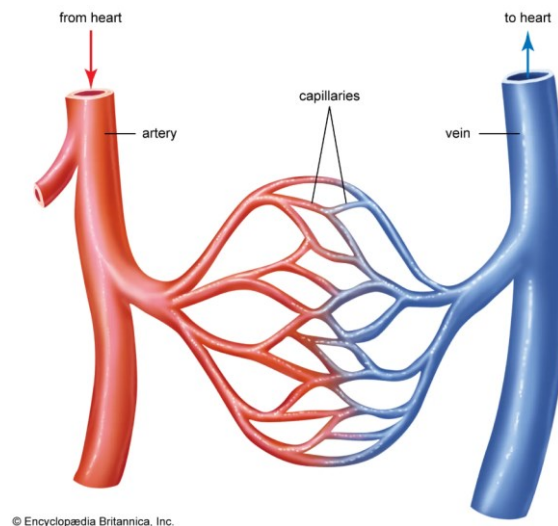


Figure 5: Simplified overview of the basic blood vessels (Britannica, Online)

Arteries are strong, muscular vessels responsible for carrying oxygen-rich blood away from the heart, contributing around 10%–15% of the body’s blood volume. Arteries branch into smaller arterioles, which help regulate blood pressure and distribute blood to various regions of the body. Veins transport deoxygenated blood back to the heart, handling about 75% of the body’s blood volume. These elastic vessels operate under low pressure, and many veins contain valves that prevent the backflow of blood, ensuring efficient circulation. Capillaries, the smallest blood vessels, connect arteries and veins, facilitating the exchange of oxygen, carbon dioxide, and other substances between blood and surrounding tissues. Through their thin walls, capillaries enable nutrient delivery and waste removal at the cellular level, playing a critical role in sustaining organ function (Suleman, 2023).

Blood vessels can also be further classified into two smaller subcategories known as “arterioles” and “venules.” Arterioles are small-diameter vessels within the microcirculation that branch off from arteries and lead directly to capillaries (Maton et al., 1993). Venules, on the other hand, are small veins within the microcirculation that facilitate the return of blood from capillary beds, gradually draining into larger veins. Veins hold approximately 70% of the total blood volume, with venules accounting for around 25% (Woods, 2010).

1.1.3 Aorta

This section focuses on the most important blood vessel in the human body, the aorta, which serves as the primary subject of study. The aorta is the largest and main artery, originating from the left ventricle of the heart. It ascends shortly after leaving the heart, then continues downward through the abdomen, eventually dividing at the aortic bifurcation into two smaller arteries known as the common iliac arteries (Maton et al., 1993).

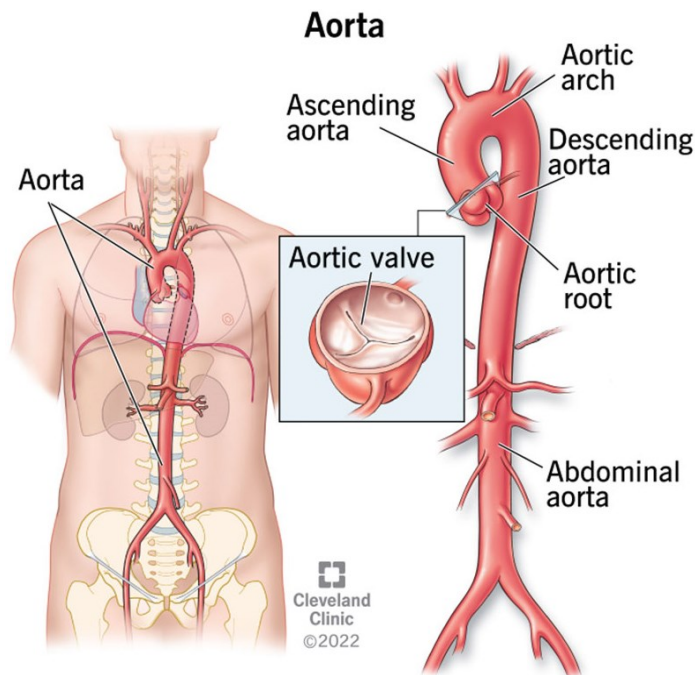


Figure 6: Aorta geometry, main sections and location in the human body (Cleveland Clinic, Online)

Figure 6 illustrates the geometry of the aorta and highlights its primary sections. Blood exits the heart through the aortic valve and flows into the ascending aorta. At the base of the ascending aorta, small pockets form between the cusps of the aortic valve and the aortic wall, known as the aortic sinuses or the sinuses of Valsalva. The left aortic sinus gives rise to the left coronary artery, while the right aortic sinus leads to the right coronary artery. These two arteries work together to supply blood to the heart (Drake et al., 2020).

After the ascending aorta, blood flows into the aortic arch, where the first three major branches are located (Figure 7). The first branch is the brachiocephalic artery, which supplies blood to the right arm, head, and neck (Dugas & Samra, 2023). The second branch is the left common carotid artery, responsible for delivering oxygenated blood to the head and neck (Ashrafian, 2007). The left common carotid artery can be divided into two sections: a thoracic (chest) part and a cervical (neck) part (Ryan et al., 2011). The third and final branch is the left subclavian artery, which supplies blood to the left arm. The left subclavian artery originates from the aortic arch, positioned behind the left common carotid artery at the level of the fourth thoracic vertebra. It ascends through the superior mediastinal cavity to the root of the neck, curving laterally towards the medial border of the scalenus anterior muscle (Woodward et al., 2018).

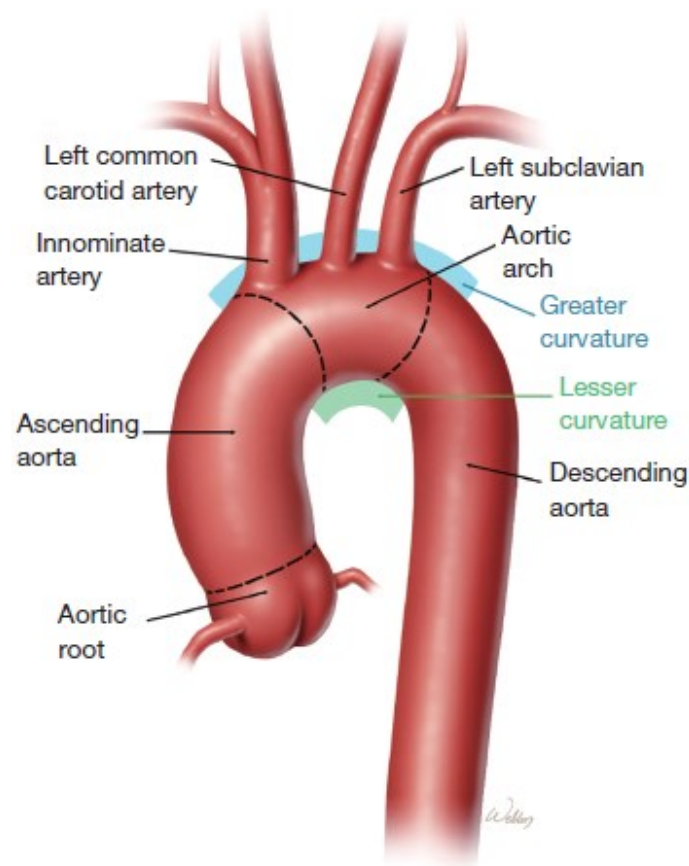


Figure 7: Detailed view of the aortic arch with all its branches visible (Orozco-Sevilla & Coselli, 2023)

The descending aorta follows the aortic arch and extends downward through the chest and abdomen. Anatomically, it is divided into two segments: the thoracic aorta, located in the chest, and the abdominal aorta, situated in the abdominal cavity. As it continues through the abdomen, the descending aorta eventually bifurcates into the two common iliac arteries, which supply blood to the pelvis and lower limbs. The descending aorta plays a crucial role in transporting oxygenated blood from the heart to the rest of the body (UF Health, Aorta anatomy, 2024).

1.2 Magnetic Resonance Imaging (MRI)

Magnetic Resonance Imaging (MRI) is a vital medical imaging technique used in radiology to produce detailed images of the body's anatomy and physiological processes (Figure 8). MRI scanners utilize strong magnetic fields, field gradients, and radio waves to visualize internal organs. Its versatility and sensitivity to various tissue properties make MRI a powerful diagnostic tool. One of the key advantages of MRI is its noninvasive nature, allowing for safe diagnosis across all age groups. Beyond diagnostics, MRI continues to provide valuable insights into the structure and function of the human body. MRI originates from the application of nuclear magnetic resonance (NMR) to radiological imaging. The term "magnetic" reflects the use of different magnetic fields, while "resonance" pertains to aligning the frequency of an oscillating magnetic field with the "precessional" frequency of nuclear spin in tissue molecules. Although the process involves nuclear properties of atoms, the term "nuclear" has been omitted due to public perception, leading to the widespread use of the acronym MRI instead of NMRI (Brown et al., 2014).



Figure 8: Depiction of an MRI structure and scan (NCI, Online)

1.2.1 Brief historical overview of Magnetic Resonance Imaging

Describing the evolution of technological advancements can often be intricate and nuanced. However, even a concise overview can offer valuable insights and serve as inspiration for students new to the subject. The development of Magnetic Resonance Imaging (MRI) traces back to 1973, marked by the pioneering work of Paul Lauterbur and Peter Mansfield (Lauterbur, 1973). By that period, it was well-established that the spin of a hydrogen proton within a magnetic field precesses at the Larmor frequency, the rate at which the magnetic moment of a particle rotates around an external magnetic field (Levitt, 2002). This frequency is directly proportional to the strength of the magnetic field (Rinck, 2024).

Lauterbur and Mansfield's breakthrough stemmed from a simple yet transformative concept, the application of a spatially varying magnetic field across an object. This induced variations in Larmor frequencies, allowing different frequency signals to be isolated, which facilitated spatial mapping and laid the groundwork for MRI. The significance of this discovery was quickly recognized, particularly when Raymond Damadian demonstrated its potential for detecting tumors (Damadian, 1971). This highlights how major technological strides often originate from straightforward but innovative ideas. The introduction of magnetic field gradients to encode spatial information echoed earlier milestones in nuclear magnetic resonance (NMR). Foundational NMR experiments were driven by the interaction between proton spin and magnetic fields, as exemplified by the work of Felix Bloch and Edward Purcell (Sohlman, 2003).

The origins of NMR can be traced to the discovery of proton spin, building upon Otto Stern and Walther Gerlach's work in the 1920s. In the following decade, Isidor Rabi expanded this knowledge by investigating how proton spin responds to magnetic fields (Goldstein, 1992). This set the stage for Bloch and Purcell's groundbreaking discoveries in 1946, where they successfully measured nuclear spin precession within magnetic fields (Hahn, 1950). Their experiments using water and paraffin samples clarified both theoretical and experimental aspects of NMR, shaping the field for future advancements. For their contributions, Bloch and Purcell were awarded the Nobel Prize in Physics in 1952.

Building on this foundation, researchers like Peter Mansfield advanced MRI technology throughout the late 1970s and 1980s, refining imaging techniques and data processing (Mansfield, 1977). In recognition of their work, Mansfield and Lauterbur were jointly awarded the Nobel Prize in Physiology and Medicine in 2003. Clinical MRI scanners began appearing in the early 1980s (Smith et al., 1981), and subsequent technological progress over the following decades has cemented MRI as a vital tool in modern medical practice (Rinck, 2024).

1.2.2 Basic principles of Magnetic Resonance Imaging (MRI)

Magnetic Resonance Imaging (MRI) relies on the behavior of atomic nuclei, primarily hydrogen protons, in response to magnetic fields and radiofrequency pulses. This imaging technique exploits the high abundance of hydrogen in water and fat molecules, making it particularly effective for soft tissue imaging (McRobbie et al., 2017).

Magnetic Field and Proton Alignment

When placed in a magnetic field, protons within the body align with the external field. The strength of this magnetic field determines the energy levels of the protons. This alignment occurs in the direction of the magnetic field (B_0). The body is mostly composed of water, and water molecules are rich in hydrogen atoms, making MRI particularly effective for imaging soft tissues, where water content is high (McGowan, 2008).

Precession and Larmor Frequency

In addition to aligning with B_0 , protons exhibit precession, meaning they wobble around the axis of the magnetic field at a specific frequency known as the Larmor frequency. This frequency depends on the strength of the magnetic field and the type of nucleus being imaged (McRobbie et al., 2017). The following equation is the Larmor equation:

$$f_0 = \gamma B_0$$

, where f_0 is the Larmor frequency, γ is the gyromagnetic ratio (a nucleus-specific constant) and B_0 is the strength of the magnetic field. The Larmor frequency determines the resonance condition necessary for energy absorption during the next phase.

Radiofrequency Pulse and Excitation

To disturb the aligned protons, an external radiofrequency (RF) pulse is applied at the Larmor frequency. This RF pulse provides energy, tipping the protons away from their equilibrium position. The angle by which the protons are flipped (commonly 90° or 180°) depends on the strength (B_1) and duration (t) of the RF pulse:

$$\theta = \gamma B_1 \tau$$

, where γ is the gyromagnetic ratio is, a constant that varies depending on the type of nuclei. This process is known as excitation, and it shifts the protons into a higher energy state (Bernstein et al., 2004).

Relaxation and Signal Generation

Once the RF pulse is turned off, the excited protons gradually return to their original alignment with B_0 . This return to equilibrium generates measurable signals, and the process of returning to the ground state is called relaxation (Haacke et al., 1999). This relaxation process occurs in two distinct ways:

- **T1 Relaxation (Longitudinal Relaxation)**: The recovery of the longitudinal component of magnetization (along the magnetic field axis). It is characterized by the time constant T_1 . The rate of recovery is exponential, and the equation for this process is:

$$M_z(t) = M_0(1 - e^{-t/T_1})$$

, where M_z is the longitudinal magnetization at time t , and M_0 is the equilibrium magnetization.

- **T2 Relaxation (Transverse Relaxation)**: The decay of the transverse component of magnetization (perpendicular to the magnetic field). It is characterized by the time constant T_2 . The equation for this relaxation is:

$$M_{xy}(t) = M_{xy}(0)e^{-t/T_2}$$

, where $M_{xy}(t)$ is the transverse magnetization at time t , and $M_{xy}(0)$ is the initial transverse magnetization.

These relaxation times vary depending on the tissue type, which gives MRI its ability to differentiate between different tissue types based on their relaxation properties.

Repetition Time (TR) and Echo Time (TE)

Repetition Time (TR) refers to the time interval between successive RF pulses applied to the same slice or tissue. TR affects the longitudinal relaxation (T_1) of protons and influences the contrast in T_1 -weighted images. Short TR values allow less time for protons to recover longitudinally, emphasizing tissues with shorter T_1 .

Echo Time (TE) is the time between the application of an RF pulse and the peak of the detected signal (echo). TE affects the transverse relaxation (T_2) and determines the amount of T_2 decay that occurs before signal detection. Short TE values minimize the T_2 effects and are often used in T_1 -weighted imaging, while longer TE values accentuate T_2 decay, used for T_2 -weighted imaging (Brown et al., 2014).

Free Induction Decay (FID) and Spin Dephasing

As transverse magnetization decays, the resulting signal forms what is known as Free Induction Decay (FID). This decay happens faster than T_2 relaxation due to small inhomogeneities in the magnetic field, which cause protons to dephase more rapidly (Brown et al., 2014). The observed transverse relaxation that includes these inhomogeneities is described by the time constant T_2^* :

$$M_{xy}(t) = M_{xy}(0)e^{-t/T_2^*}$$

, where $T_2^* < T_2$

Spin Echo and Gradient Echo

To recover signal lost due to dephasing, MRI employs techniques such as:

- **Spin Echo (SE)**: A secondary 180° RF pulse refocuses dephased protons, compensating for field inhomogeneities and allowing the measurement of T2 relaxation.
- **Gradient Echo (GRE)**: Uses gradient reversals instead of RF pulses to refocus spins, but it remains sensitive to T_2^* effects.

Slice Selection

To image specific cross-sections of the body, MRI applies a gradient along the z-axis during the RF pulse. This causes protons at different spatial positions to experience slightly different magnetic fields and thus precess at different frequencies (Brown et al., 2014). Only the protons precessing at the exact frequency of the RF pulse are excited, enabling the selection of a thin slice of tissue.

The slice selection equation is:

$$f(z) = \gamma(B_0 + G_z z)$$

, where G_z is the gradient applied along the z-axis.

Gradient Fields and Spatial Encoding

MRI spatially encodes signals using gradient magnetic fields applied along different axes (x, y, z). These gradients create small variations in the magnetic field, causing protons in different locations to precess at slightly different frequencies. Mathematically, the frequency of precession for a proton at position r can be expressed as:

$$f(r) = \gamma B(r)$$

, where $B(r)$ is the magnetic field at position r , and γ is the gyromagnetic ratio. This frequency variation is key to the spatial encoding of MRI data. By applying gradients, MRI distinguishes signals from different parts of the body, forming the basis for spatial localization (Brown et al., 2014).

Signal Detection and Fourier Transform

As the protons relax, they emit RF signals that are captured by receiver coils. The detected signals are initially in the frequency domain.

To reconstruct an image, MRI uses the Fourier Transform (FT), which converts frequency data into spatial information. This process maps the detected signals to their respective locations, creating a detailed image of the scanned tissue (Haacke et al., 1999).

K-space and Image Reconstruction

The collected signals fill a data matrix called k-space. The density and quality of data in k-space directly affect image resolution and contrast. High-resolution images require denser k-space sampling. Applying the inverse Fourier Transform (iFT) to k-space data results in the final MRI image.

Tissue Characterization and Contrast

MRI can generate different types of images based on tissue characteristics:

- **T1-weighted imaging**: Tissues with shorter T1 (e.g., fat) appear bright. This type of imaging typically uses short repetition times (TR) and echo times (TE) to minimize T1 effects and reduce the influence of T2 decay.
- **T2-weighted imaging**: Tissues with longer T2 (e.g., water, CSF) appear bright. This is achieved by using long TR to allow for more complete longitudinal relaxation and long TE to maximize T2 relaxation, which enhances the T2-weighted contrast.
- **Proton Density (PD) imaging**: Reflects proton concentration, providing structural detail with minimal emphasis on T1 or T2 differences. This technique typically employs long TR and short TE to minimize the effects of both T1 and T2 relaxation.

These varying contrasts allow MRI to distinguish between different anatomical structures, enhancing diagnostic accuracy (McRobbie et al., 2017).

1.2.3 Phase-Contrast Magnetic Resonance Imaging (PC-MRI)

Phase-Contrast MRI (PC-MRI) is an advanced Magnetic Resonance Imaging (MRI) technique that measures the speed and direction of blood flow or other moving fluids within the body. This method not only visualizes the structure of blood vessels but also tracks how blood moves through them in real-time. PC-MRI serves as a form of Magnetic Resonance Velocimetry and offers a powerful tool for Magnetic Resonance Angiography, enhancing the assessment of vascular health and fluid dynamics (Stankovic et al., 2014).

Fundamentals of PC-MRI

In MRI, atoms with an odd number of protons or neutrons possess angular spin momentum, which is randomly aligned without external forces. When subjected to a strong magnetic field, some spins align with the field's axis, creating net longitudinal magnetization. These spins precess around the magnetic field axis at a frequency proportional to the field's strength.

Applying a radiofrequency (RF) pulse temporarily shifts the axis of spin precession, exciting the spins and tilting them away from alignment. As the spins return to equilibrium, they induce signals in the receiver coils through Faraday's law of induction. Different tissues respond uniquely to this process, allowing imaging parameters to be adjusted to highlight specific tissues or flow (Brown et al., 2014).

PC-MRI leverages this principle to measure fluid flow by analyzing the phase shifts of moving spins. When protons in flowing blood encounter a magnetic field gradient, they experience a phase shift proportional to their velocity. By applying bipolar gradient pulses perpendicular to the flow direction, phase shifts are induced in moving protons. These shifts appear as differences in the MRI signal phase, which can be detected and used to calculate blood flow velocity (Mrimaster, Online).

Phase Shift and Velocity Relationship

Phase shift (φ) of a spin is a function of the Gradient field $G(t)$:

$$\varphi = \gamma \int_0^t B_0 + G(\tau)r(\tau)d\tau$$

, where γ is the Gyromagnetic ratio and $r(\tau)$ represents the position of the spins (protons) at time τ .

In practice, by acquiring two different measurements with applied magnetic gradients that are opposite to each other (bipolar gradients), the results can be combined to calculate a change in phase dependent on the gradient:

$$\Delta\varphi = \gamma G \Delta t u$$

, where $\Delta\varphi$ is the phase shift, γ is the Gyromagnetic ratio, G the gradient strength, Δt how long the gradient is applied and u the velocity of moving spins.

Velocity Encoding (VENC)

A crucial aspect of PC-MRI is the Velocity Encoding (VENC) parameter, defined as the maximum velocity that can be detected without error. For velocities exceeding the VENC, aliasing occurs, leading to inaccurate measurements. In such cases, the acquisition must be repeated with a higher VENC or corrected through post-processing to ensure accurate velocity quantification (Markl et al., 2012).

The phase shift is measured and converted to velocity using the equation:

$$u = \frac{VENC}{\pi} \Delta\varphi$$

where VENC is the maximum velocity that can be recorded, and $\Delta\varphi$ is the recorded phase shift. The previous equation implies that:

$$VENC = \frac{\pi}{\gamma G \Delta t}$$

, where γ is the Gyromagnetic ratio, G the gradient strength, Δt how long the gradient is applied.

The choice of VENC defines the range of visible velocities, known as the 'dynamic range.' Selecting a VENC below the maximum velocity in the slice can induce aliasing, where a velocity just greater than VENC is incorrectly calculated as moving in the opposite direction. Modifying the VENC involves altering the strength and duration of the velocity-encoding gradients (Markl et al., 2012). Lower velocity encoding requires larger gradient areas, resulting in longer echo times (TE) and repetition times (TR).

As with all MR imaging, the quality of PC-MRI velocity maps can be affected by noise. The amount of velocity noise is directly proportional to VENC and inversely proportional to the signal-to-noise ratio (SNR) of the corresponding magnitude images:

$$u_{noise} \propto \frac{VENC}{SNR}$$

This highlights a critical balance—selecting a high VENC prevents aliasing but increases noise, while a low VENC reduces noise but raises the risk of aliasing. To optimize results, the user should estimate the highest expected velocity to prevent phase wrapping and review the images before concluding the scan. Simultaneously, keeping VENC as low as feasible minimizes velocity noise, improving overall image quality (Markl et al., 2012).

1.2.4 4D Flow Magnetic Resonance Imaging

4D Flow MRI builds upon the foundational principles of Phase-Contrast MRI (PC-MRI) by enabling the simultaneous measurement of blood flow velocities in all three spatial directions over time. This technique provides a comprehensive, non-invasive method for evaluating complex flow patterns within vessels and cardiac chambers, offering insights into both anatomical structures and dynamic flow characteristics (Bissell et al., 2023). In this work, this technique was used for data processing and played a crucial role in achieving its outcomes.

Key Principles of 4D Flow MRI

The primary distinction between 4D Flow MRI and standard PC-MRI lies in its ability to encode velocity data along three orthogonal spatial directions (x, y, z) during each phase of the cardiac cycle. This results in volumetric data capturing the temporal evolution of flow, effectively yielding four dimensions, three spatial and the temporal (4D). Velocity encoding along three axes is achieved using three pairs of bipolar gradients applied in different orientations. This allows for the calculation of velocity vectors at each voxel within the imaged volume, which can then be visualized as streamlines or pathlines to provide detailed depictions of blood flow patterns (Markl et al., 2012).

Data Acquisition and Reconstruction

Like PC-MRI, 4D Flow MRI follows a systematic data acquisition and reconstruction process. The simplified steps are as follows:

- **Velocity Encoding**: Like PC-MRI, 4D Flow MRI employs bipolar gradients to encode velocities in the three orthogonal directions. The velocity-encoding parameter (VENC) is selected based on the expected peak velocities in the region of interest to minimize aliasing while reducing noise.
- **Spatiotemporal sampling**: A defining feature of 4D Flow MRI is its ability to capture time-resolved flow data across a 3D volume. Temporal resolution is critical to accurately capturing the dynamics of blood flow during the cardiac cycle.
- **Post-Processing**: After data acquisition, advanced algorithms reconstruct the volumetric dataset of velocity vectors. These algorithms are correct for phase aliasing and noise, ensuring the accuracy of flow quantification. This process is essential for generating meaningful and interpretable results.

Advantages and applications of 4D Flow Magnetic Resonance Imaging

The previous aspects the 4D Flow MRI provides provide unlike PC-MRI visualization of complex flow phenomena, such as vortices, turbulent flow, and secondary flow patterns (Markl et al., 2012). Additionally, it provides insights into flow dynamics across entire vascular networks or cardiac chambers, enabling detailed hemodynamic assessment and allows for post-hoc analysis of multiple planes or regions without the need for additional imaging.

These kinds of aspects can have various applications such as assessing flow in large vessels like the aorta, pulmonary arteries, and veins, identifying conditions such as aneurysms, stenosis, or abnormal flow patterns, Understanding complex flow patterns in patients with congenital anomalies and evaluating the impact of surgical interventions or medical treatments on blood flow (Azarine et al., 2019)

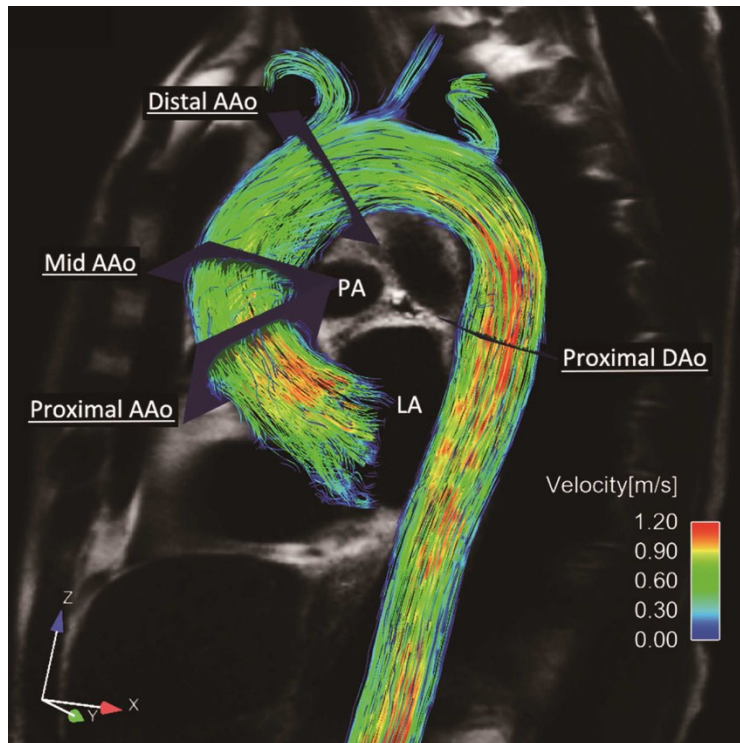


Figure 9: Example 4D Flow MRI data of the upper part of the aorta. The blood velocity distribution can be seen as well as the respective coordinate axis (Shan et al., 2017)

1.3 Fluid Mechanics

A very crucial part of this work is the study of the blood. Blood can be subsumed in the family of Fluids, therefore, to analyze its mechanical behavior, some powerful tools of the domain of fluid mechanics must be used.

1.3.1 Navier-Stokes

In the field of fluid mechanics, the Navier-Stokes equations are used to describe the fluid flows. These equations represent Newton's second law of motion for fluids. The former states that the sum of the forces applied to a body is equal to the acceleration times the mass of the body. The Navier-Stokes equations were first introduced in the 19th century by the Irish physicist Sir George Gabriel Stokes and the French physicist and engineer Claude-Louis Marie Henri Navier (Constantin & Foias, 1988). The equations are part of the differential equations with boundary conditions family with the assumption of atmospheric turbulence and they are expressed as follows:

$$\frac{\partial \vec{u}}{\partial t} + (\vec{u} \nabla) \vec{u} = -\frac{1}{\rho} \nabla p + \nu \nabla^2 \vec{u}$$

$$\nabla \cdot \vec{u} = 0$$

where \vec{u} is the velocity of the flow, p the static pressure, ν the kinematic viscosity, ρ the density, ∇p the pressure gradient and $\nabla^2 \vec{u}$ represents the second spatial derivatives of the velocity components, which quantify how the velocity gradients change across the fluid. The second equation is called the continuity equation.

In the Navier-Stokes equations each of the terms represents a physical property of the fluid.

- The term $\frac{\partial \vec{u}}{\partial t}$ represents the rate of change of velocity with respect to time at a given point. Physically, it accounts for the unsteady (time-dependent) behavior of the fluid, such as flow acceleration or deceleration over time.
- The term $(\vec{u}\nabla)\vec{u}$ (Convective acceleration) represents the change in velocity due to the movement of the fluid itself. It's a non-linear term describing how velocity changes as a fluid particle moves through the velocity field.
- The term $-\frac{1}{\rho}\nabla p$ (Pressure gradient force) represents the force exerted by pressure differences in the fluid. The negative sign indicates that fluid moves from regions of high pressure to low pressure. Dividing the pressure gradient with the density ensures the term is expressed as acceleration.
- The term $\nu\nabla^2\vec{u}$ (Viscous dissipation) accounts for the effects of viscosity, a fluid's internal friction. The Laplacian of velocity, representing how velocity gradients spread out or dissipate and the kinematic viscosity quantifies how much resistance the fluid offers to deformation.

Therefore, one can say that the left side of the Navier-Stokes equation represents the total acceleration of a fluid particle, combining time-dependent changes and changes due to motion and that the right side represents the forces acting on the fluid, the pressure forces that drive the flow and the viscous forces that resist motion.

In the continuity equation, the term $\nabla\vec{u}$ presents the net rate of fluid flow out of a point. The fact that it is equal to zero means that the fluid's volume remains constant as it flows. In other words, this enforces the conservation of mass: fluid entering a region must equal the fluid leaving it. The continuity equation complements the Navier-Stokes equations by ensuring mass conservation, which is crucial for any flow analysis.

Here it must be noted that the previous equations are not in their general forms. In this work it is assumed that the fluid is incompressible

The main advantage of the Navier-Stokes equations is that they can be used for all flows and hold true even for extremely unpredictable flows. However, the solutions given by the equations are very scarce due to the term $(\vec{u}\nabla)$, which adds non-linearity to the equations (Obligado et al., 2013).

1.3.2 Pipe Flow

One of the fundamental models in fluid mechanics is pipe flow, which refers to the movement of fluid within a closed conduit and is also known as internal flow (Çengel et al., 2014). Pipe flow can be classified into two main types: laminar flow, often described by the Hagen-Poiseuille equation, and turbulent flow, which can be analyzed using the Moody's diagram. In this study, the focus is on laminar flow.

The Hagen-Poiseuille equation describes the pressure drop in an incompressible, Newtonian fluid undergoing laminar flow through a long cylindrical pipe with a constant cross-section. This equation is expressed as follows:

$$\Delta P = \frac{8\mu L Q}{\pi R^4} = \frac{8\pi\mu L Q}{A^2}$$

, where ΔP is the pressure difference, L the length of pipe, μ the dynamic viscosity, Q the volumetric flow rate, R the pipe radius and A the cross-sectional area (Pfitzer, 1976). It should be noted that this equation is based on several assumptions: the fluid is incompressible and Newtonian, the flow remains laminar, the pipe has a constant circular cross-section and is significantly longer than its diameter, and there is no acceleration of fluid within the pipe. However, when velocity or pipe diameter exceeds a certain threshold, the flow transitions to turbulence, resulting in greater pressure drops than those predicted by the Hagen-Poiseuille equation (Pfitzner, 1976).

The Hagen-Poiseuille equation can also be derived from the Navier–Stokes momentum equations in 3D cylindrical coordinates equations following the assumptions that the flow is steady, axisymmetric, fully developed and the radial and azimuthal components of the fluid velocity are zero. By solving the Navier-Stokes equations with these assumptions considered and the application of the no slip boundary condition at the pipe wall ($u = 0$ for $r = R$), the following relation is created:

$$u = \frac{\Delta P}{4\mu L}(R^2 - r^2)$$

This equation indicates that the profile of the velocity inside of a pipe flow is parabolic (Figure 10).

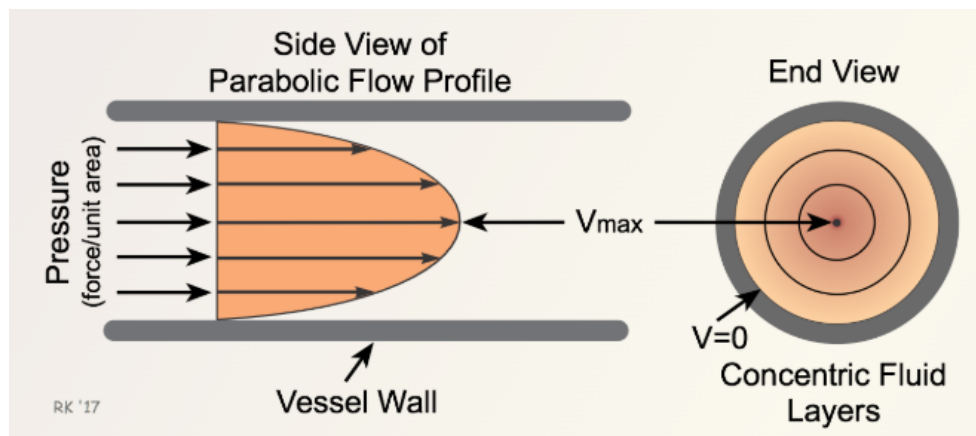


Figure 10: Depiction of the parabolic velocity profile (CV Physiology, Online)

The velocity profile equation also indicates that for $r = 0$ (pipe centerline), the maximum velocity occurs and is described by:

$$u_{max} = \frac{\Delta P}{4\mu L} R^2$$

For calculating the volumetric flow rate, the average velocity of the cross-section is needed. The value of the average velocity of the cross section can be easily calculated by:

$$u_{avg} = \frac{1}{\pi R^2} \int_0^R 2\pi r u dr = \frac{1}{2} u_{max}$$

The previous equation indicates that the average velocity is obtained after integrating over the pipe cross section. After its calculation, the volumetric flow rate is obtained by:

$$Q = \pi R^2 u_{avg}$$

The Hagen-Poiseuille equation is derived by combining the previous equations.

Shear stress is the final key quantity in fluid mechanics, arising when a real fluid, whether liquid or gas, flows along a solid boundary. The no-slip condition, previously mentioned as a boundary condition, dictates that the fluid's velocity at the boundary is zero relative to the surface, while at some distance away, it reaches its full flow velocity. The region between these points is known as the boundary layer. In laminar flow, shear stress in Newtonian fluids is directly proportional to the strain rate, with viscosity acting as the proportionality constant (Day, 1990). However, for non-Newtonian fluids, viscosity is not constant. Shear stress is transferred to the boundary due to this velocity loss, but in this work, only Newtonian fluids will be considered. To illustrate this, the shear stress at a surface element parallel to a flat plate at a given point y for a Newtonian fluid is expressed as:

$$\tau(y) = \mu \frac{\partial u}{\partial y}$$

, μ stands for the dynamic viscosity of the flow, u as the flow velocity along the boundary and y the height above the boundary.

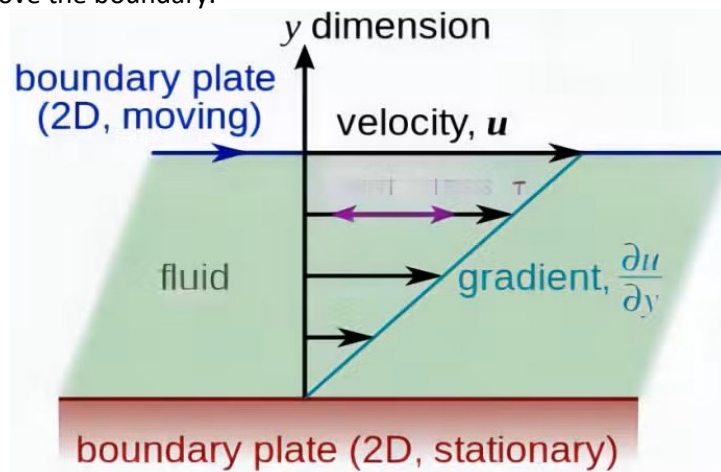


Figure 11: Visualization of shear stress profile (AOBL, Online)

From Figure 11 it is easier to see that the wall shear stress is defined as:

$$\tau_w = \tau(y = 0) = \mu \left. \frac{\partial u}{\partial y} \right|_{y=0}$$

1.3.3 Computational Fluid Dynamics

As was previously mentioned, the Navier-Stokes equations are challenging to solve analytically due to the non-linearities they introduce. A solution to this problem is provided by Computational Fluid Dynamics (CFD). CFD is a field within fluid mechanics that employs numerical techniques and data structures to analyze and solve fluid flow problems. By leveraging computer-based calculations, CFD simulates how fluids (liquids and gases) behave and interact with surfaces defined by boundary conditions.

At its core, CFD relies on numerical techniques to approximate solutions over discrete points or volumes within the geometry where the problem needs to be solved. This process, known as discretization, breaks down the fluid equations into smaller, solvable parts. For example, the geometry of the flow is divided into small volumes (called "cells" or "control volumes"), and the equations are solved iteratively at each point. These calculations progressively approximate the solution for the entire flow field (Eslahpazir, 2011).

The procedure for solving a problem using CFD can be summarized in the following steps:

- **Preprocessing:** The geometry and physical boundaries of the problem are defined using computer-aided design (CAD) tools. The data is processed and cleaned up, and the fluid domain is extracted. The fluid region is divided into discrete cells, forming the mesh. This mesh can be uniform or non-uniform, structured or unstructured, and may consist of hexahedral, tetrahedral, prismatic, pyramidal, or polyhedral elements.
- **Defining Physical Models:** The relevant physical models are specified, such as the equations of fluid motion, enthalpy, radiation, or species conservation.
- **Boundary and Initial Conditions:** Boundary conditions are set to define the fluid's behavior and properties at the domain's edges. For transient problems, initial conditions are also established.
- **Simulation:** The simulation is launched, and the governing equations are solved iteratively. This can be done in a steady-state or transient manner, depending on the nature of the problem.
- **Postprocessing:** After the simulation, a postprocessor is used to analyze and visualize the results. This step provides insights into the fluid's behavior and allows engineers to optimize the system under study.

The accuracy of CFD solutions depends significantly on the numerical methods used for discretization. Some of the most widely used methods include:

- **Finite Difference Method (FDM):** This method approximates derivatives by using differences between neighboring points in the grid. It is simple and widely used for solving differential equations in fluid dynamics (Anderson, 1995).
- **Finite Element Method (FEM):** This method divides the domain into smaller elements and applies variational principles to derive equations for fluid flow. It is often applied to complex geometries where flexibility in element shape is advantageous (Anderson, 1995).
- **Finite Volume Method (FVM):** This method divides the fluid domain into small control volumes and solves the equations for conservation laws (mass, momentum, and energy) over these volumes. It is particularly suitable for solving fluid flow problems (LeVeque, 2002).

By combining these steps with the appropriate numerical techniques, CFD enables engineers and researchers to simulate complex fluid behaviors. This capability is essential for designing and optimizing systems in various industries, such as biomedical engineering.

1.4 Hemodynamic Models

With a foundational understanding of the physiology of the circulatory system and the basics of computational fluid dynamics, the next logical step is to merge these two scientific fields. This integration enables the creation of computational models that simulate blood flow within human vessels using principles and tools from computational fluid mechanics.

1.4.1 Arterial Models

The cardiovascular system is one of the most intricate systems to understand due to the complex interplay between its various physiological processes and control mechanisms. To improve diagnosis and gain deeper insights into its physiology, several approaches have been developed.

In recent years, mathematical modeling of the human cardiovascular system has become essential for understanding cardiovascular behaviors, disorders, etc., offering tools such as computational simulations and physical device modeling. A wide variety of models have been created to represent the arterial system, and these models are classified based on the specific features of the system they aim to describe. It is crucial to recognize that models are not inherently “good” or “bad” but are instead tailored to meet the needs of particular applications (Kokaları, 2013). Although each model has a distinct purpose, their common objective is to enable non-invasive investigation of the vascular system. The primary types of arterial models include anatomically based distributed models, tube models, and lumped models (Alfonso, 2014). A schematic of such models is presented in Figure 12.

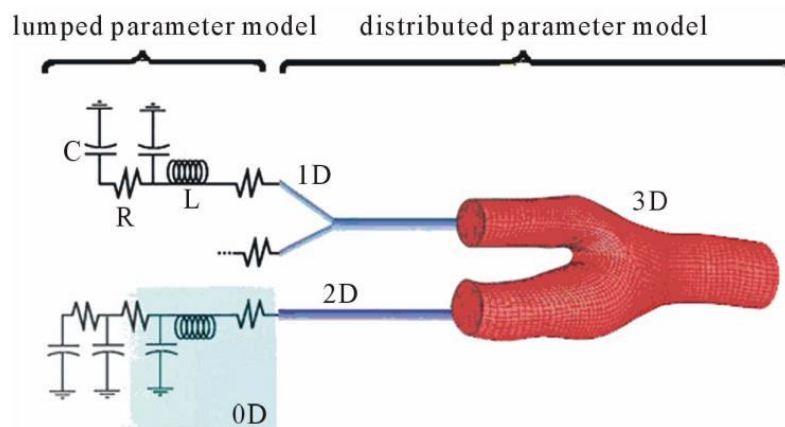


Figure 12: Description of arterial models (Perez, 2016)

This project will focus on the use of a lumped model. Lumped models are categorized as 0-dimensional (0D) because they assume that fundamental variables of the cardiovascular system, such as pressure and flow, are uniformly distributed across all compartments (e.g., organs and vessels) at any given time. However, for experiments that require consideration of spatially varying phenomena, other types of models are more suitable, such as:

- **1D models** account for wave propagation effects and allow the variation of flow velocity along a vessel to be described.
- **2D models** capture radial variations in flow velocity, particularly in tubes with axial symmetry.
- **3D models** are employed for applications requiring detailed descriptions of flow in specific regions of the arterial system, such as vessel bifurcations, within heart ventricles, or across heart valves (Kokalari, 2013).

Each type of model serves different purposes, and the selection depends on the specific requirements of the study.

Lumped models have significant limitations, primarily their inability to analyze wave transmission effects, blood flow distribution variations, or the impact of localized vascular changes. Despite these shortcomings, their functionality can be enhanced by constructing multiple compartment models. Such models divide the systemic arterial tree into separate segments rather than treating it as a single block. This approach allows for distinctions in fundamental variables, such as pressure and flow, between different vessel segments. Each segment functions as an independent lumped model, offering the advantage of flexibility and enabling more detailed analysis in specific regions of interest (Ursino, 1998). However, since this project does not require such a high level of detail, a single-compartment lumped model will be employed to represent the entire systemic arterial tree.

1.4.2 The Windkessel Models

The Windkessel model, a lumped representation of the human arterial system, is designed to simulate the systemic arterial tree. This model was developed by the German physiologist Otto Frank in the late 19th century (Frank, 1990). Its name is derived from a German term meaning "air chamber." The Windkessel model describes the systemic arterial system as an analogy of a hydraulic or electric circuit (Figure 13).

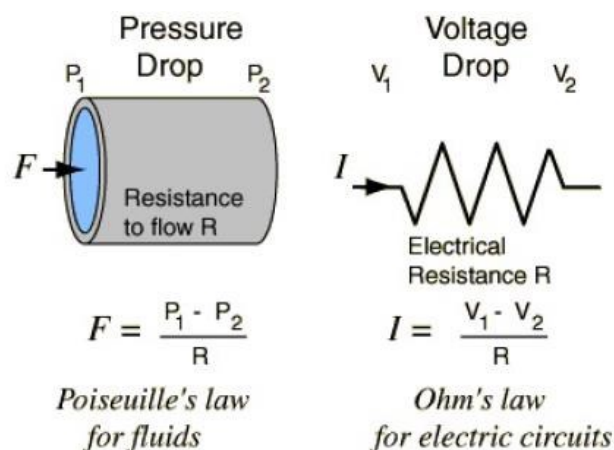


Figure 13: Analogy between Ohm's and Poiseuille's law (GSU Hyperphysics, Online)

In Otto Frank's initial design, the system consisted of a water pump connected to a chamber filled with water, leaving an air pocket. As the pump operated, the water compressed the air, which then exerted pressure to push the water out of the chamber. This concept can also be translated into an analogy with an electrical circuit, mimicking the mechanics of the heart. However, in the electrical analogy, blood is no longer represented by water but by electrons.

In this context, the driving force for electron movement is not pressure but a voltage difference. Similarly, flow is redefined as the variation of electric charge over time (current) rather than the change in volume over a given time.

The original Windkessel model, also known as the two-element Windkessel model, incorporates two primary parameters: peripheral resistance and arterial compliance (Manning, 2002). To enhance the model, additional parameters can be introduced, leading to more complex variations of the Windkessel model (Perez, 2016).

Two element Windkessel Model

As was mentioned in the previous section, the two-element Windkessel model characterizes arterial behavior using two key parameters: aortic compliance and peripheral resistance. Peripheral resistance represents the opposition encountered by blood as it moves through the systemic arterial system. An increase in resistance results in a greater pressure difference for a given flow rate. The following relation defines peripheral resistance.

$$R_p = \frac{\text{Pressure difference (Gradient)}}{\text{Difference between input and output flowrate}} = \frac{P_1 - P_2}{Q_1 - Q_2} = \frac{\Delta P}{\Delta Q}$$

It can be easily noticed that the previous formula shares similarities with the Ohm's law.

$$U = R \cdot I$$

, where in our case we have the following form:

$$\Delta P = R_p \Delta Q$$

As a result, peripheral resistance is depicted as an electric resistor in the circuit analogy. Physiologically, the peripheral (hydraulic) resistance depends on the length and the radius of the vessel, and the viscosity of the fluid. Following this principle, more resistance is encountered in small vessels, which means that the part of the system accounting for most of the resistance will be arterioles and capillaries. The peripheral resistance can be described then with the following relation.

$$R_p = \frac{8\mu l}{\pi R^4}$$

, where μ the viscosity of the fluid, l the length of the vessel and R the radius of the vessel.

Figure 14 illustrates the hemodynamic representation of the two-element Windkessel model, highlighting its equivalence to an electrical circuit with resistors and capacitors.

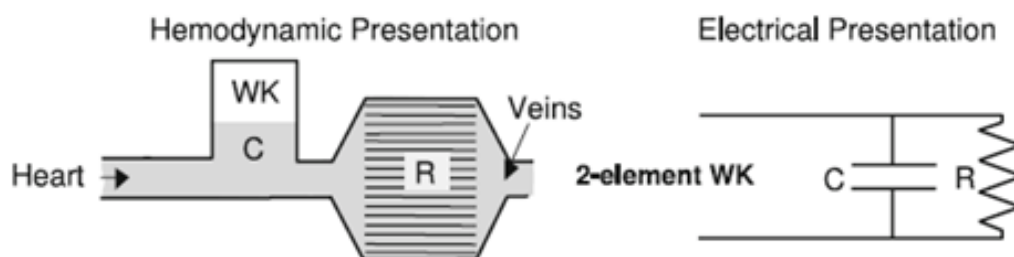


Figure 14: Hemodynamic and electrical presentation of the 2-element windkessel model (Westerhof, 2009)

In addition to peripheral resistance, larger arteries in the human body are also characterized by a property known as compliance. Compliance is defined as the capacity of an artery to accommodate changes in volume when subjected to a specific change in pressure. Mathematically, it is expressed as:

$$C = \frac{\Delta V}{\Delta P}$$

This relationship demonstrates that compliance reflects the change in volume (ΔV) of an artery for a given pressure change (ΔP) (Westerhof, 2009).

Given that flow (Q) represents the rate of volume change over time, it can be expressed as:

$$Q = \frac{dV}{dt}$$

By combining these concepts, a relationship between compliance, pressure, and flow can be established as:

$$\Delta Q = C \cdot \frac{dP}{dt}$$

This equation indicates that compliance also has an electrical circuit analogue, where it can be represented by a capacitor. In electrical terms, capacitance (C_{el}) is defined as the ratio of charge (Δq) to the change in voltage (ΔU):

$$C_{el} = \frac{\Delta q}{\Delta U}$$

Similarly, in this analogy, the flow of blood corresponds to electrical current (I), which can be expressed as:

$$I = C_{el} \cdot \frac{dU}{dt}$$

By integrating these concepts, the two-element Windkessel model assumes that the pressure-to-volume ratio remains constant and that the outflow is proportional to pressure. Volumetric inflow $Q(t)$ equals the sum of the volume stored in the capacitive element and the volumetric outflow through the resistive element. The resulting differential equation for the model is:

$$Q(t) = \frac{P(t)}{R_p} + C \frac{dP(t)}{dt}$$

, where $Q(t)$ volumetric inflow due to the pump (heart) and is measured in volume per unit time, while $P(t)$ is the pressure with respect to time measured in force per unit area, C is the ratio of volume to pressure for the Windkessel, and R_p is the peripheral resistance relating outflow to fluid pressure (Westerhof, 2009).

Three Element Windkessel Model

In this section a more complex form of the Windkessel model will be presented. The three-element Windkessel model builds upon the foundation from the two-element Windkessel model but includes a new parameter called distal (characteristic) resistance (R_d).

From bibliography (Westerhof, 2009) it can be derived that the new relation for the new parameter is:

$$R_d = \frac{v_w \rho}{A}$$

The previous question translates to the fact that characteristic resistance (R_d) is defined as wave speed (v_w) times blood density (ρ) divided by cross-sectional area (A).

Figure 15 illustrates the hemodynamic representation of the three-element Windkessel model, highlighting its equivalence to an electrical circuit with resistors and capacitors.

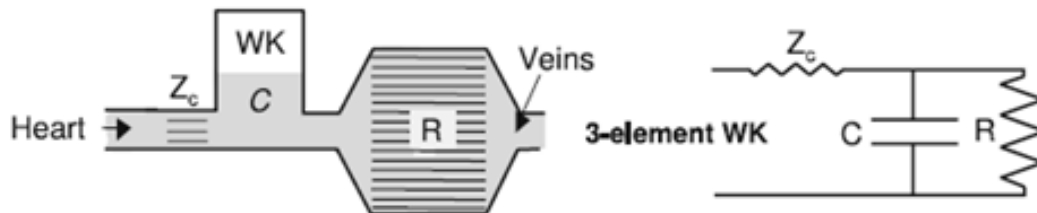


Figure 15: Hemodynamic and electrical presentation of the 3-element windkessel model (Westerhof, 2009)

The differential equation for the three-element Windkessel model is:

$$\left(1 + \frac{R_d}{R_p}\right) Q(t) + CR_d \frac{dQ(t)}{dt} = \frac{P(t)}{R_p} + C \frac{dP(t)}{dt}$$

where R_d is the characteristic resistance (this is assumed to be equivalent to the characteristic impedance), while R_p represents the peripheral resistance. This model is widely used as an acceptable model of circulation due to its ability to balance simplicity with physiological accuracy. By incorporating characteristic resistance alongside peripheral resistance and compliance, it effectively captures both steady and pulsatile flow dynamics, including wave reflections and transient phenomena. Its computational efficiency and strong experimental validation make it a versatile tool for understanding arterial hemodynamics and applying it to clinical diagnostics and cardiovascular research. (Westerhof, 2009).

Four element Windkessel Model

This section explores the final and most complex type of Windkessel model. While the three-element Windkessel model provides valuable insights, it tends to overestimate arterial compliance and underestimate the characteristic resistance of the circulatory system (Westerhof, 2009). To address these limitations, an additional parameter is introduced to account for the fluidic inertia of blood as it flows through the system. This parameter, known as inertance (L), enhances the model's physiological accuracy. Depending on how inertance is incorporated, the model can be structured as either the four-element series Windkessel model or the four-element parallel Windkessel model (Perez, 2016).

Figure 16 shows the four-element Windkessel in its two configurations. The first one in its series configuration, while the second one shows the parallel configuration of the model.

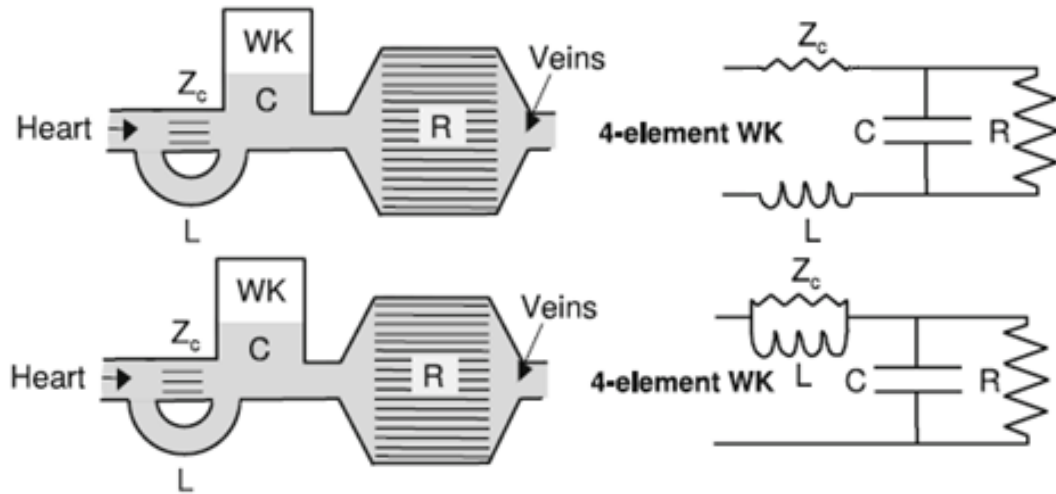


Figure 16: Four-element-series Windkessel model (a), four-element-parallel Windkessel model (b)

The new parameter of inertance is described by the relationship below:

$$L = \frac{l\rho}{A}$$

, where l is the length of the vessel, ρ is the density of the fluid and A is the cross-sectional area of the vessel.

Inertance, accounts for the inertia of blood flow and depends on the vessel's length, cross-sectional area, and the fluid's density. It is measured in units of mass per length ($\frac{M}{l^4}$) and is integrated into the proximal component of the circuit to represent the effects of blood flow inertia. This aspect is not considered in the simpler two- and three-element Windkessel models (Westerhof, 2009).

The new parameter is related to pressure and flow through the following equation:

$$\Delta P = L \frac{dQ}{dt}$$

In electrical terms, inertance has an analogue in the form of an inductor (L_{el}), with the corresponding relationship:

$$\Delta U = L_{el} \frac{dI}{dt}$$

, where ΔU is the change in voltage and I denotes the electrical current flow.

Finally, the differential equation that describes the four- element windkessel model is the following:

$$\left(1 + \frac{R_d}{R_p}\right)Q(t) + \left(CR_d + \frac{L}{R_p}\right)\frac{dQ(t)}{dt} + LC\frac{d^2Q(t)}{dt^2} = \frac{P(t)}{R_p} + C\frac{dP(t)}{dt}$$

2. Methods

In this section of this work the complete methodology that was developed for data analysis and interpretation will be presented. This will contain the 4D Flow MRI data acquisition, their pre-processing, the model reconstruction, the simulations, and the comparison of the simulation data with the patient data from the 4D flow MRI scan.

2.1 Software

Before delving into the main analysis of the methodology employed in this study, it is essential to first introduce the software used for running the CFD simulations and post-processing their results.

2.1.1 SimVascular

Simvascular is an open-source software specialized in cardiovascular simulation originally developed at Stanford University in the lab of Charles Taylor (Updegrove et al., 2017). It was designed to provide a complete pipeline for cardiovascular modeling, from medical image segmentation to patient-specific blood flow simulations and analyses. Released in 2007, it became the only tool offering an integrated workflow from model creation to simulation results. The software allows users to create accurate cardiovascular models by providing features such as boundary conditions for realistic pressure levels, a reliable finite element flow solver, and tools for fluid-structure interaction.

Initially, the need for commercial licenses limited its accessibility and hindered its widespread use. To address these challenges, the SimVascular revitalization project began in 2013, focusing on making the software fully open source. The project introduced new features to improve usability and accuracy, such as 3D segmentation, mesh repair, and modeling tools for blood flow and vessel wall interactions. Today, SimVascular offers a user-friendly interface, online documentation (<https://simvascular.github.io/documentation/quickguide.html>), and case studies, making it an accessible and powerful tool for cardiovascular research (Updegrove et al., 2017).

2.1.2 CRIMSON

CRIMSON (Cardiovascular Integrated Modelling and Simulation) is an open-source software platform designed to support cardiovascular research through computational modeling and simulation. Inspired by SimVascular, it was developed to overcome certain limitations and provide a more user-friendly, modern interface for researchers, clinicians, and students (Arthurs et al., 2021). The software offers a comprehensive pipeline that spans from medical image segmentation and finite element mesh generation to setting up boundary conditions, running simulations, and visualizing results. CRIMSON focuses on simulating blood flow in patient-specific vascular geometries using advanced tools that analyze pressure, velocity, and wall shear stress fields. These capabilities make it ideal for applications such as surgical planning, device design, and cardiovascular disease research.

Like Simvascular, CRIMSON features support for zero-dimensional modeling, which allows users to simulate reduced-order models quickly. This mode provides a rapid and cost-effective way to explore parameter effects without the computational demands of a full 3D simulation. It is especially useful for testing models, understanding parameter interactions, and teaching novices about cardiovascular modeling (Arthurs et al., 2021).

CRIMSON also like Simvascular includes parallel simulation capabilities, enabling users to run large-scale simulations efficiently. Using Message Passing Interface (MPI), the software can utilize multiple computing cores to solve complex cardiovascular problems. This flexibility allows simulations to be executed either locally or on high-performance computing systems, ensuring scalability for advanced research needs. With its focus on accessibility, CRIMSON combines powerful computational tools with an intuitive graphical interface. Features like customizable boundary conditions, interactive error prevention, and seamless workflows make it suitable for a broad audience while ensuring and accurate simulations (Arthurs et al., 2021).

2.1.3 ParaView

In the context of this work ParaView was used to interpret the results of the simulations and evaluate the simulation performance. ParaView is an open-source software designed for visualizing and analyzing large datasets, widely used in research and engineering. Developed by Kitware in collaboration with several academic and research institutions, ParaView was first released in 2002. Its primary goal is to handle massive datasets efficiently while remaining accessible to a broad user base, including scientists, engineers, and students (Ayachit, 2015).

ParaView provides tools for creating interactive visualizations, allowing users to explore data from various scientific fields. It supports a wide range of data formats and offers capabilities like slicing, contouring, volume rendering, and creating animations. These features make it versatile for analyzing simulation results, conducting post-processing, and presenting findings visually (Ayachit, 2015).

A key strength of ParaView is its scalability. It can run on a single computer for smaller projects or scale up to distributed computing environments for processing extremely large datasets. This flexibility ensures that users can adapt the software to their needs, whether for small-scale studies or advanced research requiring high-performance computing (Ayachit, 2015).

The software also offers an intuitive interface for beginners while supporting Python scripting for advanced users who need customized workflows. This balance between ease of use and advanced functionality makes ParaView an essential tool for data-driven research and visualization.

2.2 Procedure Overview

This section provides an overview of all the tools utilized in this work, along with a detailed explanation of the entire process implemented throughout the study.

2.2.1 Data Acquisition and interpretation

The study begins with the acquisition of 4D Flow MRI data. In collaboration with 4D Flow MRI specialists at Attikon Hospital in Athens, a 4D Flow scan of the thoracic aorta was obtained, covering an entire cardiac cycle. The scan was conducted using a Philips Achieva 3T MRI scanner.

The typical structure of 4D Flow data includes three main folders, each corresponding to one of the three velocity encoding directions: left-right, anterior-posterior, and foot-head. Each folder contains two types of DICOM images: magnitude images and phase images. Magnitude images provide anatomical information about the patient's vessels, while phase images capture blood flow velocity within the vessels.

Figure 17 is an example magnitude image. As can be seen from this image, basic anatomic features of the patient can be seen (e.g. aorta, heart, spine, etc.). The image also contains information about the slice position that we are looking at, the slice thickness and some technical data about the 4D Flow scan. Additionally, it can be seen that the velocity encoding direction for this image is the right-left from the initials of RL. The initials for the other two velocity encoding directions are FH for foot-head and AP for anterior-posterior.

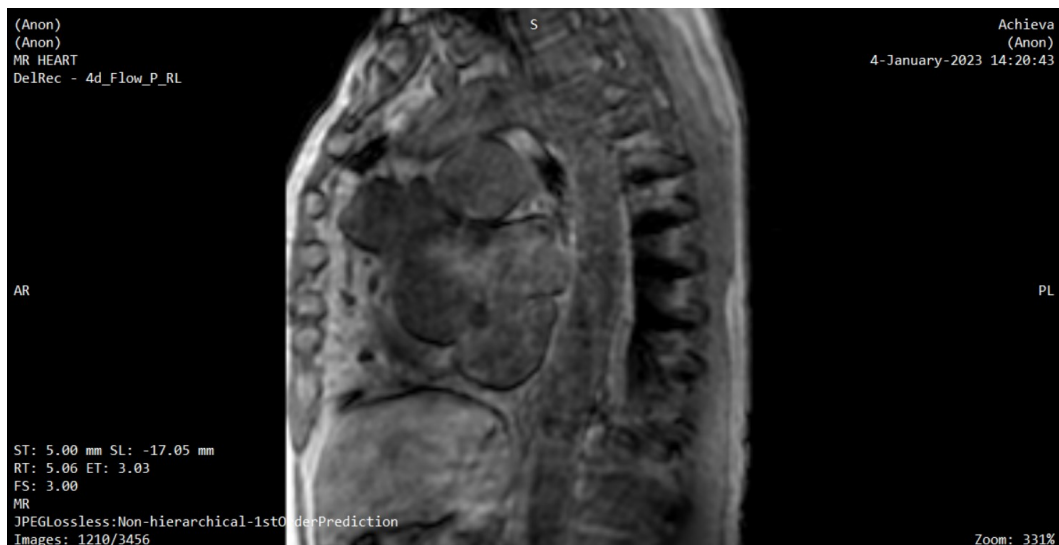


Figure 17: Sample magnitude image of the data used

Figure 18 is an example phase image. This image shares some technical details about the scan and slice but differs in its focus on what is depicted. In phase images, the pixel values represent blood flow velocity in a specific direction along the encoded spatial axes. These values are derived from phase shifts caused by the motion of hydrogen protons in the presence of magnetic field gradients. Similar to magnitude images, each phase image corresponds to one spatial direction (left-right, anterior-posterior, or foot-head). The pixel intensity indicates the velocity component in that direction, where darker pixels and brighter pixels signify flow in opposite directions, while grayer pixels almost zero flow. In the current image, the blood flow highlights the geometry of the aorta.



Figure 18: Sample phase image of the data used

A crucial aspect of phase images is the velocity encoding parameter (VENC). The velocity values are encoded within a range defined by the VENC set during the MRI scan. The relationship between pixel intensity and actual velocity is linear: positive values indicate flow in one direction, while negative values indicate flow in the opposite direction. These phase images are vital for reconstructing the full three-dimensional velocity field within the vessel. For each spatial encoding direction, the VENC parameter is identified in the DICOM tags as $VENC\0\0$, $0\backslash VENC\0$, and $0\0\backslash VENC$. These correspond to velocity encoding in the right-left, anterior-posterior, and foot-head directions, respectively. The VENC value is typically expressed in cm/s.

2.2.2 Data preprocessing and 4D velocity array creation

After data acquisition, the collected information needed to be processed to create 4D arrays for each velocity component. Each point in these arrays corresponds to the value of velocity derived from the phase images. In simpler terms, the goal was to convert the 4D Flow data into a streamlined format that is more efficient for analysis, visualization, and use in computational models.

The chosen format was a structured HDF5 file (h5), as it efficiently handles large datasets, simplifies visualization, and allows all data to be stored within 4D arrays for easy access and organization. For this task to be completed the open-source code used in the work with title “4DFlowNet: Super-Resolution 4D Flow MRI Using Deep Learning and Computational Fluid Dynamics” (Ferdian et al., 2020).

The code extracts velocity and magnitude data from DICOM files, organizes them into 4D arrays (time, 3D space), and saves them in a compact, efficient .h5 file format. This helps streamline the analysis of 4D Flow data. The script processes 4D Flow MRI data by scanning a directory to locate all relevant DICOM files and reading them to construct 3D image volumes for analysis. It extracts key metadata such as pixel spacing, slice thickness, and sequence details. The workflow identifies phase and magnitude image sets, sorts the time points, and processes each time frame to calculate velocity components for three directions.

The results, including the computed velocity data and associated metadata, are saved in a structured HDF5 file. The output is optimized for further analysis, visualization, or computational modeling, with progress updates provided during processing. The contents of the newly created h5 file contain the following:

- **dx**: An array that stores the grid spacing values of the imaging volume, representing the physical distance between adjacent grid points along the x, y, and z axes.
- **mag_u, mag_v, mag_w**: 4D arrays with dimensions Time \times Z \times Y \times X, representing the magnitude images associated with the three orthogonal velocity components (u, v, w) derived from 4D Flow MRI data.
- **triggerTimes**: An array that provides the time information for each timestep.
- **venc_u, venc_v, venc_w**: Arrays that store the velocity encoding (VENC) values for each timestep, specific to the spatial dimensions (u, v, w).
- **u, v, w**: 4D arrays with dimensions Time \times Z \times Y \times X, containing the velocity values for each spatial component (u, v, w) across all timesteps.

To view the contents of the h5 file an online h5 file viewer was used. Figure 19 shows an example of the created h5 file.

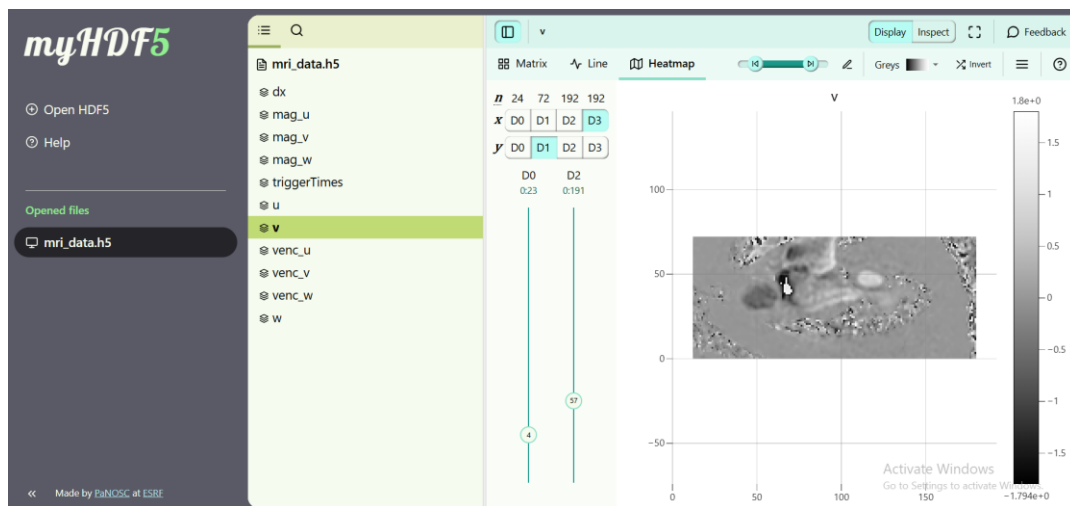


Figure 19: Sample of the contents of the h5 file used in the analysis.

An important aspect of the u, v, and w 4D arrays is that the velocity values within these arrays fall within the range of -1.8 to +1.8 m/s, corresponding to the specified VENC value. This indicates that the arrays have been correctly generated.

2.2.3 3D Model Reconstruction

This section will focus on discussing the 3D model utilized for the simulations. The construction of the model was done, by using SimVascular. Initially, the magnitude images for one trigger time from the data were loaded in the software, so the spatial domain can be defined. Figure 20 depicts the software interface with the magnitude images loaded. As shown in Figure 20, the spatial domain formed by the scan slices is displayed in the bottom-right section of the image. Additionally, the three planes defining the spatial domain are visible: the axial plane in the upper-left, the coronal plane in the bottom-left, and the sagittal plane in the upper-right section of the image.

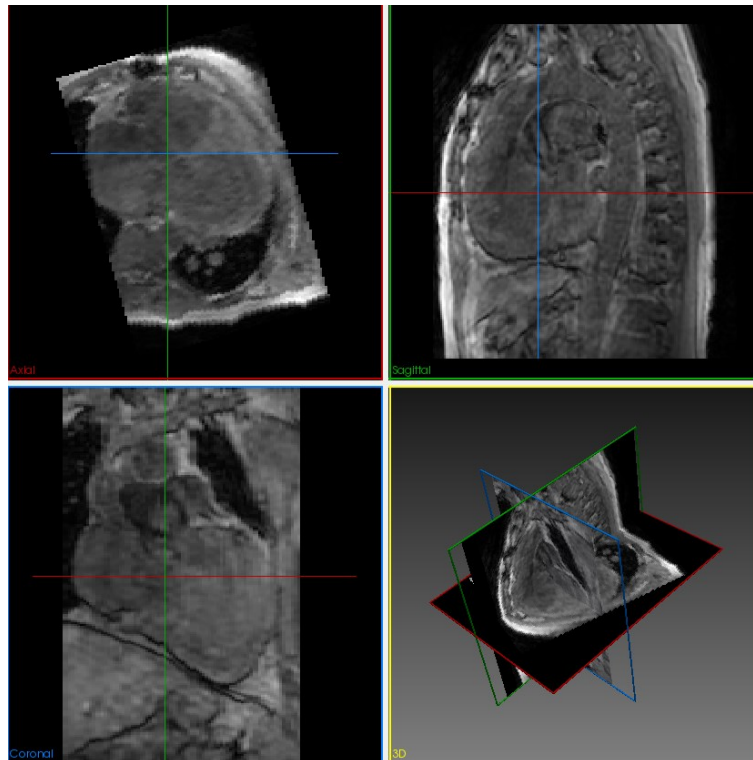


Figure 20: Spatial Domain Definition of 4D Flow Scan Using SimVascular

The next step for the creation of the 3D model was to define the paths that serve as the backbone of the model's geometry. Paths represent the centerlines of blood vessels or other anatomical structures. These paths guide the placement and orientation of the cross-sectional shapes (slices) used to reconstruct the 3D model. Defining accurate paths ensures that the geometry aligns with the actual anatomical features, enabling the creation of a realistic and precise 3D representation of the structure.

To construct the 3D model, four paths were defined: one for the main body of the aorta, and one each for the brachiocephalic artery, the left common carotid artery, and the left subclavian artery. These paths were created by positioning points along key anatomical landmarks of each artery, ensuring the geometry was accurately captured, including any complexities or abnormalities. The image below illustrates the paths used for reconstructing the main body of the aorta, along with those for the brachiocephalic artery, left common carotid artery, and left subclavian artery.

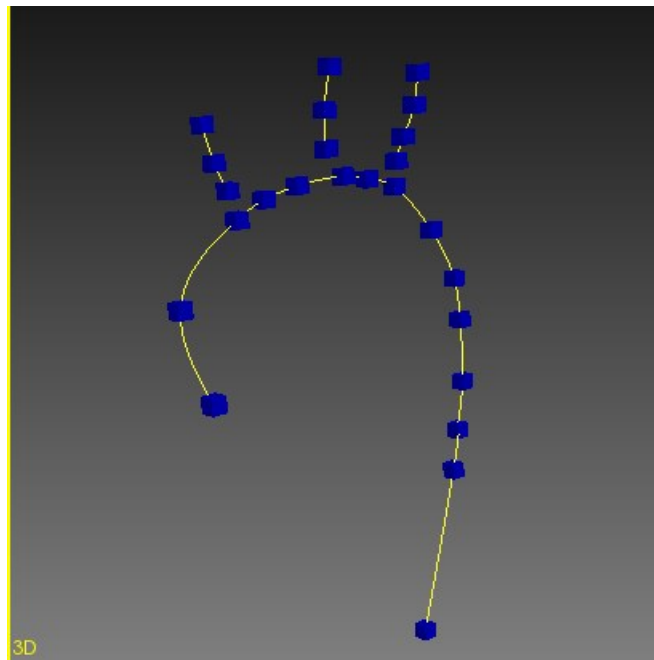


Figure 21: The paths for the aorta, brachiocephalic, left common carotid and subclavian arteries

As illustrated in Figure 21, the paths form the foundation of the model's geometry, serving as a framework for the subsequent processing steps. Each point along the path was carefully selected, typically positioned at the center of the vessel's cross-sectional area throughout the patient's anatomy. This ensured the path could act as the central axis for the segmentations used later, while also capturing the geometric complexities of the patient's anatomy with greater accuracy. Figure 22 illustrates the total number of path points used to define the aorta's backbone, along with an example of the selection process for an individual point. The same method, adhering to identical principles, is applied to create the paths for the brachiocephalic artery, left common carotid artery, and left subclavian artery.

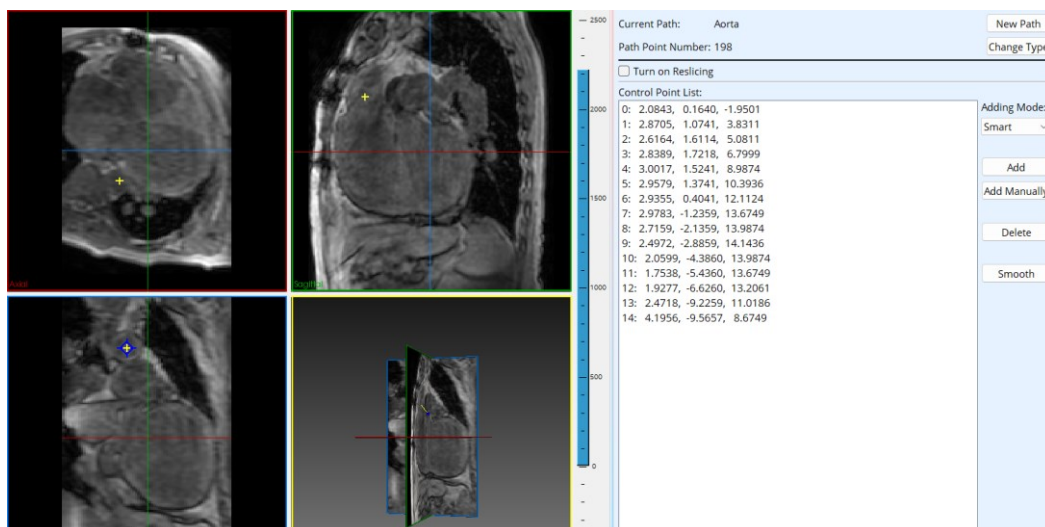


Figure 22: Selection of Path Points and Overview of Path Points Defining the Aorta's Main Body

The next step for the 3D model reconstruction is the creation of the segmentations. Segmentations play a crucial role in the reconstruction of the 3D model by defining the cross-sectional contours of the anatomical structure at various locations along the paths. These contours are extracted from imaging data and represent the precise boundaries of the vessel or organ being modeled. By combining the segmentations along the defined paths, the reconstruction process creates a smooth and accurate 3D geometry that reflects the shape, size, and any anatomical complexities or abnormalities of the structure.

Figure 23 shows the segmentations that were used for the reconstruction of the 3D model. As illustrated in Figure 23, the segmentations were created based on the paths of each artery. For the current model, eleven segmentations were used. This number was chosen to strike a balance between accurately capturing the patient's vascular anatomy and avoiding excessive complexity. Using fewer segmentations would have failed to represent the vessels' anatomy accurately, while an excessive number could introduce issues such as sharp edges, steep gradients, or abrupt changes in the cross-sectional geometry.

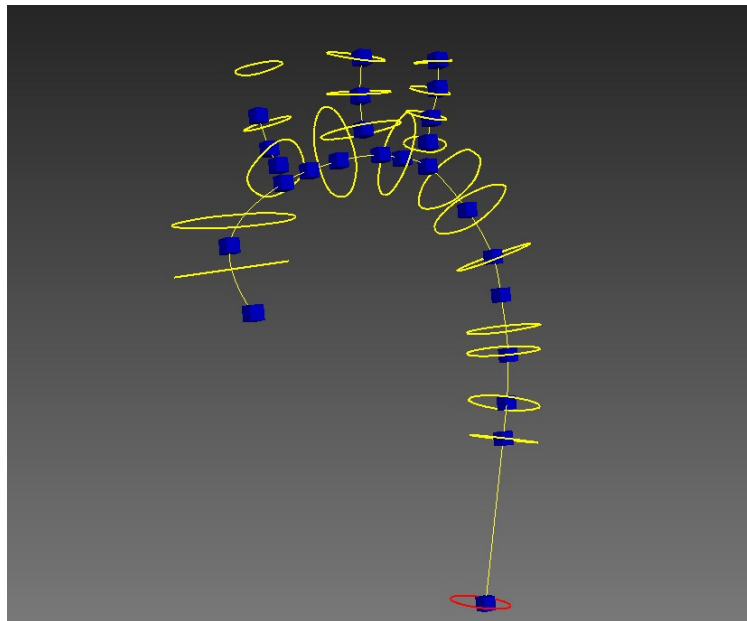


Figure 23: Segmentations used for the model reconstructions along with their respective paths

Figure 24 depicts the geometric shapes used for the eleven segmentations and provides an example of how a segmentation is selected at a path point based on the patient's specific anatomy. These segmentations define the model's geometry boundaries, accurately capturing the patient-specific anatomy derived from the 4D flow data. Extensive refinement and smoothing were performed to optimize the boundaries, ensuring a well-defined model with improved performance in the simulations.

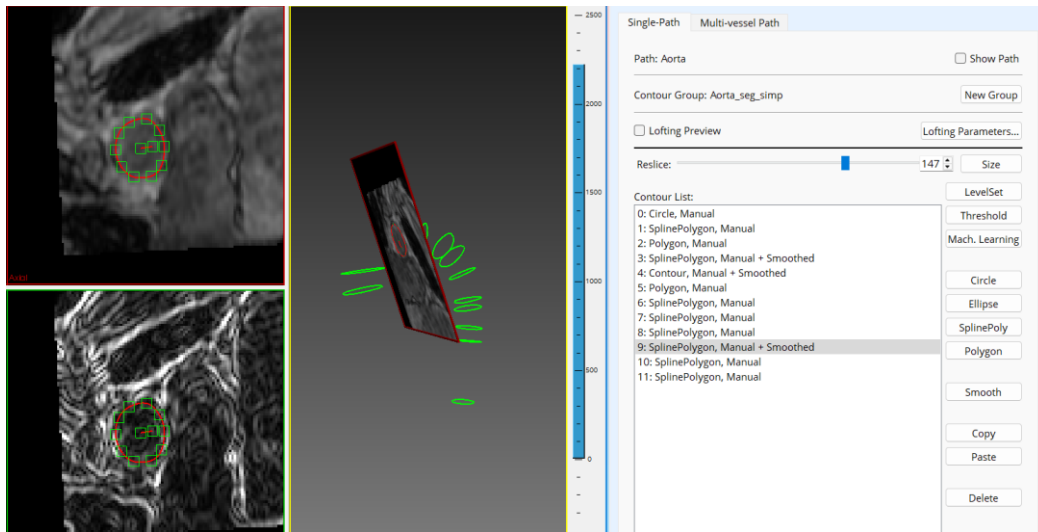


Figure 24: Example of Segmentation Selection and Overview of All Segmentations

The final stage of the 3D model reconstruction process involves assembling the model, which was completed using SimVascular software. The model was constructed as a PolyData structure, a format designed to represent and handle 3D geometric objects such as points, lines, and surfaces, along with their associated attributes like scalars and vectors. The resulting model comprises 28,658 cells and 14,331 points. Figure 25 displays the complete 3D model, representing the main sections of the aorta (ascending aorta, aortic arch, and descending aorta), along with the brachiocephalic artery, left common carotid artery, and left subclavian artery. The geometry was meticulously reconstructed to closely match the patient's anatomy while ensuring smoothness to minimize potential issues during the simulation process.

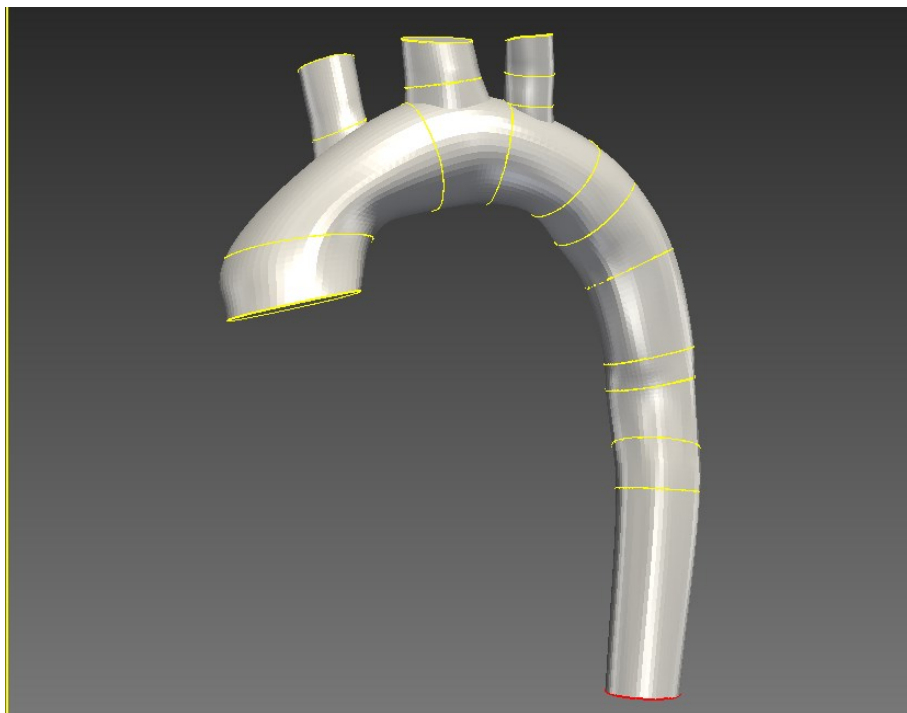


Figure 25: The complete 3D model with its respective segmentations

2.2.4 Exporting, Refining, and Integrating the 3D Model for Simulation in Crimson

In this study, simulations were conducted using both SimVascular and Crimson software to enable a comparative analysis. To ensure the comparison was accurate, the same geometric model was used in both platforms.

The process began with exporting the 3D model created in SimVascular. The exported model was saved in VTP format, a file type designed for storing and exchanging 3D geometric data such as points, lines, and polygonal surfaces, along with their attributes, in a structured and efficient manner widely compatible with visualization and computational tools like VTK.

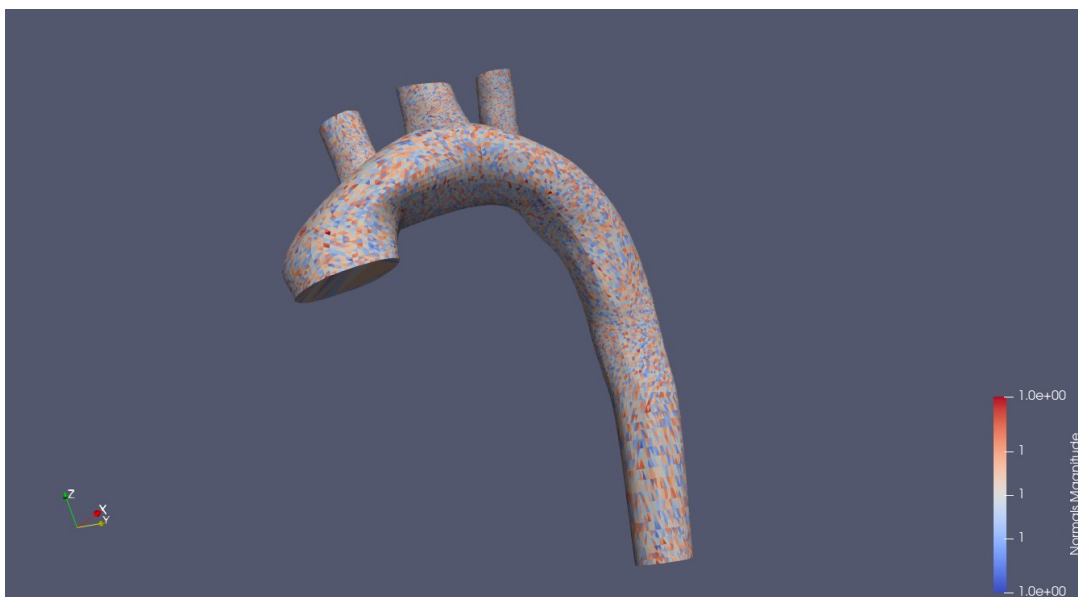


Figure 26: Visualization of the VTP model in the ParaView environment, displaying the normal (triangles) of the model.

Figure 26 shows the exported 3D model from SimVascular, along with the normals (triangles) of the model. Normals are vectors perpendicular to the surface of each triangle in the 3D mesh and are essential for defining the surface orientation. They play a key role in various computations, including shading, lighting, and surface interactions in visualization software, and are crucial for accurate rendering and simulating physical interactions.

Upon importing the model into the CRIMSON software, certain geometric features were not correctly recognized, and the software encountered difficulties distinguishing some of the model's primary faces. This highlighted the need for further adjustments to improve the surface quality and enhance the differentiation of the model's various surfaces. To address this issue, Meshmixer was utilized.

Meshmixer, developed by Autodesk, is free 3D modeling software that enables users to create, analyze, and optimize 3D models, with a particular focus on 3D printing. It offers a wide array of tools for tasks such as model combination, sculpting, surface stamping, mesh smoothing, and hollowing. Additionally, Meshmixer includes features for automatic model repair, stability and thickness analysis, and the generation of support structures for 3D printing (Sculpteo).

In Meshmixer, efforts were made to refine the geometry to ensure that the caps of the model were more distinct, and that each surface was correctly identified (with the caps as inflows and outflows and the remaining surfaces as walls). To achieve this, the caps were slightly extruded and flattened to enhance their distinction. Additionally, the rest of the model's surface was smoothed using the software's tools to eliminate any sharp points that could be misinterpreted as outflows. The outcome of this refinement process is shown in Figure 27.

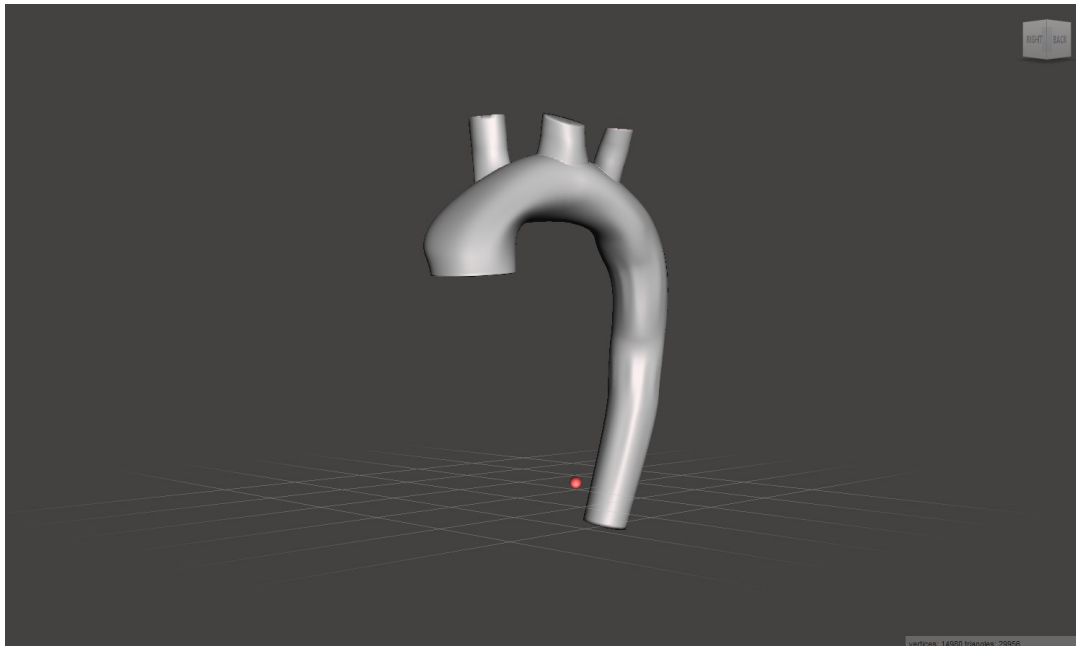


Figure 27: The test 3D model after the modifications in Meshmixer

After the modifications in Meshmixer, the model was saved in STL format and then imported into the CRIMSON software. These adjustments enhanced the overall quality of the 3D model while preserving its patient-specific anatomy with only minor deviations from the original design. Once imported into CRIMSON, the discrete model was generated, and the final model was prepared for simulation deployment.

2.2.5 Preparing the Mesh and Defining Boundary Conditions

Before conducting full simulation, preliminary test runs were performed to calibrate the software parameters and build familiarity with the tools being used. This process was made both in SimVascular and in CRIMSON. In SimVascular, the Mesher utilizes the TetGen algorithm to generate an unstructured volumetric mesh composed of 3D tetrahedral elements. Similarly, in CRIMSON, the mesh type is based on a TetGen-generated volumetric unstructured mesh, with linear tetrahedral elements used for simulations.

Table 1: Test Mesh properties

Basic Mesh Parameters	SimVascular	CRIMSON
Mesh Type	Unstructured	Unstructured
Type of elements	3D tetrahedral	3D tetrahedral
Maximum Edge Dimension	0.24	0.1
Number of nodes	52214	53320
Number of edges	27591	359679
Number of faces	18394	598082
Total Number of elements	295881	291722
Number of boundary layers	2	-
Portion of edge size	0.5	-
Layer decreasing ratio	0.8	-

Table 1 shows the calibration mesh parameters used in each of the two programs. The table shows that the meshes used in both software have a comparable number of elements. However, it is evident that the mesh in CRIMSON lacks boundary layers and their associated parameters (Portion of edge size and Layer decreasing ratio). This is due to the limitation that the open-source version of CRIMSON does not support this feature. The meshes used in SimVascular and CRIMSON are depicted in Figure 28.

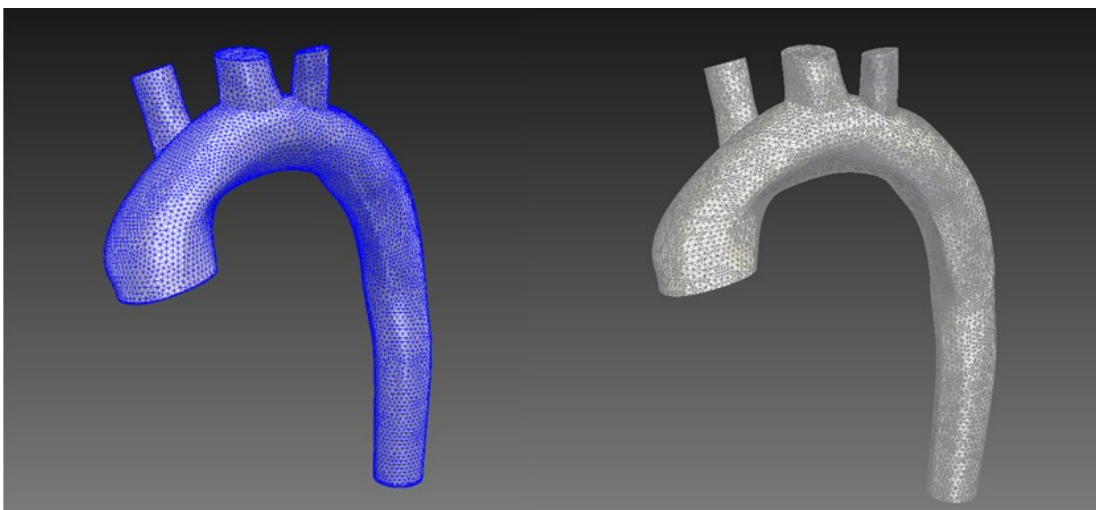


Figure 28: Test Mesh used in SimVascular (left) and in CRIMSON (right)

The next step in preparing the calibration simulation jobs involved defining suitable boundary conditions and assigning physiologically realistic values. The model includes five "caps", consisting of one inlet and four outlets. A flow rate profile was applied at the inlet, while 3-element Windkessel models (RCR) were utilized for the four outlets. The flow rate profile used as a boundary condition was derived from 4D velocity data arrays stored in an HDF5 file. The inlet cap of the model was approximately aligned with the 57th axial slice, corresponding to the anatomy of the aorta just after it exits the heart. This alignment enabled the analysis of the velocity distribution in the aortic cross-section at this slice.

A custom code was then developed to process the data and derive the flow profile. The code defines an elliptical Region of Interest (ROI) in the aorta's cross-section, encompassing all relevant pixels. Each pixel within the ROI contains velocity values from the three velocity components (u , v , and w), which are stored in separate 4D arrays within the HDF5 file. To extract these values, the code creates identical ROIs for each of the three arrays. For every timestep, the velocity values within the ROI are extracted separately for the u , v , and w components, and the mean velocity is calculated for each component and each timestep. As shown in Figure 29, the ROI is positioned within the cross-sectional area of the ascending aorta. This is identifiable by the darker pixels, which indicate ascending flow, in contrast to the brighter pixels representing descending flow in the descending aorta.

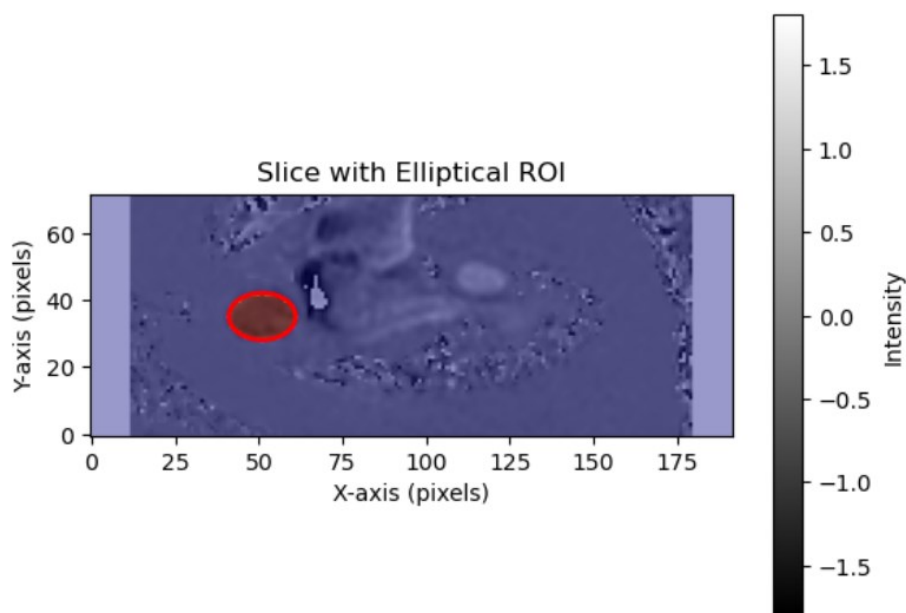


Figure 29: Region of Interest (ROI) used during systole phase of the cardiac cycle

The analysis is carried out in three stages. First, the code extracts the 57th slice of the v velocity component from the HDF5 file, applies the elliptical ROI, and visualizes the slice with the ROI overlay while displaying the pixel values within it. Next, the process extends across all timesteps, computing the mean velocity within the ROI for the v component and plotting its temporal variation. Finally, the analysis incorporates all three velocity components (u , v , and w), calculating the mean velocity and the ROI area for each timestep, with results visualized and plotted. This approach enables a detailed investigation of temporal and spatial velocity patterns in the aortic cross-section.

Figure 30 shows the physiological behavior of the patient-specific cardiac cycle. The systolic phase occurs during the first nine timesteps, transitioning into the diastolic phase for the remaining timesteps.

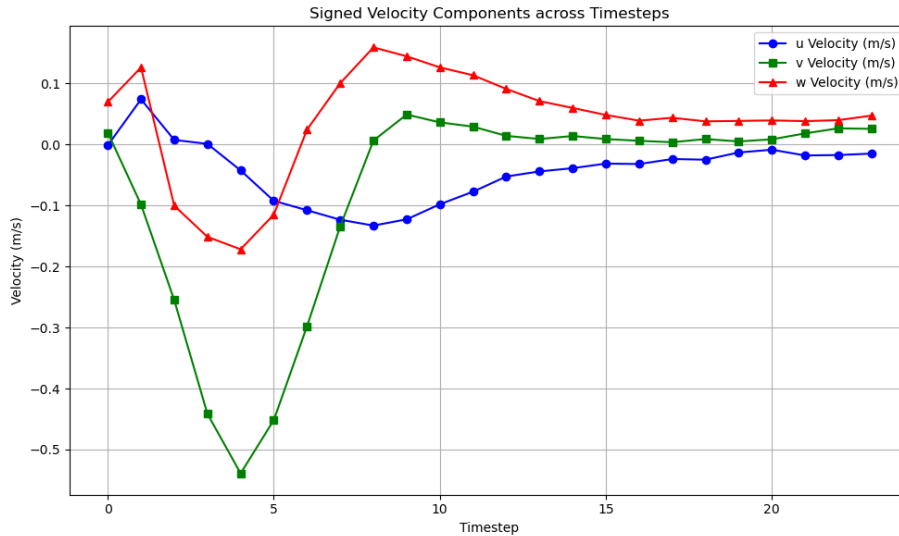


Figure 30: Flow profiles for all velocity components derived from the 4D Flow MRI data

To prepare the inflow boundary conditions, the velocity data obtained from the code were converted into volumetric flow rate values, expressed in cm^3/s . This calculation utilized only the v component due to its orientation perpendicular to the cross-sectional surface of the ascending aorta. These data are presented in Table 2 and graphically in Figure 31. The cross-sectional area, estimated at 10.1606 cm^2 , was provided by SimVascular. As mentioned earlier, the patient-specific cardiac cycle spans 0.98 seconds and is divided into 24 timesteps. The only difference between this plot (Figure 31) and the raw plot extracted from the 4D Flow MRI data (Figure 30) is that the initial velocity values were first converted to cm/s and then multiplied by the cross-sectional area of the ascending aorta (cm^2), resulting in the volumetric flow rate (cm^3/s).

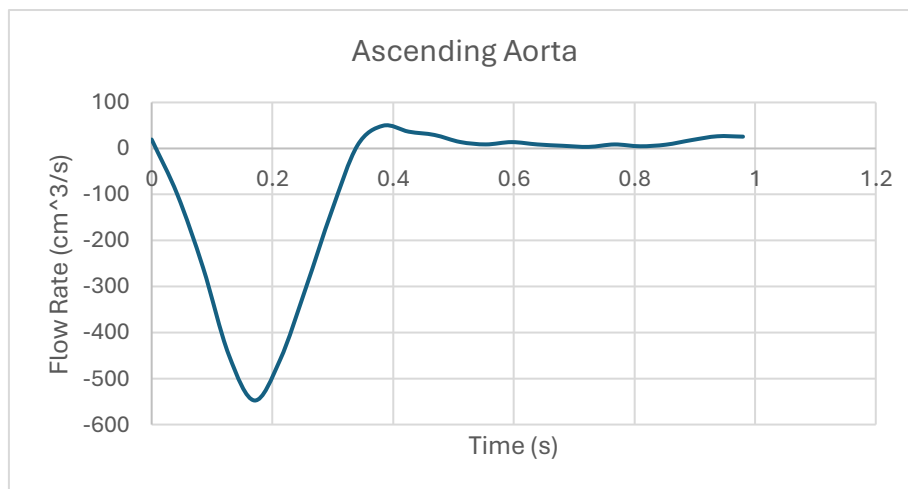


Figure 31: Volumetric flow rate of ascending aorta during one cardiac cycle

Table 2 outlines all the data utilized to create the transient table for specifying the inflow boundary condition in the test simulation. This data was input into both software platforms, and a simple parabolic velocity profile was applied for the test simulation.

Table 2: Data used as inflow boundary condition for test simulation

Time (s)	Cap_flow_rate (cm ³ /s)	Normal_velocity (cm/s)
0	19.406746	1.91
0.042609	-100.285122	-9.87
0.085217	-259.0953	-25.5
0.127826	-448.59049	-44.15
0.170435	-547.65634	-53.9
0.213043	-458.75109	-45.15
0.255652	-302.684274	-29.79
0.298261	-136.558464	-13.44
0.34087	6.197966	0.61
0.383478	49.482122	4.87
0.426087	36.476554	3.59
0.468696	29.364134	2.89
0.511304	14.021628	1.38
0.553913	8.839722	0.87
0.596522	13.818416	1.36
0.63913	8.738116	0.86
0.681739	5.791542	0.57
0.724348	3.454604	0.34
0.766957	8.738116	0.86
0.809565	4.775482	0.47
0.852174	8.230086	0.81
0.894783	18.187474	1.79
0.937391	26.519166	2.61
0.98	25.706318	2.53

Regarding the RCR boundary conditions, physiological values were required to obtain meaningful and realistic results. The initial values for the test simulation (Table 3) were adopted from the study by Pirola et al. (2017). It is important to highlight that these values were calibrated through multiple test runs to ensure the simulation results closely matched those obtained from the 4D Flow MRI machine operated by specialists. Additionally, further bibliographic research was conducted to verify that all values used fell within physiological ranges.

Table 3: Initial values used for test simulation (Pirola et al., 2017)

	Peripheral Resistance (Rp) (dynes*s/cm ⁵)	Distal Resistance (Rd) (dynes*s/cm ⁵)	Compliance (C) (cm ⁵ /dyne)
Brachiocephalic artery	630	17100	0.000101
Left common carotid artery	1760	41700	0.000041
Left subclavian artery	2410	54700	0.000031
Descending aorta	170	2400	0.000697

2.2.6 Solver setup and simulation files creation

The last part for running a simulation after setting the physics of the problem is choosing the appropriate parameters for the solvers in both SimVascular and CRIMSON. Table 4 shows the basic parameters of both solvers.

Table 4: Solver Parameters used in the software

Solver Parameters	SimVascular	CRIMSON
Number of Timesteps	100	100
Timestep size	0.01	0.01
Number of timesteps between restarts	1	1
Output Surface Stress	True	True
Force Calculation Method	Velocity Based	Velocity Based
Step Construction	10	10
Pressure Coupling	Implicit	Implicit
Backflow Stabilization Coefficient	0.2	0.2
Residual Control	True	True
Residual Criteria	0.001	0.001
Minimum Required Iterations	3	3
svLS Type	NS	memLS
Tolerance on Momentum Equations	0.001	0.01
Tolerance on Continuity Equations	0.01	0.05
Tolerance on svLS NS Solver	0.01	0.1
Time Integration Rule	Second Order	Second Order
Time Integration Rho Infinity	0.5	0.0
Flow Advection Form	Convective	Convective
Quadrature Rule on Interior	2	2
Quadrature Rule on Boundary	3	2

In the test runs, both solvers are configured with 100 timesteps and a timestep size of 0.01 seconds. The number of timesteps and their size determine the temporal resolution of the simulation, with these values selected to ensure that one complete cardiac cycle is captured accurately while keeping computational costs manageable. Both solvers restart after every timestep to save individual timestep data for post-processing.

Implicit pressure coupling solves the pressure and velocity fields simultaneously by discretizing the Navier-Stokes and continuity equations into a single coupled system. This unified system, often represented as a block matrix, ensures that velocity changes satisfy momentum and continuity constraints, maintaining stability and accuracy, especially in incompressible flows. The method avoids decoupling errors by iteratively solving pressure and velocity together within each timestep, improving stability.

A backflow stabilization coefficient of 0.2 is included to prevent numerical instabilities caused by reverse flow at boundaries, a common occurrence in cardiovascular simulations. Residual control is activated, with a residual criterion of 0.001, to monitor and ensure the convergence of the solution at each timestep with high precision. A minimum of three iterations per timestep is set to guarantee convergence reliability while avoiding unnecessary computational effort.

Both solvers use a convective flow advection form to model momentum transport, aligning well with cardiovascular dynamics. Quadrature rules are specified to ensure integration accuracy, with both solvers using a rule of 2 for interior computations. However, SimVascular applies a higher-order rule (3) for boundary integration compared to CRIMSON's rule (2), offering greater accuracy in boundary-related calculations. These settings were the default ones and remained unchanged.

A key distinction between the two solvers lies in their solver types: SimVascular uses svLS (NS), while CRIMSON uses memLS. Tolerance settings, which determine the acceptable error limits for the equations, were adjusted in response to instabilities encountered with SimVascular's solver for this specific problem. SimVascular applies stricter tolerances for momentum equations (0.001 vs. 0.01), continuity equations (0.01 vs. 0.05), and its NS solver (0.01 vs. 0.1), prioritizing precision at the cost of increased computational effort. Due to the instabilities and high residuals observed with SimVascular, the time integration rule was also modified; SimVascular uses a rho infinity value of 0.5, blending first- and second-order accuracy for better stability and precision, whereas CRIMSON uses a value of 0.0, emphasizing fully second-order accuracy for improved temporal resolution. These parameters were chosen to suit the specific demands of cardiovascular simulations, balancing accuracy, stability, and computational cost to achieve physiologically relevant and practical simulation results.

Finally, the essential simulation files generated by both software programs before running the simulation are as follows:

- inflow.flow
- geombc.dat.1
- restart.0.1
- bct.dat
- solver.inp
- numstart.dat
- rcrt.dat

The inflow.flow file contains the transient data table used as input for one of the boundary conditions. The geombc.dat.1 file stores mesh information along with the specified boundary conditions for the problem, while the restart.0.1 file defines the initial conditions. The bct.dat file provides time-dependent velocity vectors at the inflow boundary, derived from the prescribed flow wave in the inflow.flow file. The numstart.dat file contains the number 0, which the solver uses to identify the appropriate restart file for initial conditions. The solver.inp file specifies key solver parameters, including time step size, number of time steps, nonlinear iterations, and boundary condition controls. Lastly, the rcrt.dat file defines the RCR boundary conditions. This core format was the same in both software programs utilized.

Here it must be highlighted that a strong interest was developed in the contents of the bct.dat file. As was previously mentioned this file defines the inflow boundary condition both spatially and in time. The format of the file is presented in Table 5.

Table 5: BCT File Structure and Description

BCT File Structure	Description
np nl	np : Total number of spatial points.
x1 y1 z1 nl nn	nl : Total number of temporal points.
vx1 vy1 vz1 t1	(x1, y1, z1) : Coordinates of the spatial point currently being analyzed.
. . . .	nn : Mesh ID of the current spatial point.
. . . .	(vx1, vy1, vz1) : Velocity components of the current spatial point at the first temporal point.
vxnl vynl vznl tnl	(vxnl, vynl, vznl) : Velocity components of the current spatial point at the final temporal point (tnl).
. . . .	(xnp, ynp, znp) : Coordinates of the np spatial point in the mesh.
. . . .	
. . . .	
xnp ynp znp nl	

In other words, this file stores the velocity component values for each spatial point in the mesh, as well as the velocity values at every temporal point for each spatial location. As a result, the file contains a total of $3 \times (\text{np} \times \text{nl})$ velocity values, where **3** represents the three spatial components, **np** is the total number of spatial points, and **nl** is the total number of temporal points. This structured format was utilized to input a custom velocity profile derived from 4D Flow MRI data, instead of relying on theoretical profiles like parabolic distribution. The process of implementing this approach will be discussed in a later section of this work.

2.2.7 Error Quantification and Comparison with the Original 4D Flow MRI Data

After completing the simulations, the next step was to compare the results with the original data to assess the simulation's accuracy. This comparison helps identify parameters that may require further calibration to improve the results and determine if any conditions were potentially set incorrectly. To perform this comparison, the simulation data were first needed to be reconstructed into 4D arrays, similar to the original data. Then, the data were downsampled to generate "mock" MRI data, ensuring that the comparison was made on equivalent terms. The process of preparing CFD data for comparison with 4D flow MRI data involves several key steps, each designed to extract, process, and structure the data in an efficient manner. These key steps are described as follows.

First, the CFD data were extracted from a series of VTU files containing simulation data. The script iterates through the files, extracting spatial coordinates and velocity components (u, v, w) for each timestep. These values are then saved in .txt files with headers indicating the spatial coordinates and velocity components. The output data is organized for easy retrieval.

The velocity data from the text files were then loaded and converted into a structured HDF5 file format to facilitate comparison with MRI data. The script establishes spatial bounds and slices, generating 4D arrays to store velocity components at each time step while also tracking the maximum velocity values for each timestep. The selected spatial bounds (x, y, z) are derived from the original 4D Flow MRI images, ensuring that the CFD data maintains the same boundaries. The same approach is applied to the number of slices. The extracted data is then mapped onto a predefined grid and stored in the HDF5 file, along with a spatial resolution dataset, a binary mask, and the recorded maximum velocity values.

The third step involves inspecting the HDF5 file to extract the mask dataset, which is important for identifying regions with flow. The mask values are checked for integrity, and if needed, the mask array is saved in a text file for further analysis. The fourth part of the code calculates the velocity magnitude at each timestep using the velocity components (u , v , w). This magnitude is stored in a 4D array, and the results are saved into a new HDF5 file, so that they can be used for creating the new time-averaged mask.

Next, a new mask is created based on the velocity magnitude data. The script identifies regions with flow by setting the mask to 1 for nonzero velocity magnitude values and to 0 otherwise. The mask is then saved in an updated HDF5 file. The sixth step generates a time-averaged mask by averaging the mask data over all time steps. This mask represents the probability of each voxel being part of the flow region across all timesteps and is saved as a new dataset in an HDF5 file.

The seventh step updates the original HDF5 file by replacing the old mask dataset with the new time-averaged mask. The process involves deleting the existing mask, if present, and adding the updated one. The effort dedicated to the mask is justified because it defines the flow regions and guides the downsampling process by focusing on these areas. By adjusting the signal strength during augmentation and ensuring that only the relevant regions are downsampled, the mask ensures the integrity of the flow data. Afterward, it is downsampled to match the velocity data, preserving the consistency of the flow regions, which is crucial for maintaining the accuracy and relevance of the final downsampled results.

Finally, the eighth part of the script converts the velocity components from cm/s to m/s by dividing the relevant datasets by 100 to be relevant with the original data. The updated values are saved back into the HDF5 file, ensuring the data is now in the correct units for analysis. The file's contents are printed for verification. This process was done for the data of SimVascular and CRIMSON. The final representation of the 4D array reconstruction of the CFD data is depicted in Figure 32.

This structured approach ensures that the CFD data were correctly formatted, with the necessary velocity components, mask information, and unit conversions, ready for comparison with MRI data. After the creation of the h5 file containing all CFD data it was important to downsample them, while also applying the appropriate VENC value that is used in the original data. The code used for this task was the open-source code used by Ferdian et al. (2020).

This Python script essentially processes CFD velocity data stored in HDF5 files by applying downsampling to each timestep. For each timestep, the script loads the data, including the velocity components (u , v , w) and the mask, and performs downsampling using FFT-based methods. The downsampling reduces the resolution of the data while simulating different signal-to-noise ratios (SNR) by applying random SNR values. The script also applies a magnitude multiplier to the mask to augment the data. It saves the downsampled velocity components (u , v , w), magnitude data, velocity encoding (VENC) values, SNR, and the downsampled mask into new HDF5 files. Here the VENC value of 1.8 m/s is used because it is the velocity encoding value of the original 4D flow MRI data. The mask is saved only once to avoid redundant writes. The script processes all timesteps in the specified folder, outputting the downsampled data for further analysis in a new h5 file.

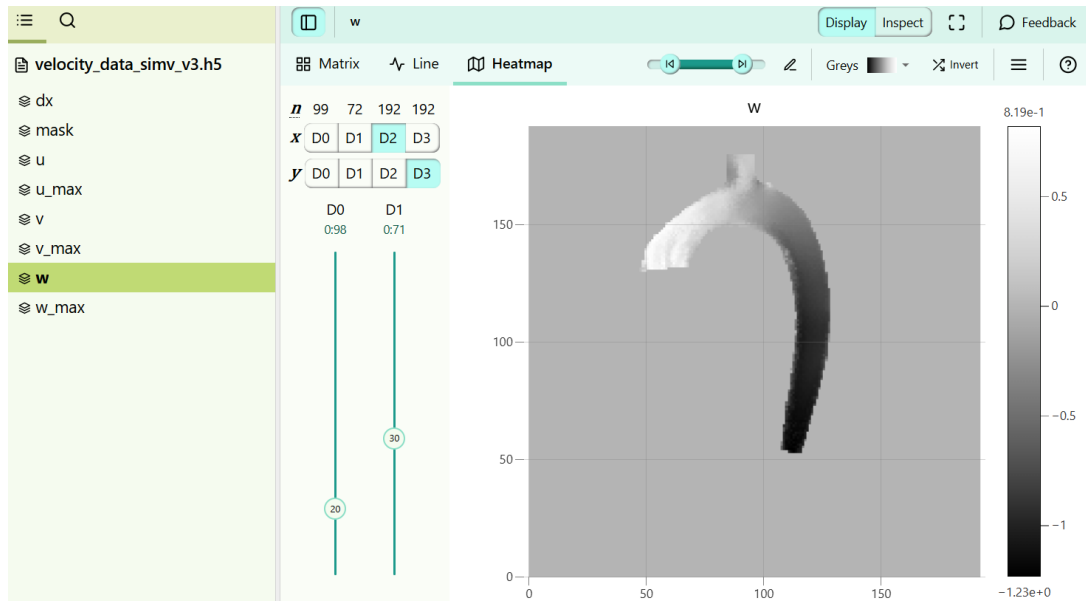


Figure 32: Representation of the CFD model's geometric reconstruction in the new HDF5 file.

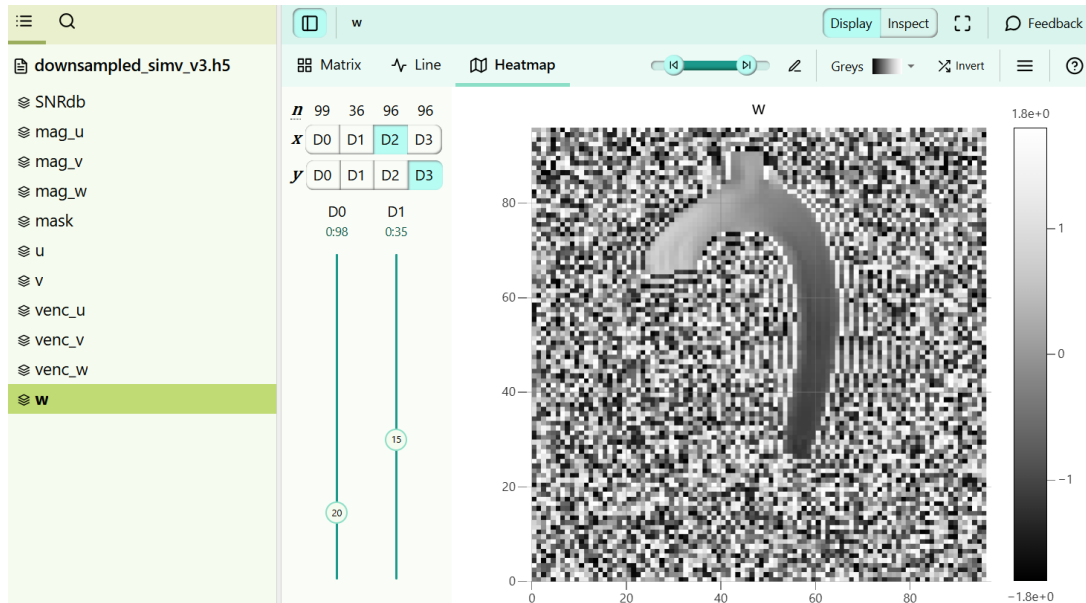


Figure 33: Representation of the downsampled CFD model's geometric reconstruction

The downsampled data shown in Figure 33 clearly demonstrates that the dimensions of the 4D arrays have been halved. White Gaussian noise was introduced in the frequency domain to simulate real MRI acquisition, and the velocity values now range from -1.8 m/s to 1.8 m/s, which aligns perfectly with the original MRI data. The CFD data can now be compared with the original MRI data.

Before starting the comparison process, some minor further adjustments were made to the original MRI data, including changing the coordinate system and vector directions to match those of the simulation. Specifically, the velocity components were transformed as follows: the w component was used as the new u component, the u component was used as the new v component, and the v component was negated to become the new w component. These transformations ensured the alignment of the MRI data with the simulation's coordinate system and orientation. The area chosen for the test comparison was selected to be a cross-sectional area where the flow is "fully-developed," making a cross-section in the descending aorta region of the model the preferred choice.

During the downsampling process, the number of slices was reduced by half. This adjustment served as a reference when selecting slices for comparison. For instance, to match a sagittal slice between the CFD data and the original dataset, the same sagittal slice was chosen, but its index in the CFD data was half that of the original dataset (e.g., sagittal slice 15 out of 36 in the CFD data corresponds to sagittal slice 30 out of 72 in the original data). This principle was consistently applied to all slice selections. Once the sagittal slice was identified, the corresponding axial slice needed to be selected for comparison. The reference point for axial slice selection was set at $y=0$ (the upper boundary of the sagittal slice). From there, an axial slice of interest was chosen in the original dataset based on its y -coordinate. Applying the same downsampling rule, the corresponding axial slice in the CFD data was selected at $y/2$, where y is the slice selected from the original data.

After selecting the matching axial slices from both the patient's MRI data and the CFD simulation for comparison, a process similar to flow profile extraction is performed. Specifically, an elliptical ROI is defined and adjusted to match the geometry of the cross-sectional area of the descending aorta in the selected axial slice. Separate ROIs are created for the MRI and CFD data. Each pixel within the ROI contains a velocity value, with the u , v , and w components stored in their respective 4D arrays. The mean velocity for each component is calculated using all pixels within the ROI. The mean values for all timesteps are stored in text files—one for the original MRI data and one for the CFD data. These files are then used in a Python script to generate three comparison graphs, each representing the velocity profile of the u , v , and w components, enabling a direct comparison between the MRI and CFD results.

2.3 Patient Specific Velocity Profile Extraction

A key aspect of this work was the use of a patient-specific velocity profile to run the simulations, rather than relying on the theoretical profiles provided by the two software programs. To complete this task, several steps had to be carried out, each requiring specific data processing. For every step presented, a custom in-house Python script was developed to execute the process.

The first thing that needed to be done was to extract the information about the cap (cross-section of the inlet). The Python script developed uses PyVista to load and visualize a VTP file representing the cap of the ascending aorta. It first reads the surface mesh from the specified file path and extracts key geometric information, including the number of elements (cells) and vertices (points). The script then prints this data, along with the coordinates of the first few vertices.

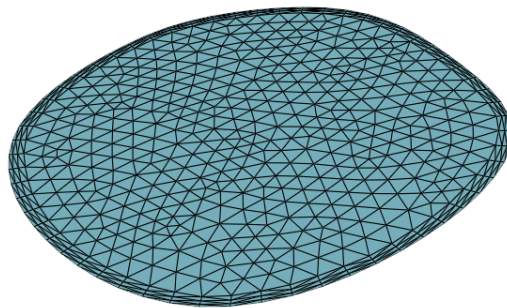


Figure 34: Visualization of the cap's mesh

The Python script initially utilizes PyVista and NumPy to process and transform the vertex coordinates of a cap geometry stored in a VTP file. It reads the file, extracts the x , y , z coordinates of the surface vertices, and saves them in a tab-separated TXT file, initializing the velocity components (u , v , w) as zero. A sample of the extracted coordinates is printed for verification.

Next, a coordinate transformation is applied by shifting all vertex coordinates relative to a predefined reference point $([9.12, -19.47, 19.46])$. This reference point was selected from the simulation coordinate system because it corresponds to the $(0,0,0)$ point in the 4D array coordinate system of the HDF5 file. This transformation ensures that the cap coordinates align with the 4D array, facilitating accurate comparisons and integration between CFD simulation data and the MRI-based velocity field. The transformed coordinates are stored in a separate TXT file in the same format, ensuring consistency for further analysis.

A crucial step in this process was ensuring that the x , y , z coordinate system of the simulation correctly aligned with the 4D Flow MRI coordinate system. To achieve this, an appropriate transformation was implemented in Python. The script loads the previously transformed cap coordinates, which contain six columns (x , y , z , u , v , w), where velocity components are initially set to zero. The transformation follows the convention:

$$x_{MRI} = y_{Simulation}$$

$$y_{MRI} = -x_{Simulation}$$

$$z_{MRI} = -z_{Simulation}$$

This effectively rotates the coordinate system to align with the MRI reference frame. The transformed coordinates are stored in a new array while keeping the velocity components unchanged. The data is then saved in a tab-separated format for compatibility with further analysis, and a sample is printed for verification. This transformation is essential for ensuring an accurate comparison between CFD simulation data and the MRI-derived velocity field.

The final step in aligning the coordinate system was scaling the cap coordinates to match the dimensions of the MRI domain. A Python script was developed to apply this scaling transformation. It first loads the previously transformed cap coordinates, where x , y , z represent the adjusted positions, and u , v , w remain zero. The scaling factors for each axis (x , y , z) are computed based on the ratio of the MRI domain dimensions to the original coordinate system:

$$(\text{Scale factor})_x = \frac{\text{Number of } x - \text{axis slices}}{x - \text{axis length}}$$

$$(\text{Scale factor})_y = \frac{\text{Number of } y - \text{axis slices}}{y - \text{axis length}}$$

$$(\text{Scale factor})_z = \frac{\text{Number of } z - \text{axis slices}}{z - \text{axis length}}$$

The transformation is then applied by multiplying each coordinate by its corresponding scaling factor. The relations applied for the transformation are the following:

$$x_{scaled} = (\text{Scale factor})_x * (x)$$

$$y_{scaled} = (\text{Scale factor})_y * (y)$$

$$z_{scaled} = (\text{Scale factor})_z * (z)$$

The scaled coordinates are stored in a new array while keeping the velocity components at zero. The transformed data is saved in a tab-separated format for future use. To ensure accuracy, the script prints a sample of the transformed coordinates for verification and displays the minimum and maximum values for each scaled coordinate axis. This final step ensures that the CFD simulation data is correctly aligned with the MRI domain, enabling accurate alignment of the velocity values from the 4D arrays.

The core concept of this process is spatial interpolation, which involves assigning velocity values (u , v , w) from the points in the 4D Flow MRI dataset to the corresponding points on the cap geometry. However, before interpolation can take place, the velocity field data must be extracted. To achieve this, a Python script was developed to extract velocity data from a 4D Flow MRI dataset stored in an HDF5 file for a specific timestep, representing the peak systolic phase.

The script first loads the velocity components (u , v , w) from the HDF5 file, where the data is arranged in a 3D grid corresponding to the sagittal (y), axial (z), and coronal (x) planes. The axis correspondence was determined based on the raw MRI images. It then iterates through all grid points, recording their coordinates (x , y , z) along with their respective velocity components, and saves the collected data in a tab-separated TXT file with a header for reference.

However, storing velocity data for the entire grid across each of the three 4D arrays (u , v , w) would result in over 2.5 million points per timestep, making the process computationally expensive. To mitigate this, a more targeted approach was needed. A Region of Interest (ROI) was defined, which focuses only on the area surrounding the cap geometry, significantly reducing computational cost while preserving relevant data for interpolation. A second Python script was developed to extract velocity data within this region of interest (ROI), which was defined based on specific index ranges along the three anatomical planes: axial ($z = 56$ to 61), sagittal ($y = 28$ to 42), and coronal ($x = 40$ to 63). These slices were chosen to align with the boundaries of the cap, ensuring that only the necessary portion of the velocity field is extracted for integration with CFD data. The script loads the velocity components from the HDF5 file within this ROI, records the corresponding coordinates and velocities, and saves the refined dataset as a structured TXT file. Finally, the script was modified to perform the same extraction process for all timesteps, ensuring a complete dataset for time-dependent analysis.

After extracting velocity data from all grids for each component (u , v , w) across all timesteps, the next step was to perform spatial interpolation to transfer these values onto the cap coordinates. A Python script was developed to achieve this by mapping velocity values from a predefined Region of Interest (ROI) to cap geometry. The script first loads coordinate and velocity data from two text files: one containing the sparse grid data and another with the cap's higher-resolution coordinates. It then extracts the x , y , and z coordinates along with the velocity components from both datasets. To handle missing velocity values in the cap dataset (where components are initially zero), the script employs Scipy's `griddata` function to perform linear interpolation based on the grid data. If any NaN values remain after interpolation, they are filled using nearest-neighbor interpolation. Finally, the interpolated velocity values are combined with the original cap coordinates and saved as a structured text file, ensuring that the cap geometry accurately represents the MRI-based velocity field.

This process is then repeated for all timesteps, allowing the generation of a patient-specific velocity profile that spans the entire cardiac cycle. The next step in applying the patient-specific velocity profile was to restore the cap coordinates used for interpolation to their original values, allowing the newly assigned velocity data to be implemented in the simulation. The developed code sequentially transforms and refines the velocity data mapped onto a cap geometry, ensuring alignment with the original simulation coordinate system. The process begins with inverse scaling, converting the transformed cap coordinates back to the MRI space using predefined min/max values. This is followed by a coordinate transformation, where axes are swapped and negated to match the reference frame. Finally, a coordinate shift is applied to restore the original positioning. Each step maintains the accuracy of the velocity data while properly aligning it for computational modeling. The final output is a text file containing the fully transformed velocity field with the original cap coordinates for each point.

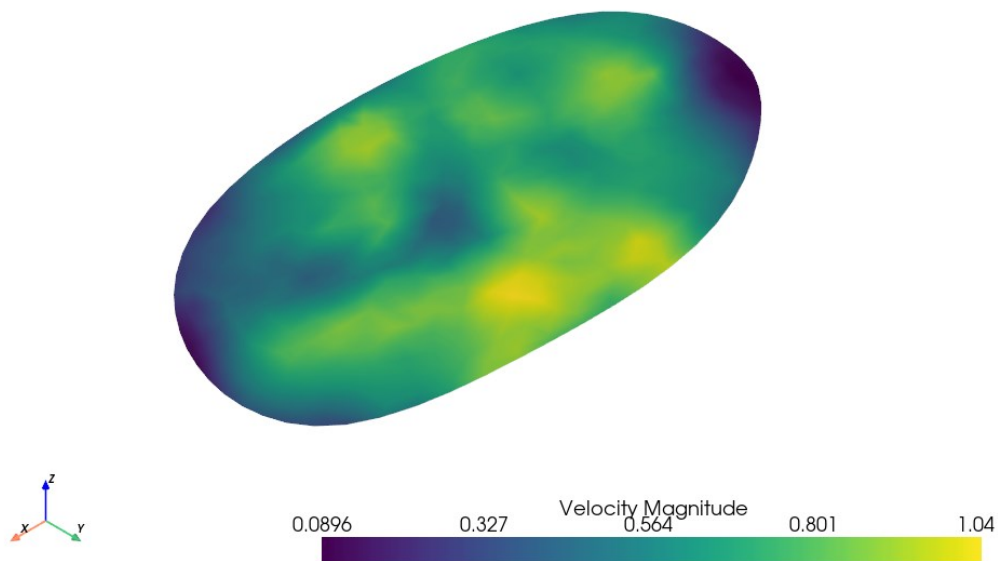


Figure 35: Patient specific velocity profile after spatial interpolation

After applying the patient-specific velocity profile to the cap geometry, additional adjustments were needed to integrate it into the simulation. The key file for this integration is the `bct.dat` file, whose format and function had been previously analyzed. The critical step was replacing the existing `u`, `v`, `w` velocity values in the `bct.dat` file with the newly assigned velocity components from the 4D flow MRI data at each mesh point of the cap. While this replacement was relatively simple, a Python script was developed to reformat the interpolated velocity data to match the original structure of the `bct.dat` file.

The script generates the `bc_interpolated.txt` file, ensuring compatibility with the simulation by adjusting the patient-specific velocity data to fit the `bct.dat` structure. It first extracts spatial point coordinates and node IDs from the `bct.dat` file and stores them in a dictionary for easy lookup. It then reads velocity data from the `txt` file, which contains cap mesh points with corresponding velocity components obtained via spatial interpolation. The script iterates through all spatial points, aligning them with their velocity values at each timestep, calculating the timestep size (`dt`) based on the given period, and ensuring temporal consistency. If a spatial point does not have velocity data, it assigns zero velocities as a fallback. The output file includes spatial headers with point coordinates, the number of timesteps, and node IDs, followed by velocity components (`u`, `v`, `w`) for each timestep, matching the format of `bct.dat`. This properly formatted file enables the accurate implementation of the patient-specific velocity profile in the simulation.

Next, the script converts the velocity components in `bc_interpolated.txt` from meters per second (`m/s`) to centimeters per second (`cm/s`) and saves the updated data. After adjusting the units, the velocity component orientations were corrected. The MRI data used a different coordinate system than the simulation, leading to discrepancies in the velocity components. The following transformation was applied to align the velocity data correctly with the simulation's coordinate system:

$$u_{simulation} = w_{MRI}$$

$$v_{simulation} = u_{MRI}$$

$$w_{simulation} = -v_{MRI}$$

This ensures that the velocity components are properly oriented and aligned with the simulation framework. The final step in preparing the input for the `bct.dat` file involved performing temporal interpolation. Temporal interpolation can be seen as a "smoothing" process for the flow curve, ensuring a more refined flow profile over time. To achieve this, a Python script was developed. This script increases the number of timesteps in the patient-specific velocity data to enhance simulation accuracy. It reads the velocity data from a formatted input file, extracts spatial coordinates and velocity components, and applies cubic spline interpolation.

The script first parses the header to determine the number of spatial points and original timesteps, then generates a new time array with `nl` (201 in this case) evenly spaced timesteps. For each spatial point, it retrieves the velocity components (u , v , w) along with their corresponding time values, applies cubic spline interpolation to create a smoother and higher-resolution velocity profile, and writes the interpolated results to a new output file. This process ensures a temporally refined velocity dataset, improving both the accuracy and stability of the simulation. A final overview of the application of the patient specific velocity profile as an inlet boundary condition can be seen in Figure 36.

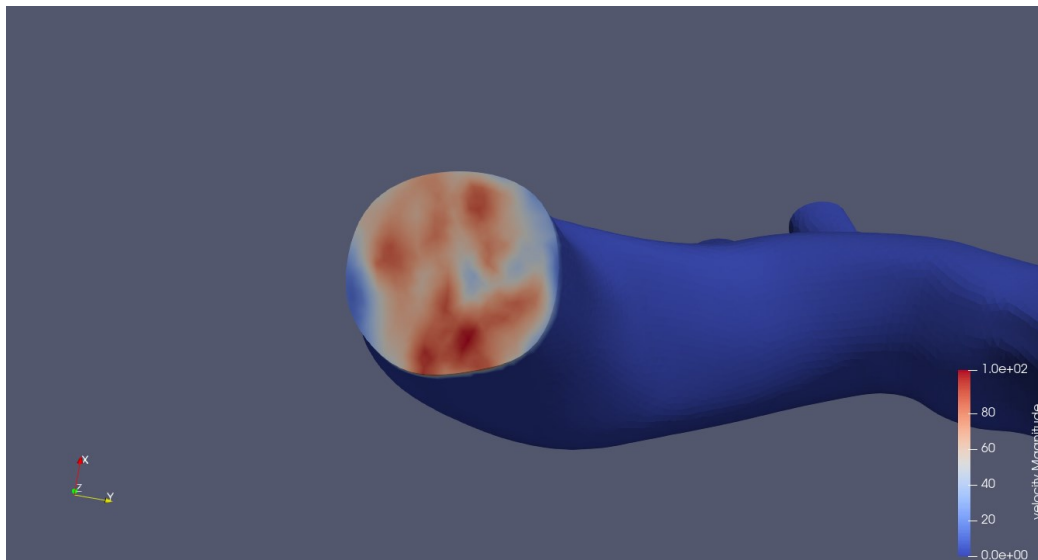


Figure 36: 3D model with patient specific velocity profile applied

3. Results and Discussion

Before running the main simulations, final smoothing and refinement operations were applied to the thoracic aorta model after calibration. As done previously, these adjustments were performed in Meshmixer. The primary goal was to smooth sharp edges, particularly in the branches of the brachiocephalic, left common carotid, and left subclavian arteries, to prevent potential solver issues such as large gradients. Additionally, the overall surface was smoothed for better simulation stability. Figure 37 shows the refined thoracic aorta model.

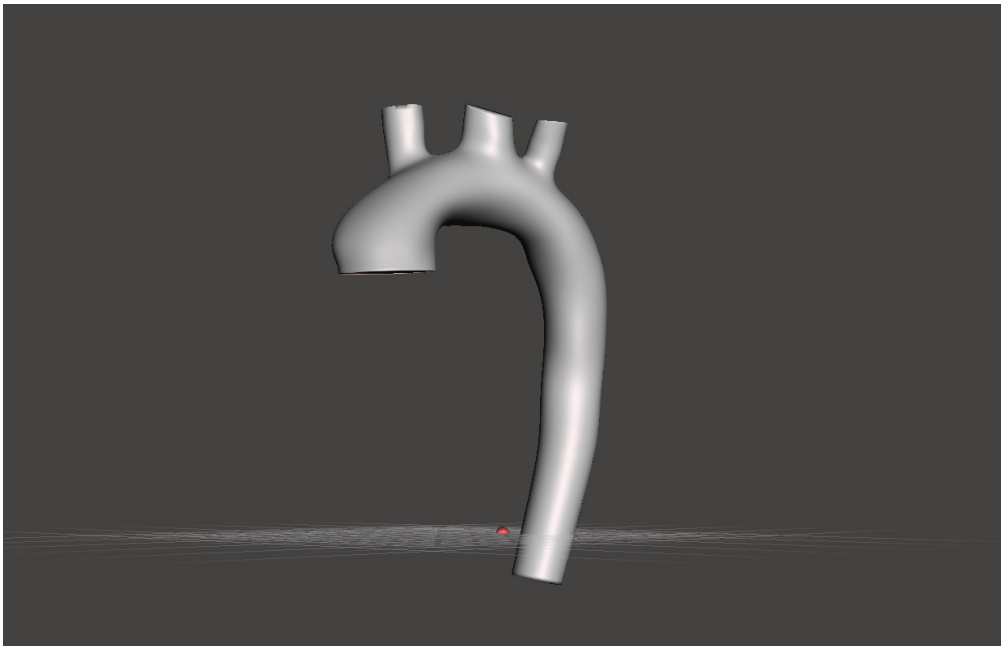


Figure 37: Refined thoracic aorta model

After the refinement process, the methodology outlined in the previous section (Methods) was implemented. The simulations incorporated the calibrated RCR boundary condition values, while two different inlet boundary conditions were tested: one using the previously discussed custom velocity profile and the other employing a parabolic profile for comparison.

First, the case of the custom velocity profile is examined, followed by the parabolic profile. Simulations were conducted using both SimVascular and CRIMSON, with the corresponding results presented for comparison. This comparison is essential for validating the consistency and reliability of the simulations, ensuring that the numerical results are not software-dependent and can be confidently used for further analysis. Additionally, the parabolic profile serves as a reference to emphasize the differences between an idealized mathematical model for assessing the mechanical properties of the thoracic aorta and a more realistic, patient-specific approach.

Throughout the analysis in this work, four key timepoints were selected to represent important phases of the cardiac cycle: one at the start of the systolic phase, one at the peak of systole, one at the end of systole, and one during mid-diastole to represent the diastolic phase. Figure 38 illustrates the selected timepoints and their respective positions within the cardiac cycle.

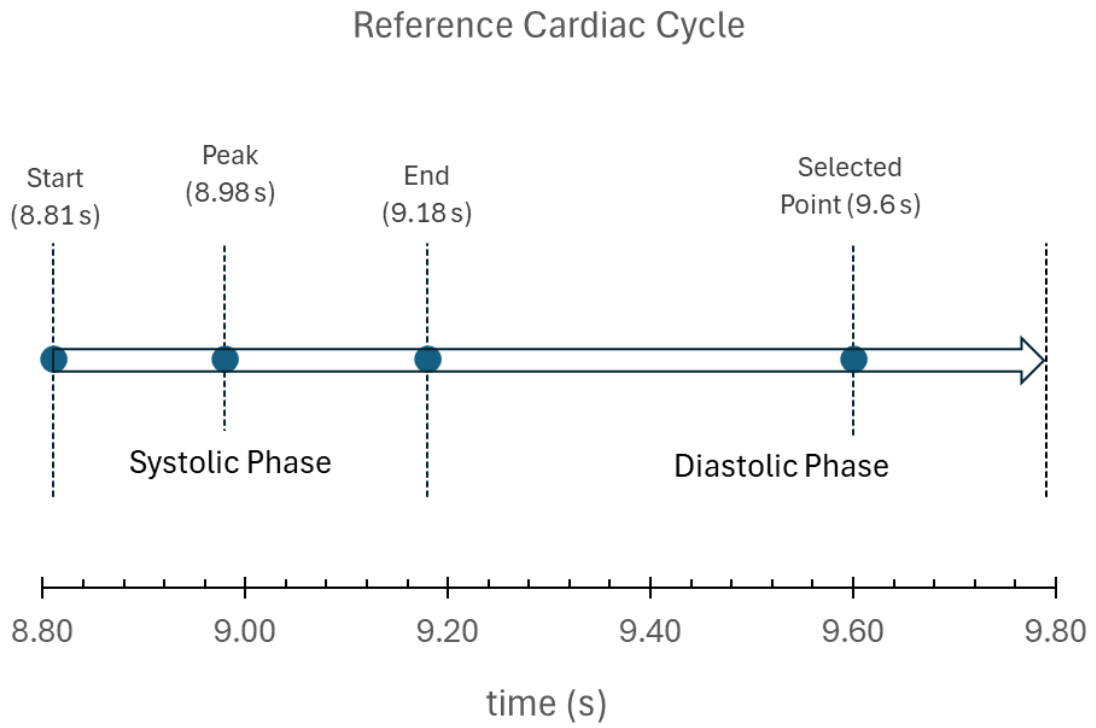


Figure 38: Timeline of Key Analysis Timepoints Across the Cardiac Cycle

3.1 Patient-specific velocity profile

3.1.1 Pressure Profile

In this section, the pressure waveforms and the 3D pressure distributions, obtained by simulations using both the SimVascular and the CRIMSON software programs, are presented and discussed.

Pressure waveforms. First, the ascending aorta inlet pressure waveforms obtained by the two programs, are presented in Figure 39. In both waveforms, approximately 10 seconds of real time with a timestep of 0.01 seconds is required for numerical convergence to a steady pressure value. One difference may be that CRIMSON calculates slightly lower pressure values than SimVascular, which can be attributed to minor differences in solver implementations and the way the 3D model is interpreted in each software. However, from a physiological perspective, both waveforms indicate that the patient exhibits stage 2 hypertension due to the elevated pressure values exceeding normal physiological limits (i.e. approximately 140 mmHg or higher systolic, and 90 mmHg or higher diastolic, NHLBI Online).

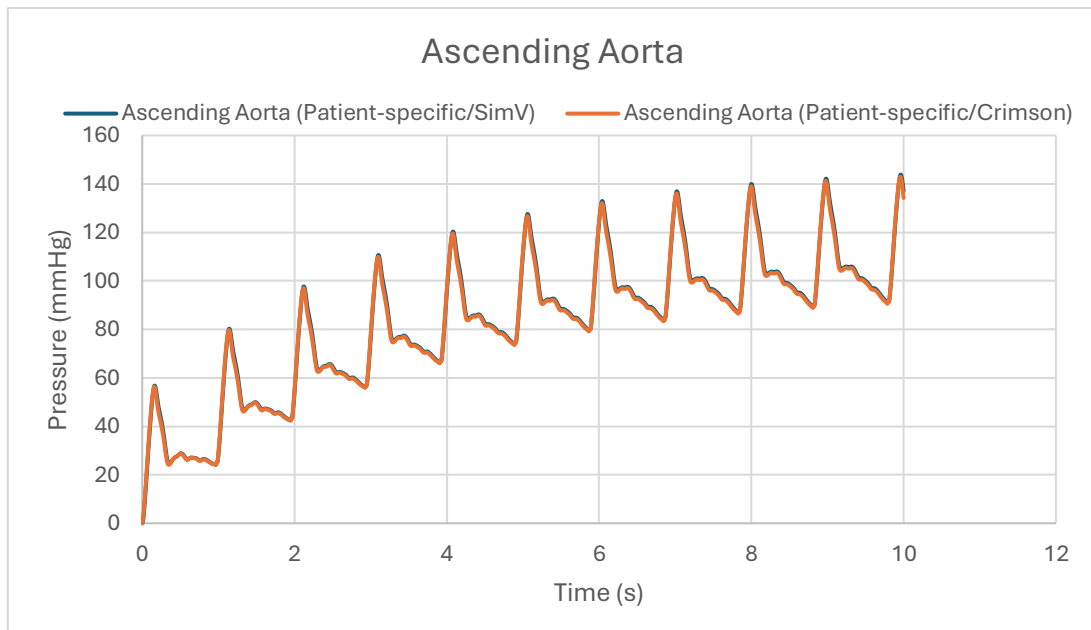


Figure 39: Pressure waveforms for Ascending Aorta

The next set of derived pressure waveforms corresponds to the descending aorta, one of the model's outlets, as shown in Figure 40. These waveforms exhibit similar convergence patterns and overall behavior like those observed in the ascending aorta. The same principles apply here as well, with the key difference being that the pressure values at the descending aorta outlet are generally lower than those at its inlet. This is expected, as the ascending aorta experiences higher pressures due to its proximity to the heart, the primary pumping mechanism. Additionally, as blood exits the aortic arch, gravitational forces contribute to the flow dynamics, reducing the pressure required to propel the blood forward.

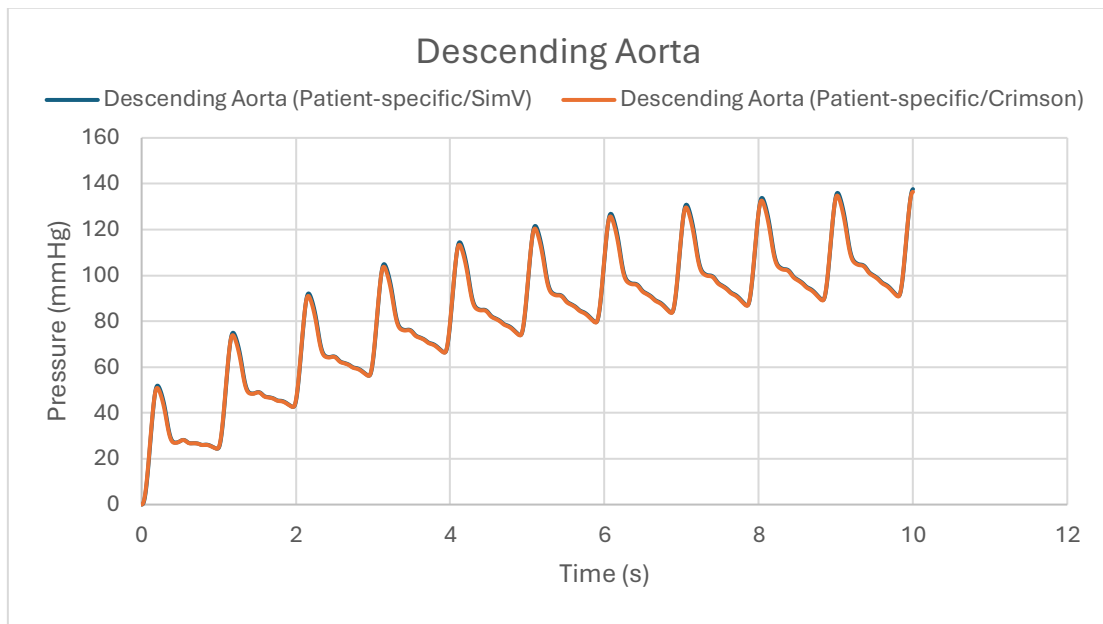


Figure 40: Pressure waveforms for Descending Aorta

After analyzing the pressure waveforms from the two main caps, the next step is to examine the pressure behavior in the three branches of the aortic arch. The following set of pressure waveforms corresponds to the brachiocephalic artery (Figure 41). Their overall behavior remains consistent with the previous waveforms, with the key distinction being slightly elevated pressure values, closer to those observed in the ascending aorta. This is expected, as higher pressure is required to drive blood flow through the brachiocephalic artery, where gravitational forces act as opposing factors.

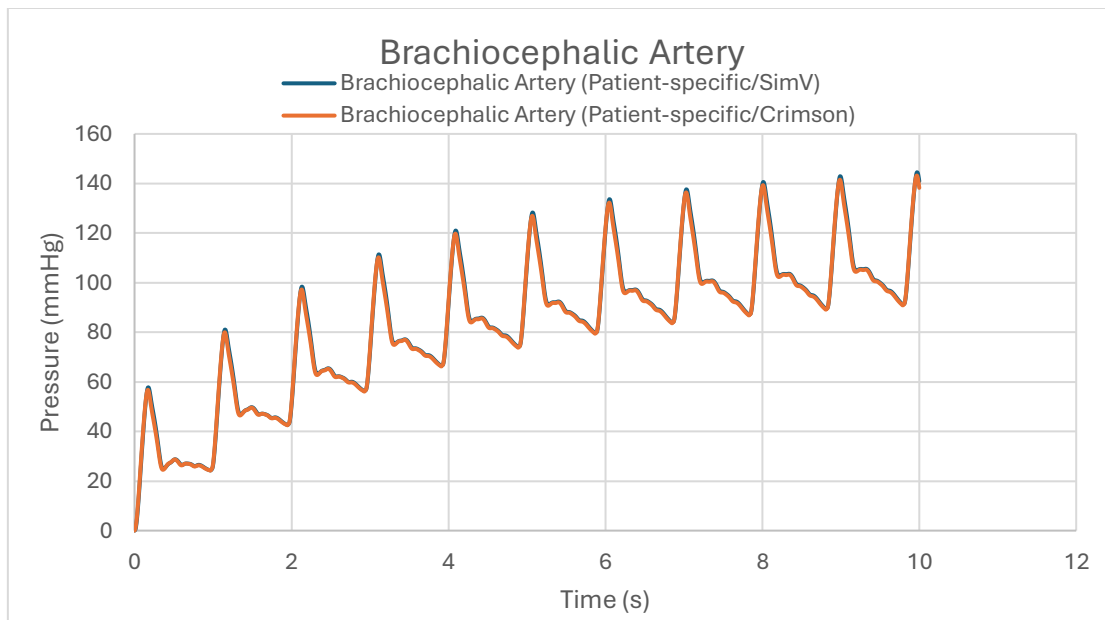


Figure 41: Pressure waveforms for Brachiocephalic Artery

Similar to the brachiocephalic artery, the pressure waveforms of the left common carotid artery (Figure 42) display consistent overall behavior across both software programs. However, the CRIMSON-derived waveform exhibits slightly lower pressure values like the

other pressure waveforms. Generally, the pressure levels are comparable to those in the brachiocephalic artery, which is expected due to the same underlying principles governing blood flow. Pressure serves as the driving force for blood distribution to the upper body. Regarding convergence, the time required for numerical stability remains unchanged.

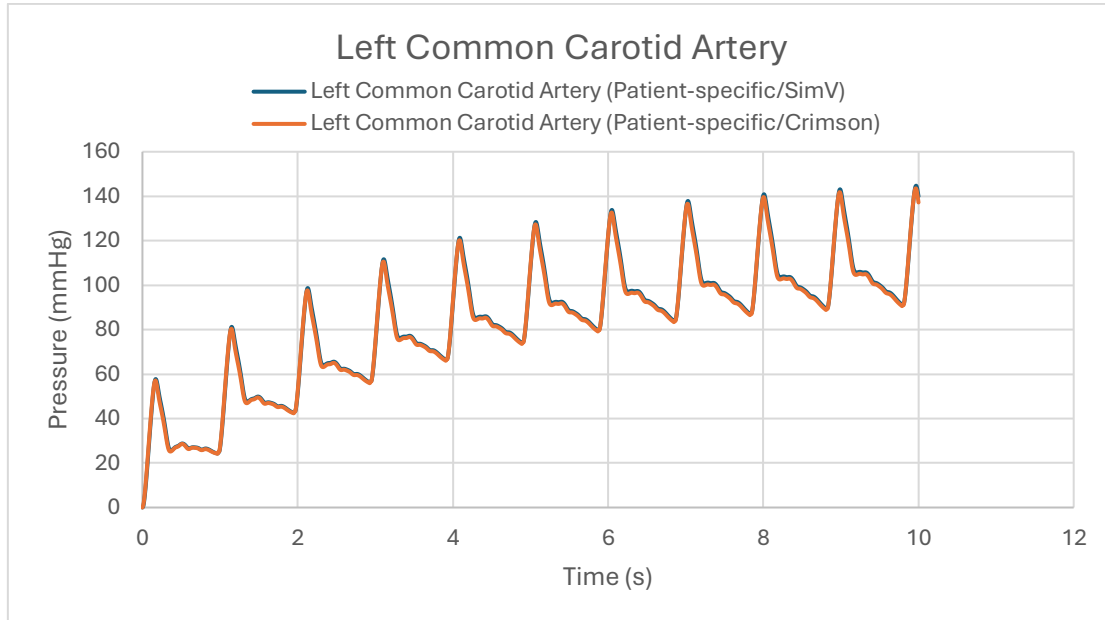


Figure 42: Pressure waveforms for Left Common Carotid Artery

Finally, the pressure waveforms of the left subclavian artery (Figure 43) follow the same pattern as those of the other two branches of the aortic arch. Once again, CRIMSON exhibits slightly lower pressure values compared to SimVascular. Notably, all three branches share similar pressure waveforms, which is to be expected due to their comparable anatomy and functional requirements within the circulatory system, as previously discussed.

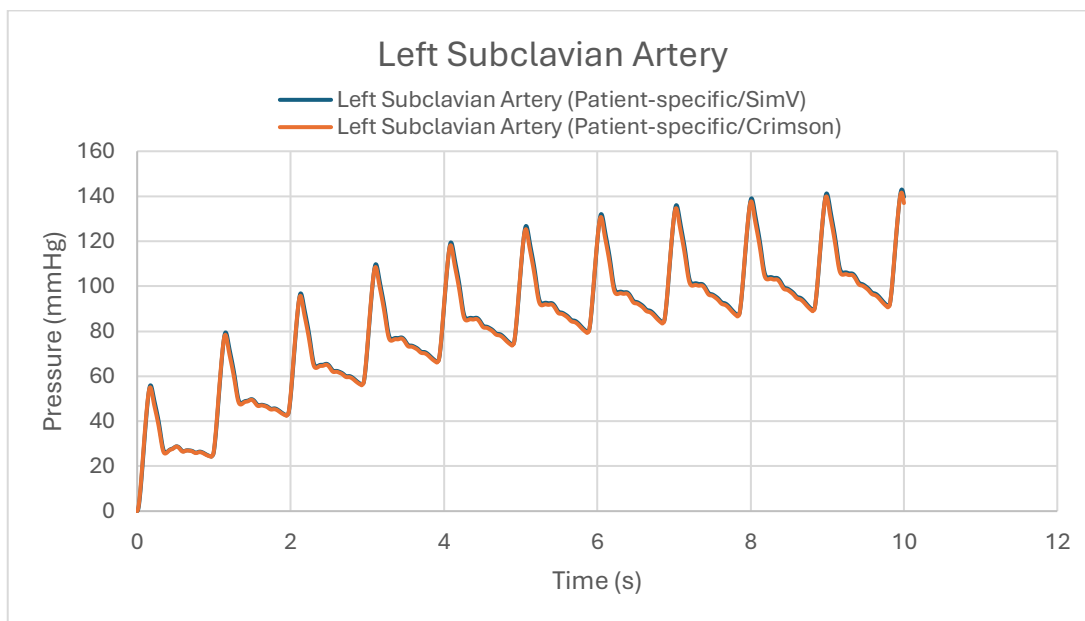


Figure 43: Pressure waveforms for Left Subclavian Artery

3D Pressure Distribution. Following the presentation of the pressure waveforms, the next step is to analyze the pressure distribution across the entire 3D model. To gain a clearer understanding of the underlying mechanisms, it is essential to examine pressure distributions at different time points. Specifically, pressure distribution is visualized at the start of the systolic phase (acceleration), the peak of the systolic phase, the end of the systolic phase (deceleration), and a random time point during the diastolic phase. These four selected time points effectively capture the key behaviors governing the problem, as explained below.

Start of the systolic phase. First, the timepoint of 8.81 seconds (timestep 881) is chosen to represent the start of the systolic phase, as the pressure values have reached convergence by this time. The calculated pressure distribution is shown in Figure 44 (SimVascular) and Figure 45 (CRIMSON).

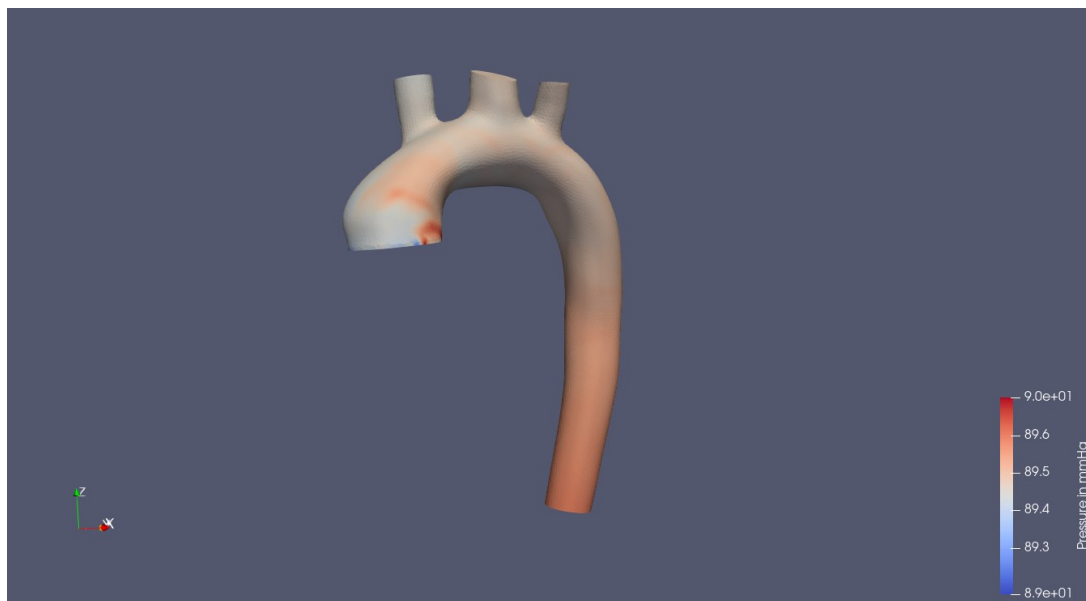


Figure 44: Pressure Distribution at start of the systolic phase (SimVascular)

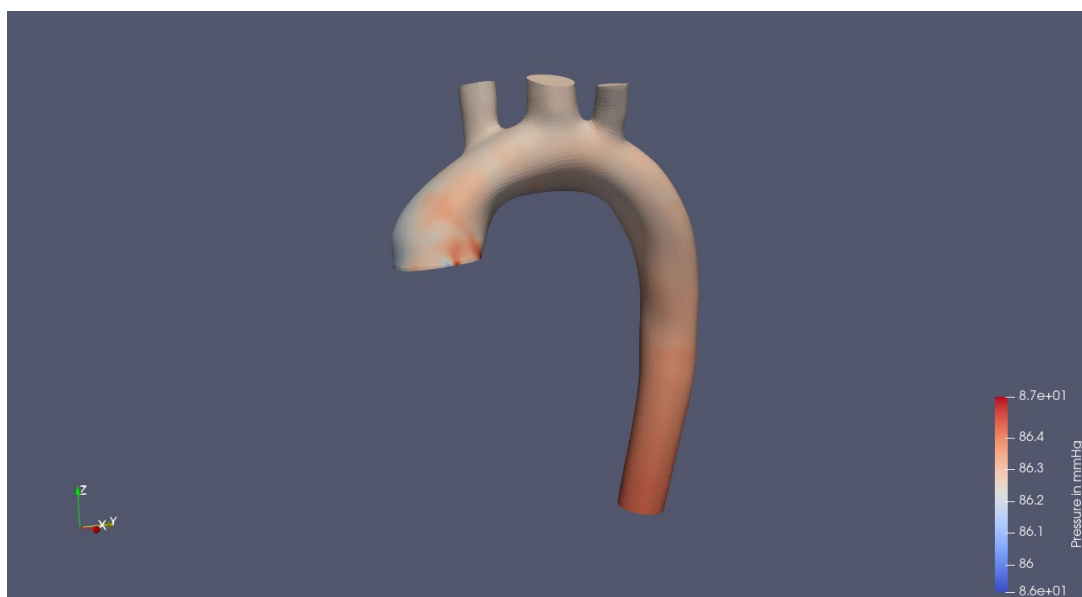


Figure 45: Pressure Distribution at start of the systolic phase (Crimson)

At the start of the systolic phase, the pressure distribution remains relatively uniform, with higher pressure values observed in the descending aorta. In contrast, the ascending aorta exhibits lower pressure values due to the heart's relaxation phase. As blood moves through the aortic arch and into the descending aorta, the pressure gradually increases. This elevation in pressure within the descending aorta is primarily driven by gravitational forces, which dominate in this region. However, localized areas of high pressure can be seen in the ascending aorta, likely resulting from the curved geometry, which introduces high gradients, and the early stages of the systolic phase, where blood is being actively pumped into the ascending aorta. Comparing Figure 44 and Figure 45, one can observe that the differences in pressure distribution between CRIMSON and SimVascular, are minimal. Like pressure waveforms, only slight variations in lower pressure values can be observed.

Peak of the systolic phase. Next timepoint is selected to be the one at 8.98 s (timestep 898) that represents the peak of the systolic phase for this cardiac cycle. The pressure distribution results are shown in Figure 46 (SimVascular) and Figure 47 (CRIMSON). At peak systole, high pressure is observed in the ascending aorta and remains elevated throughout the aortic arch. However, as blood flows into the descending aorta, pressure gradually decreases, reaching its lowest values. This decline is primarily influenced by gravity, which facilitates blood flow in the descending aorta, reducing the pressure gradient compared to the ascending aorta. Additionally, as blood moves toward distal regions, peripheral resistance increases, and vessel narrowing, along with downstream vascular beds, introduces further resistance, contributing to the pressure drop. Viscous friction and arterial branching (brachiocephalic, left common carotid, and left subclavian) also play a role in localized pressure alterations. This distribution highlights that regions closer to the heart experience higher pressures, while gravity assists blood flow in the descending aorta, easing the heart's workload. Like the pressure distribution at the start of the systole, the results from SimVascular and CRIMSON show negligible differences, with CRIMSON yielding slightly lower pressure values.

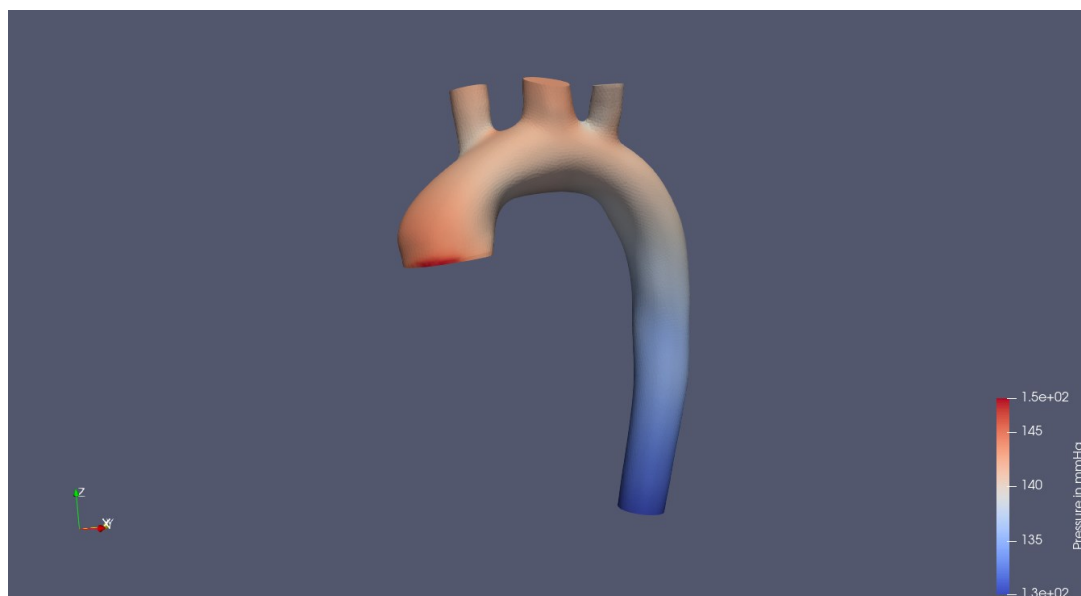


Figure 46: Pressure Distribution at peak of the systolic phase (SimVascular)

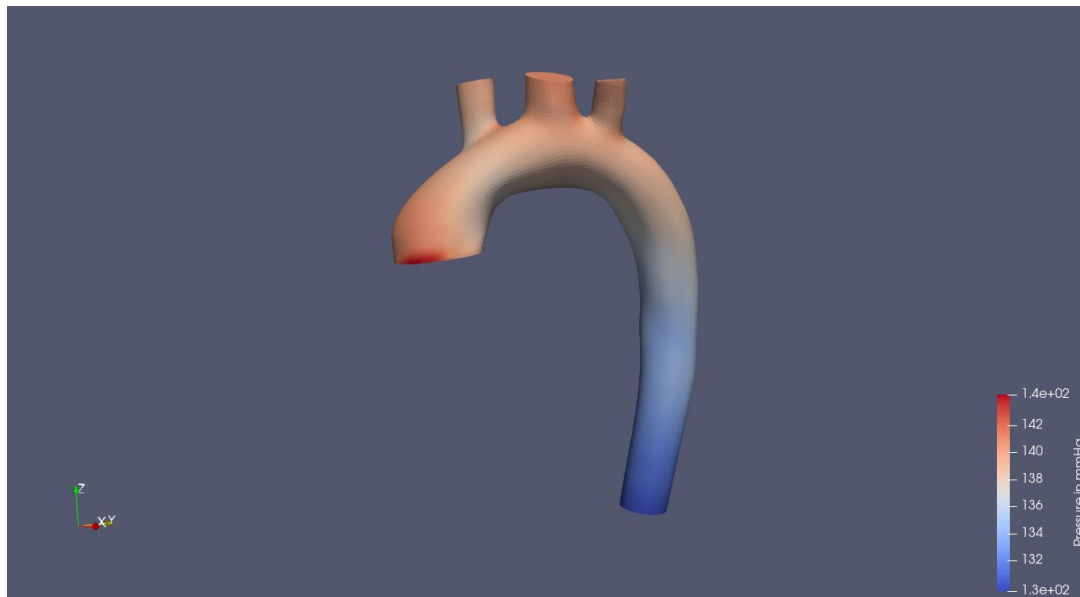


Figure 47: Pressure Distribution at peak of the systolic phase (Crimson)

End of the systolic phase. Next selected timepoint is 9.18 s (timestep 918) that represents the end of the systolic phase for this cardiac cycle. The results are shown in Figure 48 (SimVascular) and Figure 49 (Crimson). At the end of the systolic phase, the lowest pressure values are observed in the ascending aorta, gradually increasing through the aortic arch and reaching their highest values in the descending aorta. This pressure distribution reflects the transition from systole to diastole, where the heart's contraction subsides, and the blood flow dynamics shift. The decrease in pressure in the ascending aorta is due to the heart entering relaxation, reducing the driving force “pushing” blood forward. Meanwhile, in the descending aorta, residual momentum and vascular resistance contribute to maintaining higher pressures. Additionally, the effects of vessel compliance and peripheral resistance play a role in sustaining pressure in the distal regions. As seen in previous cases, the pressure distributions obtained from SimVascular and CRIMSON exhibit negligible differences.

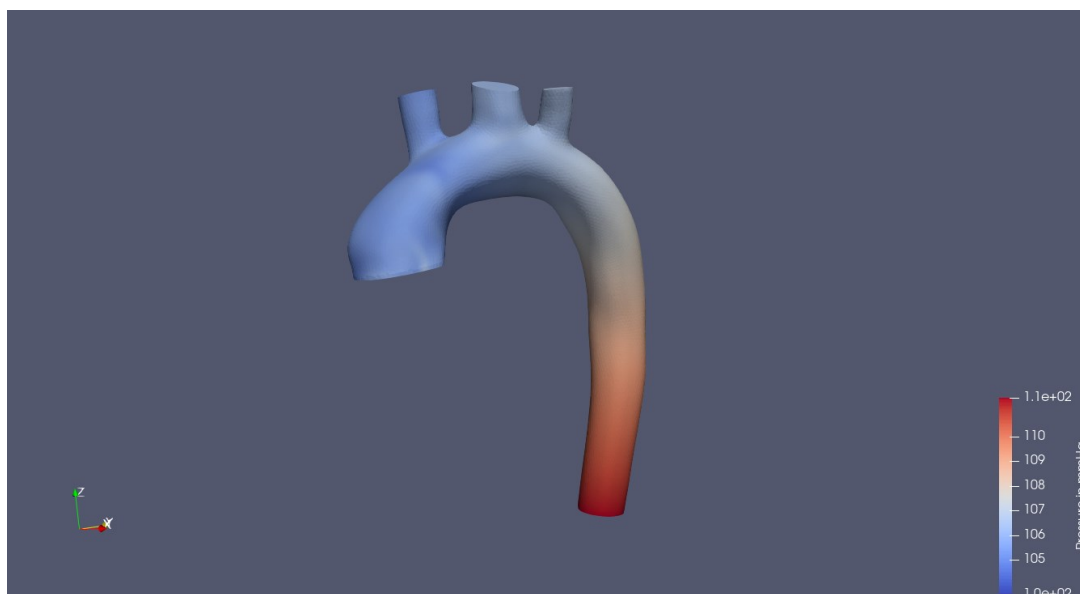


Figure 48: Pressure Distribution at the end of the systolic phase (SimVascular)

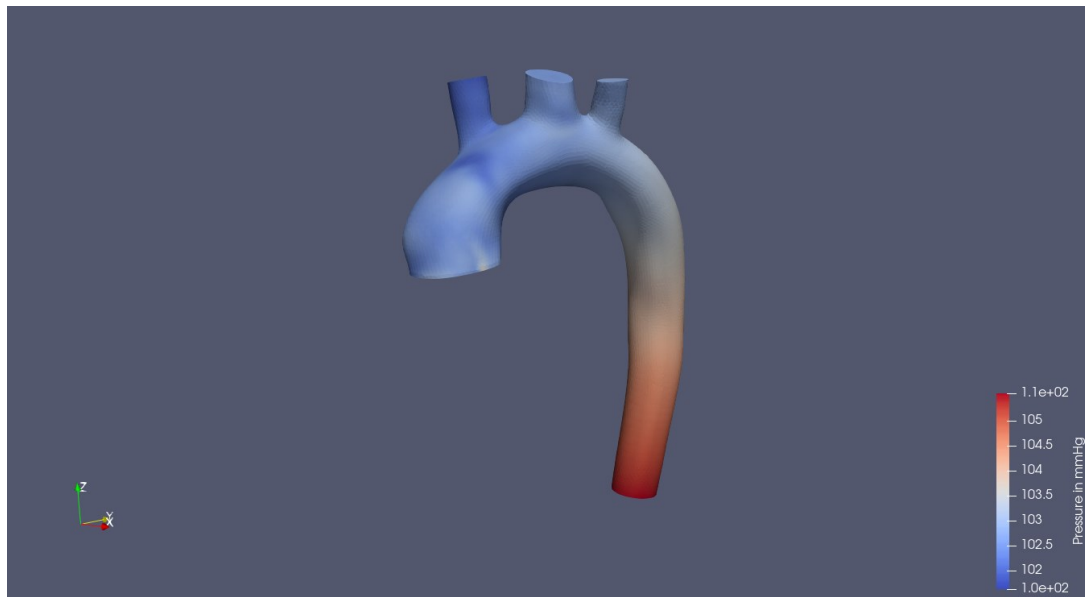


Figure 49: Pressure Distribution at the end of the systolic phase (Crimson)

During the diastolic phase. To further investigate the mechanisms of pulsatile flow, an additional timepoint from the diastolic phase was selected to capture its characteristic behavior. The chosen timepoint, 9.6 s (timestep 960), is approximately in the middle of the diastolic phase, making it a representative snapshot of the flow dynamics during this period. The results are shown in Figure 50 (SimVascular) and Figure 51 (CRIMSON).

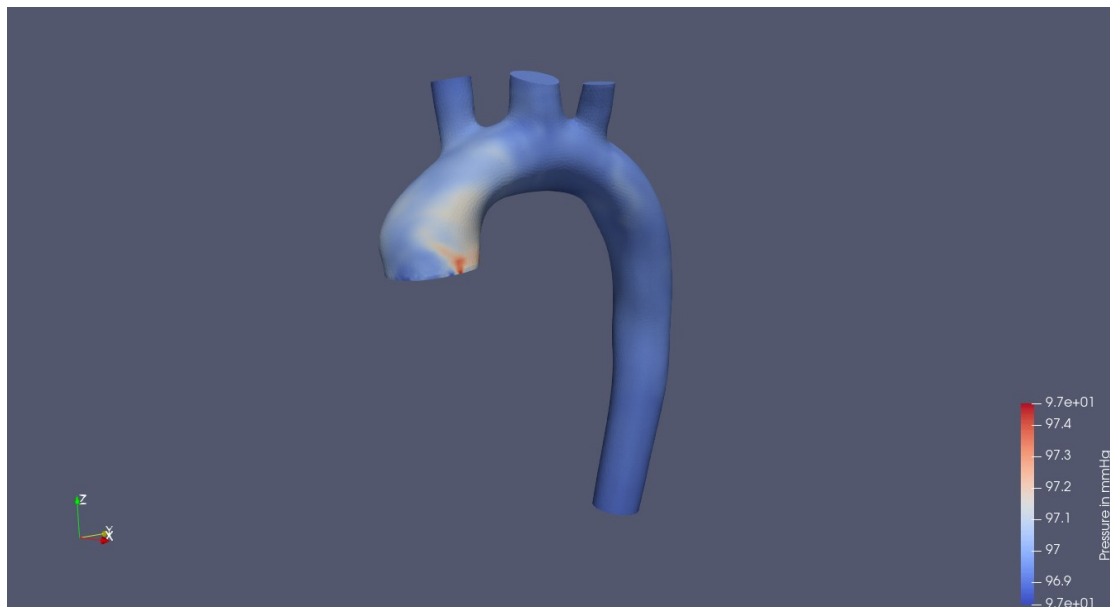


Figure 50: Pressure Distribution during the diastolic phase (SimVascular)

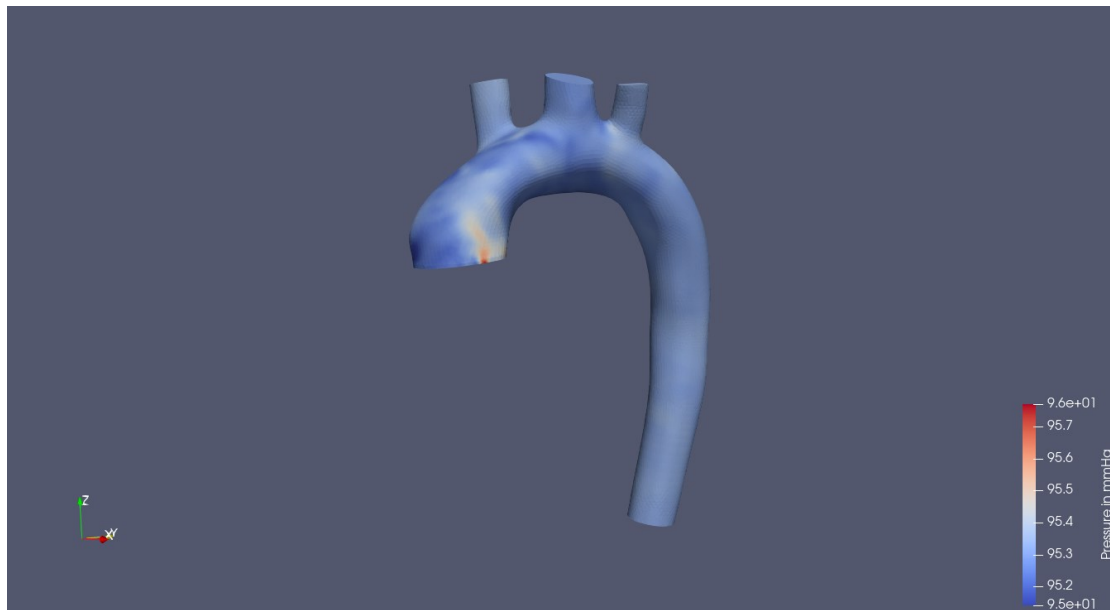


Figure 51: Pressure Distribution during diastolic phase (Crimson)

During the diastolic phase, most of the aortic model exhibits low pressure values, which is expected as the heart "relaxes" and no longer actively pumps blood into the aorta. As a result, the blood flow experiences little to no driving force. The only region with relatively higher-pressure values is the initial segment of the ascending aorta, which is closest to the heart. During diastole, the initial segment of the ascending aorta exhibits relatively higher-pressure values due to the closure of the aortic valve being susceptible to more flow variations. As the heart enters diastole, the aortic valve closes to prevent backflow into the left ventricle, generating a dicrotic notch in the pressure waveform and momentarily sustaining higher pressure in the proximal aorta. Additionally, pressure waves propagate through the arterial system and reflect at branch points, such as the three main branches in the aortic arch, with some of these reflected waves returning to the ascending aorta, causing a slight pressure elevation.

Since the simulation does not incorporate fluid-structure interaction (FSI), arterial wall elasticity is not explicitly modeled. However, the resulting pressure distribution remains consistent with expected physiological behavior, where the absence of active pumping leads to lower pressures throughout the aorta, except in regions influenced by wave reflections and more susceptible to backflows. As shown in Figure 51, the pressure values computed by CRIMSON closely match those from SimVascular in Figure 50, with only minor differences, as observed in previous timesteps.

3.1.2 Flow rate profile and velocity vector field

Following the analysis of pressure profiles, it is essential to examine the flow rates entering the ascending aorta and exiting through the remaining outlets. Additionally, velocity vector fields should be presented to evaluate the flow behavior within the thoracic aorta and assess various physiological conditions it may exhibit. Furthermore, as discussed in previous sections, the patient-specific velocity profile is derived from 4D flow MRI data for each time point throughout the simulation. Therefore, it is crucial to visualize this patient-specific velocity profile at selected time points to understand how the flow propagates through the anatomical structure of the model. The flow profile graphs for the parabolic velocity profile were omitted because they convey the same overall information as the patient-specific profile. In both cases, the total fluid volume entering and exiting the model remains unchanged, ensuring mass conservation. However, the velocity distribution differs, which may influence local flow patterns variations. While the parabolic profile provides a more idealized inlet condition, the patient-specific profile may capture secondary flow structures and skewness due to upstream influences, potentially impacting localized hemodynamic metrics.

Flow rate profiles. First, the flow rate profiles for the inlet (Ascending Aorta) and each outlet (Descending Aorta, Brachiocephalic Artery, LCCA, LSA) are presented to analyze their magnitude and behavior throughout the simulated time. Like the pressure waveforms, the flow waveforms are computed using both SimVascular and CRIMSON to facilitate a comparison between the two software programs.

Observing the graph in Figure 52, it is evident that the inlet flow in the ascending aorta follows a pulsatile waveform, aligning well with expected physiological behavior. During the diastolic phase of the cardiac cycle, the flow rate oscillates around zero, which is typical due to wave reflections and downstream resistance causing minor backflows in the arteries. Both software programs exhibit the same fundamental flow mechanisms, demonstrating consistency in the simulated cardiac cycles.

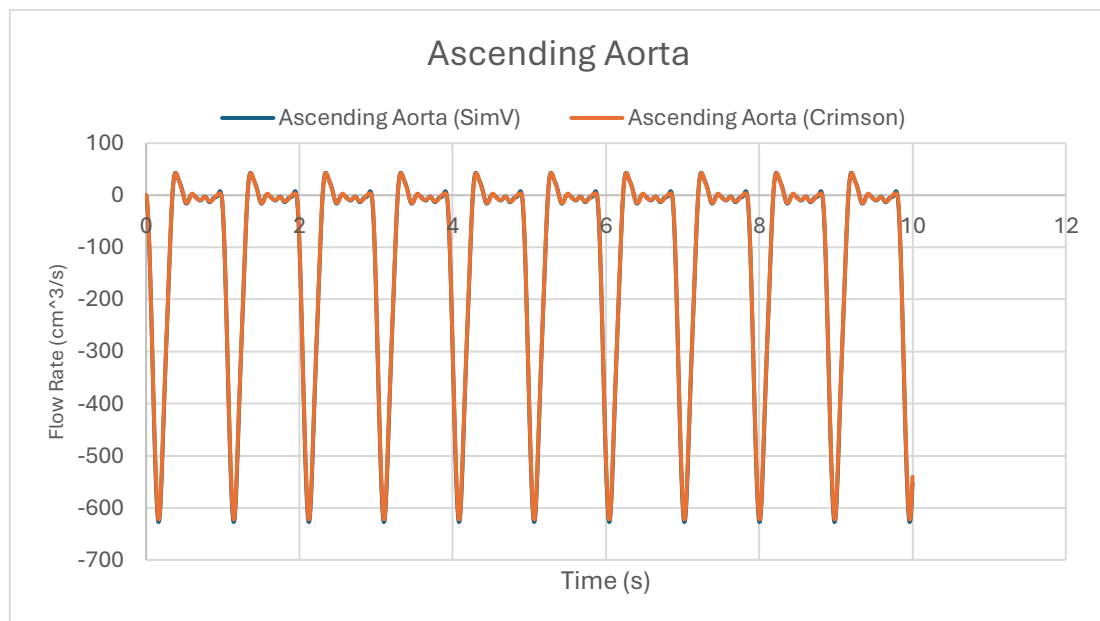


Figure 52: Flow rate in ascending aorta (inlet)

A minor discrepancy between SimVascular and CRIMSON is observed in the peak flow rate values during the systolic phase. SimVascular calculates a peak value of ca. $-621 \text{ cm}^3/\text{s}$, while CRIMSON reports ca. $-615 \text{ cm}^3/\text{s}$. This discrepancy is likely due to differences in how each software interprets the cap area. Since the velocity input, derived from 4D flow MRI data, is identical in both cases, the variation most likely stems from differences in STL file processing and the unique meshes generated by each program. Although both meshes contain approximately the same number of elements, their distribution differs between the two meshers. In SimVascular, the cap area mesh has slightly more elements than in CRIMSON, resulting in a greater number of velocity values being assigned to the inlet vertices. This, in turn, leads to differences in the computed flow rate. Despite the observed variation in flow rate, the velocity values remain consistent between the two programs. These observations can be further analyzed using the mathematical equation for flow rate, i.e.: $Q = uA$, where Q is the flow rate, u the flow velocity and A the cross-section area of the flow.

After analyzing the flow rate at the ascending aorta (inlet), the next step is to examine the flow rates at the outlets, starting with the Descending Aorta (Figure 53). The flow rate waveform of the descending aorta exhibits a clear pulsatile pattern, mirroring the behavior observed at the inlet. Following the systolic phase, a minor backflow appears, marking the onset of the diastolic phase, with flow oscillations occurring near zero, an expected physiological characteristic due to wave reflections and downstream resistance.

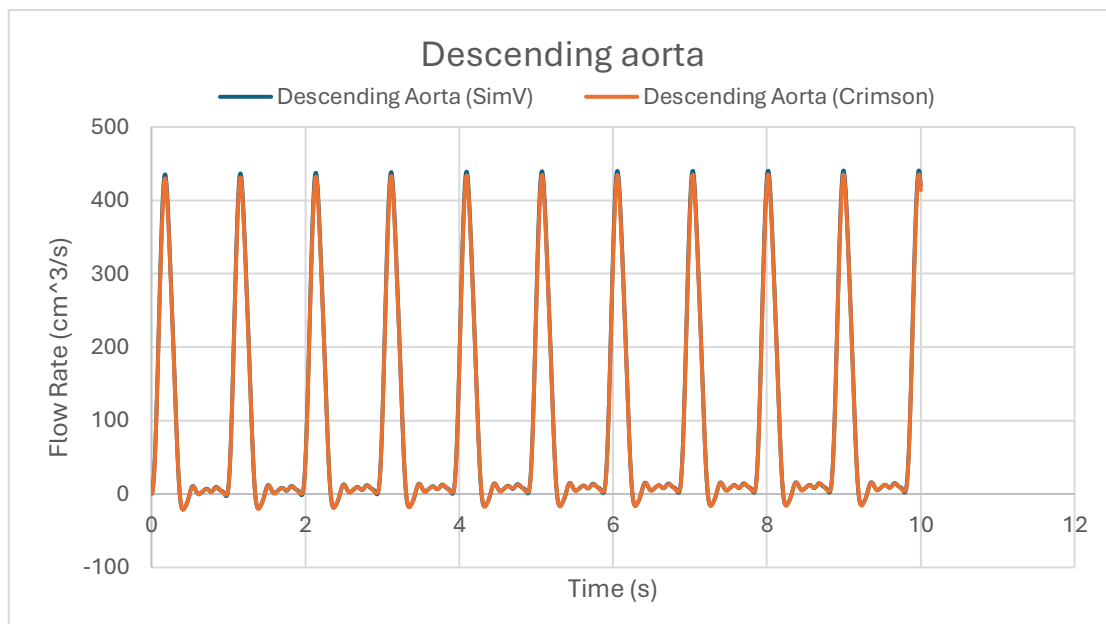


Figure 53: Flow rate in descending aorta (outlet)

A minor discrepancy is observed in the peak flow rate values between the two software programs. The positive sign, in contrast to the inlet values, indicates that this is an outlet where blood exits the domain. This variation in peak values stems from the same underlying cause as seen in the ascending aorta, the differences in how each software generates meshes, resulting in slight variations in the computed cap area. Since the velocity input remains identical in both cases, these discrepancies are most likely due to differences in geometry processing, particularly in the meshing approach used by each program.

Next outlet is the Brachiocephalic Artery that has the flow rate waveform presented in Figure 54. As observed in the previous outlet, the flow in the brachiocephalic artery exhibits a similar behavior. The flow rate waveform in this artery follows a pulsatile pattern similar to the inlet, with peak flow occurring during the systolic phase. During the diastolic phase, a backflow is observed, which is more pronounced compared to the descending aorta. Specifically, the backflow reaches approximately $-35 \text{ cm}^3/\text{s}$ in the brachiocephalic artery, whereas in the descending aorta, it is around $-16 \text{ cm}^3/\text{s}$. This greater backflow is expected due to differences in vascular branching and the artery's resistance.

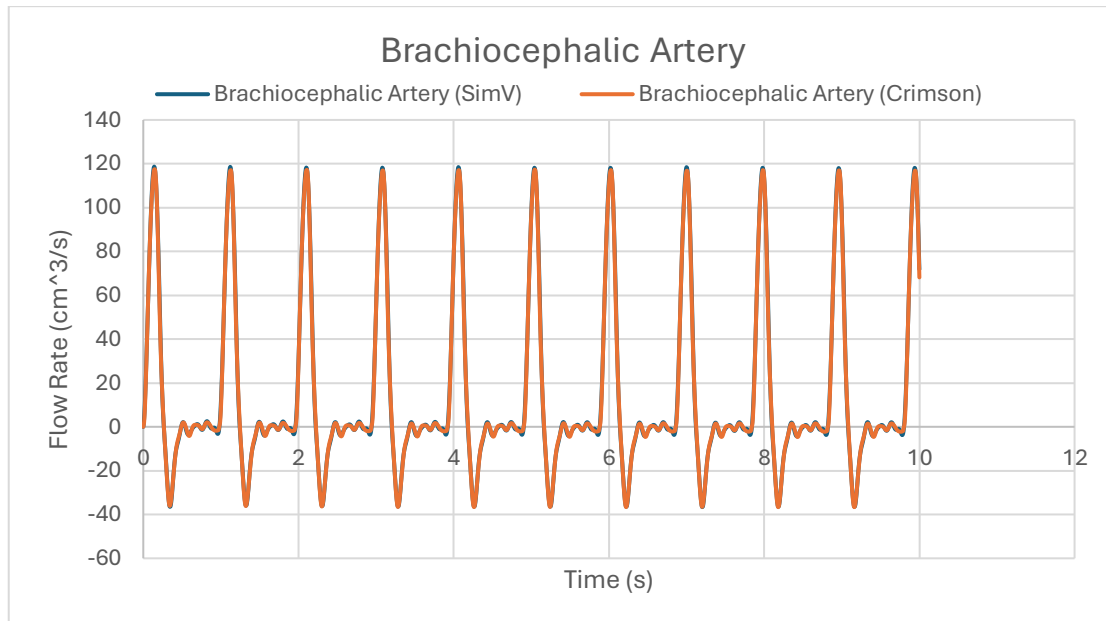


Figure 54: Flow rate in brachiocephalic artery (outlet)

Being closer to the aortic arch, the brachiocephalic artery experiences stronger wave reflections, which contribute to a more significant retrograde flow during diastole. In contrast, the descending aorta, positioned further downstream and with a larger diameter, dissipates these reflections more gradually, resulting in reduced backflow. Additionally, the brachiocephalic artery supplies both the right subclavian and right common carotid arteries, which lead to higher-resistance vascular beds, intensifying pressure wave reflections and further increasing retrograde flow. Moreover, the descending aorta, with its greater compliance, absorbs pressure fluctuations more effectively, whereas the brachiocephalic artery, being a smaller branch, experiences a relatively larger percentage of flow reversal. Regarding peak systolic flow, the discrepancies between the two software programs can be considered insignificant, with both programs reporting approximately $115 \text{ cm}^3/\text{s}$ during the peak systolic phase.

Next outlet is the Left Common Carotid Artery, which is the next branch of the aortic arch. As observed in the previous outlets, the flow in the left common carotid artery (Figure 55) follows a characteristic pulsatile waveform. During diastole, a maximum backflow of approximately $-10 \text{ cm}^3/\text{s}$ is present, which is lower than that observed in the brachiocephalic artery ($-35 \text{ cm}^3/\text{s}$) but remains physiologically expected due to wave reflections and downstream vascular resistance. As a direct branch of the aortic arch, the left common carotid artery experiences retrograde flow during diastole due to reflected pressure waves. However, given that it primarily supplies the brain region with high metabolic demand and relatively low vascular

resistance, the magnitude of the backflow is less pronounced compared to the brachiocephalic artery. Furthermore, its smaller diameter and lower compliance compared to the descending aorta contribute to localized pressure fluctuations and some degree of flow reversal. Regarding peak systolic flow, compared to the previous cases the flow profiles from the two programs have a very similar pattern and no notable discrepancies.

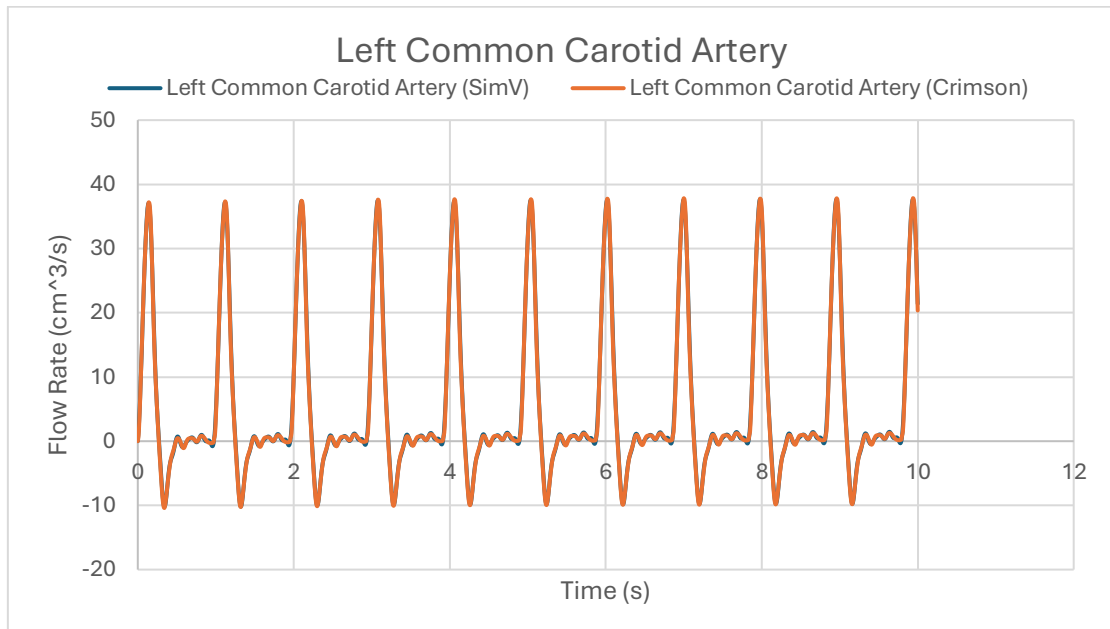


Figure 55: Flow rate in left common carotid artery (outlet)

The last branch of the aortic arch and last outlet of the aorta model used is the Left Subclavian artery (Figure 56). Among the examined outlets, the left subclavian artery (LSA) exhibits an important characteristic, that it must reach convergence first, meaning that after several cardiac cycles, the flow rate drops below zero during the diastolic phase.

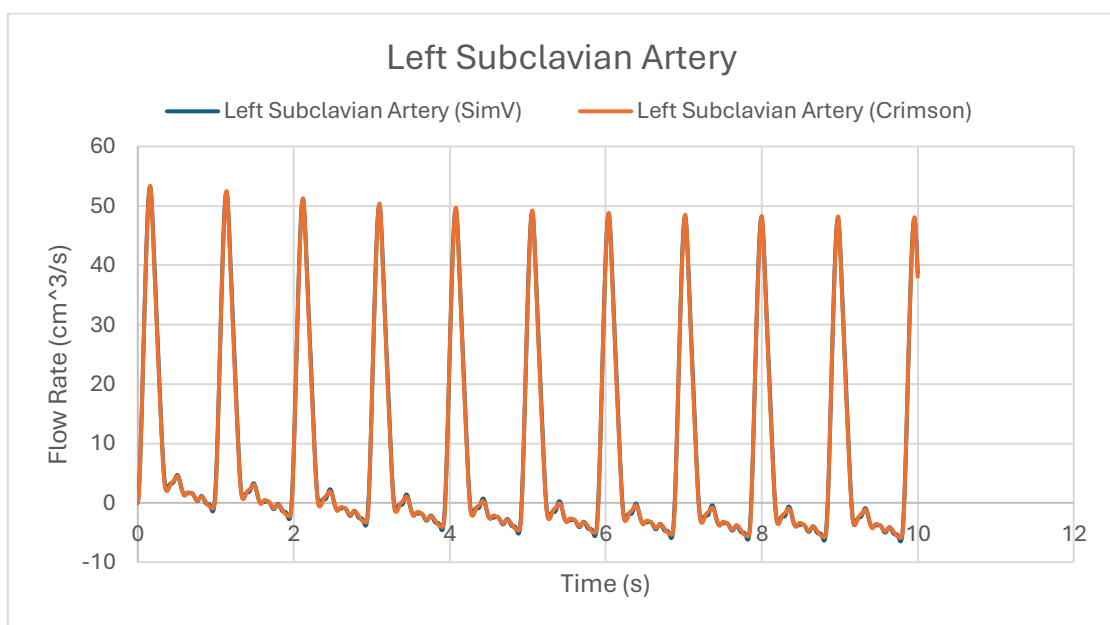


Figure 56: Flow rate in left subclavian artery (outlet)

The flow rate waveform in the LSA follows a pulsatile pattern, with a peak systolic flow of approximately 48 cm³/s and a decline during diastole. Notably, during diastole, the flow rate falls below zero, indicating retrograde flow (backflow). However, this backflow remains relatively small (ca. -5 cm³/s) compared to the peak forward flow, suggesting a minor physiological reversal rather than a pathological concern. The presence of backflow can be attributed to wave reflections from distal vascular beds, a drop in aortic pressure during diastole, and high peripheral resistance, which momentarily pushes blood back toward the aorta. In both cardiovascular simulations and in vivo studies, such backflow in the LSA is a commonly observed phenomenon and is considered normal hemodynamic behavior, provided that the negative values remain small and transient.

Overall, comparison between SimVascular and CRIMSON shows that both software programs generate nearly identical flow waveforms, demonstrating strong agreement. This indicates that the numerical methods, boundary conditions, and model setups are well-matched, leading to a converged solution with minimal numerical discrepancies between the two solvers. The final aspect to be verified is whether the conservation of mass is satisfied. This can be checked with the following equation:

$$Q_{AA} = Q_{DA} + Q_{BA} + Q_{LCCA} + Q_{LSA}$$

, where Q_{AA} is the inlet flow in the ascending aorta, Q_{DA} is the outlet flow of the descending aorta, Q_{BA} is the outlet flow of the brachiocephalic artery, Q_{LCCA} is the outlet flow of the left common carotid artery and Q_{LSA} is the outlet flow of the left subclavian artery.

According to the previous equation, the flow entering the ascending aorta should be equal to the total flow exiting through the three branches of the aortic arch and the descending aorta. To evaluate the conservation of mass, four specific time points are selected: one at the beginning of the systolic phase (acceleration), one at the peak of systole, one at the end of systole (deceleration), and one during the diastolic phase. These timepoints are taken from the last complete cardiac cycle to ensure that the numerical solution has reached convergence.

Table 6: Flow Rates at the Inlet and Outlets with Mass Conservation Verification

SimVascular						
Timepoints	Q_{DA}	Q_{BA}	Q_{LCC}	Q_{LSA}	SUM	Q_{AA}
8.85	27.797536	19.594263	7.368213	1.368647	56.128659	56.128955
8.98	430.85519	113.130095	35.294379	47.743448	627.02311	627.023399
9.12	164.95003	-21.008423	-5.06231	7.896852	146.77615	146.775567
9.4	9.541789	-4.212523	-0.4386	-3.794627	1.096039	1.095136
CRIMSON						
Timepoints	Q_{DA}	Q_{BA}	Q_{LCC}	Q_{LSA}	SUM	Q_{AA}
8.85	25.052857	17.4076265	7.06854927	0.9115684	50.440601	50.4422422
8.98	423.464824	113.799549	36.2270305	48.210785	621.70219	621.7133555
9.12	162.395174	-21.172078	-5.382089	7.45922404	143.3002	143.281573
9.4	10.174332	-4.2253342	-0.4946868	-3.8885836	1.565727	1.54536978

Table 6 demonstrates that the total outlet flow rates closely match the inlet flow rate, indicating that mass conservation is largely preserved in both SimVascular and CRIMSON. It presents the flow rate values for the ascending aorta and the outlets, including the descending aorta, brachiocephalic artery, left common carotid artery, and left subclavian artery, comparing their sum to the inlet flow rate. The minor discrepancies observed between the sum of the outlets and the inlet likely stem from numerical factors such as interpolation, discretization, and solver-specific handling of boundary conditions. SimVascular shows higher flow rates across most caps and timepoints, except at 9.4 s in the diastolic phase. This discrepancy may be due to minor backflow or recirculation during diastole, with differences in numerical stabilization causing CRIMSON to yield slightly higher flow rates. In practical terms, both programs exhibit negligible differences, suggesting an accurate enforcement of mass conservation. Overall, these results confirm that both solvers provide reliable hemodynamic predictions while maintaining mass conservation.

Velocity vector fields. After assessing the flowrate waveforms at the inlet and outlets, the next step is to analyze the velocity vector field within the patient's anatomy, along with the inlet velocity profile, for a deeper understanding of the flow dynamics. Similar to the pressure analysis, four key timepoints are selected: the start, the peak, and the end of the systolic phase, as well as a random point during diastole.

Start of the systolic phase. The timepoint of 8.81 seconds (timestep 881) is chosen to represent the onset of systole (acceleration), as the simulation has reached convergence by this stage. The analysis begins with an examination of the patient-specific inlet velocity profile to compare how each software interprets it. The patient-specific velocity profiles at the start of the systolic phase, shown for SimVascular (Figure 57) and CRIMSON (Figure 58), display cross-sectional velocity distributions within the vessel, with color maps indicating different velocity magnitudes. In SimVascular, the peak velocity reaches approximately 49 cm/s, whereas in CRIMSON, it is slightly higher at 53 cm/s, possibly due to differences in the spatial interpolation during the patient-specific velocity profile extraction. The velocity distribution in both cases is asymmetric, with high-velocity regions concentrated in specific areas rather than being uniformly distributed, which could result from the complex 3D geometry of the artery, secondary flow structures, or flow recirculation zones. The central region exhibits higher velocities, while lower velocities appear near the vessel walls possibly due to the no-slip condition. Flow disturbances and irregular high-velocity patches suggest the presence of wave reflections or patient-specific anatomical variations.

While the overall velocity patterns are similar, slight variations are observed; CRIMSON displays more defined high-velocity streaks, whereas SimVascular has a more diffused distribution, likely influenced by differences in the mesh of the cap, SimVascular and CRIMSON have approximately similar number of vertices but SimVascular has a more refined mesh in the inlet cap area having also boundary layers which give its mesh higher resolution. Despite minor variations, both simulations effectively capture the essential hemodynamic characteristics of the patient's vascular flow, highlighting solver-based differences and different mesh resolution while maintaining physiological relevance.

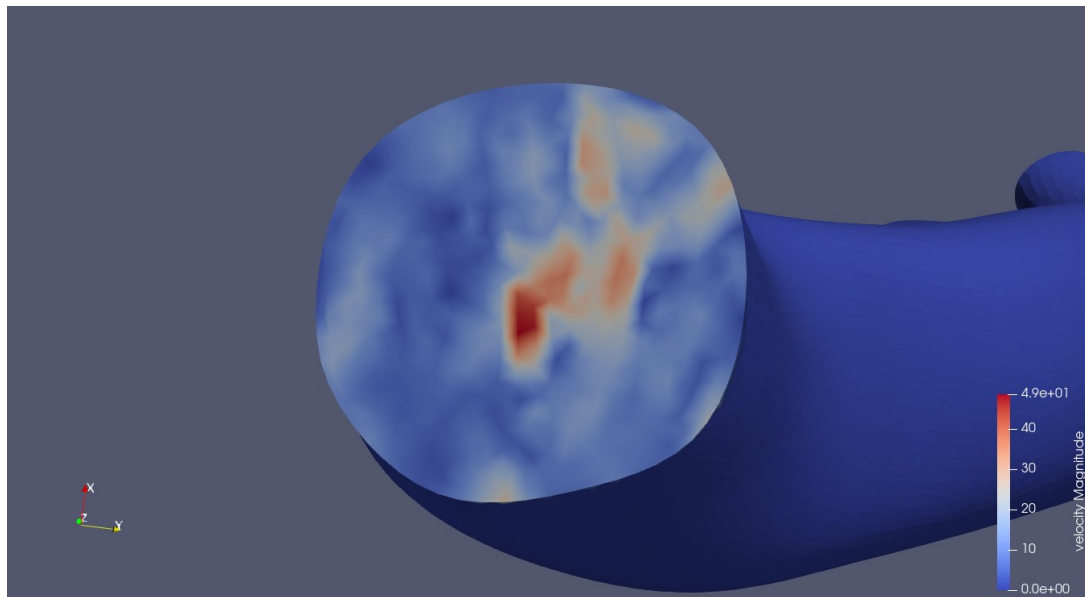


Figure 57: Patient-specific velocity profile at the start of the systolic phase (SimVascular)

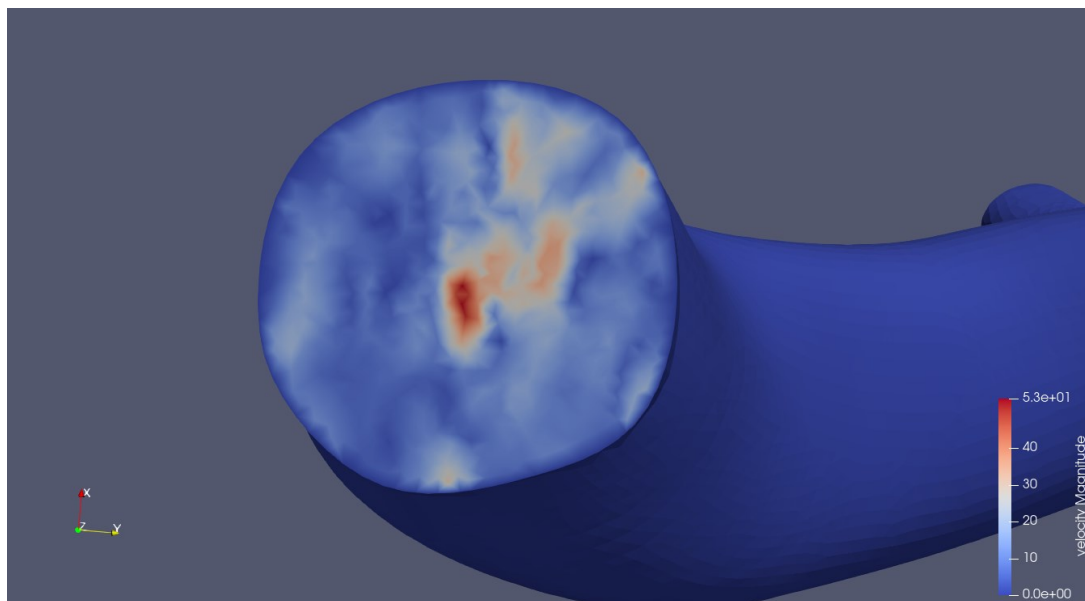


Figure 58: Patient-specific velocity profile at the start of the systolic phase (CRIMSON)

The velocity vector field calculated from both software programs is presented in Figure 59 and Figure 60. The velocity profiles in SimVascular and CRIMSON at the start of the systolic phase exhibit several important characteristics that provide insight into the flow dynamics in the patient's vascular model. In both simulations, the velocity field and streamlines illustrate the overall direction and intensity of blood flow. The SimVascular velocity field shows a well-defined, structured flow with higher velocity magnitudes near the central regions of the vessels, as indicated by the red zones in the color map. The streamlines indicate areas of localized recirculation and complex flow structures, particularly in the branching regions. Similarly, the CRIMSON velocity field demonstrates structured flow patterns, with slight variations in the velocity magnitude distribution.

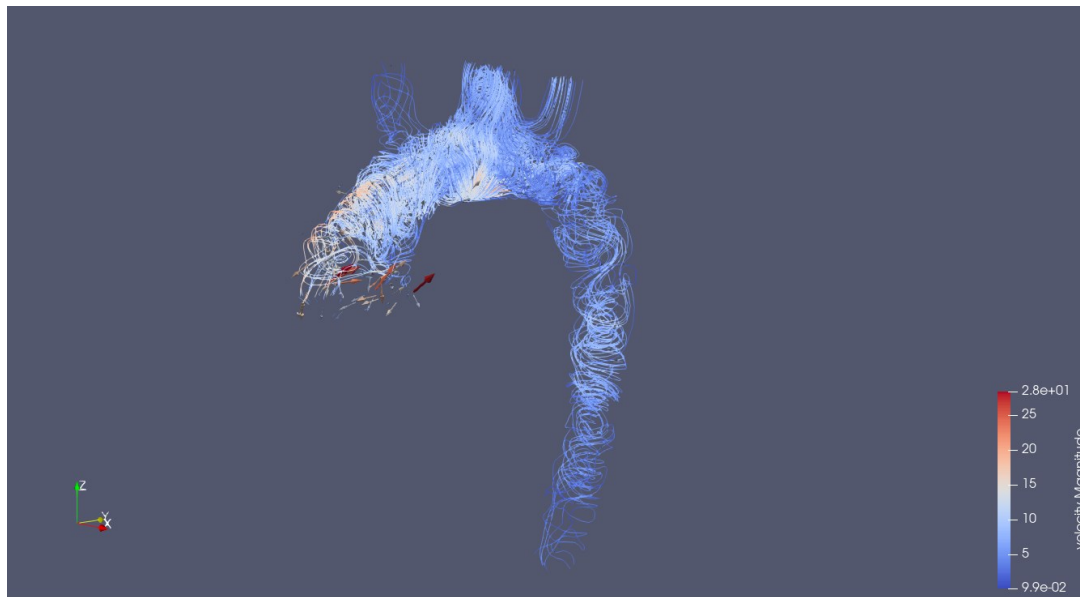


Figure 59: Velocity vector field and streamlines at start of systolic phase (SimVascular)

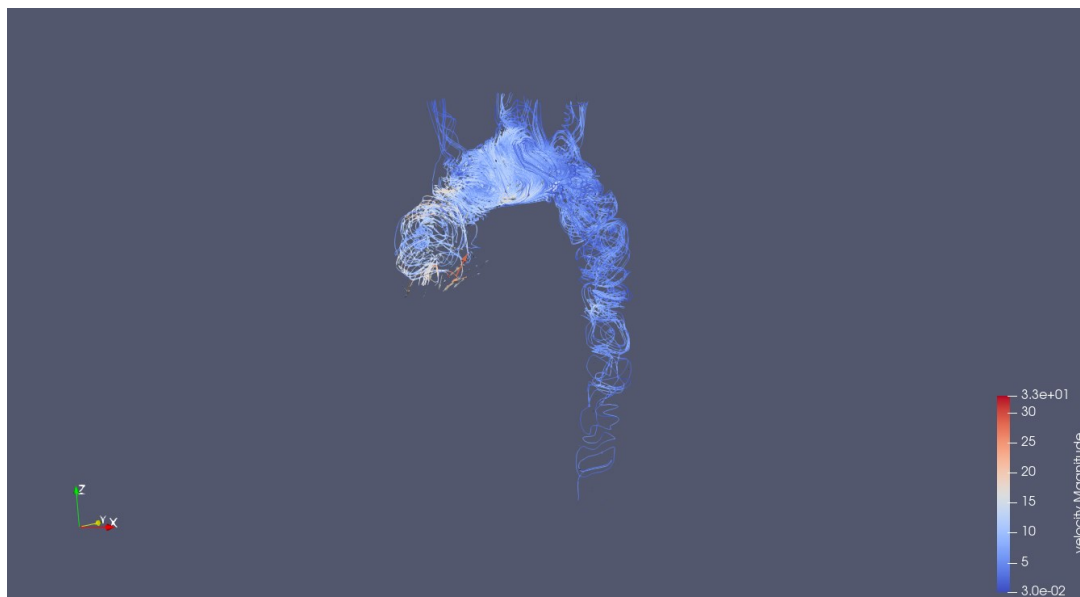


Figure 60: Velocity vector field and streamlines at start of systolic phase (Crimson)

The peak velocity values appear slightly higher in CRIMSON, while both simulations reveal flow acceleration in the aortic arch and the formation of secondary flow structures in the branch arteries. Vortical structures are present, potentially indicating areas prone to flow separation. The high-velocity regions suggest zones where blood accelerates, impacting the downstream vasculature. In the descending aorta, the vector field shows circulation and backflows, which occur due to the lack of a pumping force from the heart during the diastolic phase. Despite minor differences, the streamline patterns are mostly similar in both simulations, indicating that the overall flow behavior remains consistent between SimVascular and CRIMSON. These discrepancies could arise from variations in numerical solvers, spatial discretization, and mesh resolution, which influence the results. Overall, both simulations effectively capture the fundamental physiological behavior of the flow at the start of systole, with negligible variations.

Peak of the systolic phase. Next timepoint at 8.98 s (timestep 898) represents the peak of the systolic phase for this cardiac cycle. The patient-specific velocity profile from each software program is depicted in Figure 61 and Figure 62. At the peak of the systolic phase, the velocity profile exhibits an irregular distribution, with multiple high-velocity regions (red zones) scattered across the cross-section rather than forming a single centralized peak. These high-velocity regions indicate areas of concentrated forward flow, likely influenced by upstream geometric effects, vessel curvature, or secondary flow structures. The presence of lower-velocity areas (blue zones) near the periphery suggests the influence of boundary layer effects and potential regions of flow recirculation. The non-uniform distribution of velocity could also be indicative of complex hemodynamic phenomena such as skewed flow patterns, secondary vortical structures, or local disturbances caused by upstream branches.

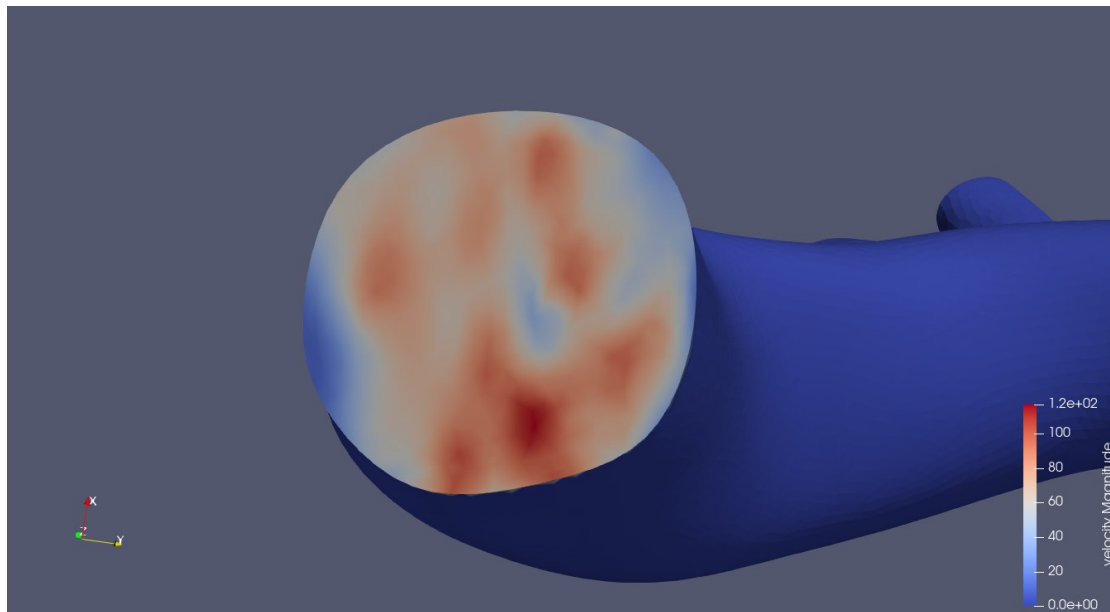


Figure 61: Patient-specific velocity profile at the peak of the systolic phase (SimVascular)

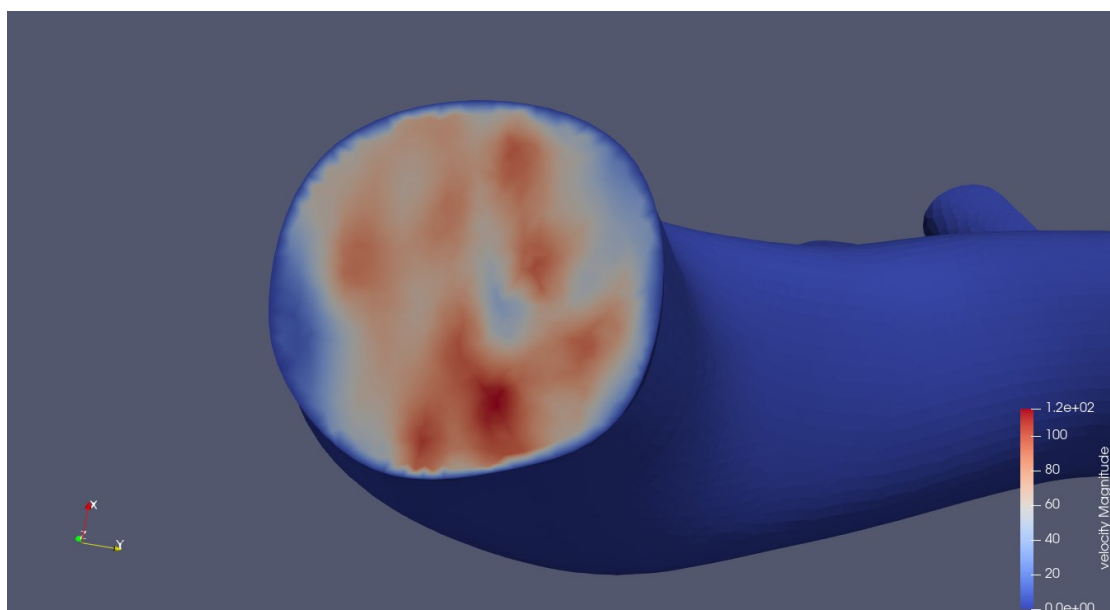


Figure 62: Patient-specific velocity profile at the peak of the systolic phase (Crimson)

Comparing SimVascular and CRIMSON, both velocity profiles share similar structural features with only small differences in the boundary of the inlet cap. These differences are attributed to mesh resolution and boundary condition implementations as was observed previously during the start of the systolic phase (acceleration). Despite these minor variations, both simulations effectively capture the fundamental characteristics of systolic flow, with strong forward velocity and distinct high-speed regions, emphasizing the intricate nature of patient-specific blood flow dynamics.

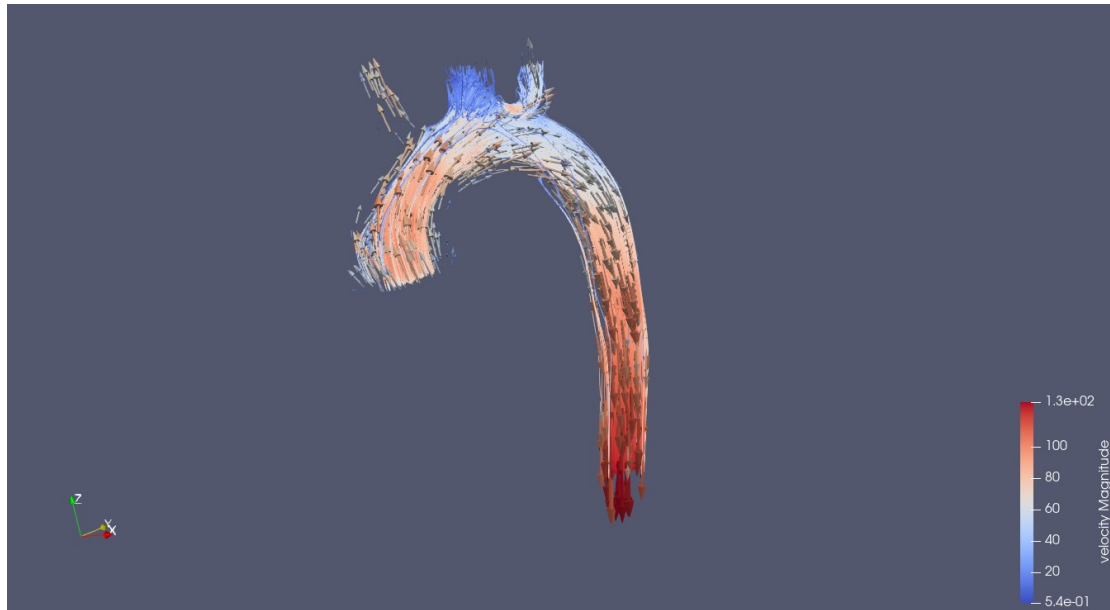


Figure 63: Velocity vector field and streamlines at peak of systolic phase (SimVascular)

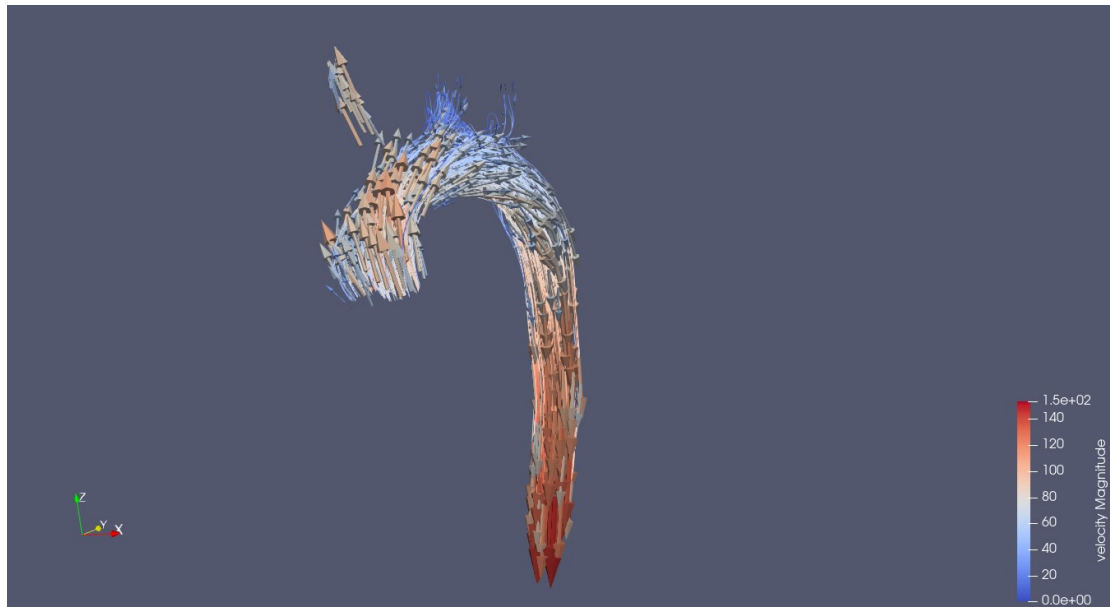


Figure 64: Velocity vector field and streamlines at peak of systolic phase (Crimson)

The vector field and streamlines from both software programs (Figure 63, and Figure 64) exhibit a similar pattern: blood enters the ascending aorta at a relatively high velocity, reaching approximately 80 cm/s. As the flow progresses into the aortic arch, its velocity decreases due to the division into the three branch arteries. Upon entering the descending aorta, the velocity magnitude is around 60 cm/s and gradually increases as the flow continues downstream. Among the three branches of the aortic arch, the highest velocity values are observed in the brachiocephalic artery, followed by the left subclavian artery, with the lowest velocities occurring in the left common carotid artery. The lower velocity in the left common carotid artery is likely due to its relatively larger cross-sectional area compared to the other branches. This flow behavior is patient-specific, as it is influenced by the individual's aortic anatomy. Since aortic morphology can vary significantly between patients, differences in cross-sectional areas of the branches may lead to distinct flow patterns in different cases. The flow patterns between the two software programs show minimal differences. However, the most notable distinction is that CRIMSON calculates a higher velocity magnitude in the descending aorta. This discrepancy is likely due to differences in the mesh used in CRIMSON, which may result in a slightly narrower cross-sectional area, leading to an increase in flow velocity.

End of the systolic phase. After reaching the peak of the systole phase, the heart relaxes, thus reducing the flow velocity. At the end of the systole phase at 9.18 s (timestep 918), the inlet velocity profile has the following form, as presented in Figure 65 and Figure 66. Examining the custom velocity profiles at the end of the systolic phase, it is evident that both software programs produce an almost identical pattern. The highest velocity values are concentrated near the center of the cross-section, with some additional regions displaying relatively high velocities. The overall profile resembles that of the peak systolic phase, but with a general reduction in magnitude across most areas, marking the transition into the diastolic phase. Like previous observations, the primary difference between the two programs is that in CRIMSON, the velocity near the boundary of the cross-section approaches zero. This discrepancy is likely due to differences in mesh resolution, with SimVascular employing a finer mesh near the edges, thus by having “smaller” cross-section, CRIMSON exhibits slightly higher velocity values, possibly because of this effect.

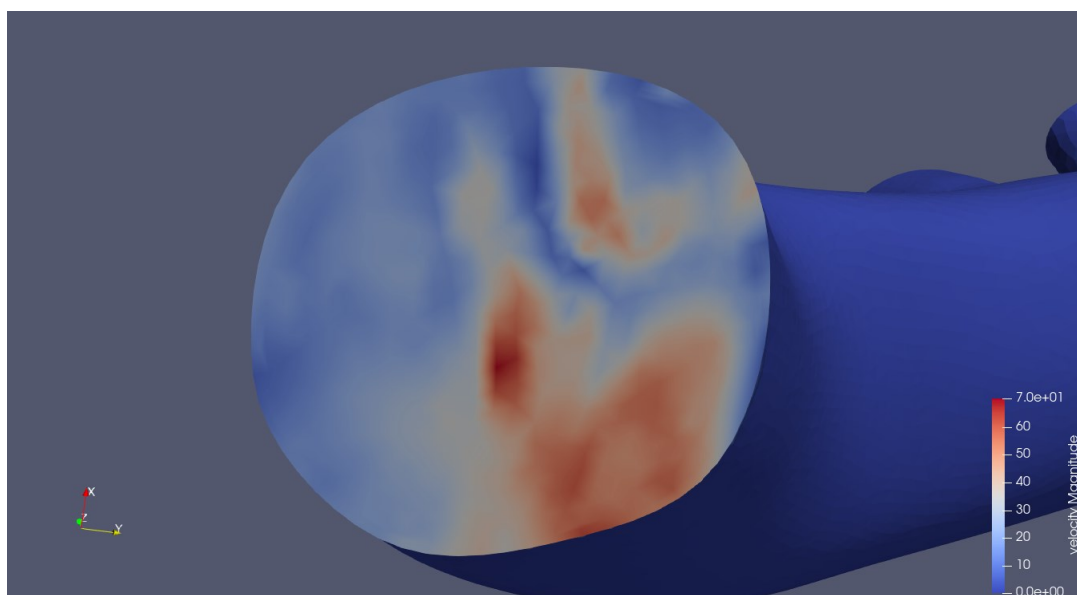


Figure 65: Patient-specific velocity profile at the end of the systolic phase (SimVascular)

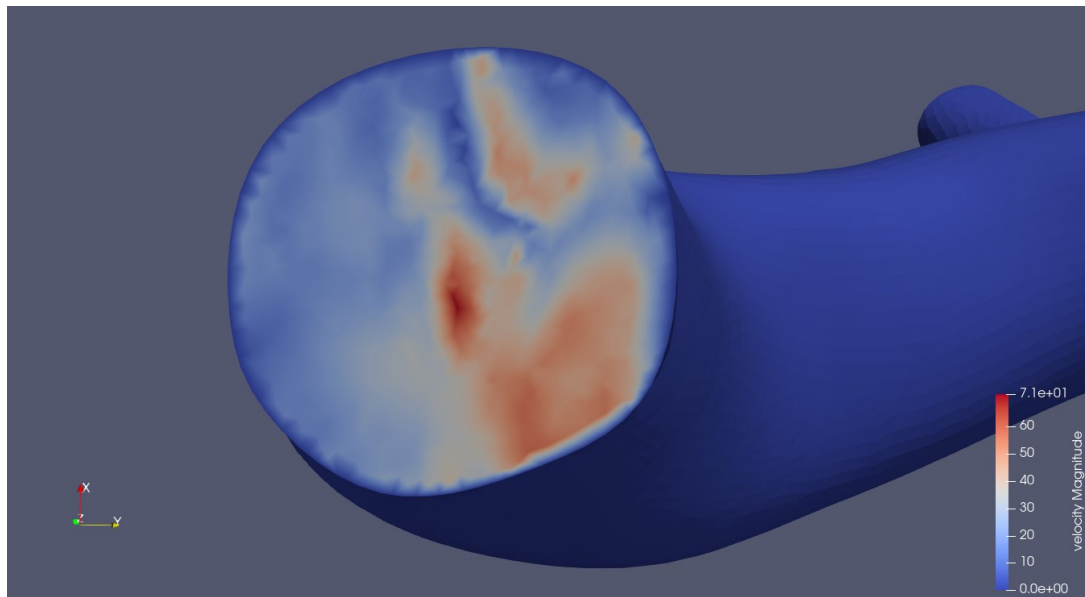


Figure 66: Patient-specific velocity profile at the end of the systolic phase (Crimson)

The vector field and the streamlines of the flow are presented in Figure 67 and Figure 68. In both simulations, a significant backflow is observed, which is expected at this specific phase due to the slight suction effect exerted by the heart at the end of systole. This backflow results in extensive vorticity throughout the flow domain, with the most prominent effects occurring in the ascending aorta region. Here, the flow has completely reversed direction compared to the rest of the systolic phase, during which it maintained a consistent forward direction. Additionally, the velocity remains relatively low across most regions, with some areas exhibiting values close to zero. Higher velocity magnitudes are primarily seen in the ascending aorta, which is expected due to the abrupt shift in flow direction caused by the heart's relaxation phase. This sudden reversal generates vorticities that propagate through the entire flow field. Notably, in the descending aorta, after the flow has developed, a vortex-dominated yet relatively uniform pattern emerges. A similar behavior is also observed in the three branches of the aortic arch.

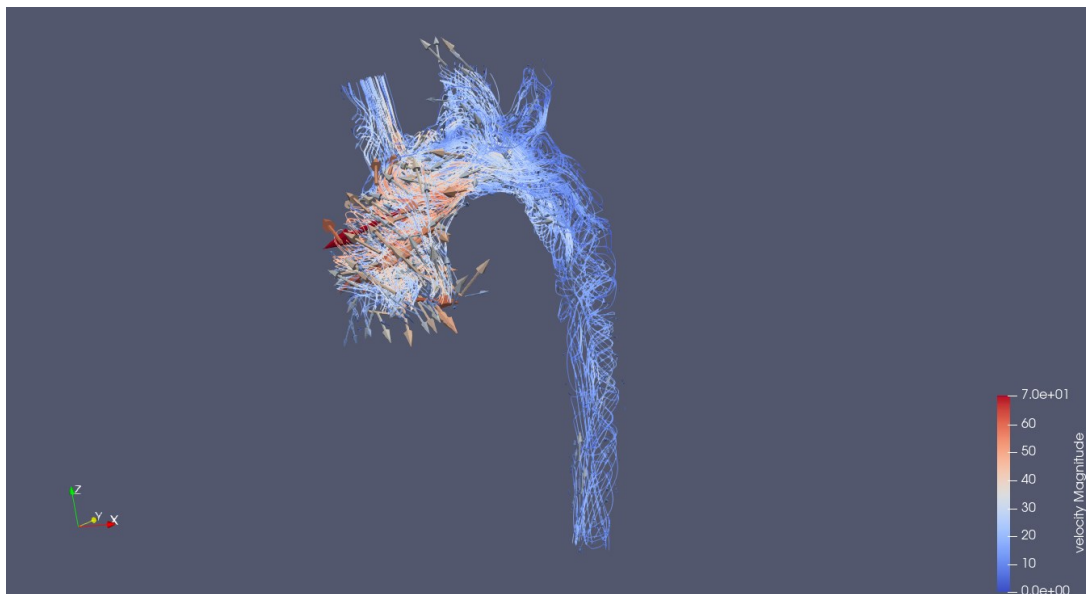


Figure 67: Velocity vector field and streamlines at end of systolic phase (SimVascular)

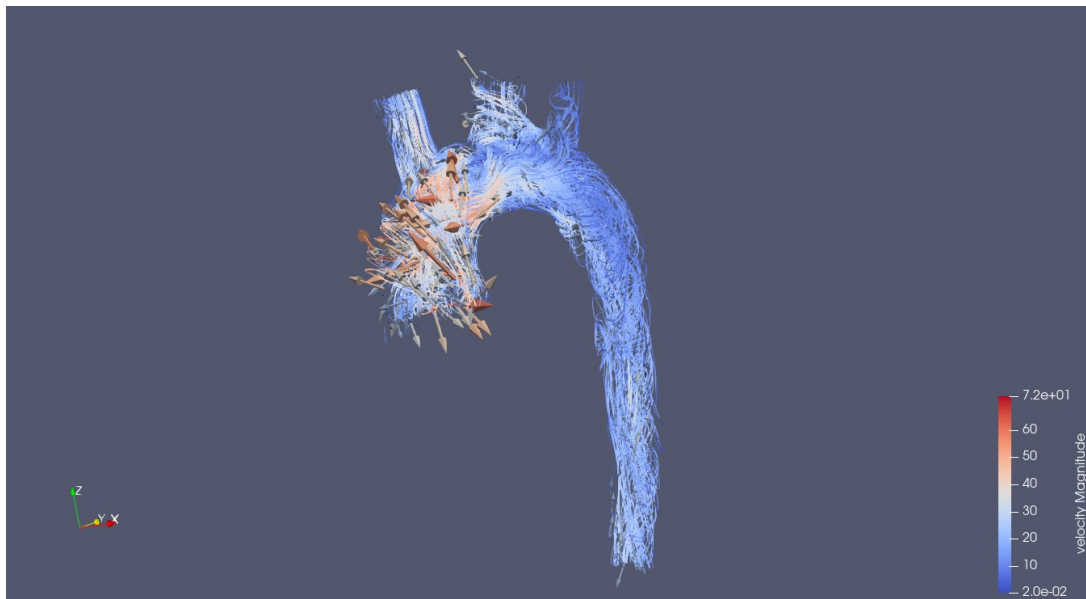


Figure 68: Velocity vector field and streamlines at end of systolic phase (Crimson)

During the diastolic phase. The final flow examined occurs during the diastolic phase, where flow relaxation is the dominant characteristic. Similar to the pressure analysis, the selected time point for evaluation is 9.6 seconds (timestep 960). Observing the inlet velocity profile during the diastolic phase (Figure 69, and Figure 70) the flow exhibits relatively low velocity magnitudes across most of the inlet cap area, which is expected due to the absence of cardiac output actively driving the flow. The remaining velocity values primarily result from the stabilization required after the significant backflow that occurred at the end of the systolic phase. The velocity profile pattern from the end of systole remains largely unchanged, with the primary difference being a reduction in magnitude across most regions. However, the peak velocity remains in the same area of the inlet cap, emphasizing the consistency of the flow pattern throughout the diastolic phase. From the end of the systolic phase, the peak velocity magnitude decreases from approximately 70 cm/s to 56 cm/s, a reduction attributed to the stabilization of velocity following the backflow at the end of systole. The differences between the two programs remain minimal, with the only notable distinction being that velocity values near the boundaries of the cap mesh in CRIMSON are nearly zero, a result of the different meshing approach used in the software.

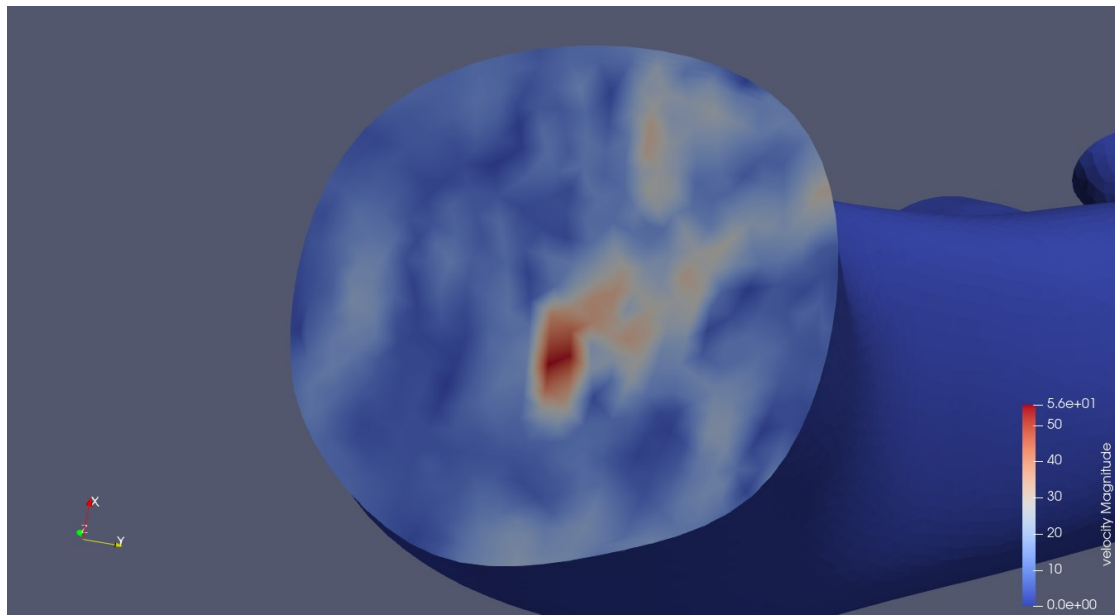


Figure 69: Patient-specific velocity profile during the diastolic phase (SimVascular)

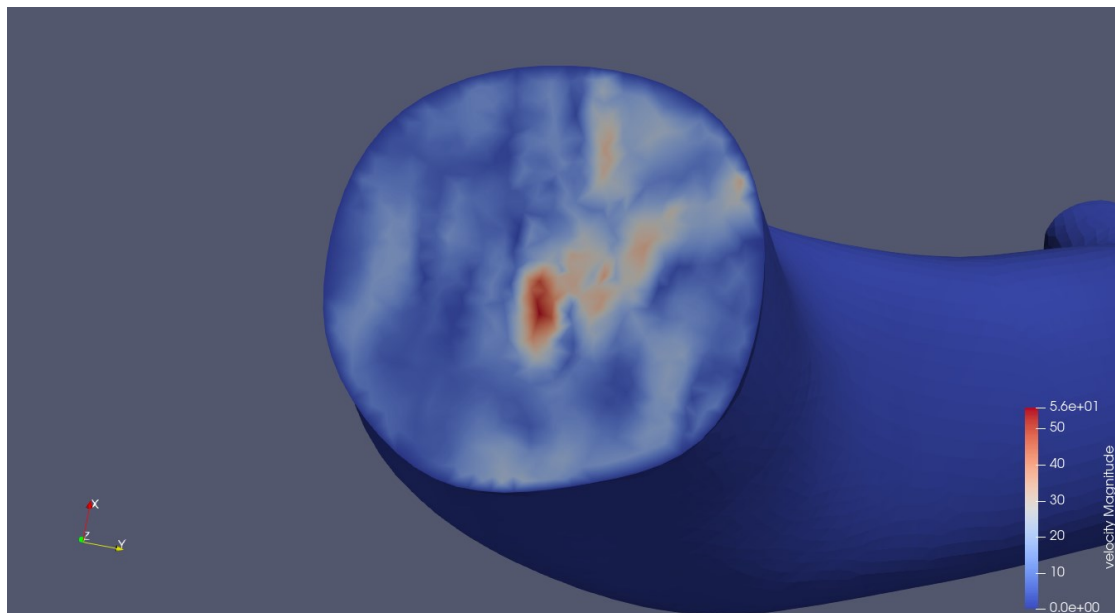


Figure 70: Patient-specific velocity profile during the diastolic phase (Crimson)

The vector field and streamlines of the flow, shown in Figure 71 and Figure 72, closely resemble those observed at the end of the systolic phase. However, as expected, backflows are significantly reduced, and the velocity vector field exhibits less vorticity. This behavior is anticipated due to the stabilization of the flow throughout most of the diastolic phase, during which velocity values remain relatively constant. This stabilization is evident in both figures, where the streamlines display relatively uniform values across the flow domain. Slightly elevated velocities are noticeable in the ascending aorta, which is expected given its proximity to the heart. Additionally, some higher velocity values appear in the inlet cross-sectional area, as previously discussed. Similar flow patterns are observed across other regions of the 3D model, consistent with those at the end of the systolic phase. The differences between SimVascular and CRIMSON are minimal, with both producing nearly identical flow patterns.

The only notable distinction is that SimVascular yields slightly higher velocity values for only the diastolic phase, though this does not affect the overall flow dynamics during the diastolic phase.



Figure 71: Velocity vector field and streamlines during the diastolic phase (SimVascular)

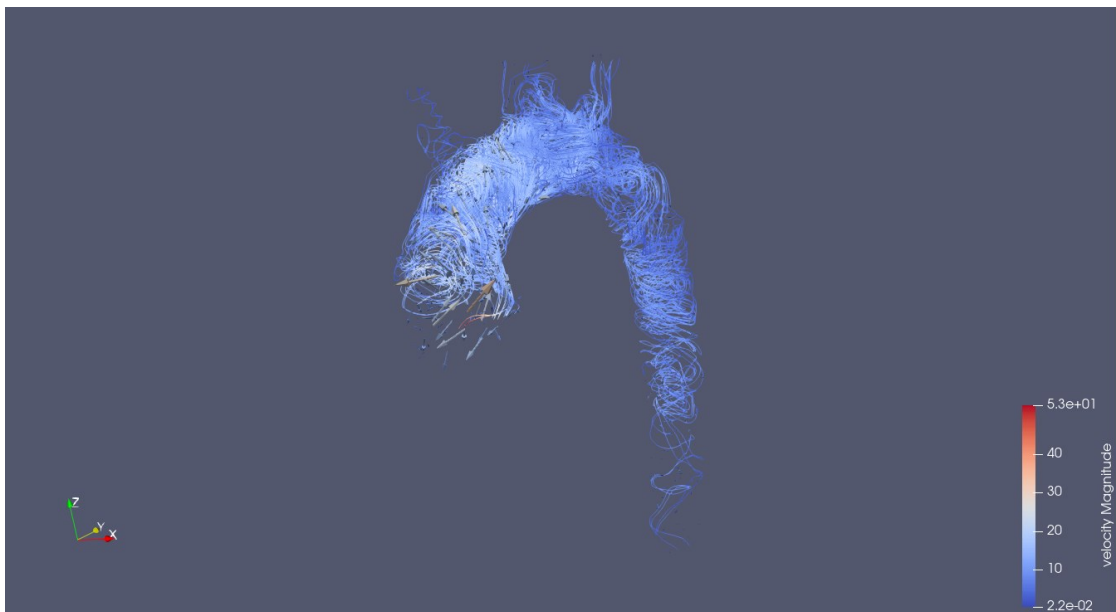


Figure 72: Velocity vector field and streamlines during the diastolic phase (Crimson)

3.1.3 Wall shear stress

This section focuses on the wall shear stress (WSS) generated by blood flow along the walls of the aorta. As it was discussed in the Methods section, WSS is the tangential force per unit area exerted by flowing blood on the vessel wall. It plays a crucial biomechanical role in vascular health, endothelial function, and disease progression, particularly in the aorta and other major arteries. WSS arises from the interaction between blood flow and the arterial wall. Moderately elevated WSS is beneficial, as it promotes normal endothelial function and helps prevent conditions such as atherosclerosis. However, excessively low WSS is linked to flow recirculation and stagnation, which can lead to endothelial dysfunction, plaque formation, and increased risk of atherosclerosis. Conversely, high WSS, commonly found in regions of vessel narrowing, can cause endothelial damage and elevate the risk of aneurysm development. Similar to the previous analyses, WSS will be examined at four key time points throughout the cardiac cycle to evaluate its variations and potential impact on cardiovascular health.

Start of the systolic phase. The first timepoint analyzed is 8.81 seconds (timestep 881), representing the onset of the systolic phase. From Figure 73 and Figure 74, it is evident that at the onset of the systolic phase, when the heart begins pumping blood into the aorta, higher wall shear stress (WSS) values are observed in the ascending aorta. This is primarily due to the anatomical curvatures of the aorta, which force changes in flow direction, creating shear forces between the blood flow and the vessel walls. In the aortic arch, WSS is also present but with lower values compared to the ascending aorta region. These values are influenced by the bifurcations of the three major branches. As the blood enters the descending aorta, WSS reaches its lowest levels among all regions, with values gradually decreasing as the flow continues downstream.

A general observation from the WSS distribution in this timepoint is that higher values or an increase in WSS occur whenever the geometry of the model alters the main flow direction of the blood. This pattern is clearly distinguishable in the presented model. In terms of comparison between SimVascular and CRIMSON, no significant differences are observed in the WSS distribution.

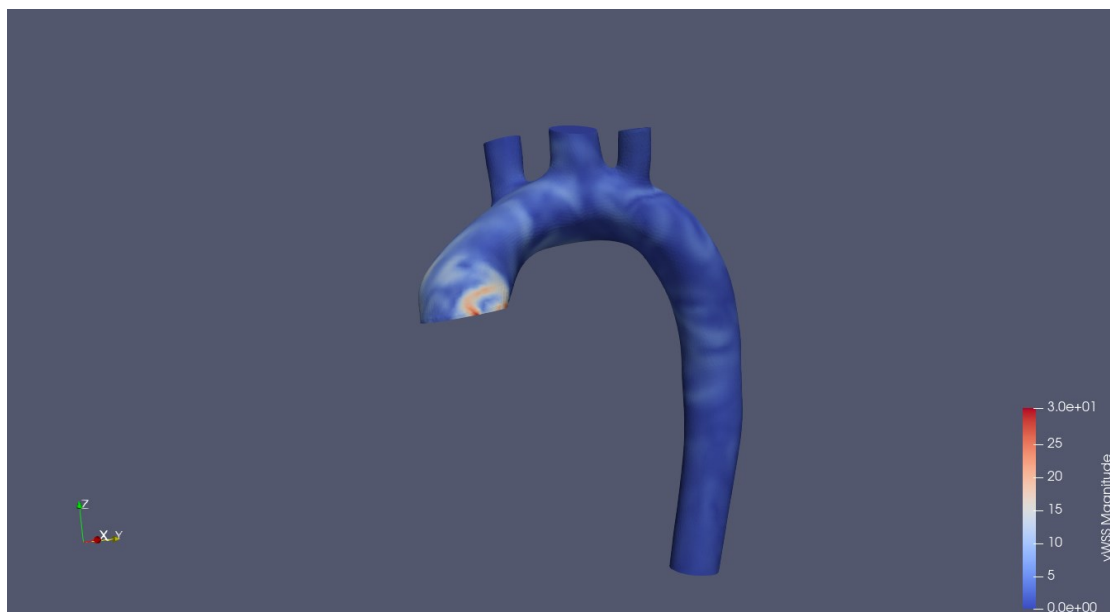


Figure 73: Wall shear stress of the aortic wall at the start of the systolic phase (SimVascular)

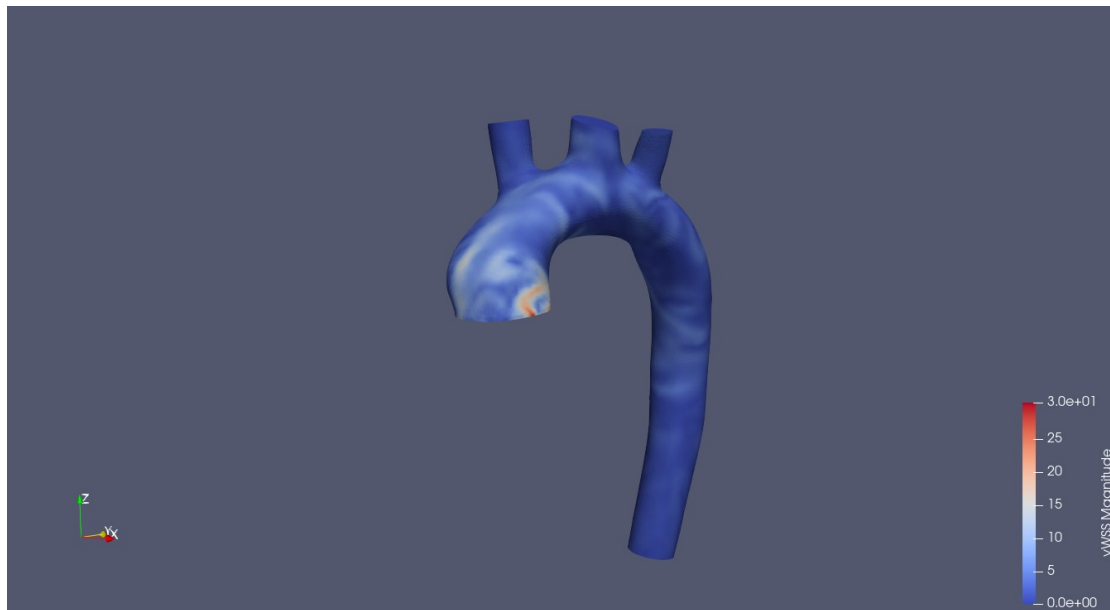


Figure 74: Wall shear stress of the aortic wall at the start of the systolic phase (Crimson)

Peak of the systolic phase. At the peak of the systolic phase (timepoint 8.98 s or timestep 898) the wall shear stress has the distribution depicted in Figure 75 and Figure 76. WSS values significantly increase due to the elevated blood flow entering the aorta. The highest WSS values are observed in the ascending aorta, which is expected since this region experiences the greatest flow rate immediately after blood exits the heart. Additionally, the anatomical curvature of the aorta contributes to these elevated values by altering the flow direction and generating shear forces along the vessel walls. Similarly, high WSS values are observed at the branching points of the aortic arch, where the main flow splits into three branches. This division disrupts the primary flow direction, contributing to localized shear stress increases.

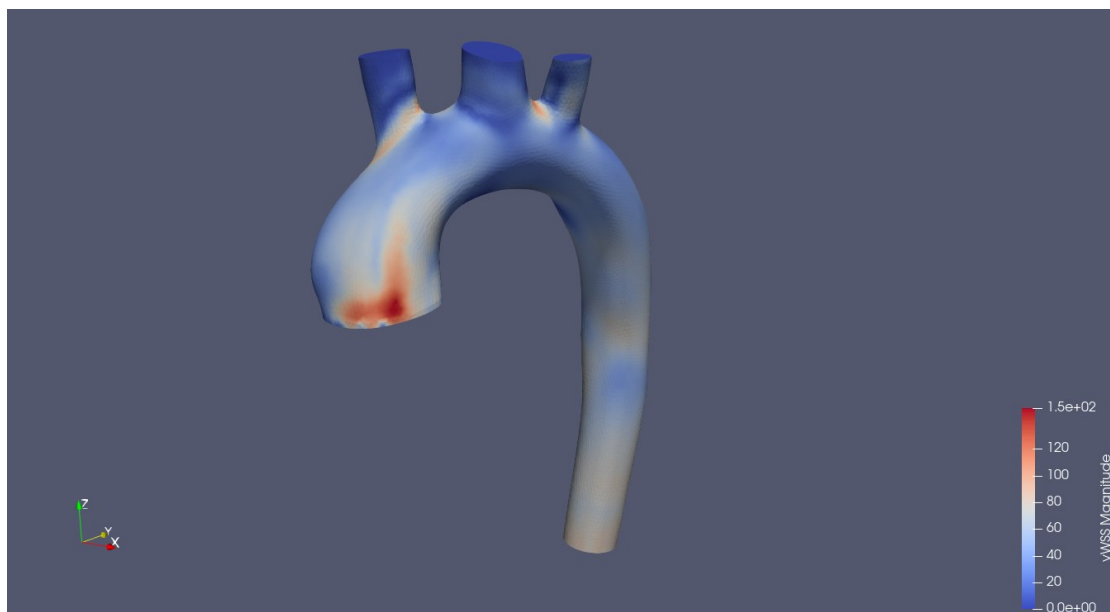


Figure 75: Wall shear stress of the aortic wall at the peak of the systolic phase (SimVascular)

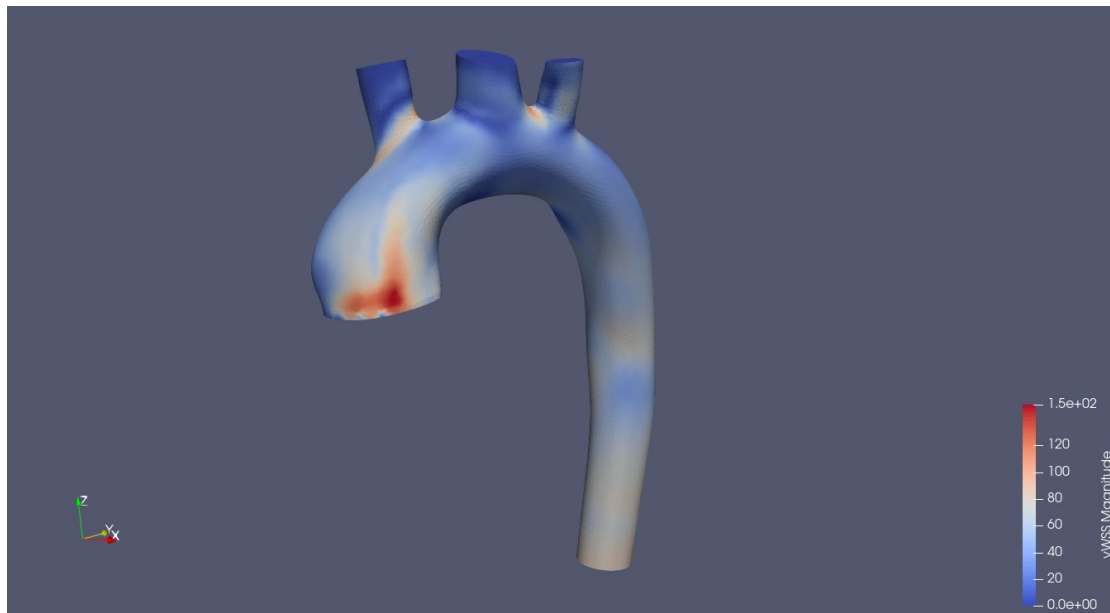


Figure 76: Wall shear stress of the aortic wall at the peak of the systolic phase (Crimson)

In the descending aorta, WSS values generally decrease, with the lowest values appearing in regions with minimal geometric changes. However, a slight increase in WSS is observed in the lower part of the descending aorta, likely due to local velocity increases in that region, consistent with the velocity vector field there. Overall, the WSS patterns are consistent between SimVascular and CRIMSON, with no significant differences observed between the two simulations.

End of the systolic phase. At the end of the systolic phase (timepoint 9.18 s or timestep 918) the wall shear stress has the distribution presented in Figure 77 and Figure 78. The wall shear stress (WSS) distribution in the aorta at the end of systole shows distinct patterns that align with physiological expectations. The ascending aorta exhibits the highest WSS values, highlighted by red regions, due to the backflows of the flow as the heart starts its relaxation phase. The curvature of the ascending aorta enhances shear forces as the flow direction changes. The aortic arch shows moderate WSS, with an increase near the origins of the brachiocephalic, left common carotid, and left subclavian arteries, where blood is redirected into smaller vessels, creating localized shear stress peaks. The descending aorta, in contrast, has lower WSS values, marked by blue areas, as flow velocity decreases, especially in the straight sections where flow is more stable.

The highest WSS is observed in the ascending aorta and inner curvature of the arch, corresponding to flow acceleration, while the lowest WSS is in the “walls” of the descending aorta. The transition between high and low WSS is generally smooth, except near bifurcations, where abrupt changes highlight localized hemodynamic stresses. The gradual decrease in WSS from the arch to the descending aorta aligns with the expected reduction in blood velocity after peak systole. Overall, the WSS patterns are consistent between SimVascular and CRIMSON, with no significant differences observed between the two simulations.

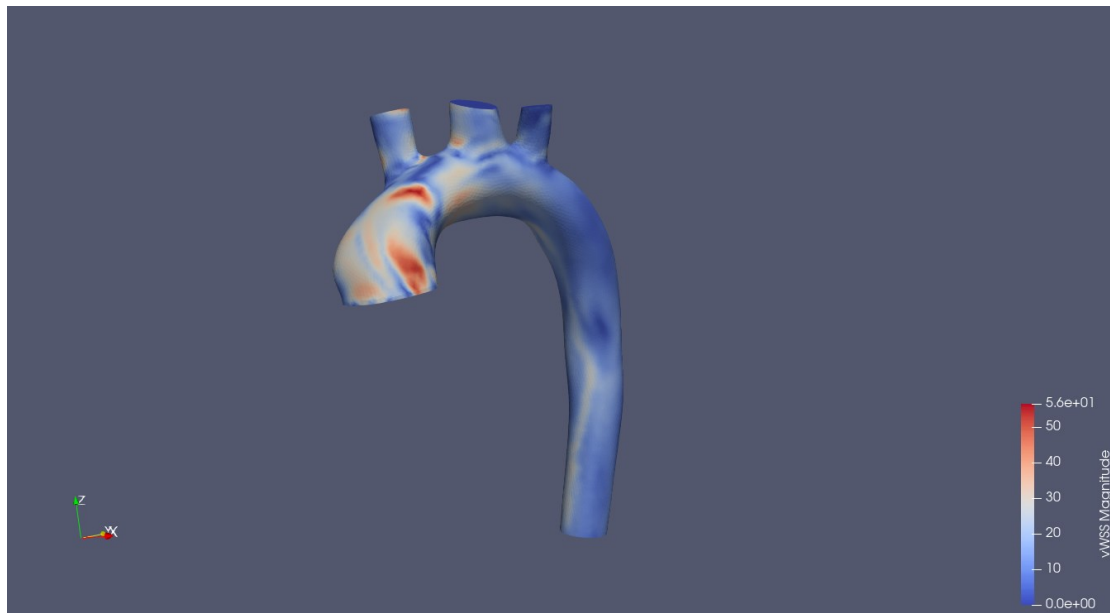


Figure 77: Wall shear stress of the aortic wall at the end of the systolic phase (SimVascular)

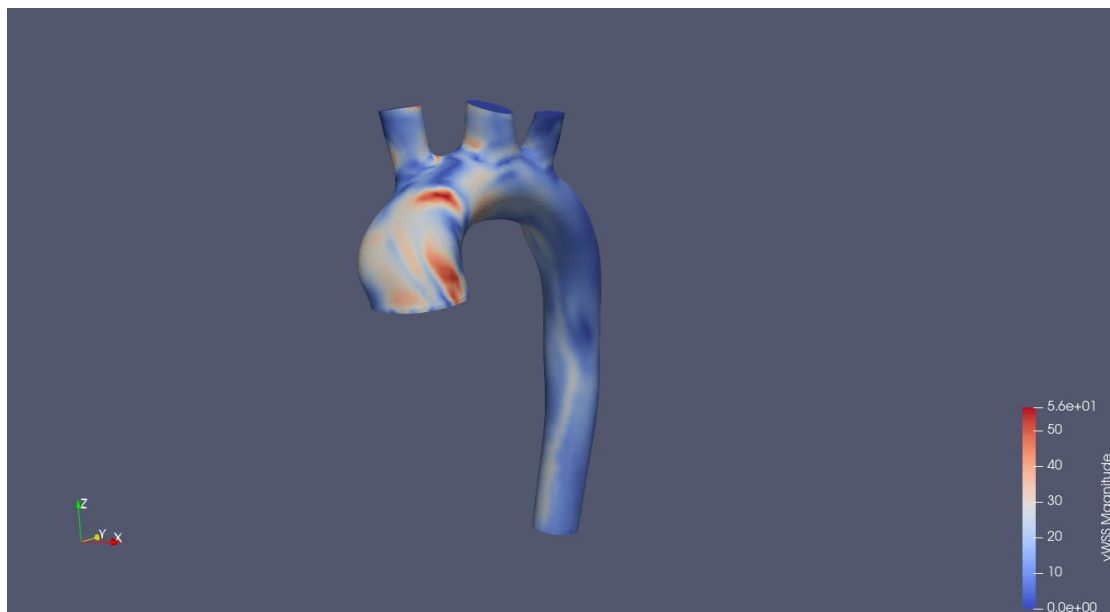


Figure 78: Wall shear stress of the aortic wall at the end of the systolic phase (Crimson)

During the diastolic phase. At a timepoint during the diastolic phase (timepoint 9.6 s or timestep 960) the wall shear stress has the distribution shown in Figure 79 and Figure 80. During the diastolic phase, the WSS distribution follows a similar pattern to the early systolic phase. The highest WSS values are observed in the ascending aorta, where flow fluctuations are most pronounced due to its proximity to the heart and the changes in geometry that affect the flow direction. In the aortic arch, moderate WSS values are observed, consistent with the flow direction changes and the presence of the three branches where flow separation occurs. In the descending aorta, WSS values are minimal or nonexistent, as there is little to no flow in this region. Throughout the diastolic phase, the flow velocity fluctuates but keeps low values, resulting in negligible or absent flow movement and, consequently, very low WSS. Both simulation programs show nearly identical behavior in this phase as well.

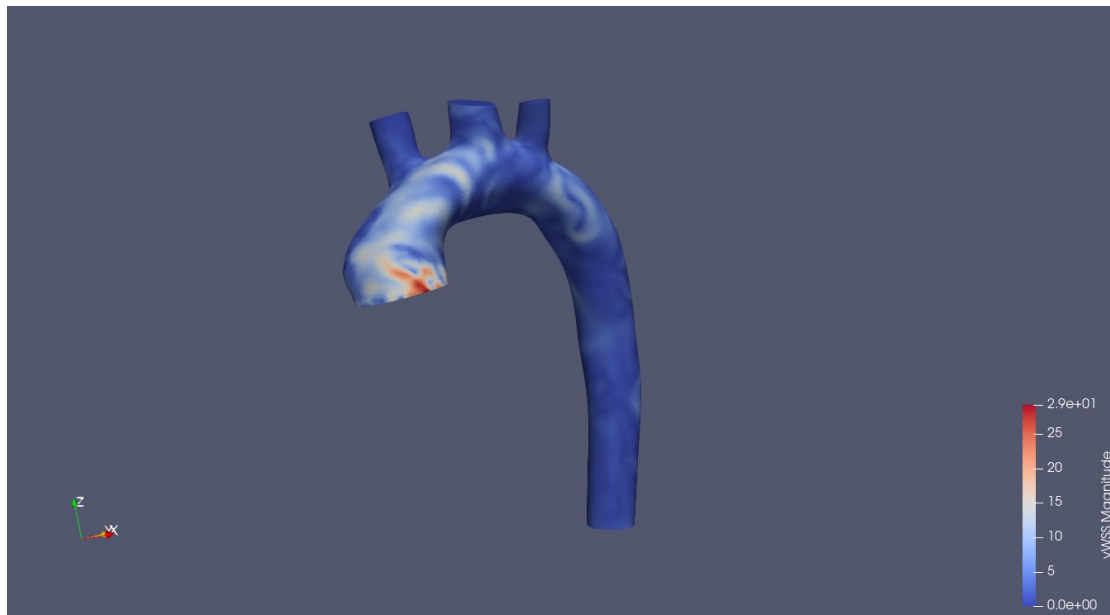


Figure 79: Wall shear stress of the aortic wall during the diastolic phase (SimVascular)

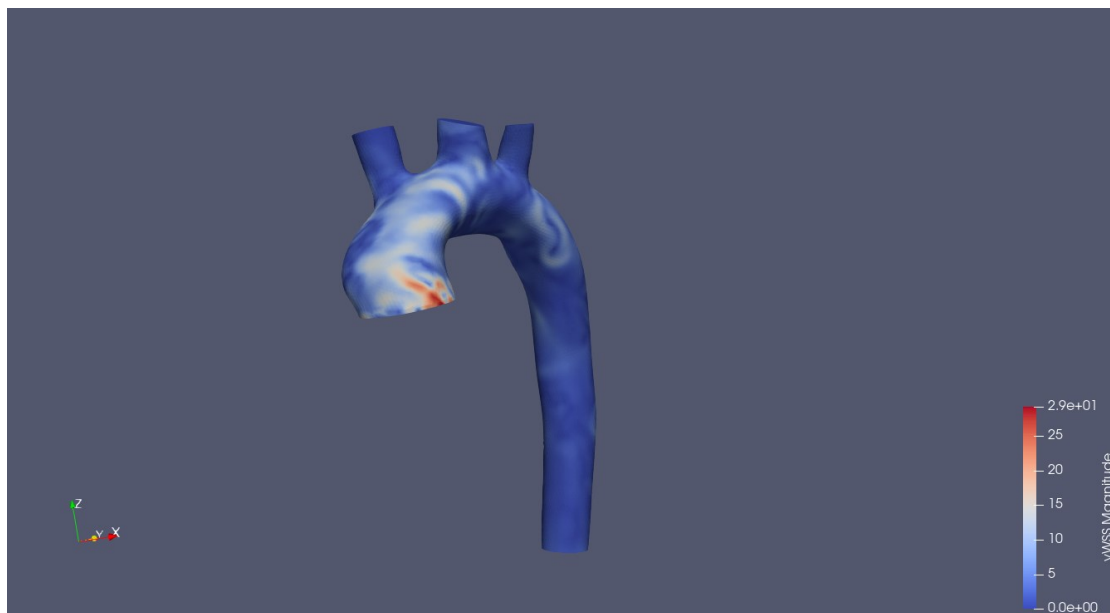


Figure 80: Wall shear stress of the aortic wall during the diastolic phase (Crimson)

Time-averaged wall shear stress. To conclude the analysis of wall shear stress, the time-averaged wall shear stress (TAWSS) for one cardiac cycle is presented, allowing for conclusions about the behavior of WSS throughout the entire cycle. The last simulated cardiac cycle is chosen for this analysis since the WSS values have fully converged by that point. The TAWSS distribution is shown in Figure 81 and Figure 82. The time-averaged wall shear stress (TAWSS) throughout the cardiac cycle follows similar patterns to those discussed earlier in the analysis. The highest TAWSS values are observed in the ascending aorta, gradually decreasing as the flow moves toward the lower part of the descending aorta. Elevated TAWSS values are seen between the bifurcations of the three branches in the aortic arch, while the lowest values are found in the descending aorta, with an increase in the lower part due to the increased velocity magnitude there during the peak of the systolic phase.

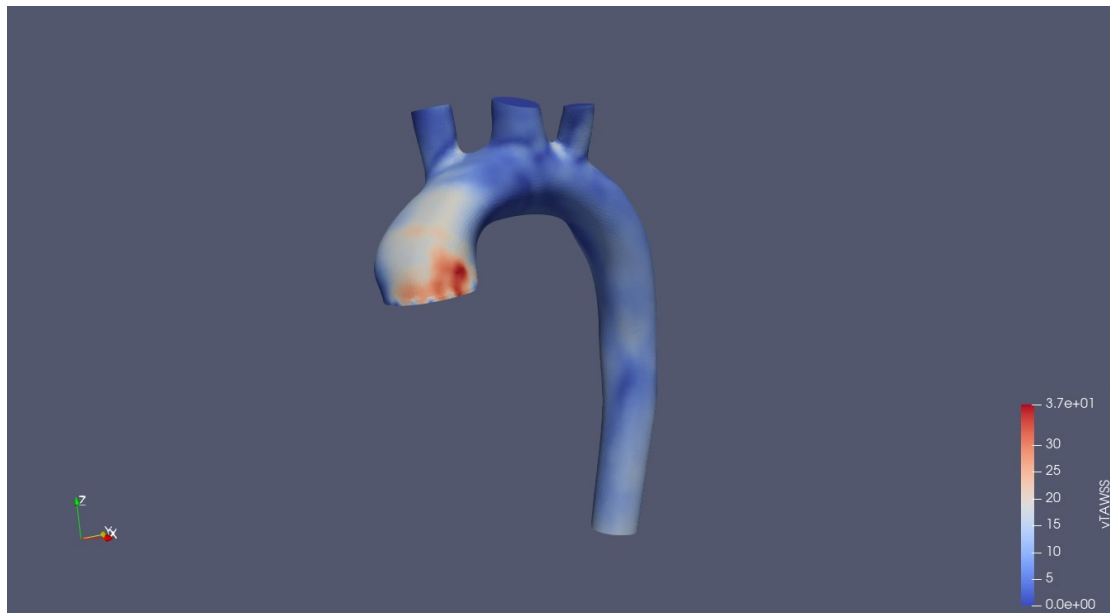


Figure 81: Time averaged wall shear stress for one cardiac cycle (SimVascular)

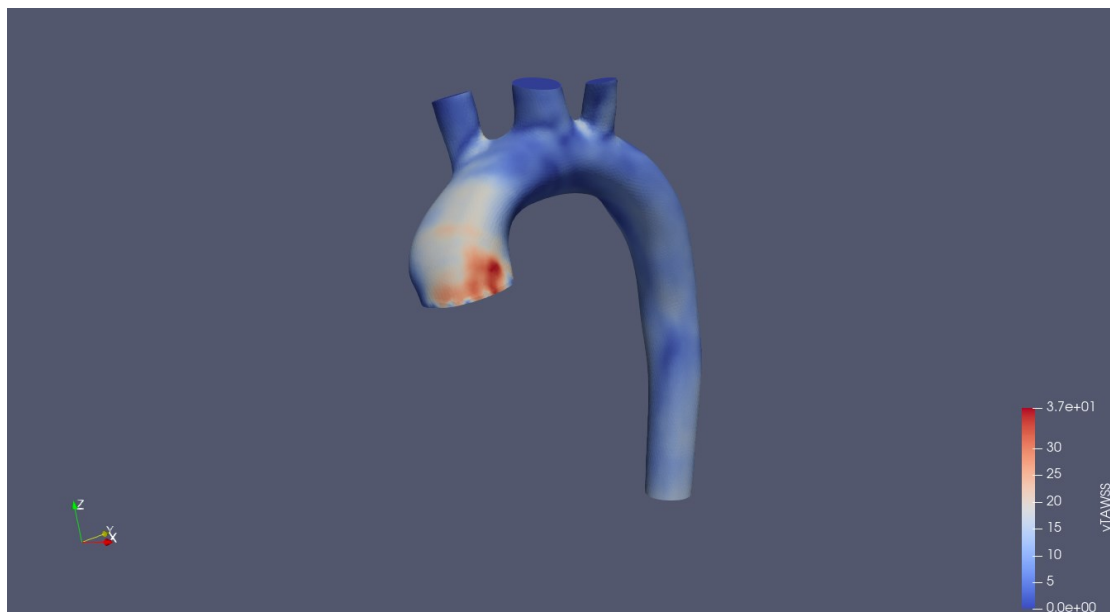


Figure 82: Time averaged wall shear stress for one cardiac cycle (Crimson)

In conclusion, several physiological assumptions can be made based on the analysis. The highest TAWSS values in the ascending aorta indicate significant mechanical stress, which may contribute to endothelial damage and increase the risk of aneurysm formation. Elevated TAWSS near the bifurcations of the three branches in the aortic arch suggests areas of flow separation, which play a crucial role in regulating blood flow to the major arteries. The lower TAWSS values in the descending aorta point to reduced flow activity, potentially raising the risk of atherosclerosis in this region. The gradual decrease in TAWSS from the ascending aorta to the descending aorta aligns with the expected reduction in shear stress as blood moves farther from the heart, reflecting the transition from high-pressure, high-flow areas to lower-pressure, lower-flow regions.

3.1.4 Velocity comparison between the CFD data and patient-MRI data

Methodology. The final step of the analysis involves comparing the CFD data with the “real” patient MRI data, as discussed in the Methods section. To achieve this, three 4D arrays were created, each corresponding to one of the three velocity components (u , v , w), all stored in an HDF5 file. For this comparison, the bounds of the CFD data reconstruction were selected as follows (Table 7). These bounds were selected because they match the geometric space of the MRI data, allowing for a direct comparison with the CFD results.

Table 7: Location bound to create the 4D velocity arrays

Location (cm)	Start Bound	End Bound
Axial (z)	-10,39	19,46
Sagittal (x)	-7,96	17,52
Coronal (y)	-19,47	14,15

After determining the appropriate bounds, the number of slices for each direction (axial, sagittal, coronal) needed to be defined. The same number of slices as in the original 4D MRI data was selected. However, after the downsampling process, the number of slices will be reduced by half. Doubling the original number was not considered due to the excessive disk space it would require. As shown in Table 8, the number of time slices remained unchanged since the downsampling process was applied only to the spatial domain. Both the 24 temporal slices of the MRI data and the 99 temporal slices of the CFD data represent one cardiac cycle, which in this case spans from 0 to 0.98 seconds (99 timesteps). The same temporal range is captured in the MRI data over 24 timesteps. Figure 83 and Figure 84 illustrate the distribution of CFD data within the 4D velocity arrays, both in their initial form and after downsampling.

Table 8: Number slices used in each 4D velocity array

Number of Slices	MRI arrays	CFD arrays	CFD arrays (downsampled)
Time	24	99	99
Axial	192	192	96
Sagittal	72	72	36
Coronal	192	192	96

From Figure 83, it is evident that the velocity distribution is stored in a $99 \times 72 \times 192 \times 192$ 4D array for each velocity component. In the grayscale representation, values close to zero appear gray, brighter values indicate positive velocities, and darker values represent negative velocities, allowing visualization of the direction of each velocity component. Beyond the slice-by-two reduction, the downsampling process, as discussed in the Methods section, also adjusts the velocity value range to match the VENC value used in the MRI scan. In this case, the scan was conducted with a VENC of 180 cm/s, so after downsampling, the new velocity range is set from -180 cm/s to 180 cm/s (or -1.8 m/s to 1.8 m/s) to generate the “mock” MRI data for comparison. The next image (Figure 84) reveals the introduced noise and the adjusted velocity value range that is used for comparison.

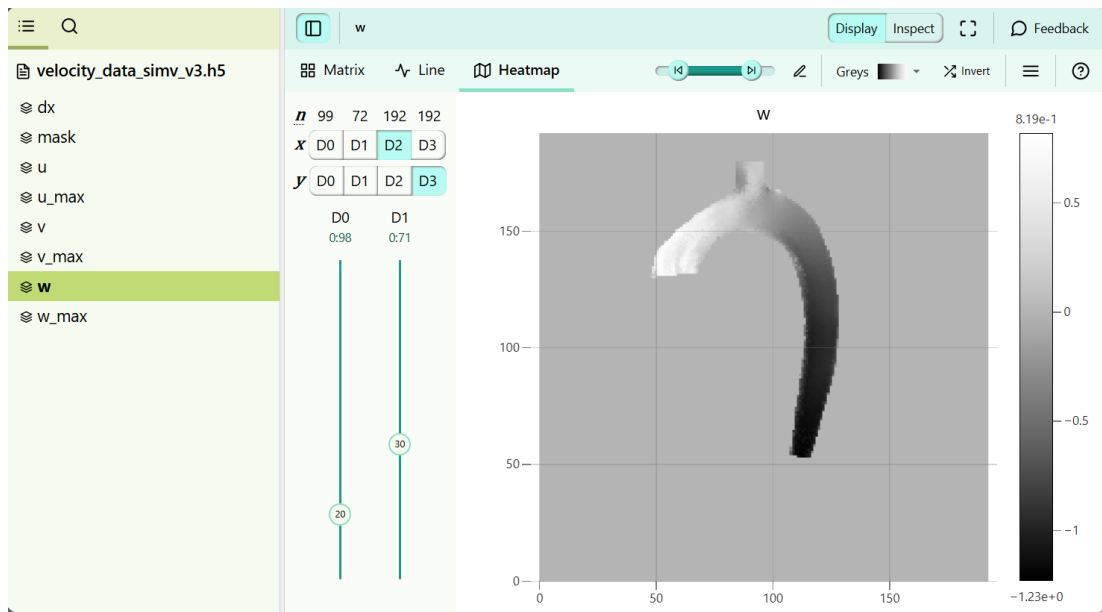


Figure 83: CFD data in the initial 4D array form

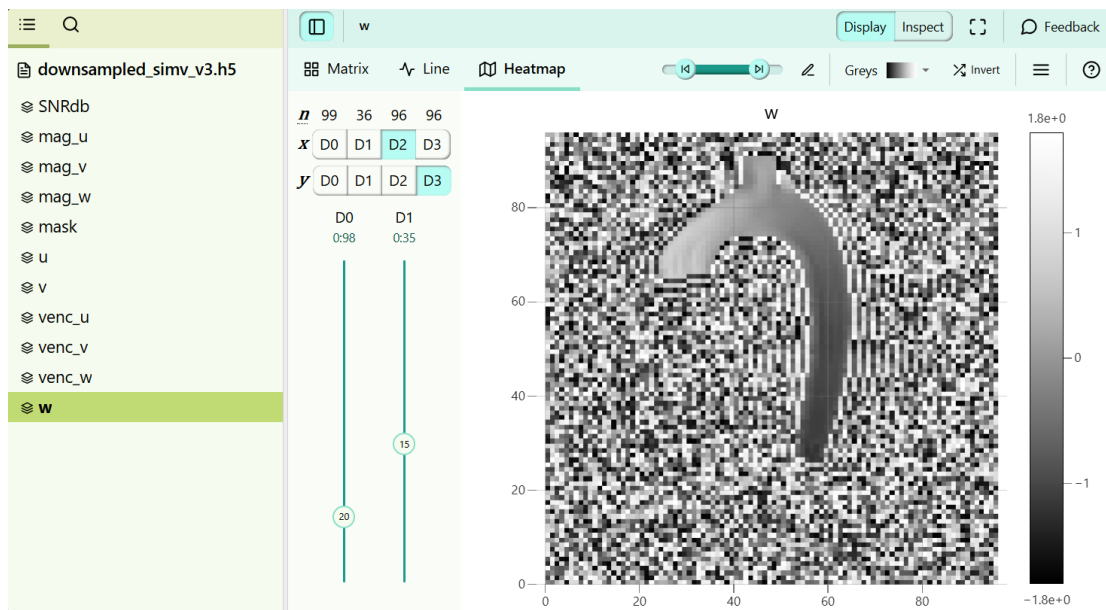


Figure 84: CFD data in the downsampled 4D array form

A key advantage of the methodology presented is that the downsampled array closely resembles the initial array generated from the MRI data. This similarity is achieved by selecting the same spatial bounds, with the only difference being the reduction in the number of slices in the downsampled CFD data to half that of the MRI data. As a result, slice selection is simplified, as each selected slice from the downsampled CFD data corresponds directly to every second slice in the MRI data, enabling straightforward comparisons. For the CFD data comparison, a region with fully developed flow was chosen. Additionally, key anatomical locations of the aorta were selected to evaluate the model's performance in these critical areas.

Upper descending aorta. To begin the comparison, we focus on a region in the upper descending aorta, just after the flow exits the aortic arch. The axial slice representing this region is slice 71 in the CFD data and slice 50 in the MRI data as seen in Figure 85. As previously explained, slice 71 in the CFD data is determined using the formula $96 - (50/2)$, where 96 is the total number of axial slices in the CFD dataset, $50/2$ accounts for the downsampling process, and the subtraction is applied due to the inverse orientation of the MRI data relative to the CFD data. For both the CFD and MRI data, velocity-containing pixels in the selected slices were identified, their values extracted, and the mean velocity calculated. This allowed the creation of a flow profile in the selected region for both datasets. The process was performed for both SimVascular and CRIMSON. In each case the flow graphs of the three velocity components (u , v , w) are shown as well as the velocity magnitude graph.

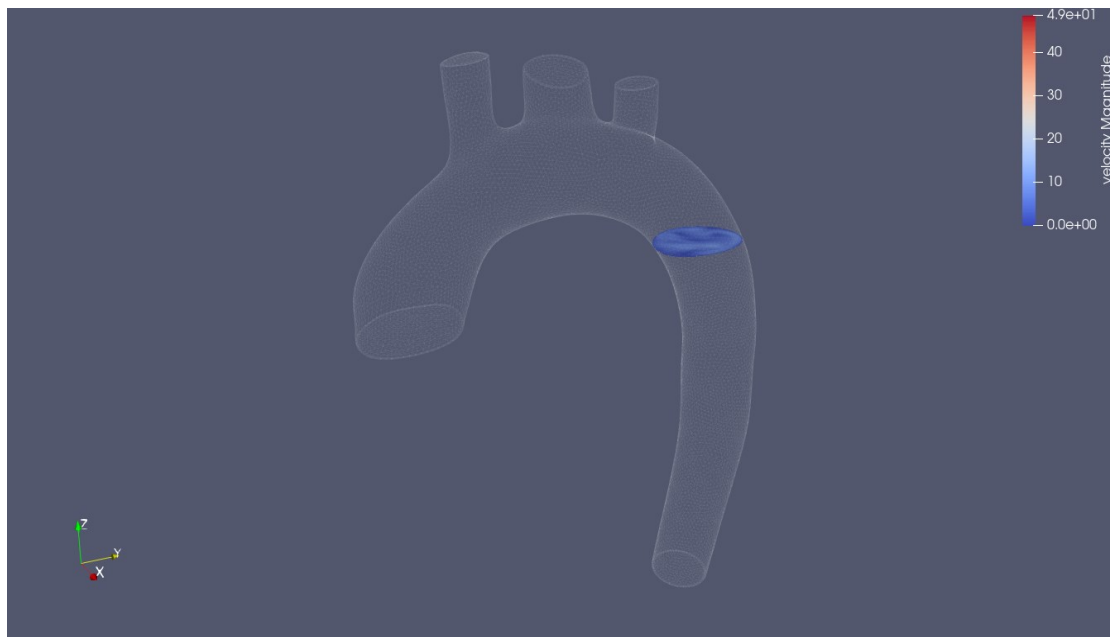


Figure 85: Axial slice for the upper descending aorta

Examining the graph in Figure 86 for the u -velocity component, it is evident that CRIMSON more accurately captures the flow behavior, as it accounts for variations in u -velocity during the systolic phase of the cardiac cycle. In contrast, SimVascular maintains a nearly constant value close to zero throughout the cycle, suggesting a negligible u -component. However, these differences have a minimal impact on the overall velocity magnitude due to their relatively small values. For the v -velocity component (Figure 87), both software programs capture the flow behavior well, with CRIMSON providing slightly better results. SimVascular tends to overestimate the v -velocity component, while Crimson slightly underestimates it but offers a more accurate representation of the flow dynamics.

As far as the w -velocity is concerned, it can be seen in Figure 88 that once again both programs capture the dynamics of the flow in that region with SimVascular slightly underestimate the max velocity and CRIMSON slightly overestimates it but after the peak value in the systolic phase, both programs have similar results and diverging only slightly from the MRI data. To gain a comprehensive understanding of velocity behavior in the region under study, the velocity magnitude graphs provide an overall perspective. As observed, both programs effectively capture the flow dynamics, with SimVascular slightly underestimating velocity during the systolic phase and Crimson slightly overestimating it.

However, throughout most of the cardiac cycle, both programs produce similar results aligning with the pattern observed in the MRI data.

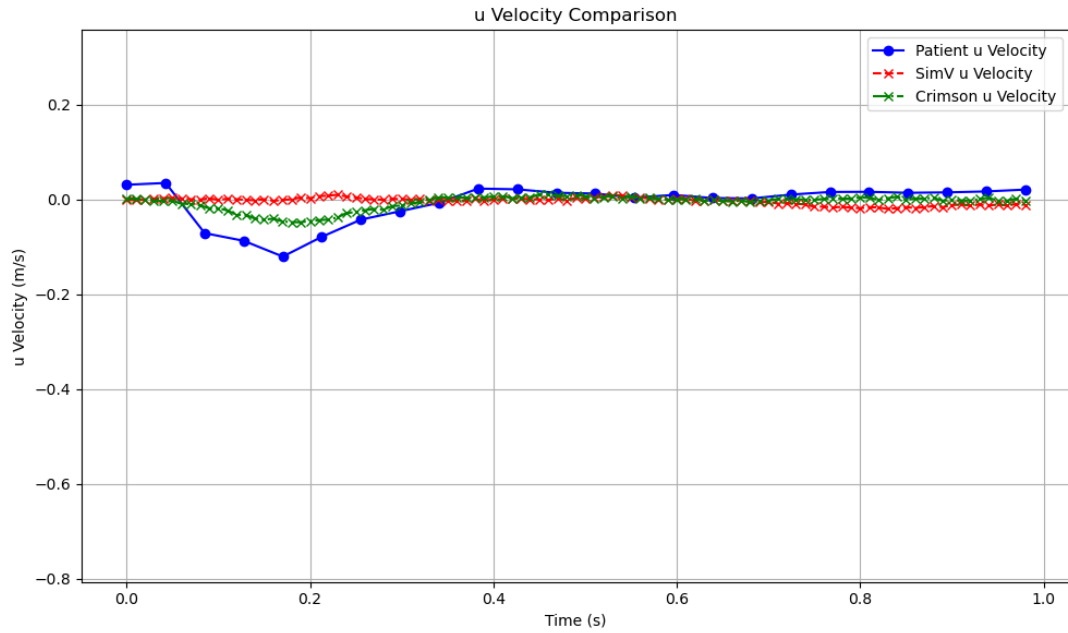


Figure 86: Graph comparing the u-velocity component in the upper descending aorta

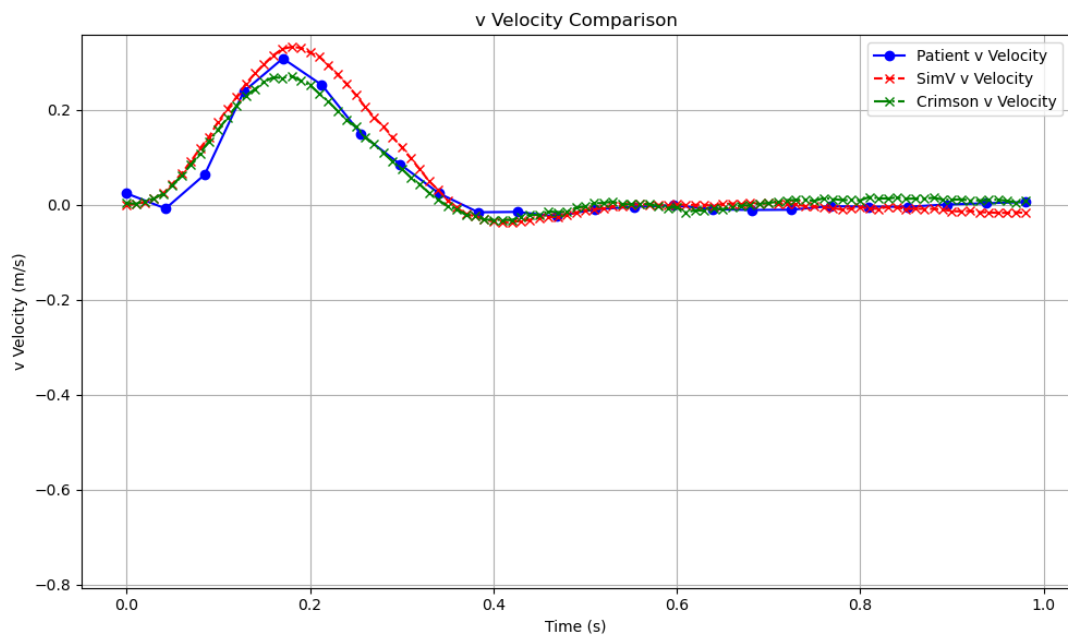


Figure 87: Graph comparing the v-velocity component in the upper descending aorta

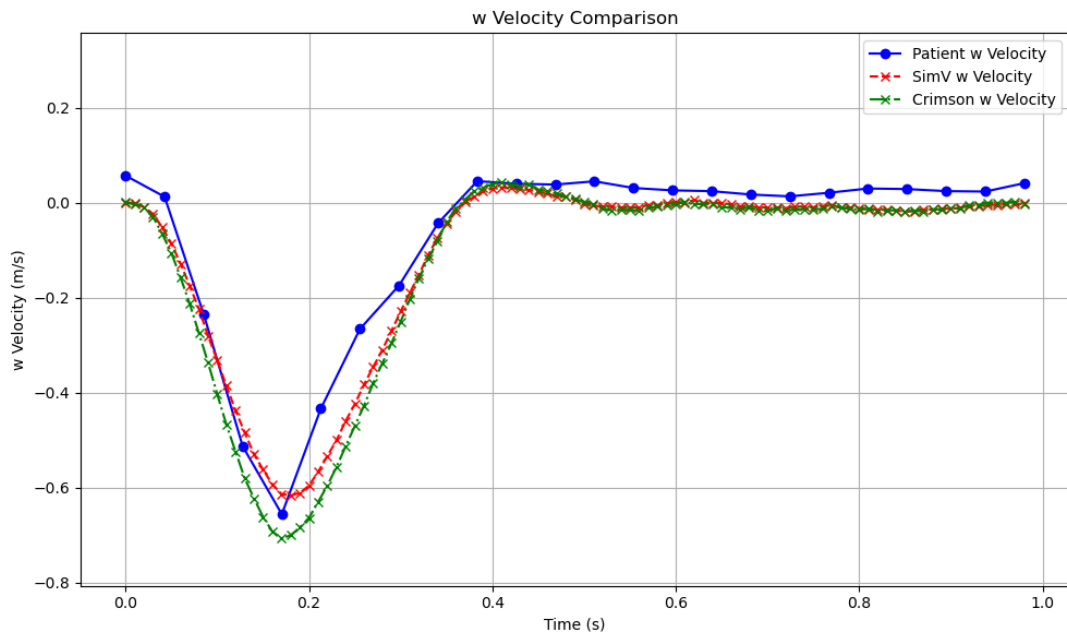


Figure 88: Graph comparing the w-velocity component in the upper descending aorta

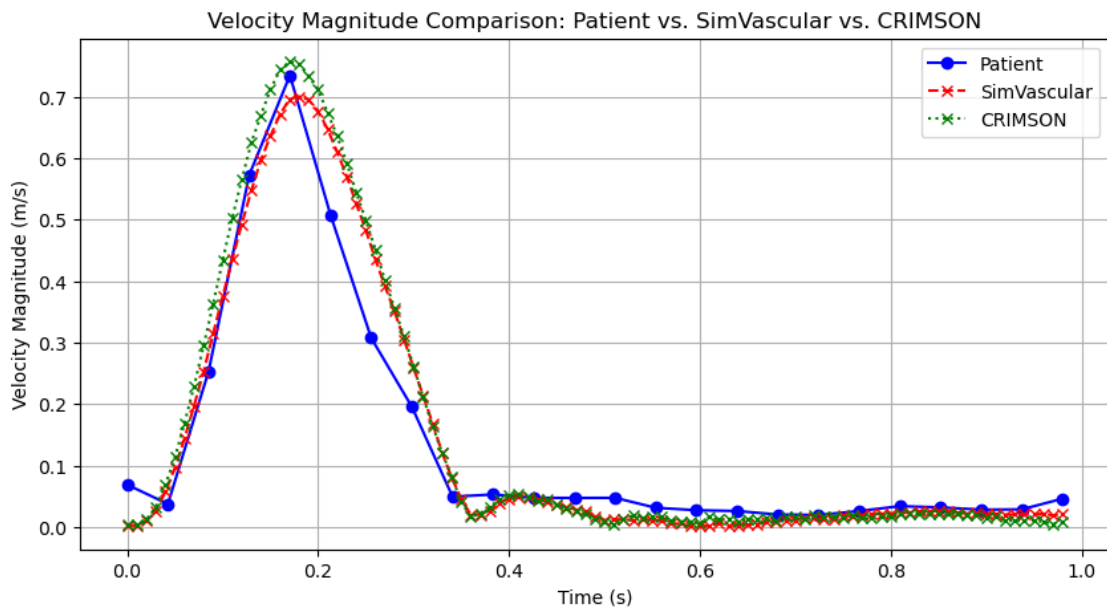


Figure 89: Graph comparing the velocity magnitude in the upper descending aorta

Ascending aorta. The next region examined is the ascending aorta, just before the flow reaches the first branch of the aortic arch, the brachiocephalic artery. For this location, an axial slice of 48 from the MRI data and an axial slice 72 from the CFD data are selected as seen in Figure 90. The same methodology as before is applied to generate comparison graphs. The graph in Figure 91 shows that both programs effectively capture the overall pattern of the u-velocity component, particularly during the systolic phase. However, some deviations appear during the diastolic phase, where both programs underestimate the original values and exhibit oscillatory patterns that are not present in the MRI data.

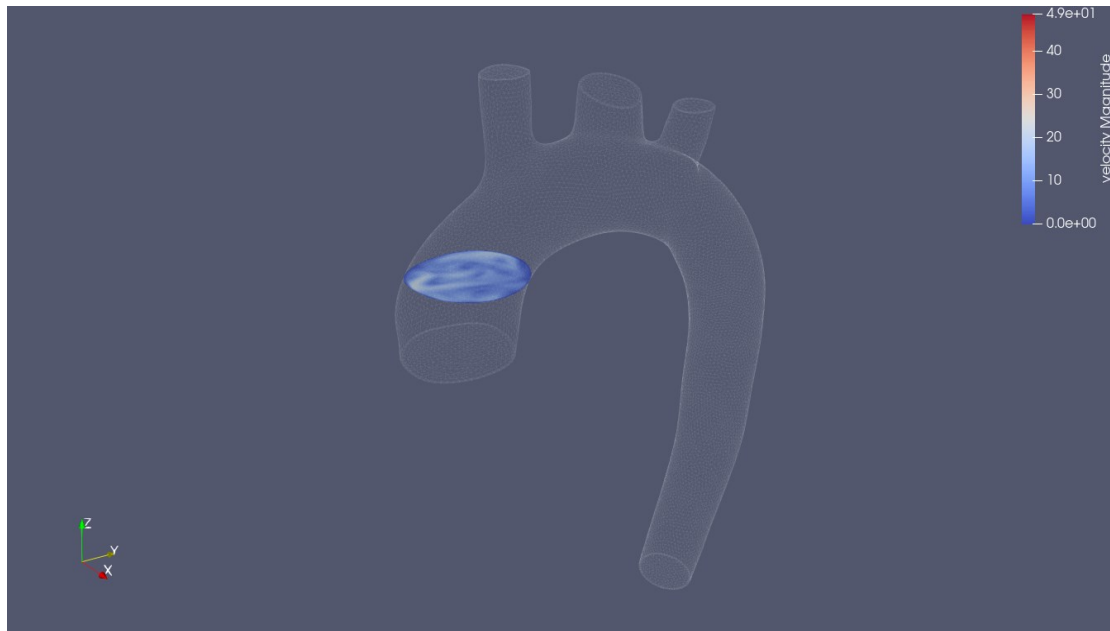


Figure 90: Axial slice for the ascending aorta

The same as before can be observed in the graph of the v-velocity component presented in Figure 92. Both programs follow the same pattern, however, a key difference from the MRI data is that they exhibit more intense backflow and overestimate slightly the velocity. In contrast, the MRI data maintains a steadier flow, gradually approaching zero during the diastolic phase. The graph in Figure 93 shows that both programs accurately capture the w-velocity component patterns throughout the cardiac cycle, with only minor and negligible differences.

The overall velocity behavior in this region can be observed in the graph in Figure 94, which illustrates the flow velocity magnitude before entering the aortic arch. The graph clearly shows that both programs accurately capture the flow velocity pattern during the systolic phase, with only minor differences, such as slightly higher values compared to the MRI data. However, during most of the diastolic phase, the software results deviate from the MRI data and exhibit some oscillatory patterns. Around 0.8 s, or approximately 81.63% of the cardiac cycle, the results converge with the MRI data. These deviations can likely be attributed to the absence of fluid-structure interaction (FSI) in simulations. A deformable arterial wall would absorb these oscillations and, due to its variable cross-sectional area, help maintain more stable velocity values that change gradually and smoothly, particularly during the diastolic phase.

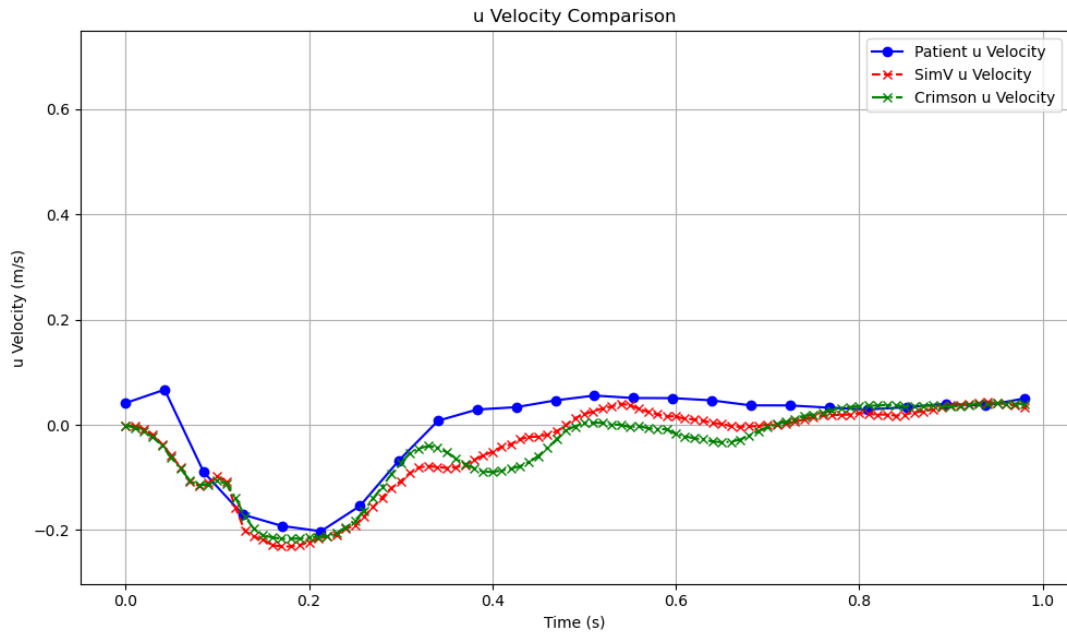


Figure 91: Graph comparing the u-velocity component before the flow enters the aortic arch

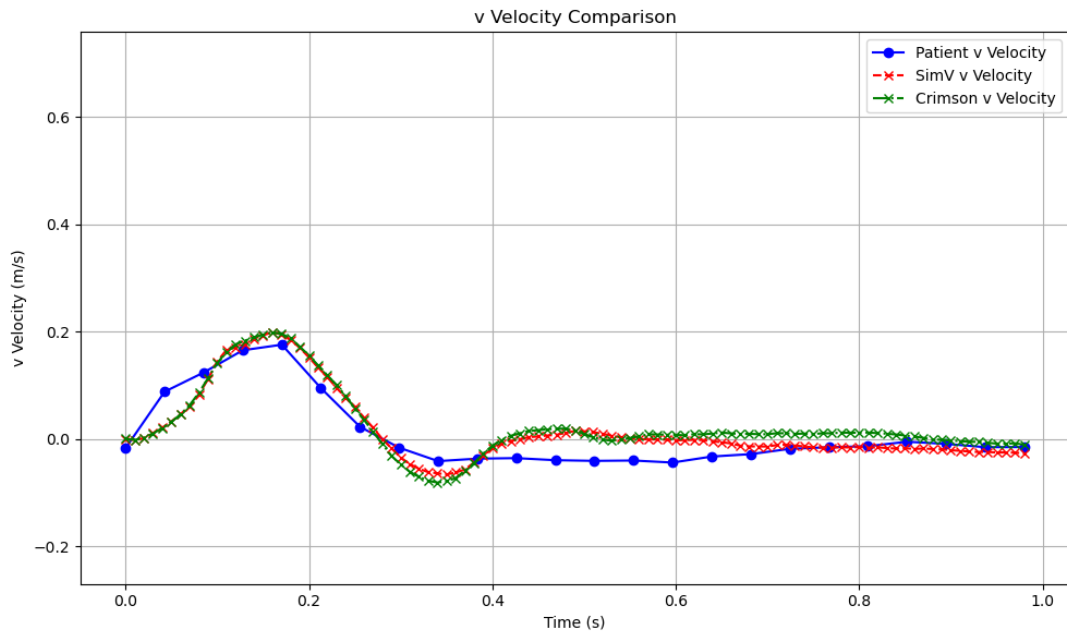


Figure 92: Graph comparing the v-velocity component before the flow enters the aortic arch

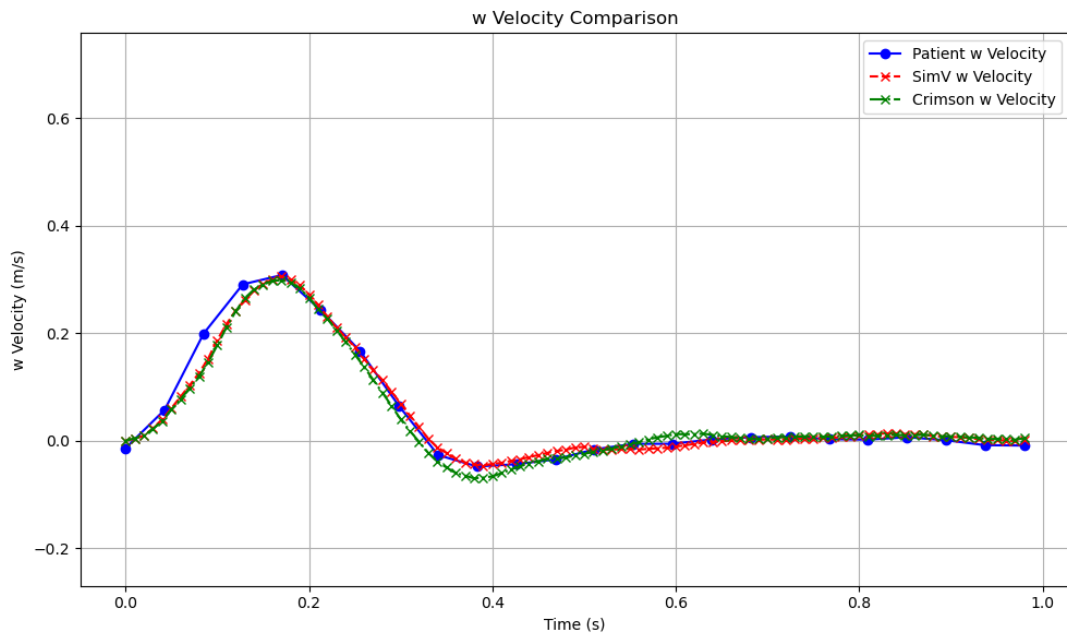


Figure 93: Graph comparing the w-velocity component before the flow enters the aortic arch

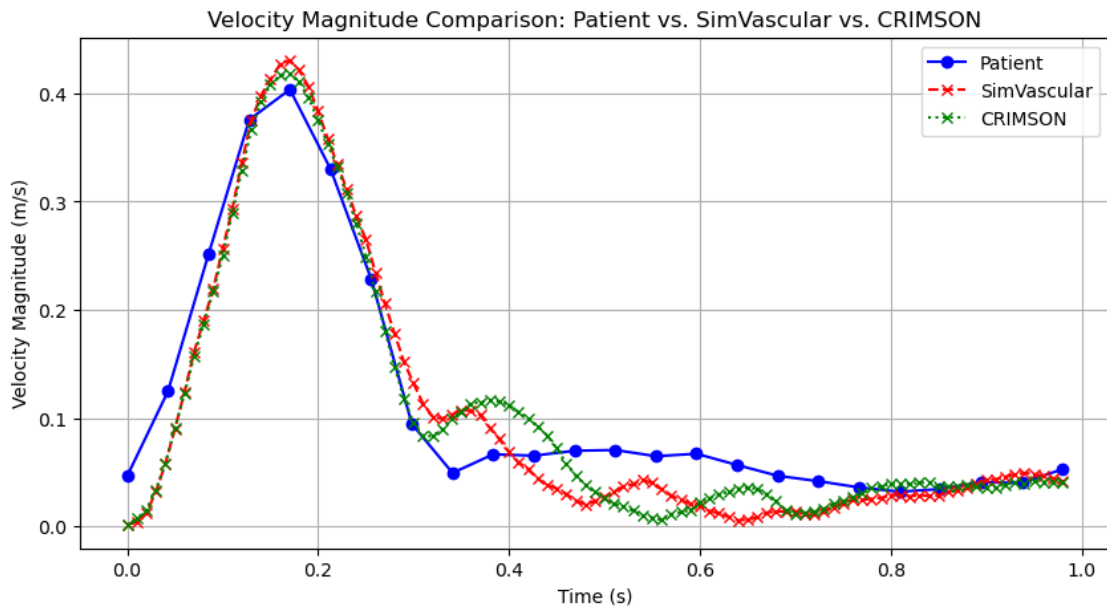


Figure 94: Graph comparing the velocity magnitude before the flow enters the aortic arch

Before the LCC branch of the aortic arch. The next region under investigation is the aortic arch, just before its second branch, the left common carotid artery. To analyze this region, coronal slice 78 from the MRI data and coronal slice 39 from the CFD data were selected as seen in Figure 95. The selection follows the criterion 78/2, as the coronal slices are not inverted between the MRI and CFD datasets, unlike the axial slices.

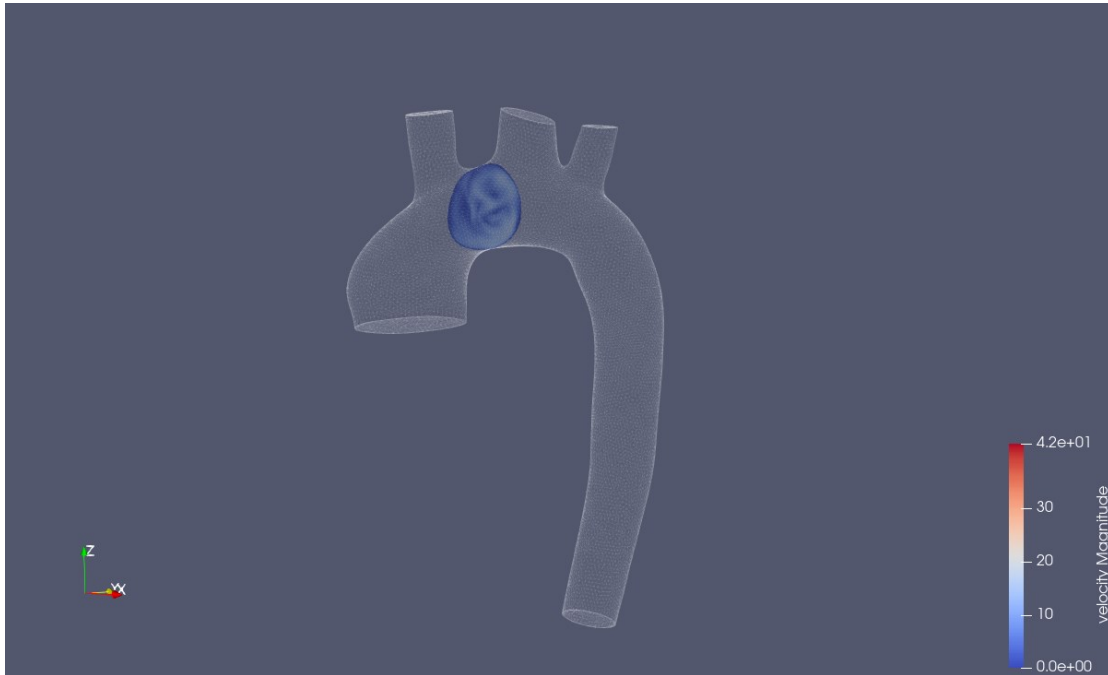


Figure 95: Coronal slice before LCC branch

The u-velocity component graph derived from these slices is shown in Figure 96. It reveals that the simulation results exhibit a different pattern compared to the MRI data. Furthermore, after the systolic phase of the cardiac cycle, the simulation results begin to diverge, with SimVascular's results aligning more closely with the MRI data. The MRI data maintains a relatively constant velocity throughout the entire cardiac cycle. However, it is important to note that the variations in velocity values in this region are on the order of 10^{-2} , which is one order of magnitude lower than the other velocity components. As a result, these differences have a minimal effect on the overall velocity magnitude and flow direction.

Figure 97 presents the v-velocity component for the current region, which represents the primary flow direction. Compared to the previous component, both simulation programs produce results that have similar patterns to each other, and they closely follow the pattern observed in the MRI data. The peak velocity values from both software programs closely match the peak velocity of the MRI data, and the CFD curves effectively capture the flow behavior in this region. In this specific area, the v-velocity component aligns with the flow direction, making it the dominant component. As a result, the CFD simulations accurately represent the primary flow mechanics.

The next graph in Figure 98 illustrates the w-velocity component. The CFD simulations predict higher peak w-velocity compared to MRI data, suggesting that the CFD models calculate stronger secondary flow components. This may indicate enhanced flow rotation or helical motion in the simulations compared to the actual patient data. Between 0.4–0.6 s, the MRI data show a reduction in w-velocity, whereas the CFD results maintain noticeable oscillations that are less prominent in the MRI data. After 0.7 s, the patient w-velocity remains closer to zero, with the Crimson results showing significant accuracy, while the SimVascular results deviate slightly. However, the velocity values remain below 0.1, indicating that these variations have a limited impact on the overall flow. Despite some overestimation of secondary flow effects, the CFD results successfully capture the key flow characteristics, including directional changes and general flow behavior.

To gain a clearer understanding of the overall flow behavior in this region, the graph depicting the velocity magnitude is presented in Figure 99. Overall, the CFD simulations overestimate the peak velocity during the systolic phase. Additionally, during diastole, the MRI data maintain a relatively steady velocity with smooth, minor increases, whereas the CFD results exhibit fluctuations throughout the entire diastolic phase. Notably, the fluctuations between the two CFD programs do not follow a consistent pattern, suggesting a phase shift. These discrepancies can be attributed to several factors, with a key contributing factor being the lack of fluid-structure interaction (FSI) in the simulations.

In vivo, the aortic walls deform in response to pulsatile flow, which helps to dampen peak velocities, delay systolic flow, and smooth secondary flow oscillations. In contrast, rigid-wall CFD simulations tend to overestimate velocity magnitudes, particularly in secondary flow components. Additionally, wall motion in patient data plays a crucial role in pressure wave propagation and energy dissipation, leading to a more natural flow behavior. Rigid-wall simulations, on the other hand, can exaggerate velocity fluctuations, especially during late systole phase and early diastole phase. These combined possible factors explain why the CFD results display stronger oscillations and slight phase shifts compared to the MRI data.

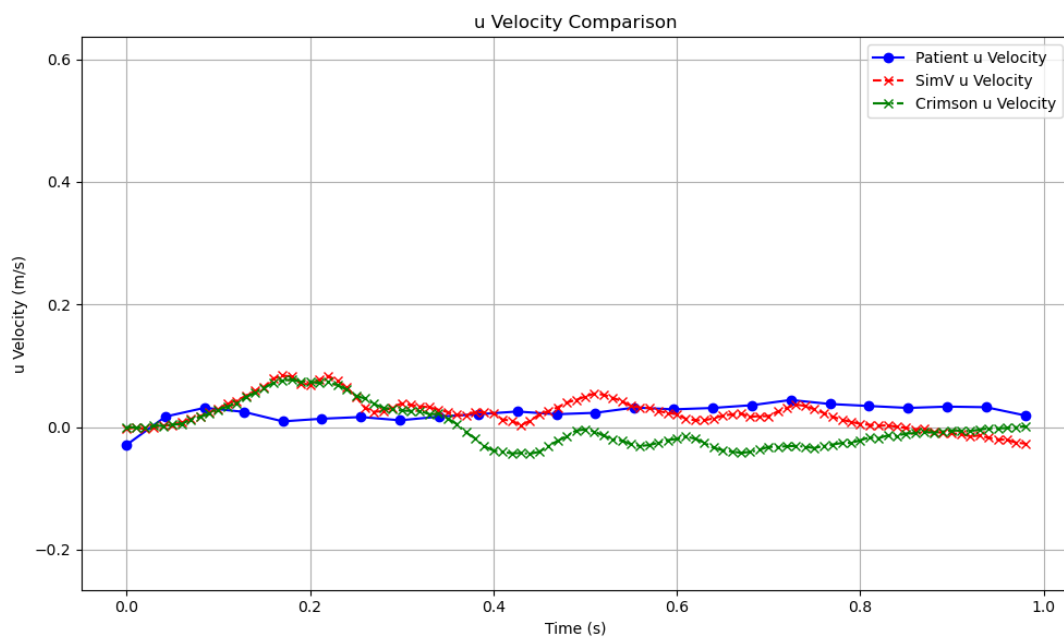


Figure 96: Graph comparing the u-velocity component before the LCC branch of the aortic arch

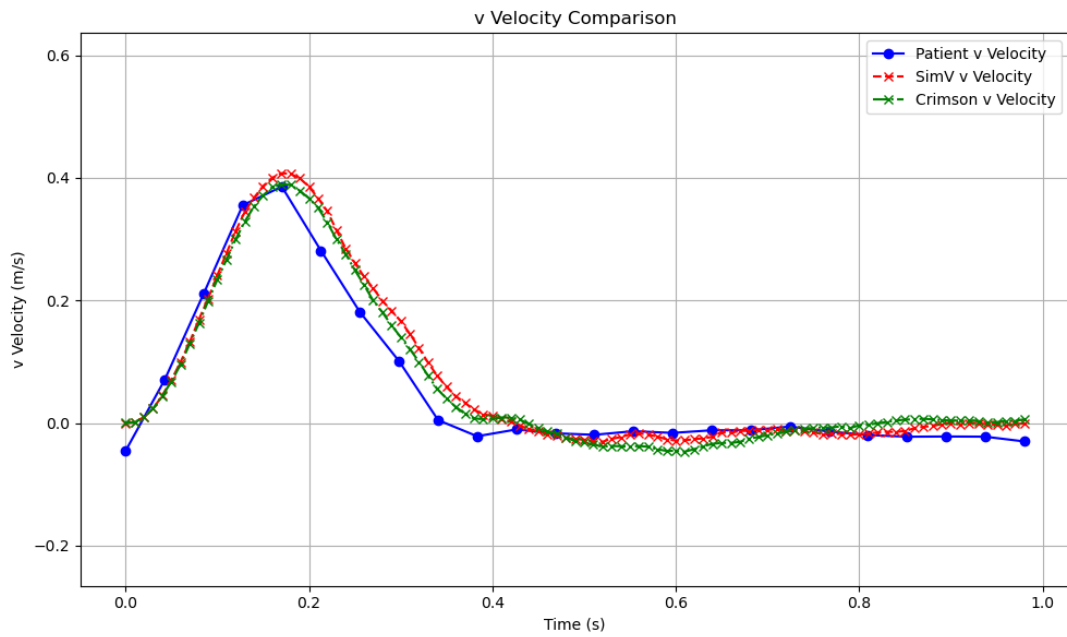


Figure 97: Graph comparing the v-velocity component before the LCC branch of the aortic arch

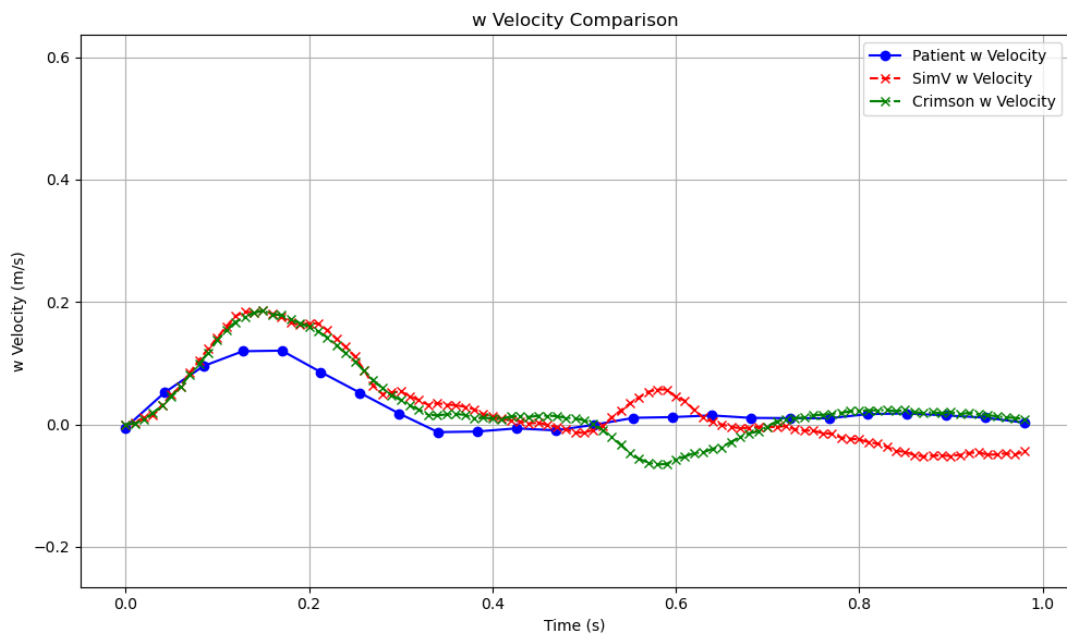


Figure 98: Graph comparing the w-velocity component before the LCC branch of the aortic arch

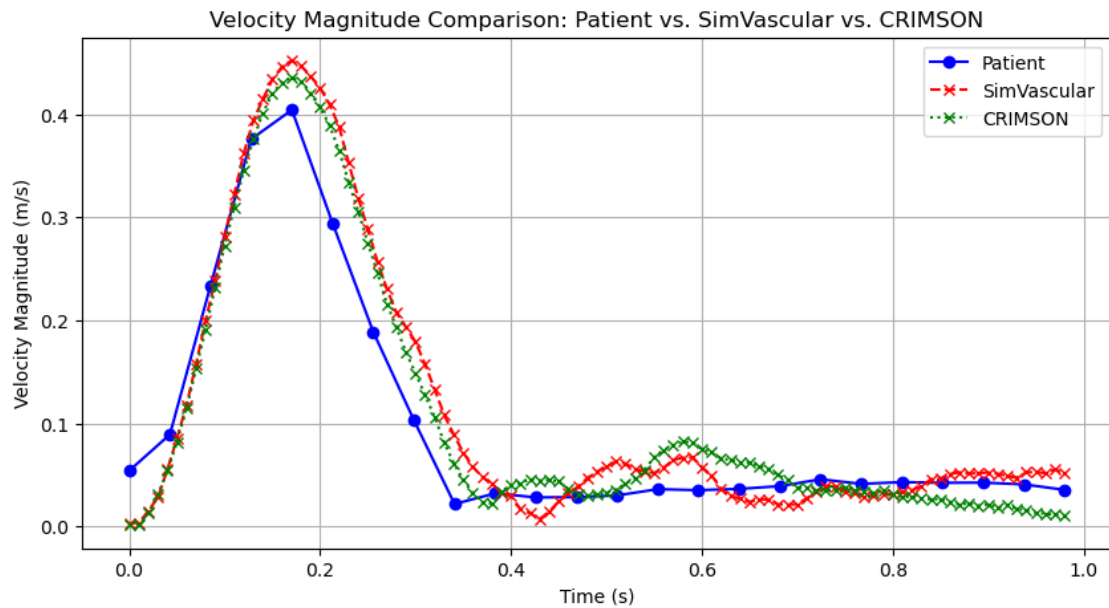


Figure 99: Graph comparing the velocity magnitude before the LCC branch of the aortic arch

Before the LSA branch of the aortic arch. Another reference region selected for extracting velocity component graphs is located just before the flow enters the final branch of the aortic arch, the left subclavian artery (LSA) as seen in Figure 100.

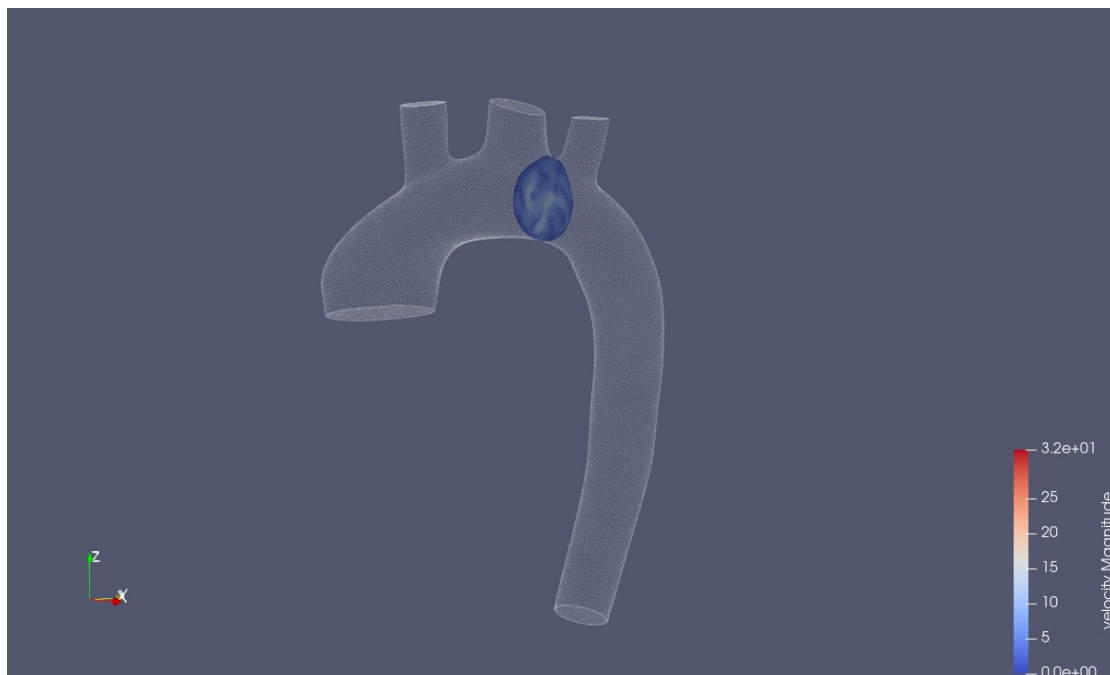


Figure 100: Coronal slice before LSA branch

The u -velocity component (Figure 101) derived from MRI data in this region reflects the patient's physiological flow pattern. A comparison of the u -velocity before the LSA branch indicates that CFD simulations tend to overestimate velocity magnitudes, particularly during systole. The computational models exhibit a steeper increase and a higher peak velocity, suggesting a more pronounced acceleration of flow than observed in the patient data.

Additionally, a phase shift is evident, where the simulated velocities reach their peak earlier than those measured in the patient, likely due to the rigid-wall assumption in the simulations, whereas the patient's aortic walls are compliant, affecting flow propagation. Later in the cardiac cycle, the velocities between the CFD models and patient data begin to converge, though minor discrepancies persist, especially in the oscillatory behavior seen in the simulations but less prominent in the patient data. These variations as well as the low velocity values of the patient may be attributed to boundary condition assumptions, or patient-specific physiological differences.

Regarding the *v*-velocity component, the CFD results show a significant improvement in accuracy compared to the *u*-velocity component. The comparison of the *v*-velocity component before the LSA branch indicates that the CFD simulations generally follow the trend observed in the patient data, showing improved agreement. However, the CFD models tend to slightly overestimate the peak velocity during the systolic phase and depict a steeper acceleration phase. A key difference arises in the later phase of the cardiac cycle, where a brief backflow is evident in the patient data, while the CFD simulations do not fully capture this phenomenon, instead maintaining near-zero or slightly positive velocities. This discrepancy suggests that the computational models may not fully account for localized flow recirculation effects. As the cardiac cycle progresses, the simulated and patient velocities align more closely. As previously observed, the *v*-component remains the primary flow direction component, indicating that the simulations effectively capture the main flow dynamics with reasonable accuracy.

Lastly, the *w*-velocity component in this reference region is presented in Figure 103. The comparison of the *w*-velocity component before the LSA branch reveals that the CFD simulations largely follow the patient data trend but with key discrepancies. Initially, the patient data exhibits an early positive velocity peak, which is absent in the simulations. Shortly after, a pronounced negative velocity phase is observed in all datasets, but the patient data shows a steeper drop compared to the CFD results. Around mid-systole, the simulated velocities rise more smoothly, while the patient data shows sharper fluctuations. In the later phase of the cardiac cycle, the patient data remains closer to zero, while the CFD simulations predict more sustained oscillations that are not as pronounced in the measurements. These differences suggest that the computational models may not fully capture localized secondary flow effects, transient instabilities, or patient-specific flow disturbances.

Like the previously analyzed regions, the overall velocity magnitude graph (Figure 104) offers valuable insights into the flow dynamics, speed, and fluctuations. While the CFD simulations generally follow the same pattern as the MRI data, there are some notable discrepancies. The most significant difference lies in the peak velocity during systole, which is overestimated by both computational models, with SimVascular showing the largest deviation. Additionally, during diastole, the CFD simulations display velocity fluctuations, in contrast to the MRI data, which remains relatively steady. Around 0.35 s, the MRI data show changes in velocity indicative of backflow, a phenomenon not captured by the simulations. These discrepancies can be attributed to several factors, primarily the assumption of rigid aortic walls in the CFD models. Unlike the real aortic walls, which deform under pulsatile flow to dampen peak velocities, the rigid-wall assumption leads to overestimation of systolic velocities.

The absence of fluid-structure interaction (FSI) in the CFD models also prevents them from capturing the natural damping effects of the walls during diastole, contributing to the observed fluctuations in the CFD data. Additionally, the increase in velocity observed around 0.35 s in the MRI data, indicative of backflow, may be due to pressure wave reflections from

downstream arteries, a feature that the CFD models, with their simplified boundary conditions, fail to replicate. Despite these discrepancies, the CFD results gradually align with the MRI data after the initial diastolic oscillations, suggesting that the simulations eventually converge with the steady-state flow behavior observed in the MRI data. This convergence suggests that although the CFD models have difficulty capturing the intricate dynamics of systole and early diastole, they still provide a reasonable approximation of overall flow behavior, offering valuable insight into flow development.

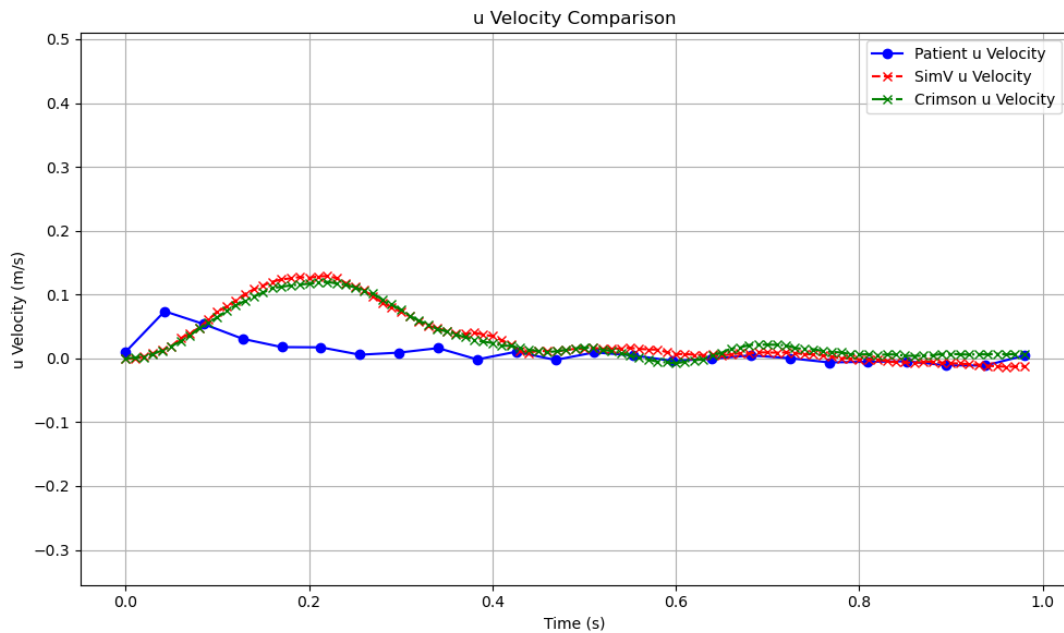


Figure 101: Graph comparing the u-velocity component before the LSA branch of the aortic arch

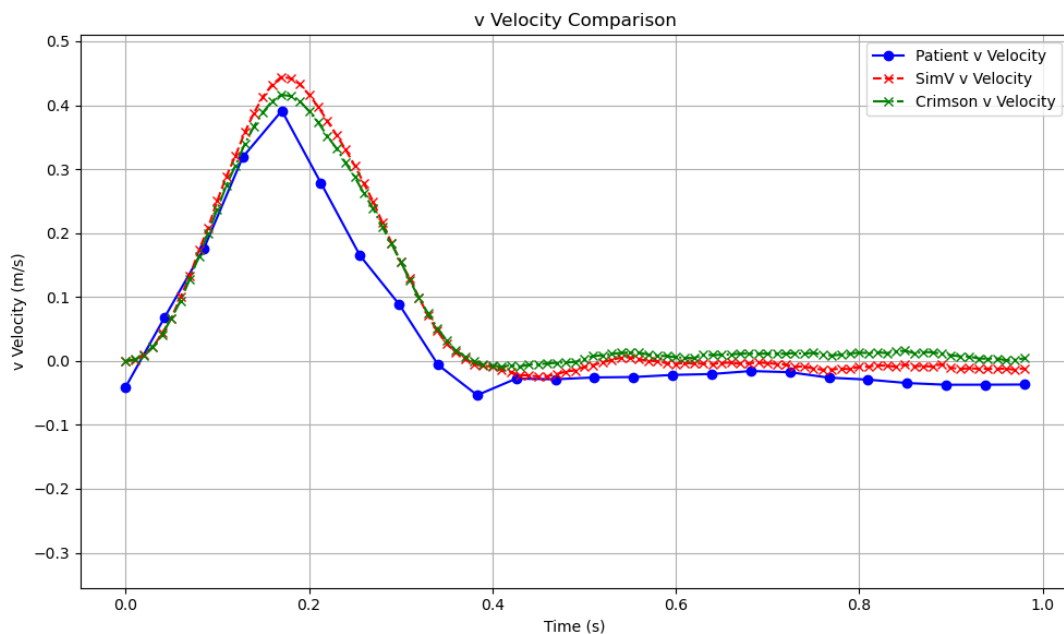


Figure 102: Graph comparing the v-velocity component before the LSA branch of the aortic arch

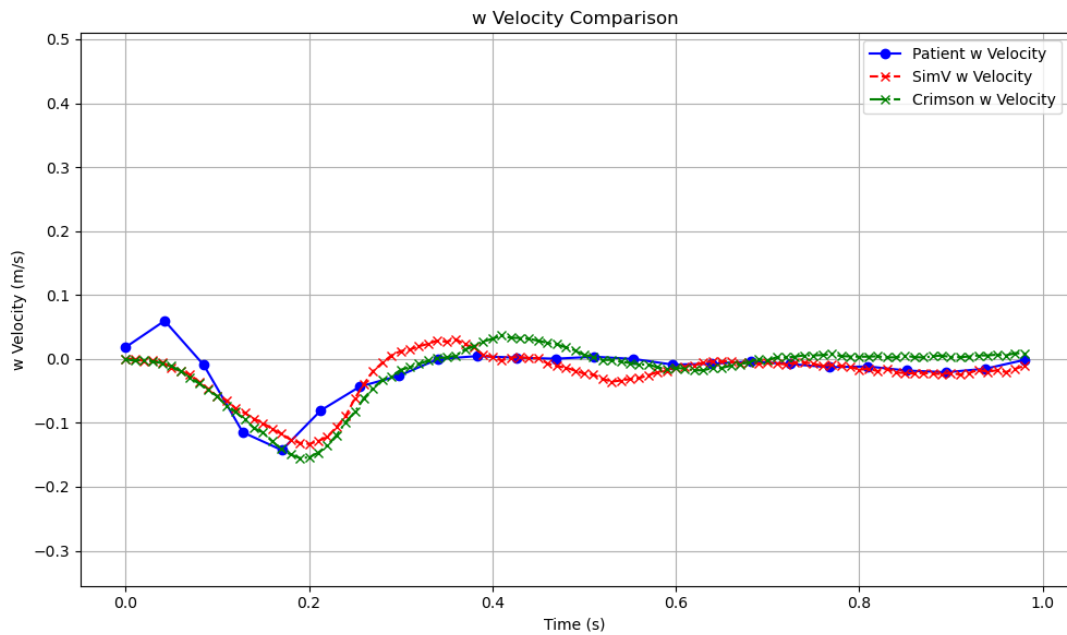


Figure 103: Graph comparing the w-velocity component before the LSA branch of the aortic arch

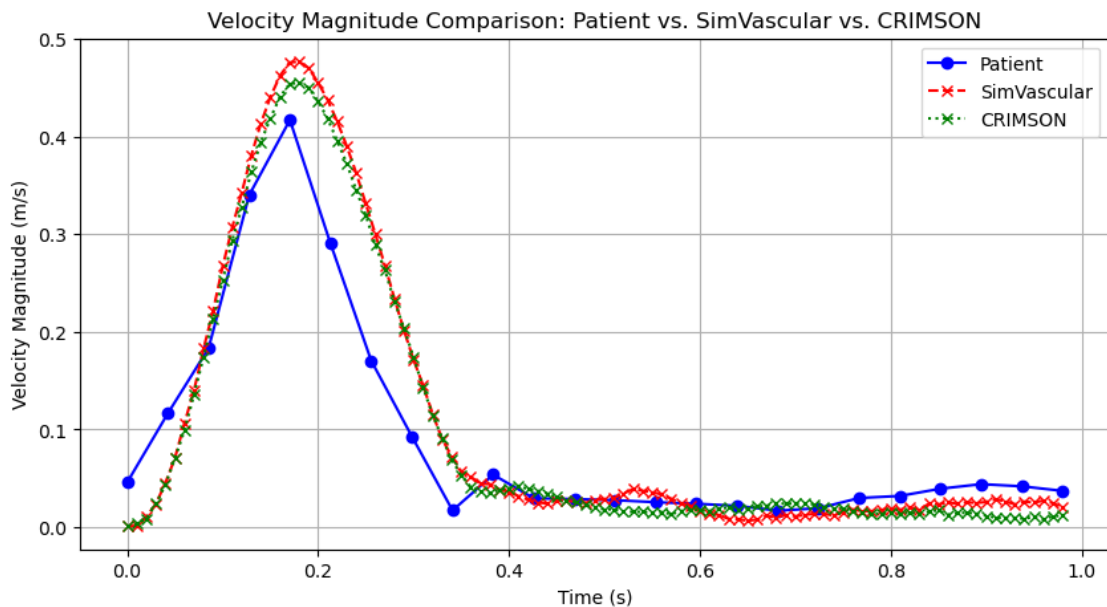


Figure 104: Graph comparing the w-velocity component before the LSA branch of the aortic arch

In conclusion, the analysis suggests that the CFD simulations successfully captured the physiological mechanisms of the studied case to a large extent. The most accurate results were observed in the descending aorta, as expected, due to the fully developed flow and simpler anatomy in that region. As demonstrated, all velocity components were well represented by the simulations in this area. On the other hand, the aortic arch exhibited the greatest discrepancies, which was anticipated due to the complex factors influencing the flow in this region. These factors include the division of flow into the three branches, the absence of fluid-structure interaction (FSI) in the simulations, leading to a lack of damping in velocity

oscillations and the challenges of capturing pressure wave reflections from downstream arteries, which are sometimes inadequately modeled by the 3-element Windkessel model.

Finally, to provide a clearer perspective, Table 9 presents the Reynolds number calculated at the peak of the systolic phase for each of the previously analyzed cross-sections.

Table 9: Reynolds numbers of each cross-section at the peak of the systolic phase

Cross-sections	Cross-section location (cm)	Cross-section area (cm ²)	Reynolds number (approx.)
Upper descending aorta	11.92 (z-axis)	7.556	4800
Ascending aorta	12.23 (z-axis)	22.361	3300
Before the LCC branch of the aortic arch	-5.67 (y-axis)	9.797	3300
Before the LSA branch of the aortic arch	-2.48 (y-axis)	9.09	3700

Based on the Reynolds numbers calculated at the peak of the systolic phase for each cross-section, it can be inferred that the flow briefly enters a transitional regime. The CFD model employed in this study assumes laminar flow throughout the domain. However, under transitional conditions, this assumption may lead to the appearance of residual oscillations in the simulated flow, particularly visible during the diastolic phase in certain regions. Furthermore, the presence of transitional flow increases the sensitivity of the simulation to boundary conditions, where small perturbations in boundary values can significantly impact the results.

Potential solutions to these effects include refining the mesh in regions prone to non-laminar behavior and verifying that the numerical schemes used can handle enough flow instabilities. Nevertheless, since the transitional regime persists for a very short duration (less than 0.1 s), its overall impact on the simulated flow remains relatively limited. Despite this brief transitional period, the overall physiological relevance of the results is preserved, as the flow remains within the laminar regime for the majority of the cardiac cycle.

3.2 Parabolic velocity profile

3.2.1 Pressure Profile

Pressure waveforms. As with the patient-specific velocity profile discussed earlier, the pressure graphs for each artery (five boundary conditions) are presented to compare the differences between them and between the different velocity profiles.

As before, the ascending aorta is shown first (Figure 105). The difference between the two waveforms is negligible, as they exhibit the same behavior throughout the entire simulation with no noticeable variations. However, compared to the pressure waveforms from the patient-specific velocity profile, the pressure values are slightly higher. The increased pressure values in the parabolic case result from changes in velocity distribution, momentum transfer and solver-specific handling of boundary conditions. However, since the overall flow rate remains the same, these variations are minor and do not significantly impact global hemodynamics.

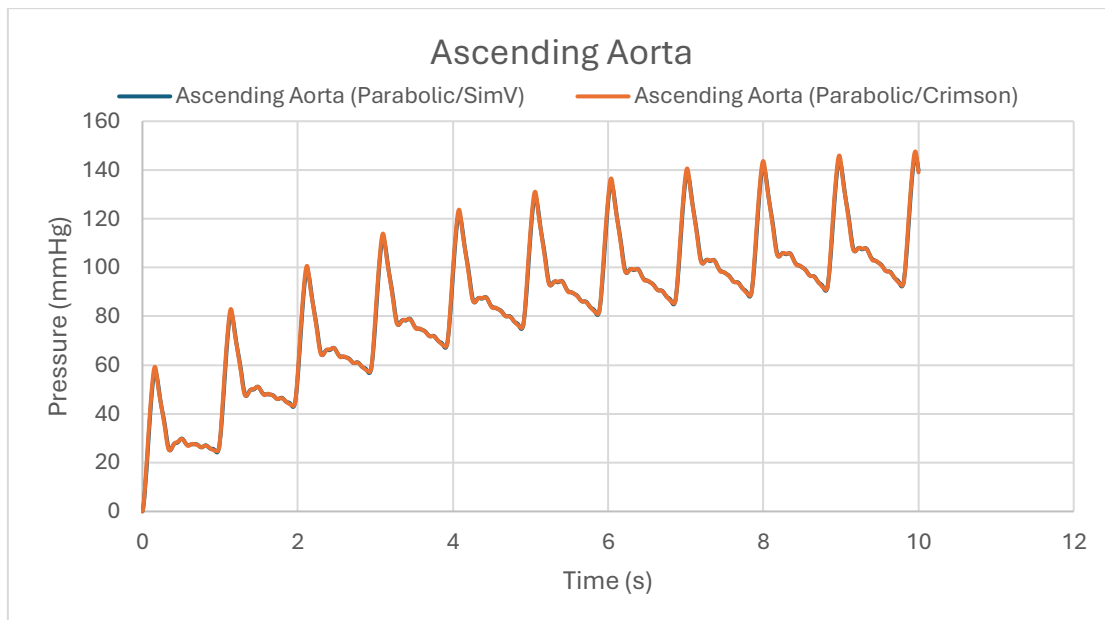


Figure 105: Pressure waveforms for Ascending Aorta (Parabolic)

Next is the pressure waveform of the descending aorta depicted in Figure 106. Similar to the ascending aorta, the pressure waveforms in the descending aorta exhibit the same overall behavior across both software programs, with no significant differences observed. Additionally, both waveforms show slightly higher-pressure values compared to those from the patient-specific velocity profile.

Next, we examine the pressure waveforms of the brachiocephalic artery depicted in Figure 107. Once again, both programs exhibit identical pressure waveform behavior, along with an increase in pressure values compared to the patient-specific velocity profile. This pattern is also observed in the pressure waveforms of the left common carotid artery, which are presented next in Figure 108. Finally, the same pattern previously discussed is also present in the left subclavian artery, the last branch of the aortic arch (Figure 109).

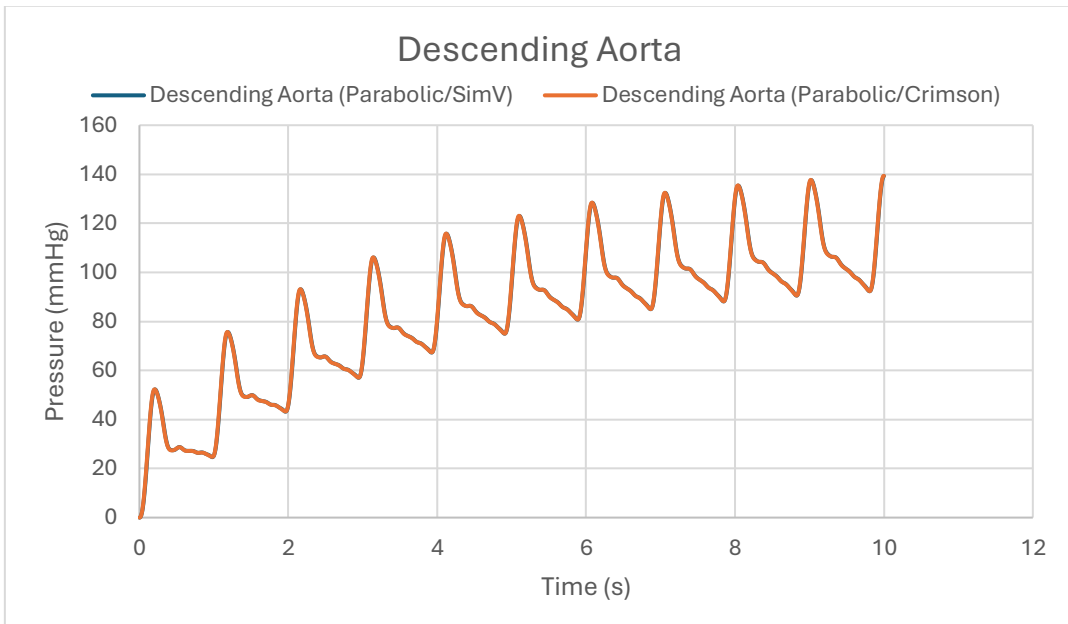


Figure 106: Pressure waveforms for Descending Aorta (Parabolic)

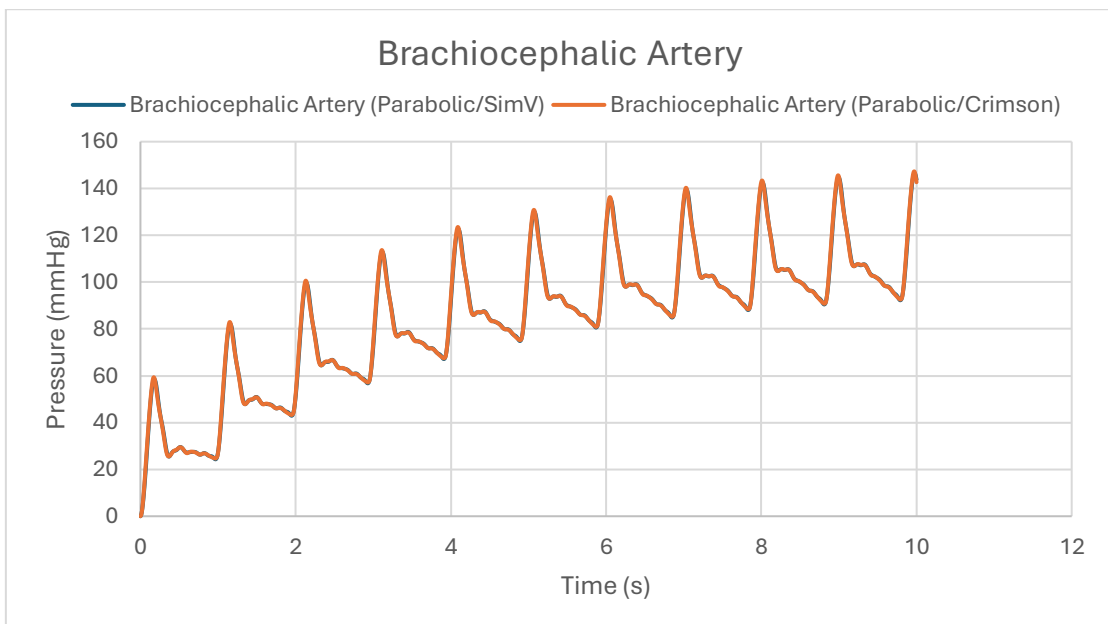


Figure 107: Pressure waveforms for Brachiocephalic Artery (Parabolic)

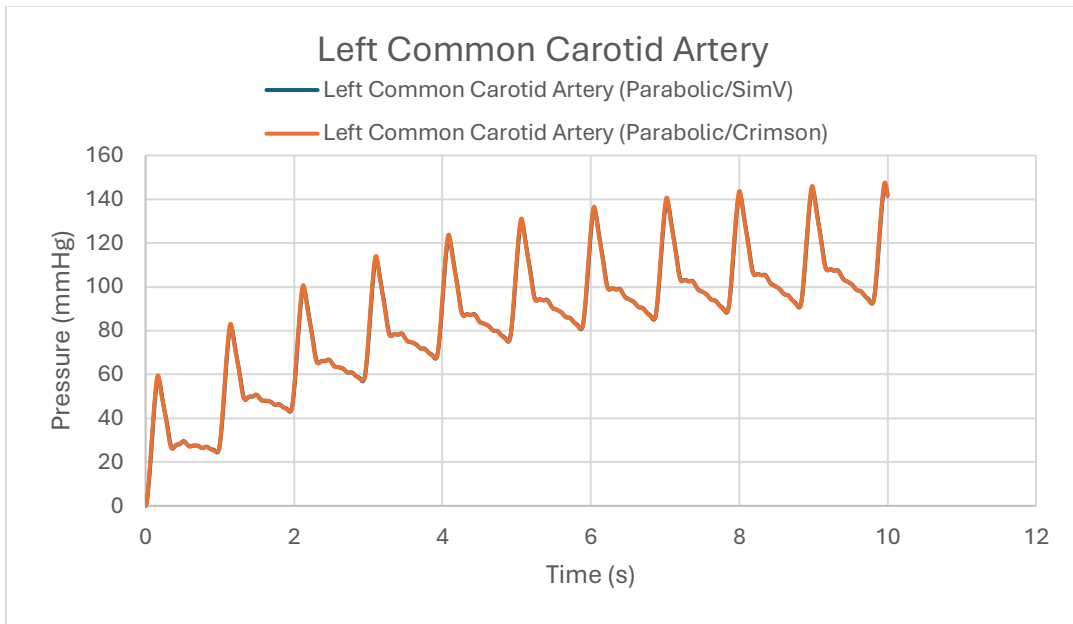


Figure 108: Pressure waveforms for Left Common Carotid Artery (Parabolic)

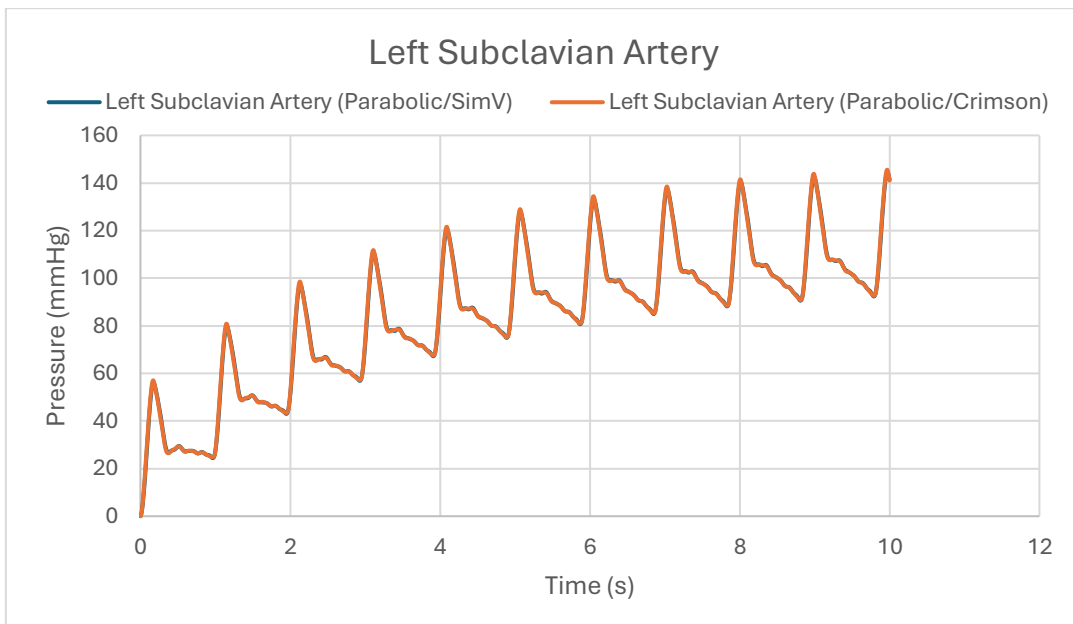


Figure 109: Pressure waveforms for Left Subclavian Artery (Parabolic)

3D Pressure distribution. As with the pressure distribution of the patient-specific velocity profile, the same timepoints are selected for reference.

Start of the systolic phase. The first reference point is at 8.81 seconds (timestep 881), marking the start of the systolic phase. In both programs, the pressure distributions follow a similar pattern, as shown in Figure 110 and Figure 111, with lower values in the ascending aorta that gradually increase toward the descending aorta, where the highest values are observed. However, the pressure values range slightly higher, around 90 mmHg to 91 mmHg, which is marginally greater than those of the patient-specific velocity profile, as shown in the graphs.

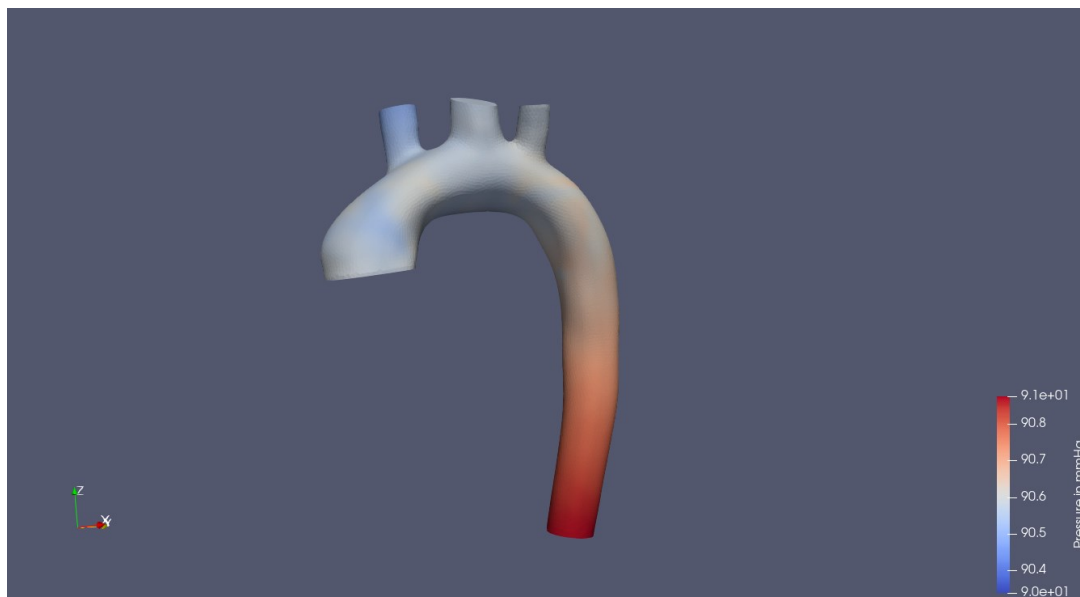


Figure 110: Pressure Distribution at start of the systolic phase (Parabolic profile/SimVascular)

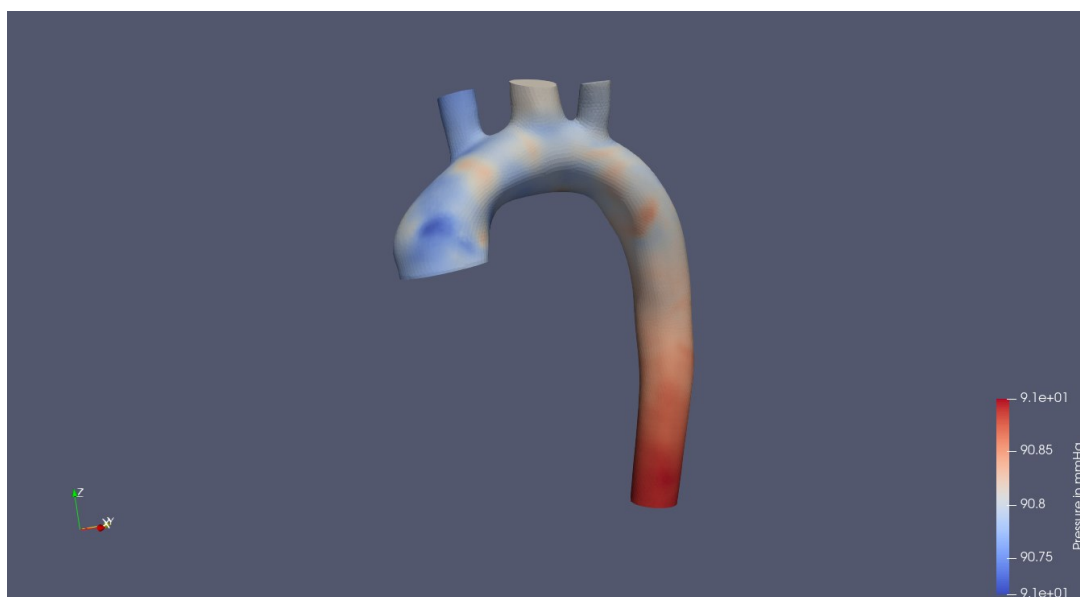


Figure 111: Pressure Distribution at start of the systolic phase (Parabolic profile/Crimson)

Peak of the systolic phase. The pressure distribution of the next timepoint selected, the one at 8.98 s (timestep 898) that represents the peak of the systolic phase for this cardiac cycle, is presented in Figure 112 and Figure 113. At this timepoint, the pressure distribution follows the same pattern as its patient-specific counterpart. Higher pressure values are observed in the ascending aorta, gradually decreasing as the flow progresses through the model, with the lowest values in the descending aorta. This trend is consistent in both programs. Additionally, the pressure values for the parabolic profile are slightly higher compared to the patient-specific profile.

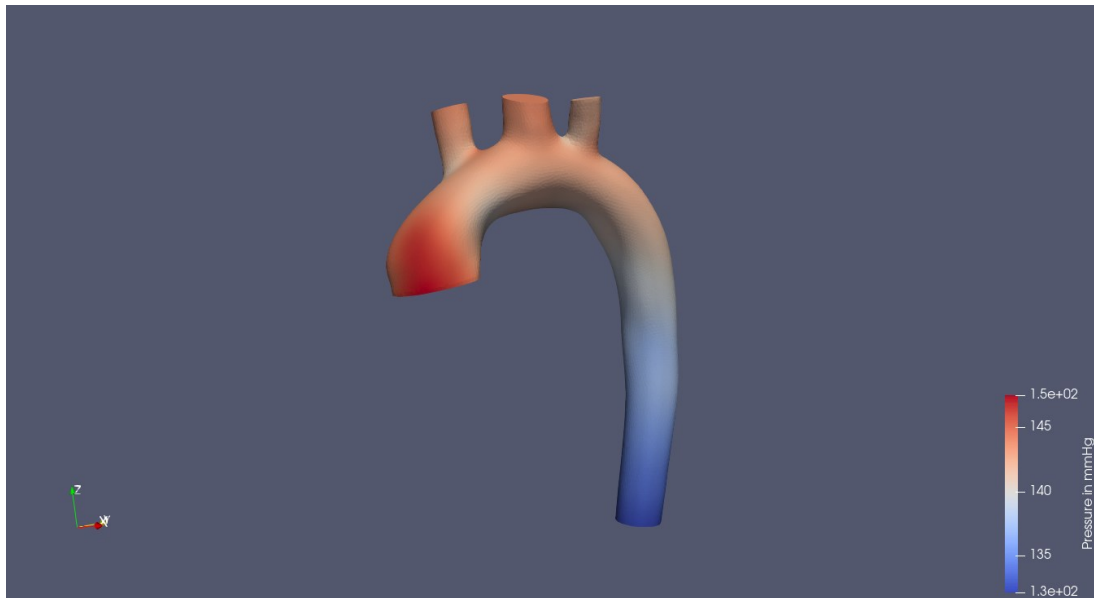


Figure 112: Pressure Distribution at the peak of the systolic phase (Parabolic profile/SimVascular)

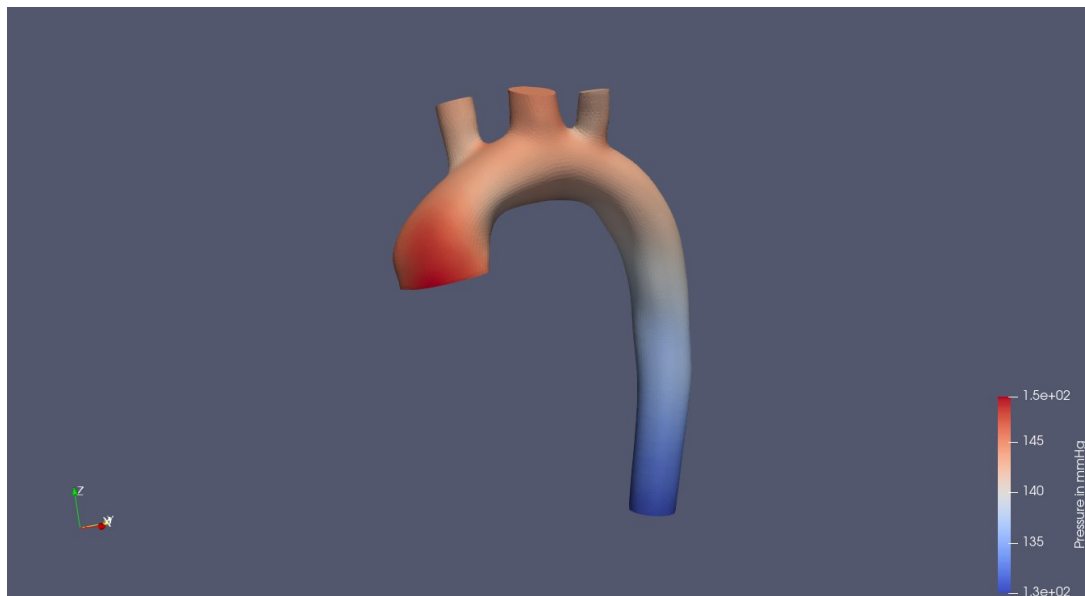


Figure 113: Pressure Distribution at the peak of the systolic phase (Parabolic profile/Crimson)

End of the systolic phase. The next pressure distribution, shown at the 9.18 s time point (timestep 918) in Figure 114 and Figure 115, represents the end of the systolic phase for this cardiac cycle. At the end of the systolic phase, the pressure distribution follows the same pattern as the patient-specific velocity profile. The lowest values appear in the ascending aorta and gradually increase along the flow domain, reaching their peak in the descending aorta. Both software programs compute similar pressure ranges, with the parabolic profile once again showing a slight increase in pressure.

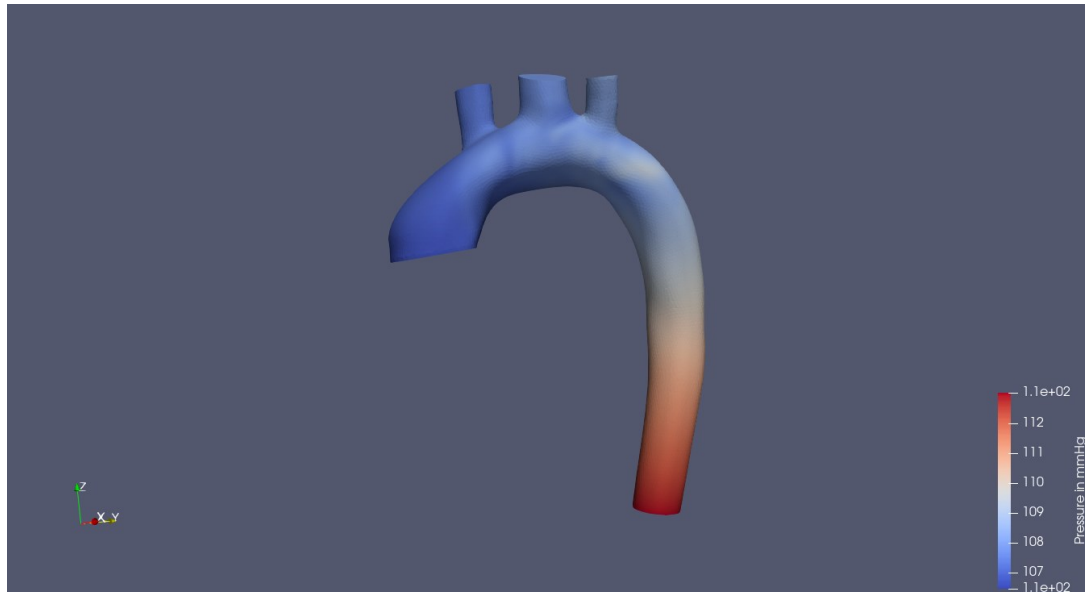


Figure 114: Pressure Distribution at the end of the systolic phase (Parabolic profile/SimVascular)

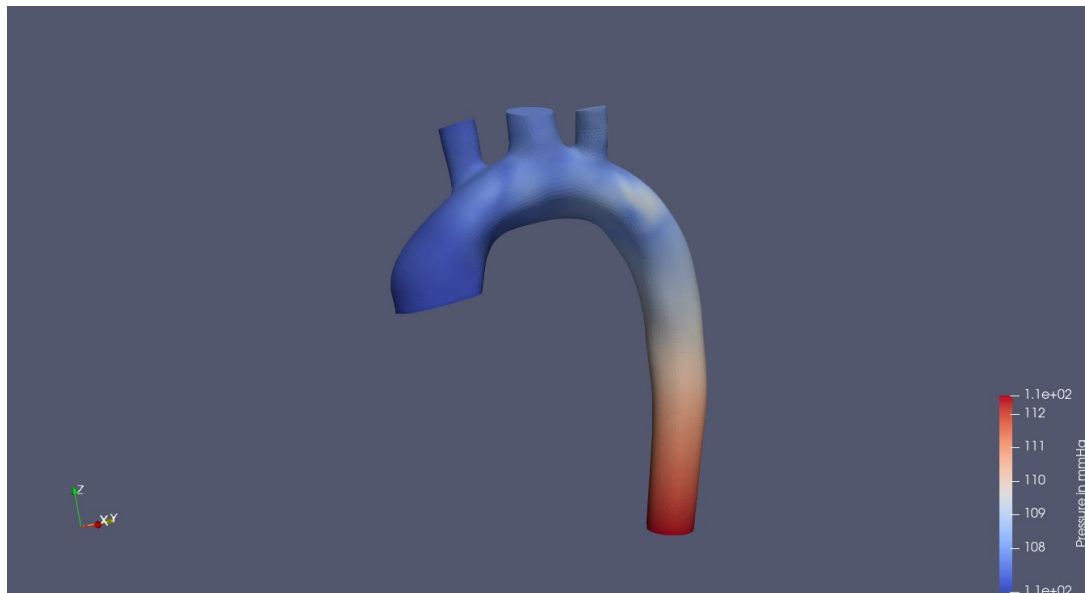


Figure 115: Pressure Distribution at the end of the systolic phase (Parabolic profile/Crimson)

During the diastolic phase. The final pressure distribution is presented at the 9.6 s time point (timestep 960), which, as previously mentioned, falls approximately in the middle of the diastolic phase, providing a representative snapshot of the flow dynamics during this period (Figure 116 and Figure 117). During the diastolic phase, similar to the patient-specific velocity profile, the pressure remains within a narrow range, with slight elevations in certain regions of the model. Both software programs compute a nearly identical pressure distribution throughout the 3D model, with only minimal variations between them while maintaining consistent pressure values. As observed in the systolic phase, the pressure values obtained using the parabolic velocity profile are slightly elevated, though this increase is smaller compared to the systolic phase.

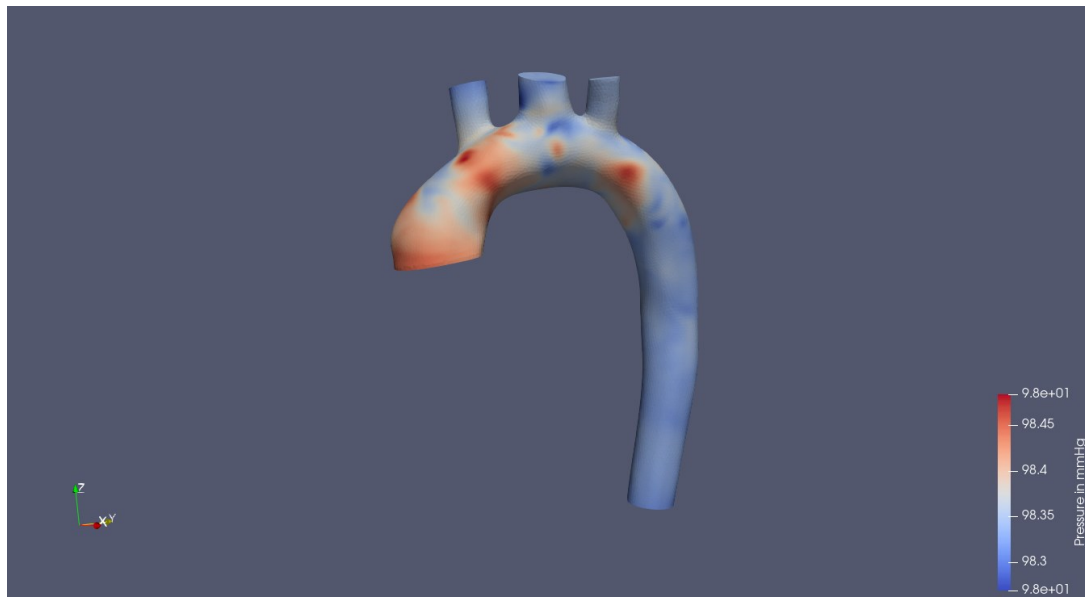


Figure 116: Pressure Distribution during the diastolic phase (Parabolic profile/SimVascular)

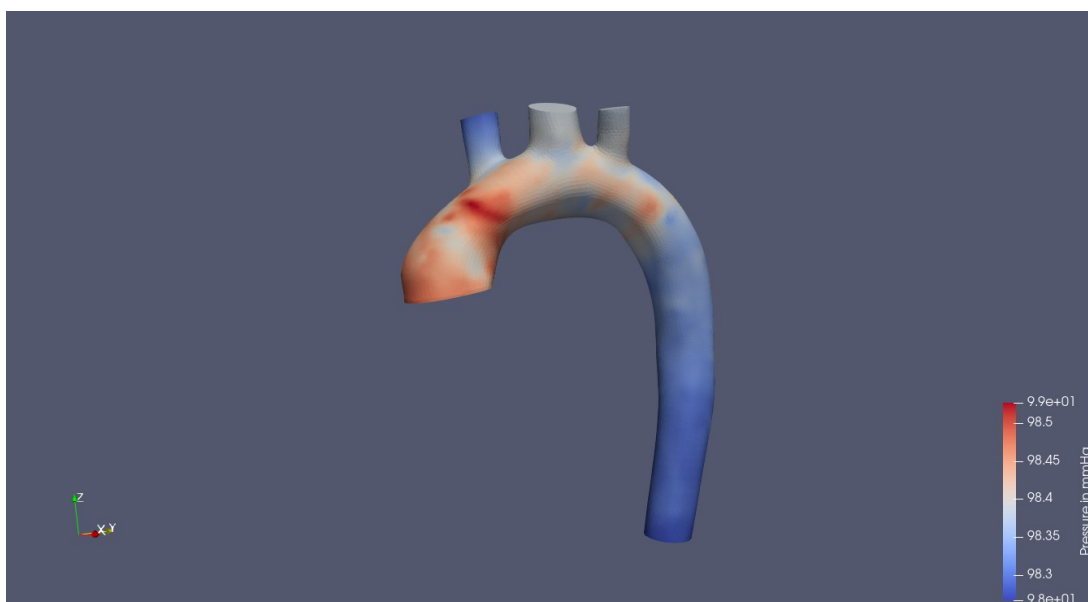


Figure 117: Pressure Distribution during the diastolic phase (Parabolic profile/Crimson)

Overall, using the parabolic velocity profile as a reference indicates that it results in slightly higher-pressure values, particularly during the systolic phase, compared to the patient-specific velocity profile. While the pressure distribution remains largely similar during systole for both profiles, some differences emerge during diastole. The patient-specific profile exhibits a more uniform pressure distribution, whereas the parabolic profile shows minor elevations in the region of the ascending aorta.

3.2.2 Flow rate profile & velocity vector field

In this section, as with the previous profile, the simulation results related to velocity will be analyzed. However, the flow graphs for the major arteries (one inlet and four outlets) will be omitted, as they are identical to those in the patient-specific profile discussed in the previous section. Since the same inlet profile is applied and the same RCR values are used at the outlets, the overall flow distribution remains unchanged, ensuring consistent flow across all outlets in both profiles. As with the rest of this study, the same timepoints representing the cardiac cycle are used.

Start of systolic phase. The analysis begins with the timepoint at 8.81 seconds (timestep 881), marking the onset of the systolic phase. As shown in Figure 118, and Figure 119, both profiles display a uniform velocity distribution across the cap area, with higher values concentrated in the center. Unlike the patient-specific velocity profile, however, there is no backflow.

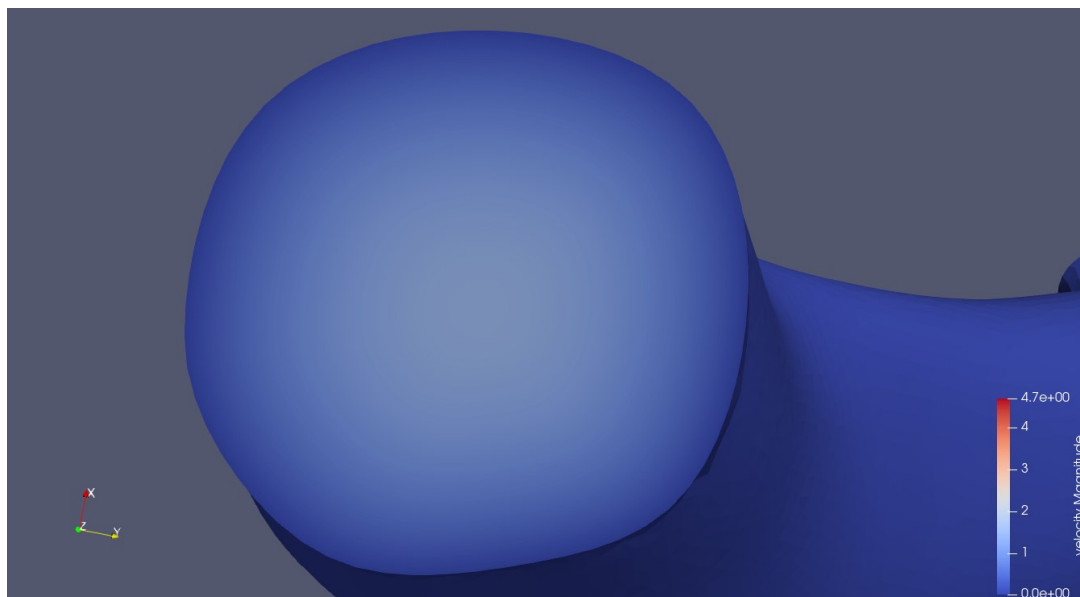


Figure 118: Parabolic velocity profile at the start of the systolic phase (SimVascular)

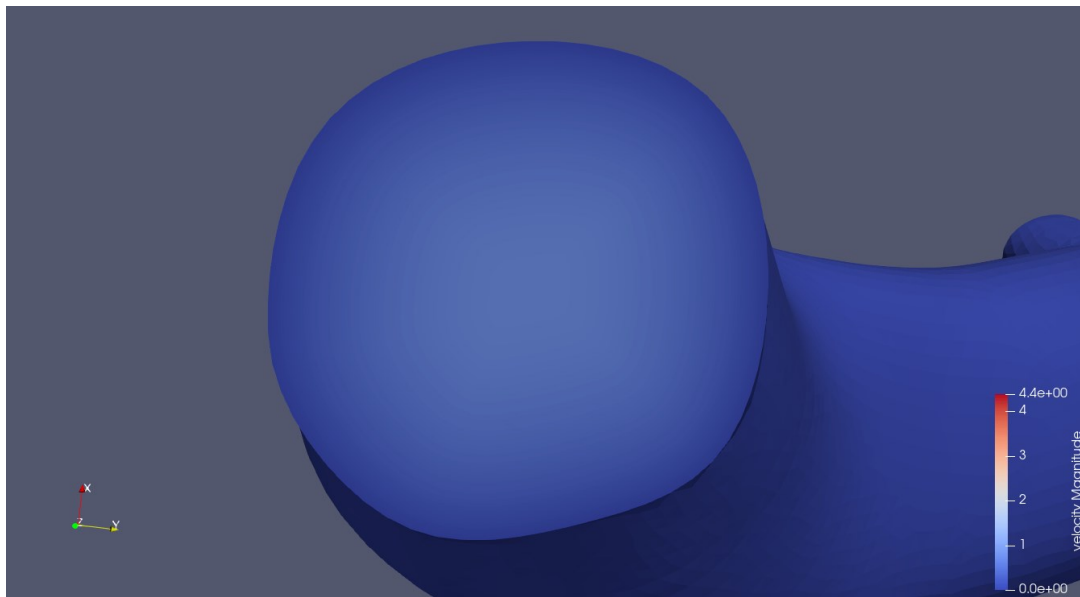


Figure 119: Parabolic velocity profile at the start of the systolic phase (Crimson)

The velocity vector field exhibits similar patterns to the patient-specific profile across both programs, as shown in Figure 120 and Figure 121. The flow remains well-organized, with higher velocities (red) concentrated in specific regions, such as the ascending aorta, the aortic arch, and its branches, while lower velocities (blue) are predominant in the descending aorta. Additionally, certain areas display signs of vorticity. The swirling motion of the streamlines in these regions suggests localized flow disturbances, likely caused by vessel geometry changes and bifurcations. These areas of vorticity indicate secondary flow patterns and mild recirculation zones, which are expected in realistic arterial flows, particularly in curved sections like the aortic arch.

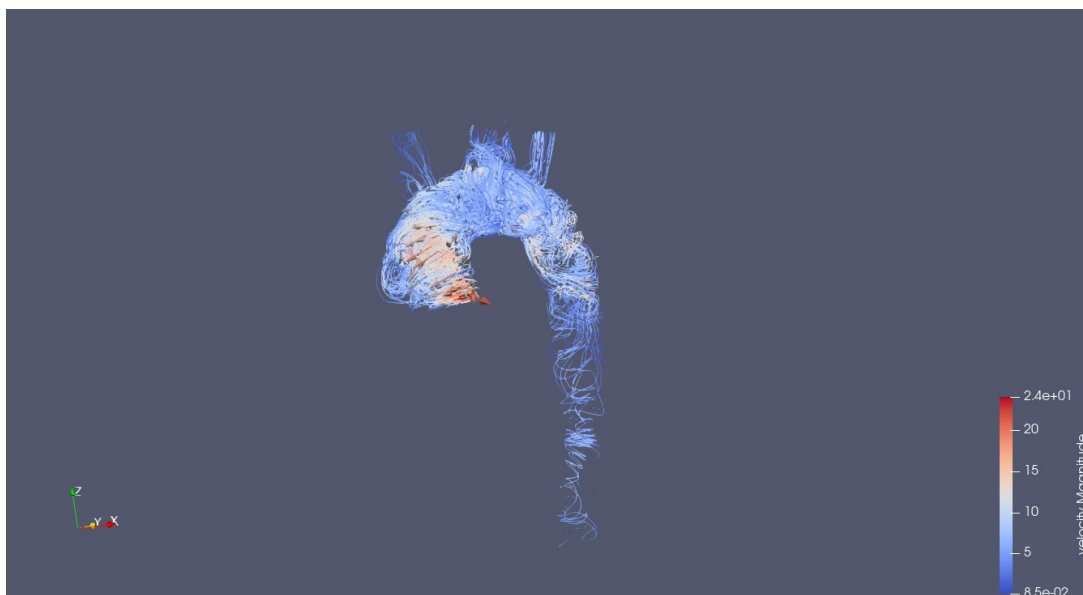


Figure 120: Velocity vector field and streamlines at the start of systolic phase (SimVascular)

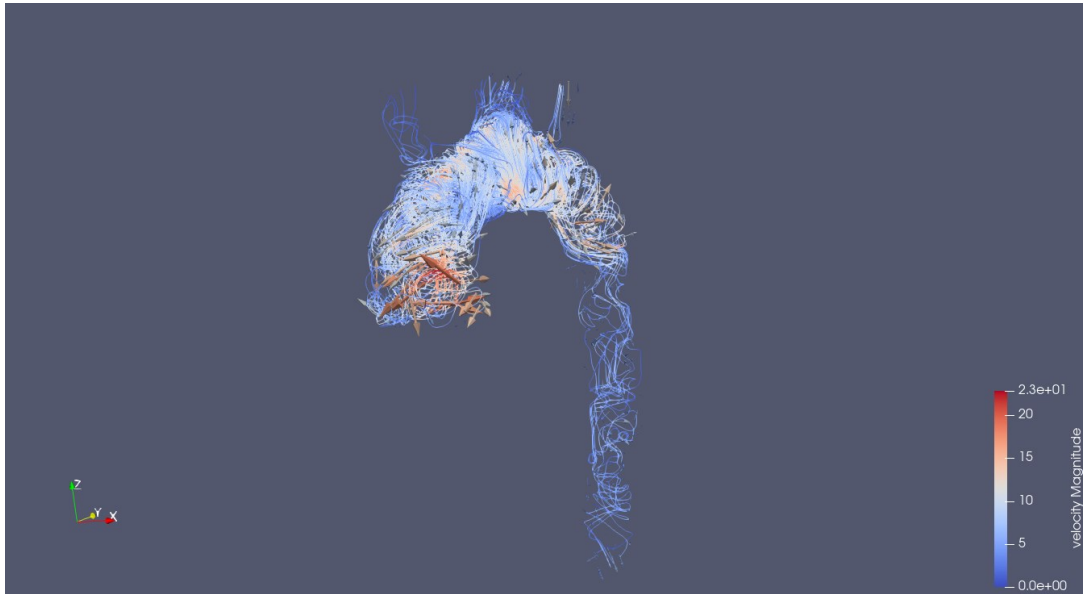


Figure 121: Velocity vector field and streamlines at the start of systolic phase (Crimson)

Peak of the systolic phase. At the peak of the systolic phase (timestep 898), the parabolic velocity profile maintains the same uniform pattern as before, with lower values near the boundaries that gradually increase toward the center of the cross-sectional area, where the highest velocity is observed (Figure 122, Figure 123). As expected, the velocity values are significantly elevated at this phase.

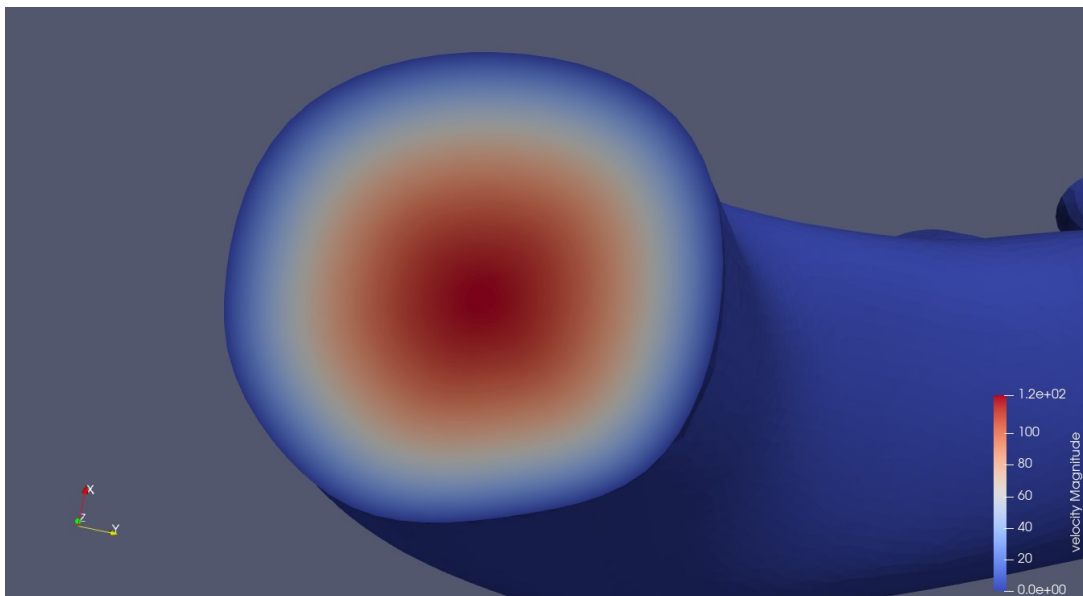


Figure 122: Parabolic velocity profile at the peak of the systolic phase (SimVascular)

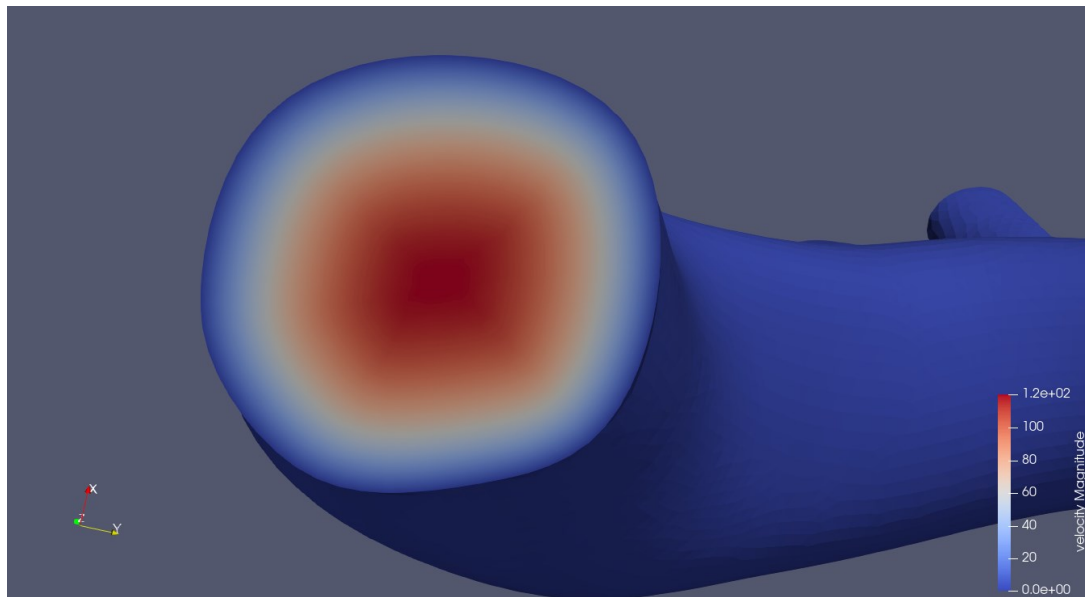


Figure 123: Parabolic velocity profile at the peak of the systolic phase (Crimson)

The vector field and streamlines reveal that the highest velocity (red) is concentrated along the centerline of the descending aorta, reflecting a parabolic velocity profile (Figure 124, Figure 125). High velocities are also evident in the ascending aorta and near the aortic branches, indicating strong forward flow during systole. As blood is ejected from the heart, it accelerates through the ascending aorta and curves through the arch, where a slight velocity reduction occurs due to flow division at the branches. Swirling streamlines suggest flow vorticity in these regions, likely caused by geometric changes and flow separation. In the descending aorta, velocity increases due to vessel narrowing and momentum conservation, forming a more structured, parabolic profile without helical structures, enabling efficient downstream transport. This pattern is consistent in both software programs.

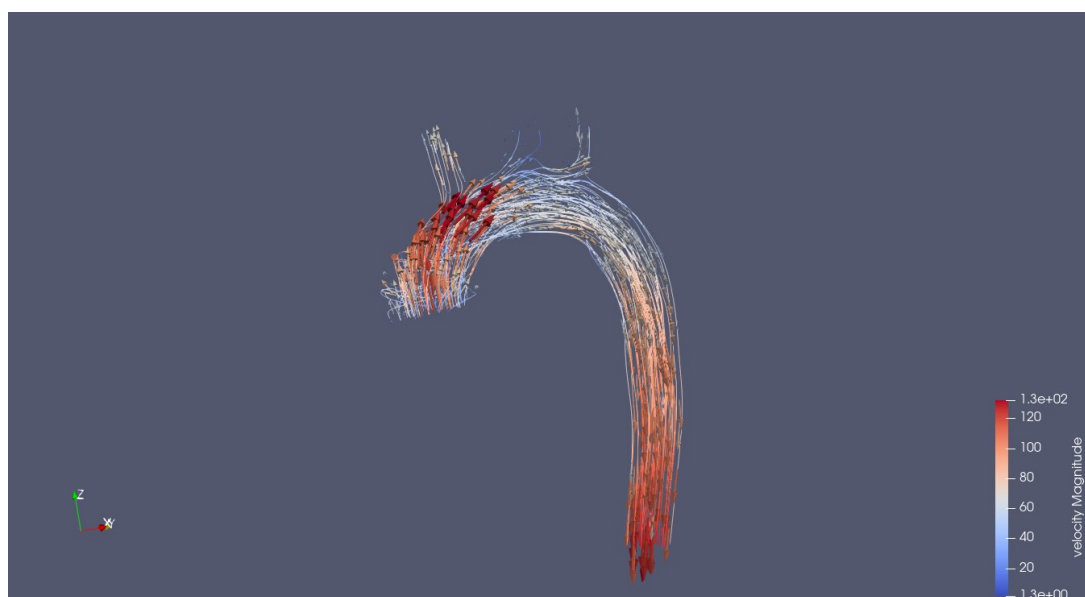


Figure 124: Velocity vector field and streamlines at the peak of systolic phase (SimVascular)

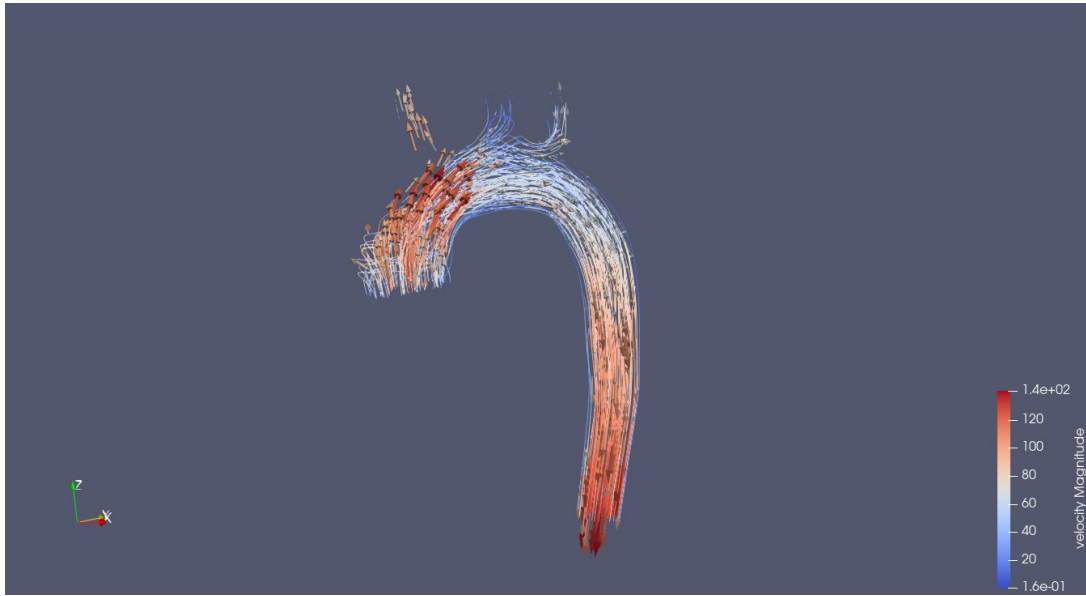


Figure 125: Velocity vector field and streamlines at the peak of systolic phase (Crimson)

End of the systolic phase. At timestep 918, the parabolic velocity profile remains consistent, but with significantly lower velocity values across the entire cross-sectional area of the inlet (Figure 126, Figure 127). Despite this reduction, the parabolic pattern is preserved. Both programs exhibit similar behavior in this regard.

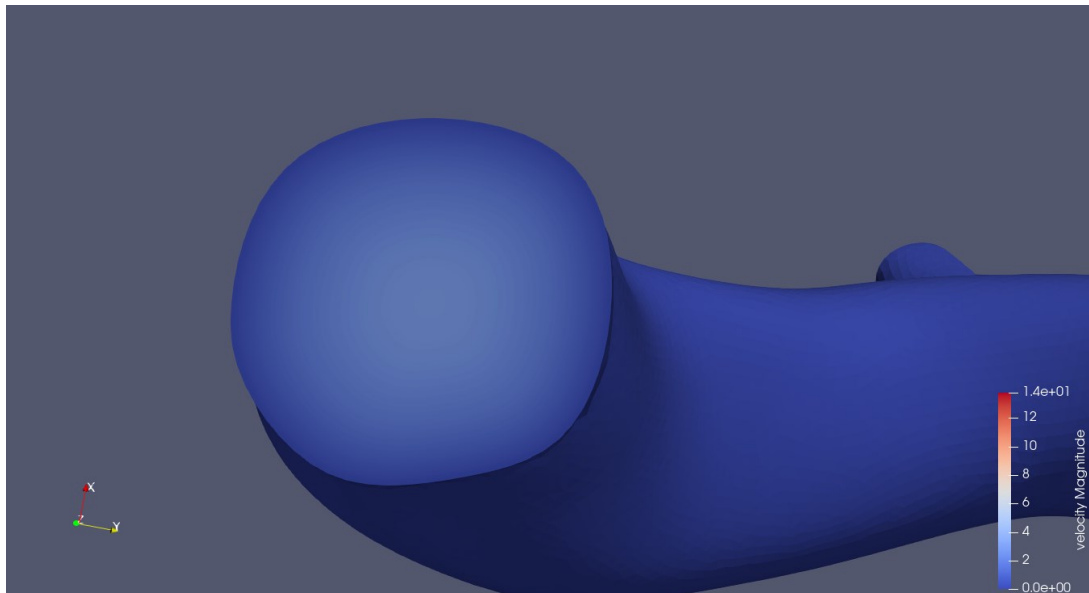


Figure 126: Parabolic velocity profile at the end of the systolic phase (SimVascular)

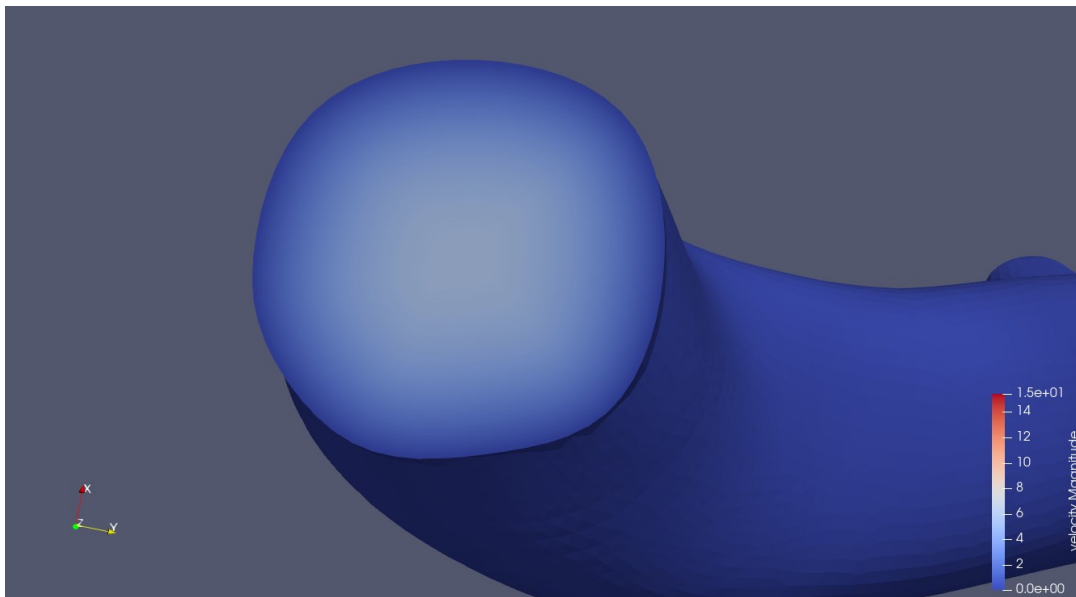


Figure 127: Parabolic velocity profile at the end of the systolic phase (Crimson)

Regarding the velocity vector field and streamlines at this timestep, several key observations can be made (Figure 128, Figure 129). This flow field corresponds to the end of the systolic phase, where backflow becomes most pronounced, particularly around the aortic arch and branches, as evident from the blue regions in the magnitude velocity. These areas of low or negative velocity indicate transient flow separation as systole concludes. Despite the overall flow deceleration, certain regions, especially near the aortic branches, still exhibit high residual velocity, signifying lingering forward flow while backflow develops elsewhere. The swirling and disorganized streamlines suggest localized vorticity, particularly in the curved sections of the aortic arch, where rapid flow deceleration creates secondary flow structures and temporary flow separation. Meanwhile, the descending aorta maintains a more structured flow with smaller changes, marking the transition into the diastolic phase as forward momentum continues to diminish. This pattern is present in both software programs.

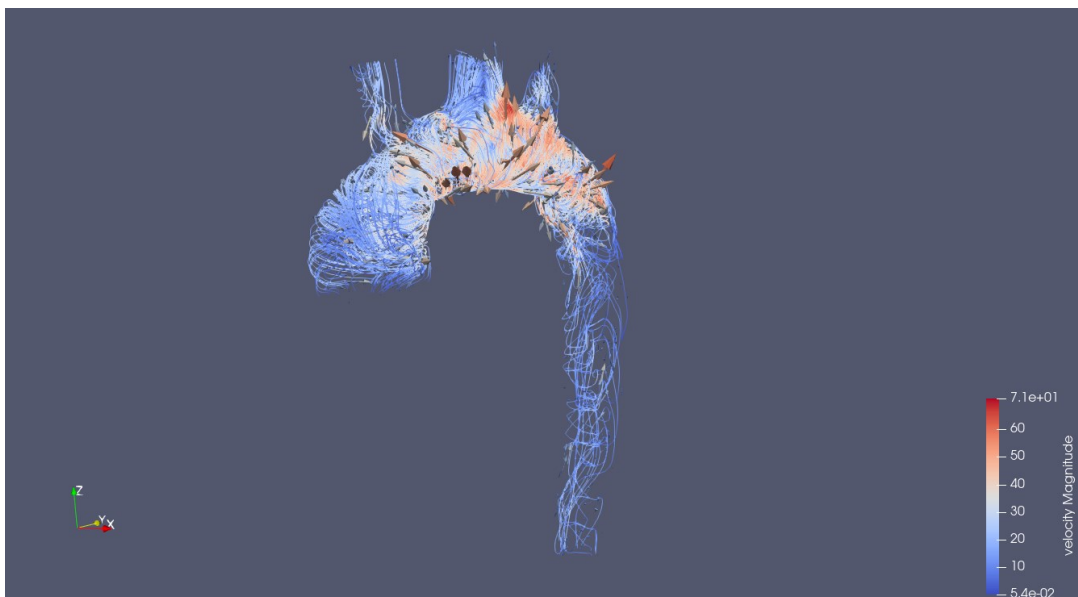


Figure 128: Velocity vector field and streamlines at the end of systolic phase (SimVascular)

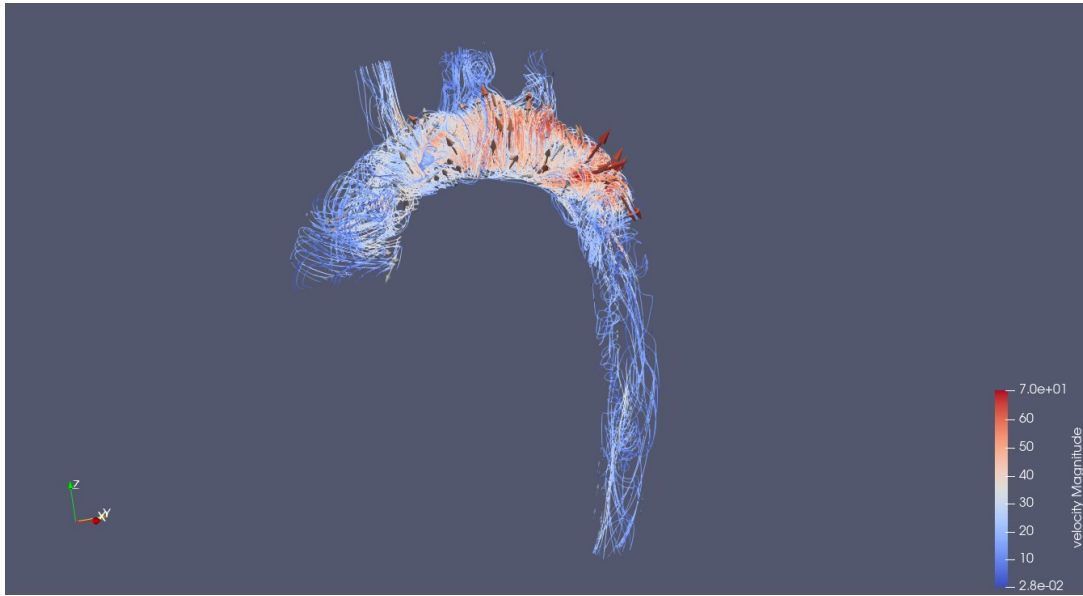


Figure 129: Velocity vector field and streamlines at the end of systolic phase (Crimson)

During the diastolic phase. The parabolic velocity profile remains consistent during the diastolic phase, just as in other phases of the cardiac cycle. In the timestep studied (960), its uniform pattern persists, with velocity values approaching or reaching zero, which is expected due to the absence of the heart's pumping action during this phase (Figure 130, Figure 131).

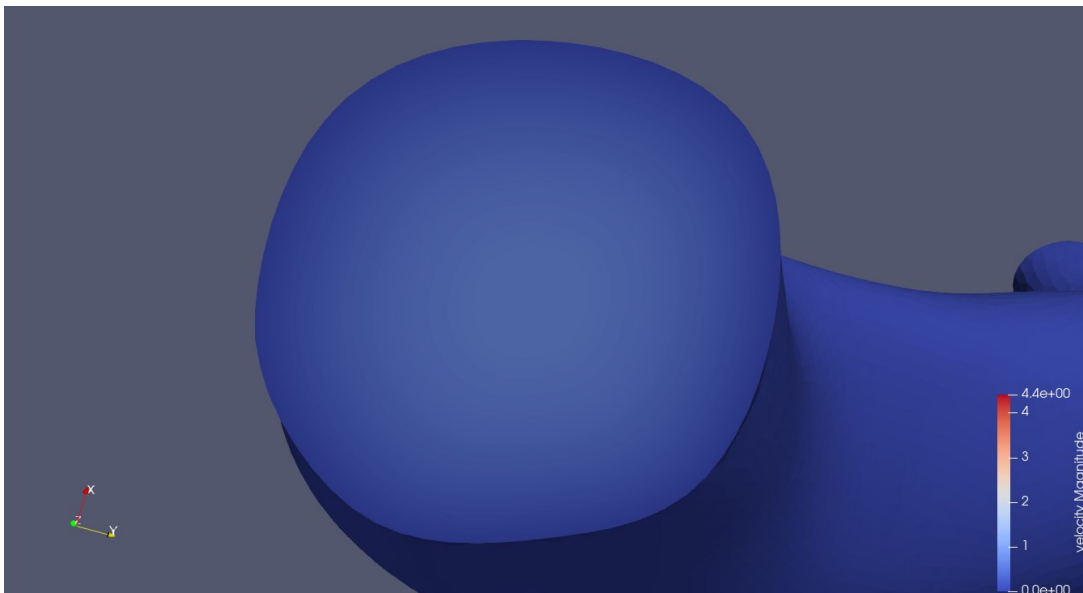


Figure 130: Parabolic velocity profile during diastolic phase (SimVascular)

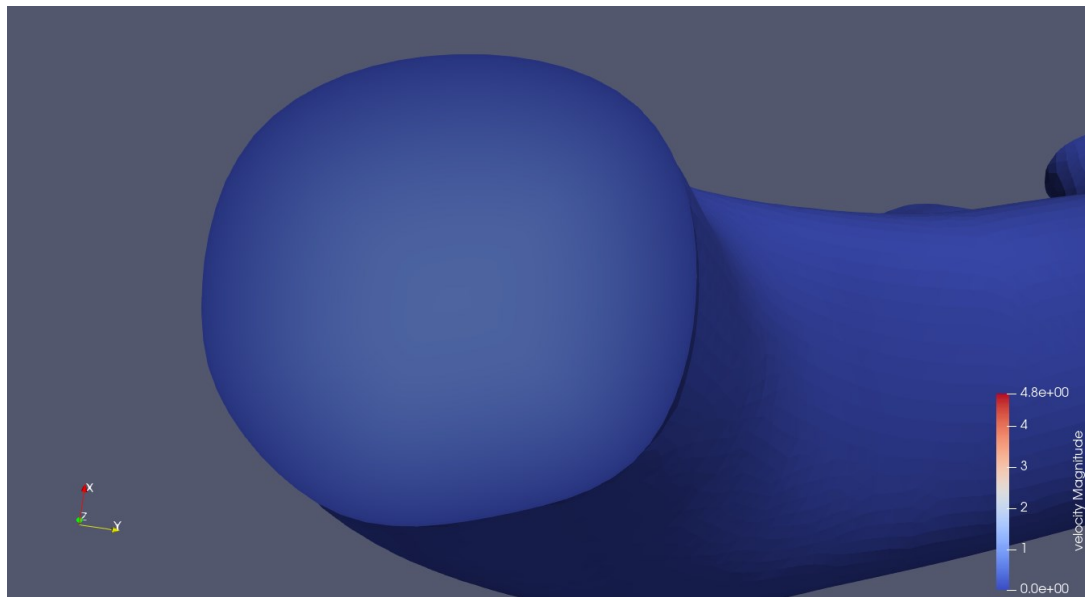


Figure 131: Parabolic velocity profile during diastolic phase (Crimson)

At this timestep, several key observations can be made regarding the velocity vector field and streamlines during the diastolic phase (Figure 132, Figure 133). Compared to the end of the systolic phase, backflow is less pronounced. The maximum velocity magnitude is significantly reduced (around 28 cm/s, down from 71 cm/s at the end of systole). Elevated velocities are still observed in the ascending aorta and near the exit of the aortic arch, likely due to the frequent changes in flow direction in these regions. Crimson calculates slightly higher velocities in the aortic arch compared to other areas. Despite the reduced velocities overall, flow vorticity is still present across the entire flow domain, with the most noticeable regions being the aortic arch and ascending aorta. The streamlines indicate a more disorganized flow pattern than in systolic phase, primarily due to the absence of a driving force, which reflects the heart's relaxation during the diastolic phase.

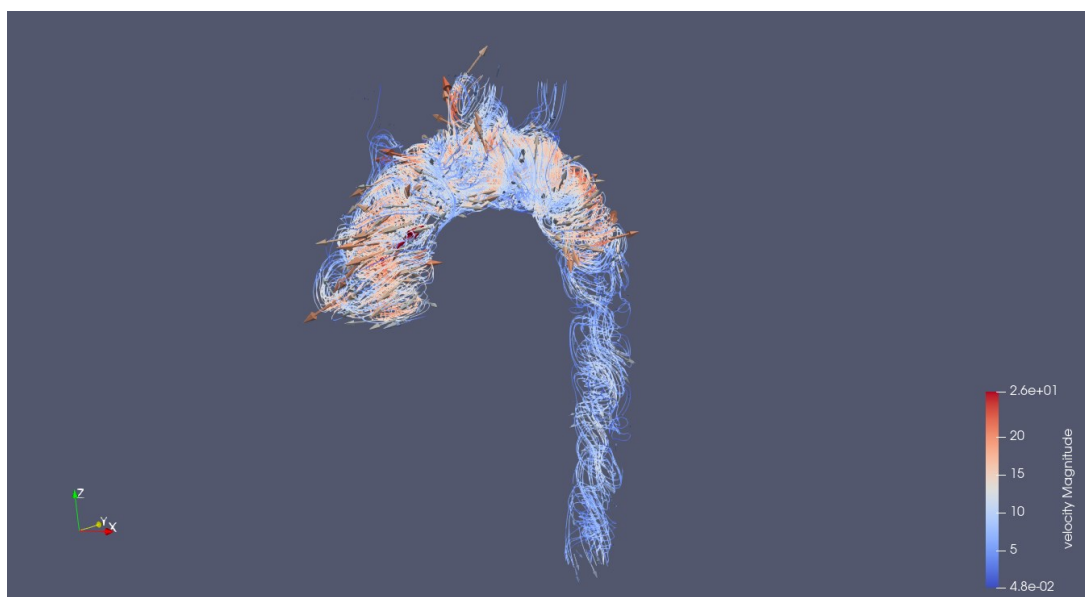


Figure 132: Velocity vector field and streamlines during the diastolic phase (SimVascular)

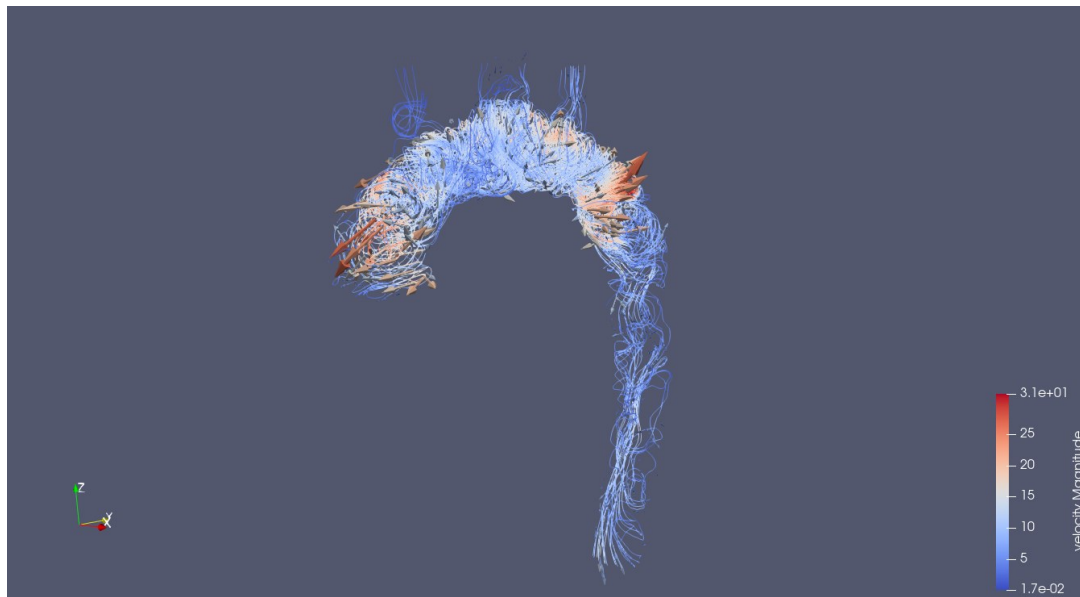


Figure 133: Velocity vector field and streamlines during the diastolic phase (Crimson)

To summarize the velocity vector field and velocity profile analysis, key characteristics of both the patient-specific and parabolic velocity profiles should be highlighted. Regarding the velocity profile, the parabolic profile maintains a consistent, uniform shape throughout the entire cardiac cycle, with the only variation between timesteps being the velocity magnitude. In contrast, the patient-specific profile exhibits unique patterns for each timestep, with some characteristics persisting across the entire cycle while others change dynamically at different phases. Additionally, the patient-specific profile features significant backflow and regions with large velocity differences. However, these variations are balanced across the flow domain, ultimately resulting in the same overall flow rate as the parabolic profile.

The velocity vector field and streamlines also exhibit notable differences between the two profiles. During most of the systolic phase, both profiles show similar flow behaviors and streamline patterns across the flow domain. However, at the end of systole and throughout diastole, distinctions between them become more pronounced. In the patient-specific profile, the highest velocity values at the end of systole are concentrated in the ascending aorta, indicating increased vorticity in that region. Conversely, in the parabolic profile, the highest velocities are found where the aortic arch transitions into the descending aorta.

During diastole, the patient-specific profile displays increased flow vorticity throughout the entire flow domain, with generally lower velocity magnitudes. Some localized velocity increases are observed in the ascending aorta and at the beginning of the aortic arch, where vortical structures are most prominent. In contrast, the parabolic profile exhibits higher velocity values in both the ascending aorta and aortic arch, with magnitudes greater than those in the patient-specific profile. Additionally, in the parabolic profile, velocity increases are observed as the flow exits the aortic arch and enters the descending aorta.

These differences possibly arise due to the fundamental nature of the two profiles. The parabolic profile, being a mathematically idealized inlet condition, leads to a more structured and symmetrical flow distribution, resulting in higher velocities in expected regions, such as where flow accelerates into the descending aorta. The patient-specific profile, on the other hand, reflects real physiological conditions, including flow patterns influenced by vessel

geometry, pulsatility, and secondary flow effects. As a result, it generates localized velocity variations, particularly in areas where flow separation and recirculation occur. These complex interactions lead to a more dispersed velocity distribution during diastole, rather than the concentrated high-velocity regions seen in the parabolic profile.

3.2.3 Wall Shear Stress (Parabolic)

In the parabolic profile, the wall shear stress calculated will be discussed in this section. The timepoints used will be the same, i.e.: timepoint 8.81 s at the start of the systolic phase, timepoint 8.98 s at the peak of the systolic phase, timepoint 9.81 s at the end of the systolic phase and, timepoint 9.6 s during the diastolic phase.

Start of the systolic phase. At timepoint 8.81 s (timestep 881) the wall shear stress distribution obtained by the two programs can be seen in Figure 134 and Figure 135. At the start of the systolic phase, the wall shear stress (WSS) distribution varies significantly across the aortic wall. Elevated WSS values are primarily concentrated in the ascending aorta and along the inner curvature of the aortic arch, where the initial systolic pulse induces strong forward flow, creating high shear forces due to steep velocity gradients. Moderate WSS levels appear near the proximal branches of the aortic arch, indicating early interactions between the flow and bifurcations. Conversely, lower WSS values (blue regions) dominate much of the descending aorta and the outer curvature of the arch, where flow velocity remains relatively low. This pattern is characteristic of early systole before peak acceleration occurs. The distribution suggests that shear forces are still developing along the aortic length but are already pronounced in high-velocity regions. Comparing the parabolic and patient-specific profiles, the former exhibits slightly higher WSS in the region where the flow exits the aortic arch into the descending aorta, whereas the patient-specific profile maintains relatively lower WSS in this area.

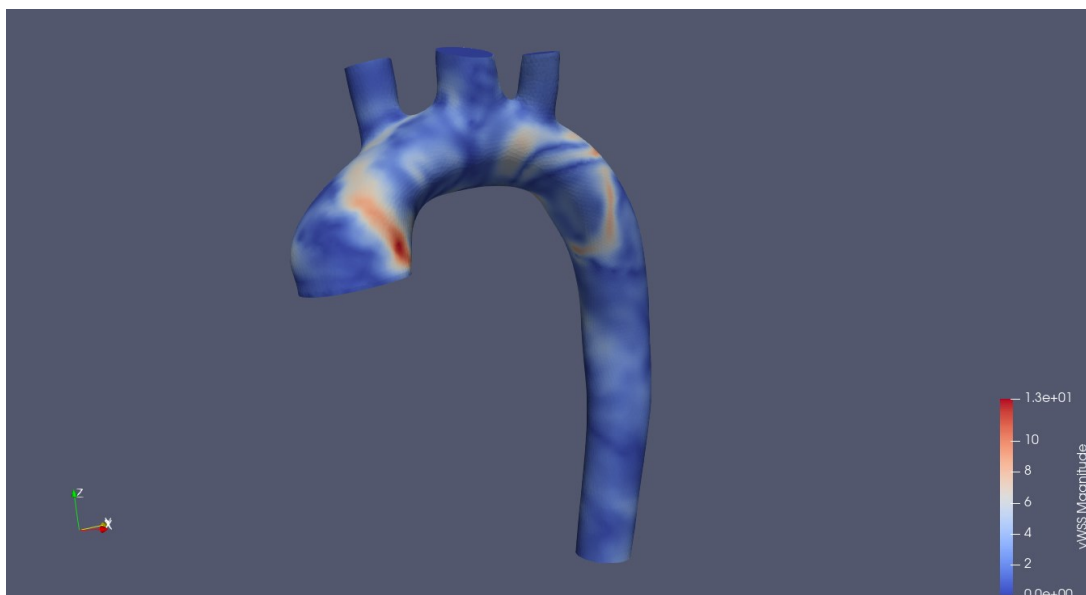


Figure 134: Wall shear stress of the aortic wall at the start of systolic phase (Parabolic/SimVascular)

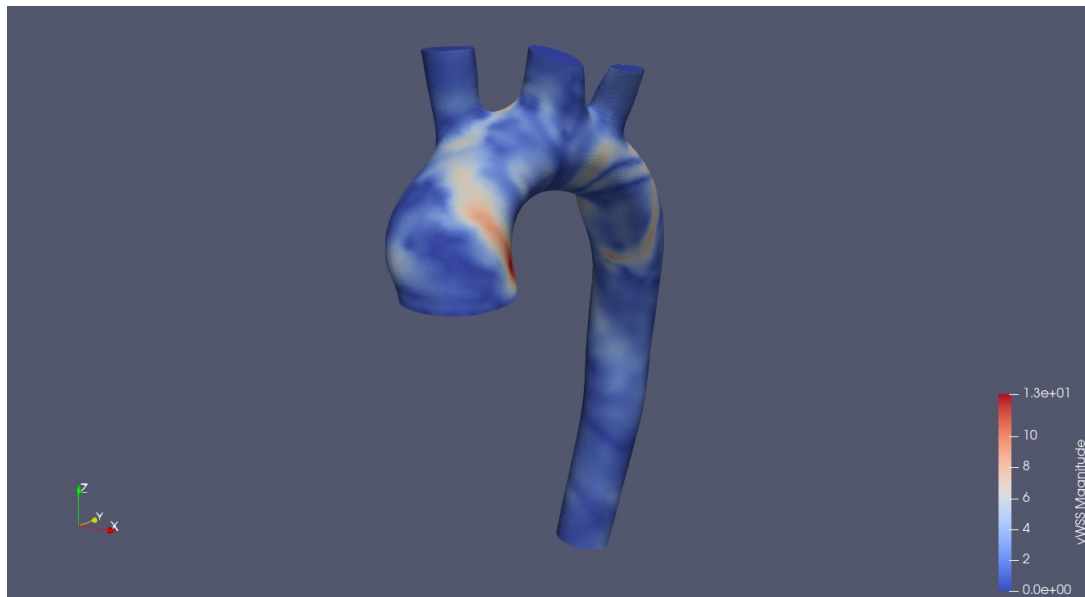


Figure 135: Wall shear stress of the aortic wall at the start of the systolic phase (Parabolic/Crimson)

Peak of the systolic phase. At timepoint 898, corresponding to the peak systolic phase, the wall shear stress distribution for the parabolic profile is illustrated in Figure 136 and Figure 137. At the peak of the systolic phase, the wall shear stress (WSS) distribution shows significantly elevated values in specific regions of the aortic wall, particularly in the ascending aorta. The red zones indicate areas of high WSS, which is expected due to the strong forward flow and steep velocity gradients at peak systole. The ascending aorta, receiving the direct ejection of blood from the left ventricle, experiences the highest shear forces. Moderate WSS values are observed along the descending aorta, with slightly elevated shear stress along the outer wall, where flow accelerates due to vessel curvature. The outer curvature of the aortic arch displays a mix of high and lower WSS levels, with higher values primarily occurring between the branch vessels, where flow separation leads to steep velocity gradients.

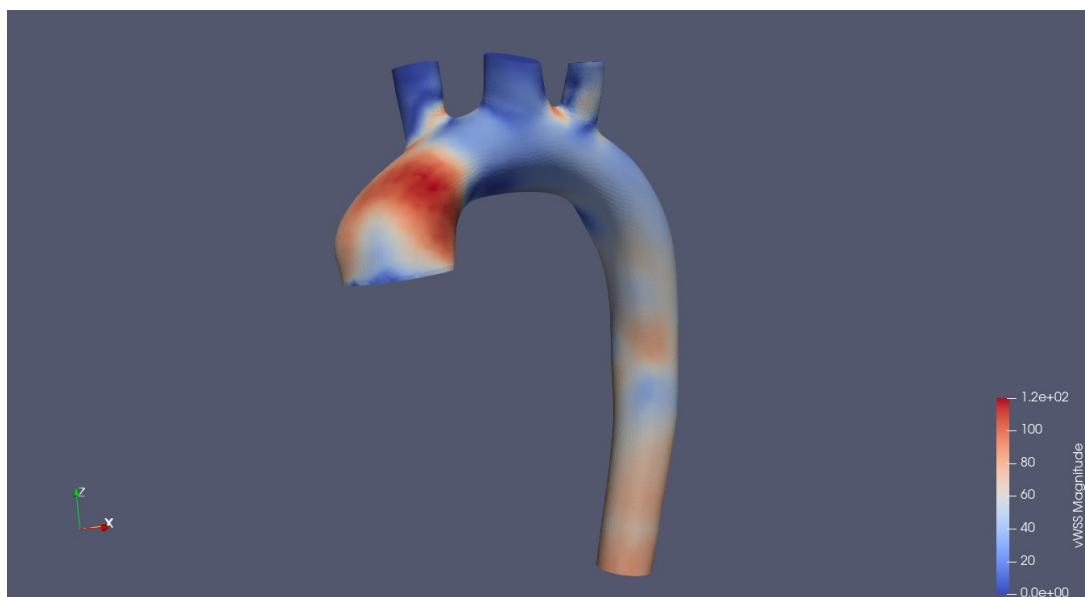


Figure 136: Wall shear stress of the aortic wall at the peak of the systolic phase (Parabolic/SimVascular)

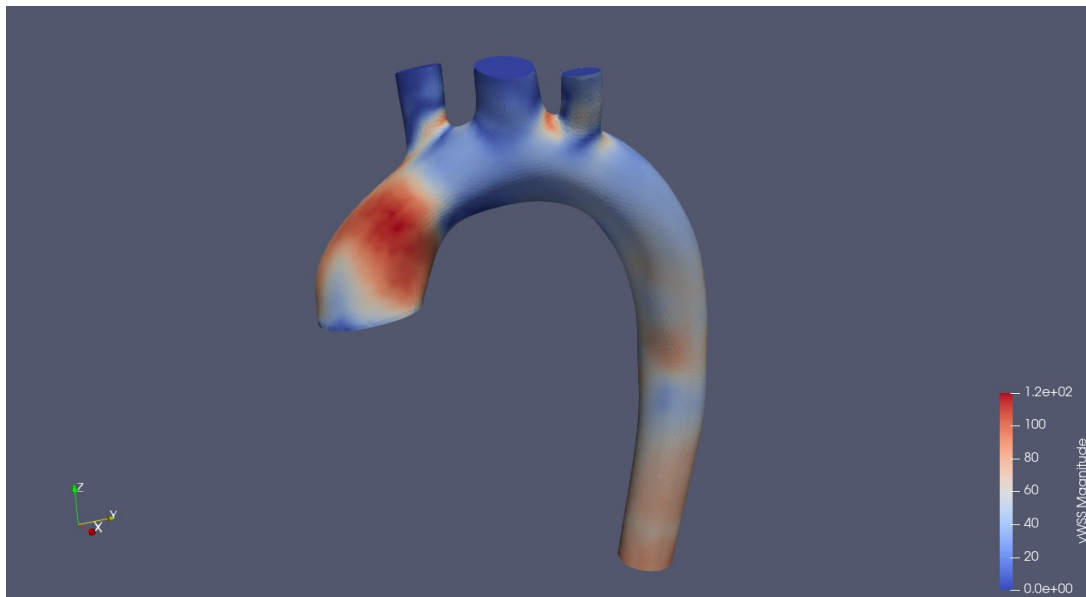


Figure 137: Wall shear stress of the aortic wall at the peak of the systolic phase (Parabolic/Crimson)

Lower WSS values are predominant in certain sections of the descending aorta and the lateral walls of the arch, likely corresponding to areas with more uniform flow distribution and minor recirculatory effects. An increase of WSS is observed in the lower part of the descending aorta, this suggests that there is an increase in velocity in this region, aligning with the velocity values seen in the velocity vector field. The WSS distribution from the patient-specific velocity profile follows a similar pattern. However, the highest WSS values are concentrated at the very beginning of the ascending aorta, suggesting that the peak velocity for the patient-specific profile occurs in this region. Overall, both simulations from SimVascular and CRIMSON yield nearly identical WSS results.

End of the systolic phase. At timepoint 9.18 s corresponding to the end of the systolic phase, the wall shear stress distribution for the parabolic profile is illustrated in Figure 138 and Figure 139. At the end of the systolic phase, the wall shear stress (WSS) distribution shows a noticeable decrease compared to the peak systolic phase. High WSS regions (red areas) are primarily concentrated near branch points of the aortic arch, particularly around the left common carotid and left subclavian arteries. This is likely due to their close anatomical proximity, where flow separation occurs, resulting in persistent shear forces as systole concludes. In contrast, the ascending and descending aorta exhibit predominantly lower WSS values, indicating a decline in flow velocity and shear forces as the forward momentum of blood decreases.

The overall distribution at this phase reflects the transition from high-energy flow to the late stages of systole, where recirculatory effects and flow deceleration become more prominent. Both the patient-specific and parabolic velocity profiles produce similar WSS trends, with the main differences arising in the ascending aorta and the beginning of the aortic arch. The patient-specific profile tends to predict higher WSS values in these regions, suggesting slight variations in how each profile captures velocity distribution and flow dynamics.

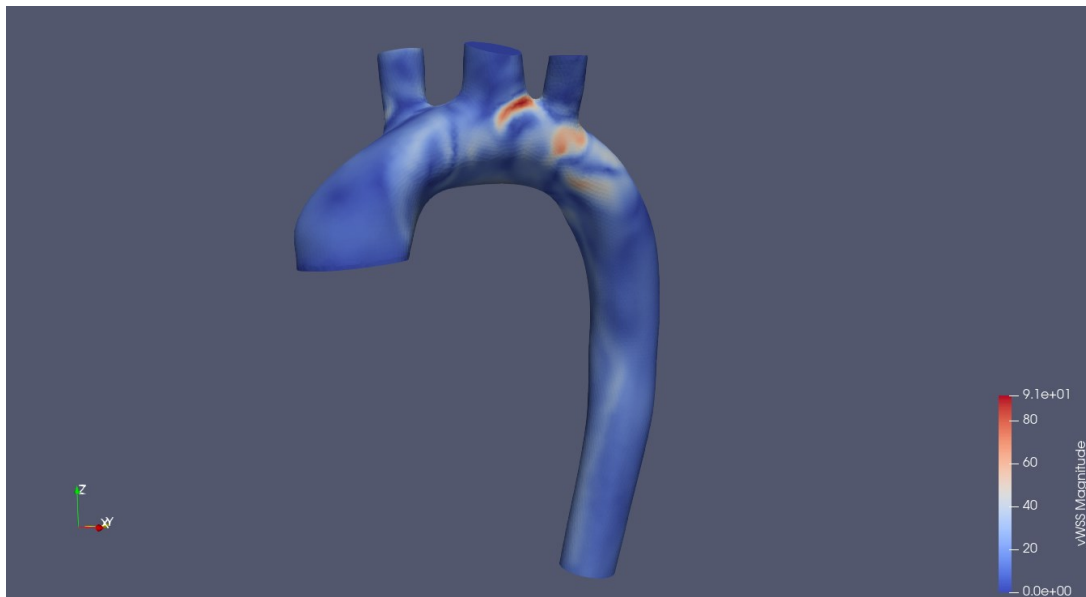


Figure 138: Wall shear stress of the aortic wall at the end of systolic phase (Parabolic/SimVascular)

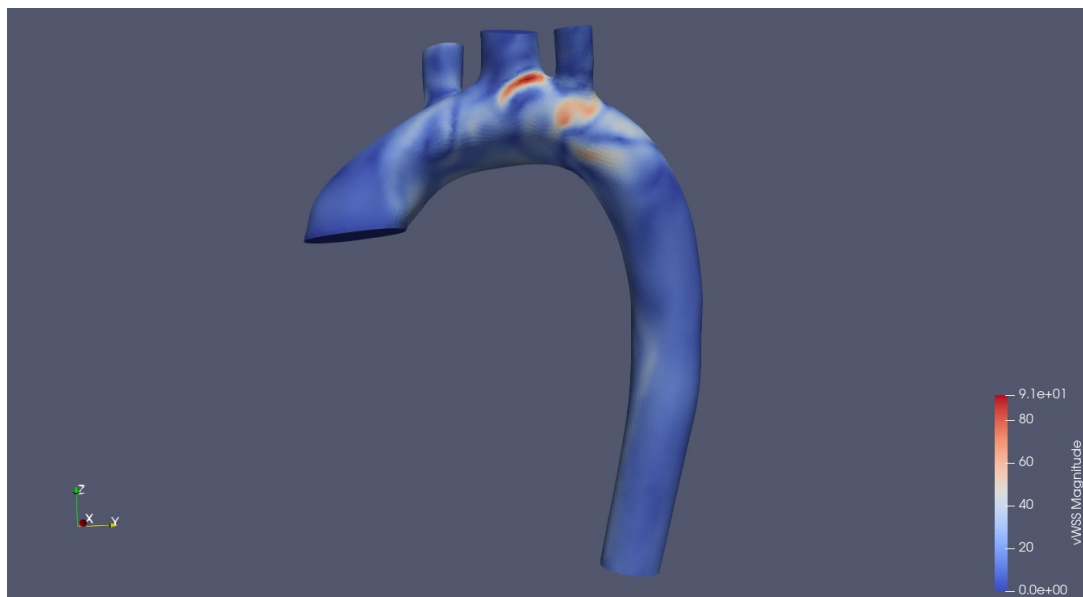


Figure 139: Wall shear stress of the aortic wall at the end of systolic phase (Parabolic/Crimson)

During the diastolic phase. At the final timepoint (9.6 s), corresponding to the diastolic phase, the wall shear stress distribution for the parabolic profile is depicted in Figure 140 and Figure 141. During diastole, wall shear stress (WSS) is significantly lower than in systole due to reduced flow velocity and shear forces. Most of the aortic wall experiences low WSS, with localized increases near the aortic arch and branch points, driven by velocity gradients and flow separation. However, the overall WSS range remains much smaller than in systole, reflecting the lower velocities in this phase. Comparing the patient-specific and parabolic profiles reveals distinct differences in WSS distribution. The patient-specific profile shows higher WSS in localized regions, particularly in the ascending aorta and proximal arch, where velocity gradients are most concentrated.

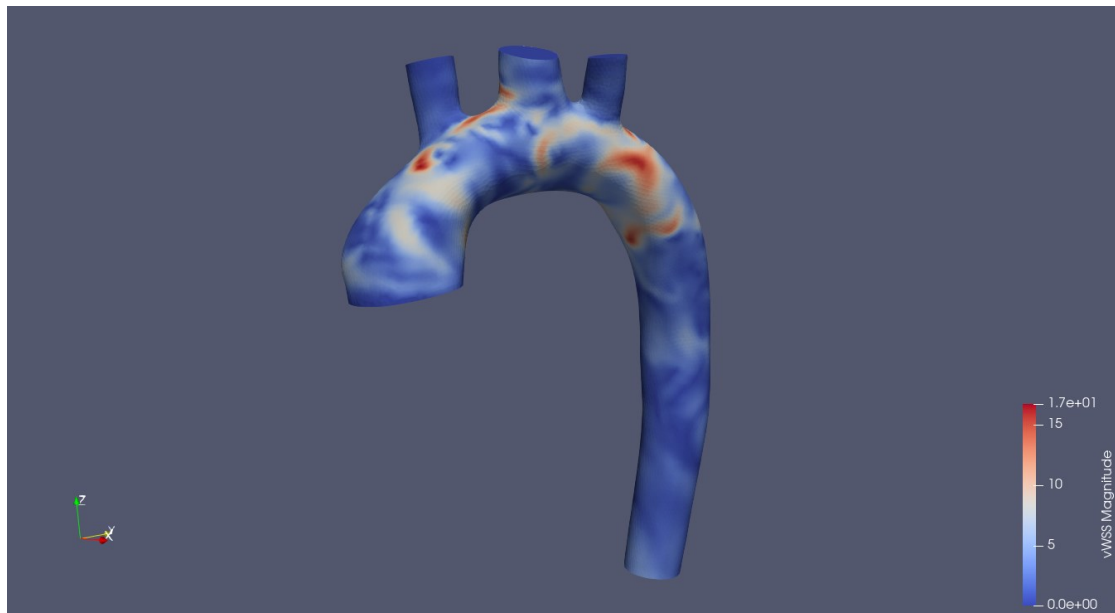


Figure 140: Wall shear stress of the aortic wall during diastolic phase (Parabolic/SimVascular)

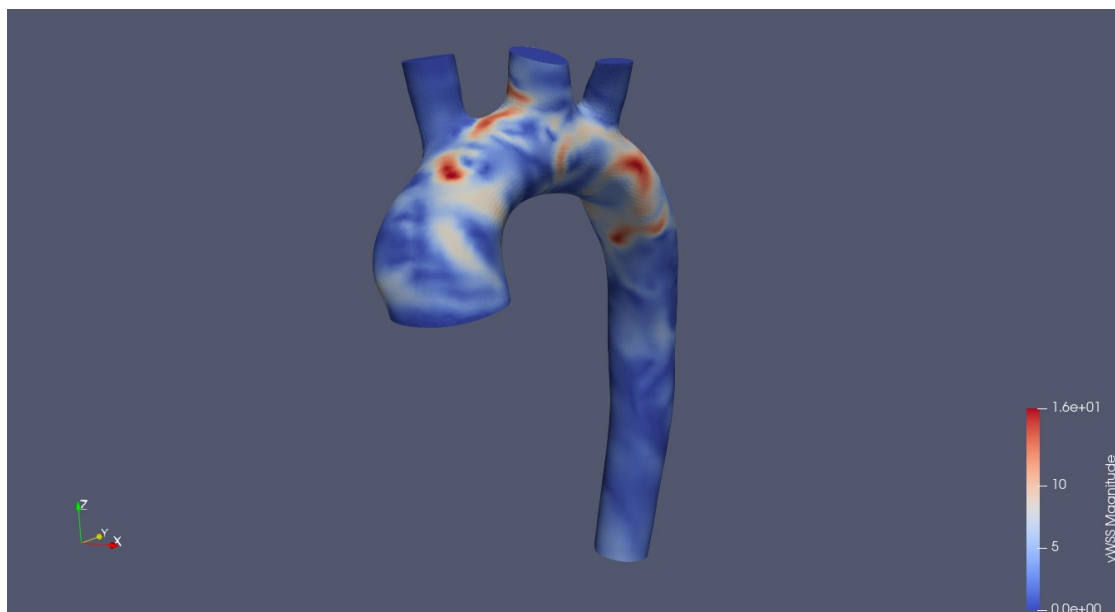


Figure 141: Wall shear stress of the aortic wall during diastolic phase (Parabolic/Crimson)

In contrast, the parabolic profile produces a more uniform WSS distribution with lower magnitudes across the arch and descending aorta, with peak values occurring in the aortic arch. These differences indicate that the parabolic profile induces stronger secondary flows and recirculatory effects in the arch, while the patient-specific profile results in higher WSS in the ascending aorta due to elevated velocities and less pronounced secondary flows elsewhere.

Time-averaged wall shear stress. Like the patient-specific velocity profile analysis, the time-averaged wall shear stress will also be presented to provide a comprehensive overview of WSS behavior throughout the entire cardiac cycle. These are shown in Figure 142 and Figure 143.

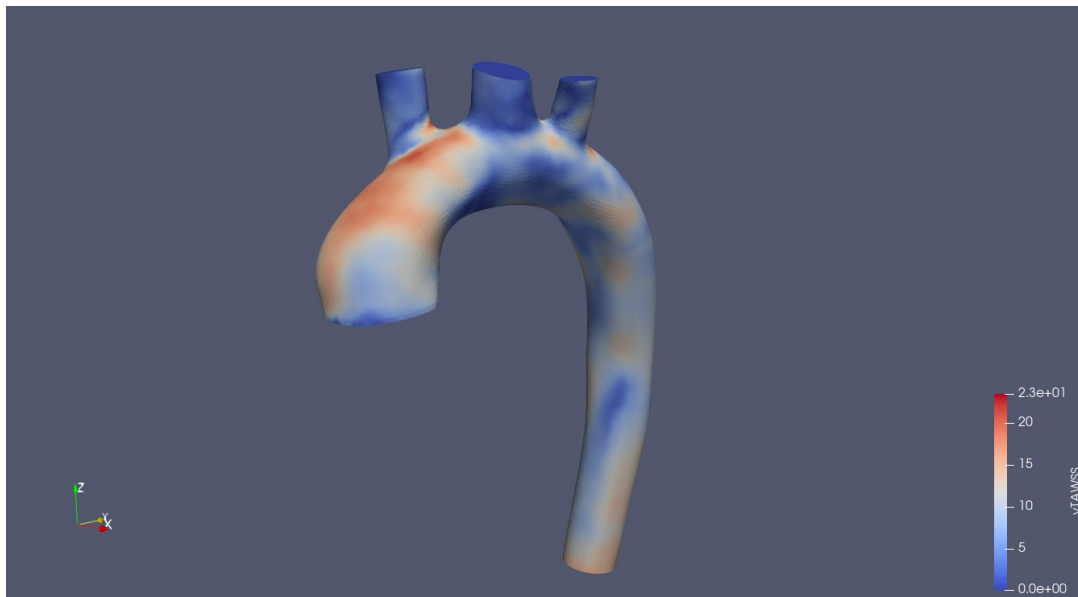


Figure 142: Time averaged wall shear stress for one cardiac cycle (Parabolic/SimVascular)

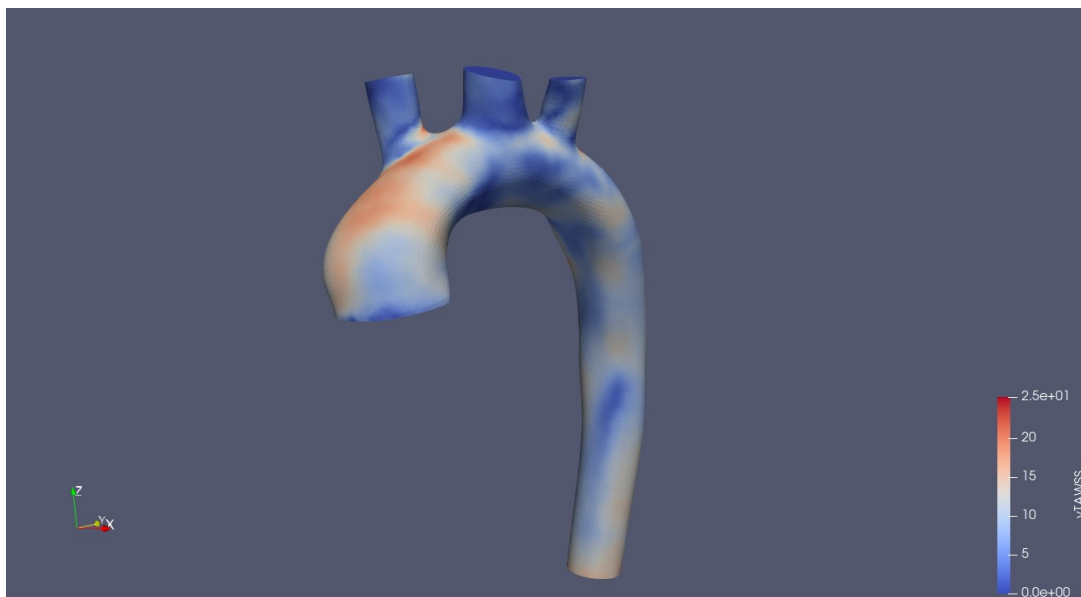


Figure 143: Time averaged wall shear stress for one cardiac cycle (Parabolic/Crimson)

The time-averaged wall shear stress (TAWSS) distribution over a full cardiac cycle provides critical insight into the shear forces acting on the aortic wall. The highest TAWSS values are primarily concentrated in the aortic arch and near the branch points of the supra-aortic arteries, where flow disturbances and secondary flow structures intensify shear stress.

For the parabolic velocity profile, peak TAWSS values appear at the transition from the ascending aorta to the aortic arch, especially along the outer curvature. This results from the parabolic velocity distribution, where the highest velocities are concentrated at the center of the vessel, leading to increased shear forces as the flow interacts with the aortic curvature. The TAWSS results from CRIMSON and SimVascular are nearly identical, with CRIMSON producing slightly higher values.

In contrast, the patient-specific velocity profile (previously analyzed) also shows peak TAWSS in the ascending aorta, but in a more localized and pronounced manner. Lower TAWSS values extend further along the descending aorta, likely due to differences in velocity gradients and the reduced formation of large secondary flow structures. The absence of abrupt geometric changes downstream further contributes to a smoother shear stress distribution. Both profiles exhibit a TAWSS increase in the lower part of the descending aorta. Unlike the parabolic profile, the patient-specific inflow lacks a uniform velocity distribution, introducing transient accelerations and decelerations that shape the overall TAWSS pattern. The higher TAWSS values in the patient-specific profile suggest elevated velocity near the aortic wall, whereas the parabolic profile maintains higher velocities further from the walls.

Overall, TAWSS provides a more stable representation of shear stress compared to instantaneous WSS during systole and diastole, as it averages out transient fluctuations and highlights regions of sustained hemodynamic forces. The differences between parabolic and patient-specific profiles emphasize the importance of realistic inflow conditions, as they significantly impact shear distribution of stress and may influence vascular adaptation and disease progression.

3.2.4 Velocity comparison between the CFD data and patient-MRI data (Parabolic Velocity Profile)

As with the patient-specific velocity profile, velocity graph comparisons are also necessary for the parabolic profile to complete the study. This allows for a better understanding of how the parabolic profile influences velocity throughout the flow domain in both programs and how closely it aligns with patient data. The process of generating comparison data and selecting slices follows the same methodology as before.

Upper descending aorta. The axial slice representing this region corresponds to slice 71 in the CFD data and slice 50 in the MRI data, located in the upper descending aorta (Figure 85). Graphs of the three velocity components are shown for comparison. In the graph of the u-component (Figure 144), the patient's flow velocity fluctuates during the systolic phase and stabilizes near zero during diastole. Both simulations exhibit minimal variations in the u-component, with some oscillatory behavior after the systolic phase ends (around 0.4 s), and they struggle to capture the velocity increase during systole while showing changes in velocity during diastole. SimVascular results display slightly greater deviations compared to CRIMSON but ultimately converge more closely with the MRI data by the end of the cardiac cycle.

The graph of the v-velocity component (Figure 145), on the other hand, shows that both simulations accurately capture its changes, with only a slight overestimation of the peak velocity during the systolic phase. During diastole, both simulations exhibit very similar behavior, with negligible differences between them. The simulations also yield accurate results for the w-velocity component (Figure 146), which is particularly important as it represents the primary flow direction in this region. The results closely match the patient data, with the peak velocity value close to that of the patient and maintaining a consistent value throughout most of the diastolic phase. However, the simulations predict a slightly higher backflow velocity compared to the patient data.

The velocity magnitude graph (Figure 147) provides an overall view of the flow behavior in this region. Both simulations effectively capture the main physiological trends and closely align with the MRI data. However, they both underestimate the peak velocity during systole, with SimVascular reporting a slightly lower value. Additionally, both exhibit some oscillatory patterns during diastole but ultimately converge to values near the MRI data. Overall, both simulations successfully capture the flow dynamics in this region and provide a reliable representation of the flow.

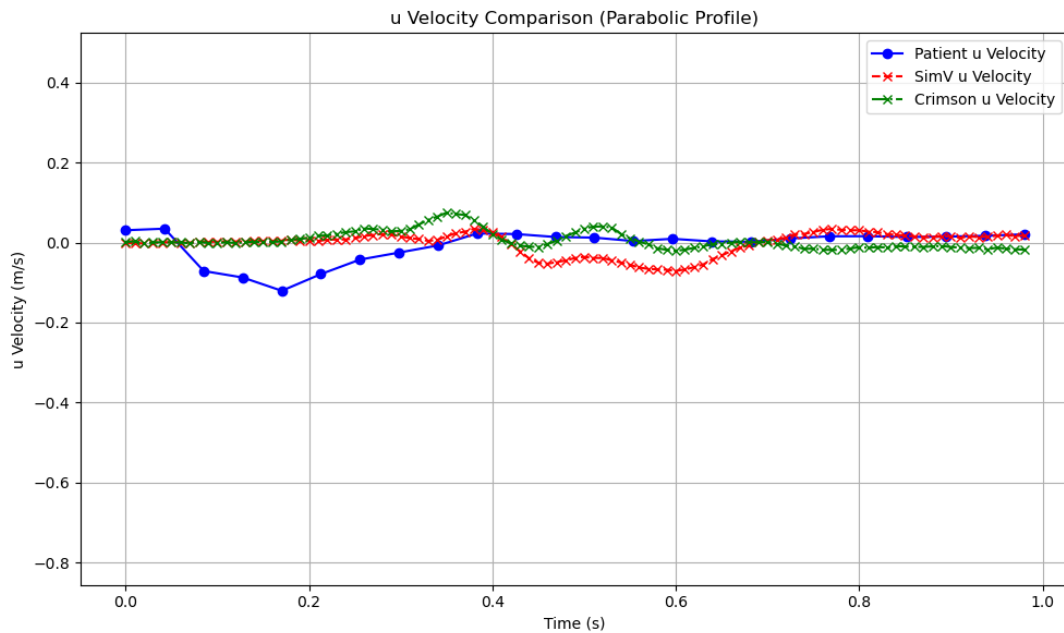


Figure 144: Graph comparing the u-velocity component at the upper descending aorta

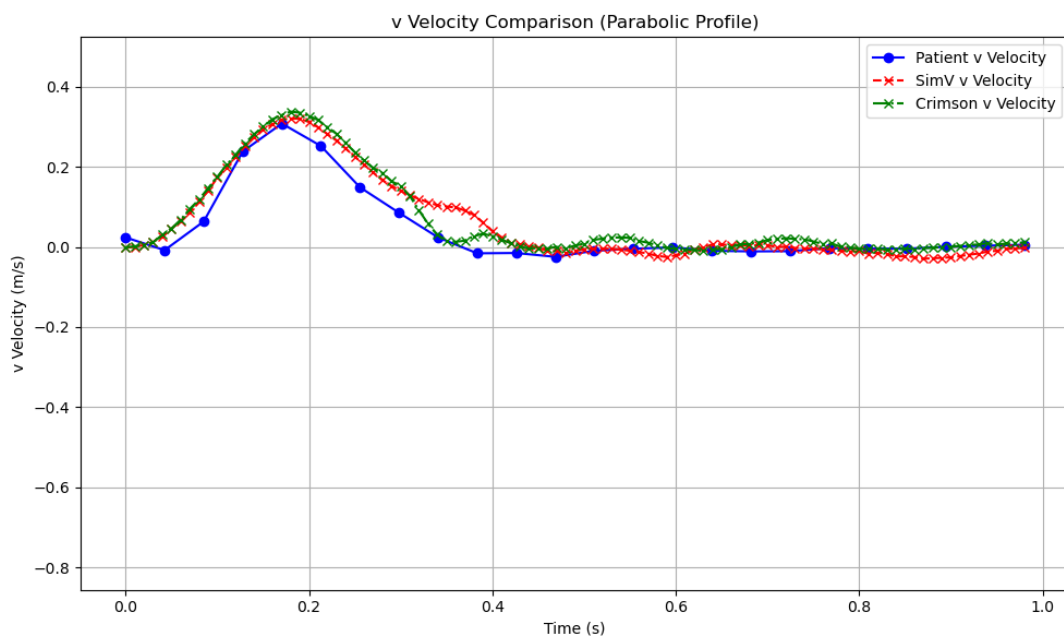


Figure 145: Graph comparing the v-velocity component at the upper descending aorta

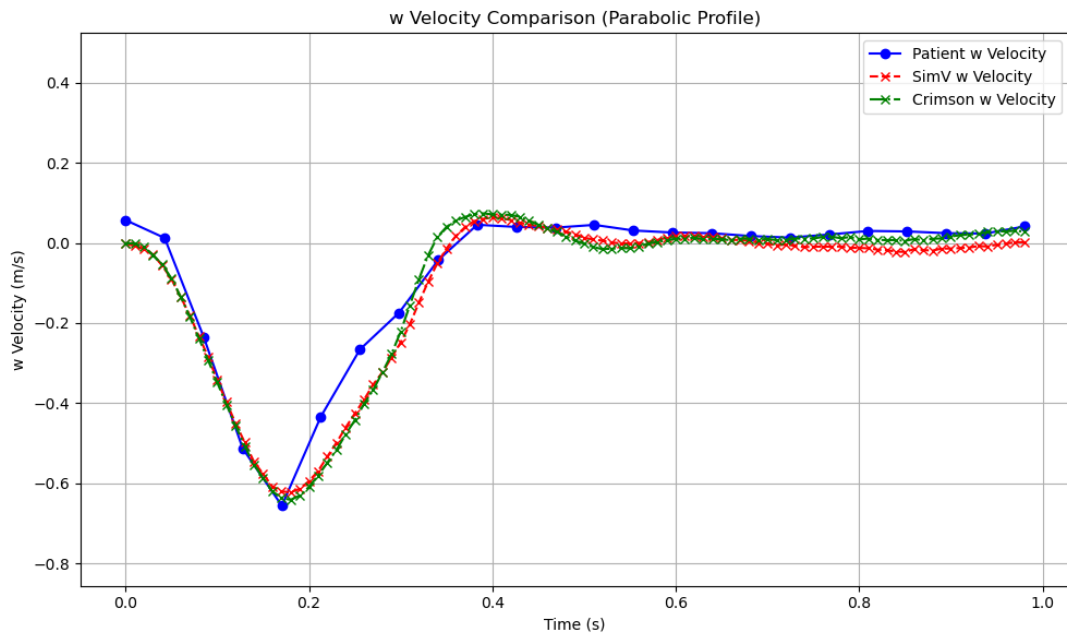


Figure 146: Graph comparing the w-velocity component at the upper descending aorta

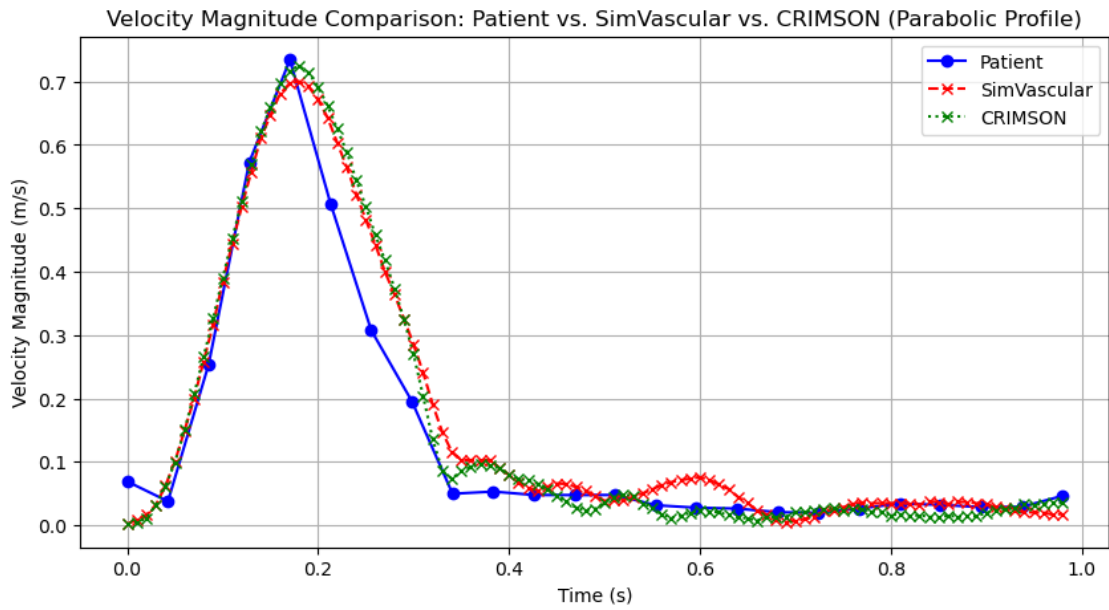


Figure 147: Graph comparing the velocity magnitude at the upper descending aorta

Ascending aorta. The next analyzed region is in the ascending aorta, just before the flow reaches the brachiocephalic artery, the first branch of the aortic arch. Axial slice 48 from the MRI data and axial slice 72 from the CFD data were selected for comparison (Figure 90).

The u-component graph (Figure 148) indicates that both simulations capture the overall physiological trend of this component in the region, but some differences are present. During systole, both simulations exhibit an unexpected velocity change, while in diastole, SimVascular produces results that are closer to the MRI data. However, both simulations ultimately converge to a small value, closer to zero than the MRI data. Additionally, both exhibit an oscillatory pattern during systole, where the peak velocity occurs earlier than in the MRI data, followed by a secondary increase at a lower magnitude, which occurs at the same time as the peak velocity of the MRI data.

The graph of the v-velocity component (Figure 149) shows that the simulations capture the overall flow behavior, though with some differences. The peak velocity occurs earlier than observed in the MRI data, and both simulations exhibit similar deviations from the MRI data during the diastolic phase. However, both simulations eventually converge to a value that is close to the MRI data. In both simulations, the flow characteristics in general are overestimated but eventually converge to relatively close values.

However, the w-velocity component (Figure 150) demonstrates a significantly improved representation of the flow velocity in this region. Both simulations produce nearly identical values during the diastolic phase and accurately capture the velocity behavior in the systolic phase. They slightly overestimate the peak velocity but maintain a very similar velocity gradient during both the acceleration and deceleration phases of systole.

Examining the overall flow velocity pattern from the graph in Figure 151, it can be observed that both simulations capture the systolic phase relatively well, with discrepancies mainly occurring around the peak velocity, where CRIMSON provides a closer match. During the diastolic phase, deviations are more pronounced, with differences between the two simulations, and SimVascular yielding results that align more closely with the MRI data. These discrepancies can be attributed to several factors, including the use of a parabolic velocity profile instead of a patient-specific one, minor anatomical inaccuracies in the model, and most importantly, the absence of fluid-structure interaction (FSI) in the simulations.

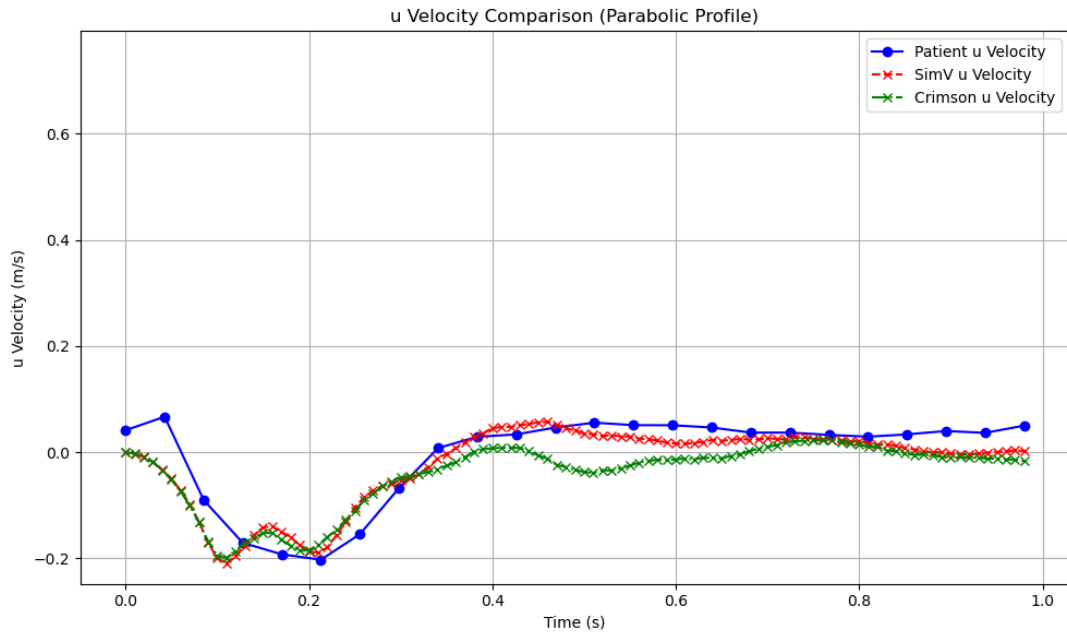


Figure 148: Graph comparing the u-velocity component before entering the aortic arch

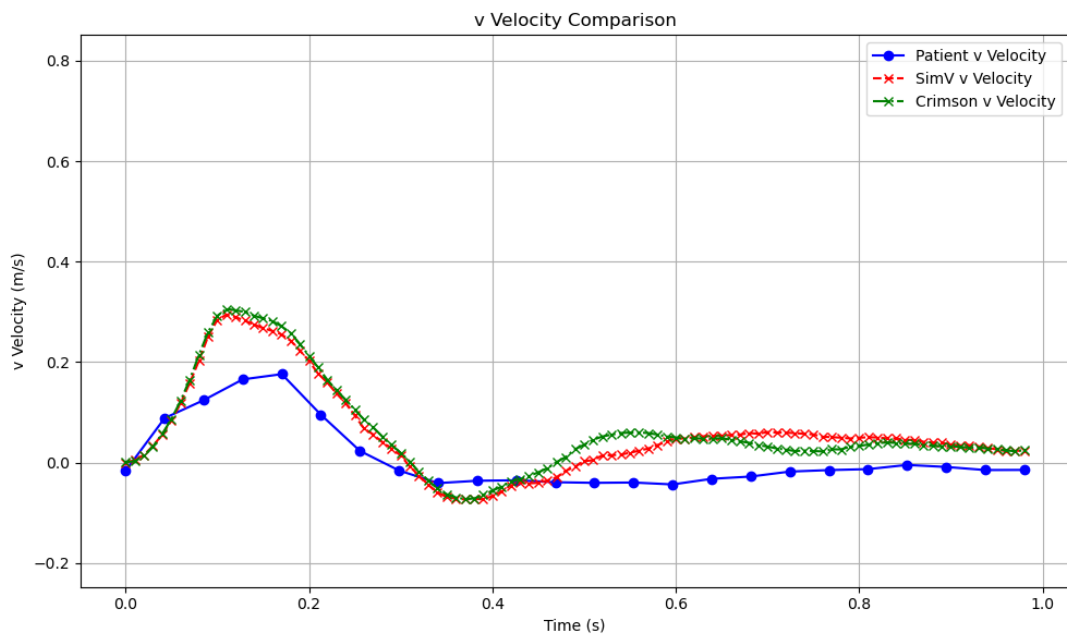


Figure 149: Graph comparing the v-velocity component before the brachiocephalic artery

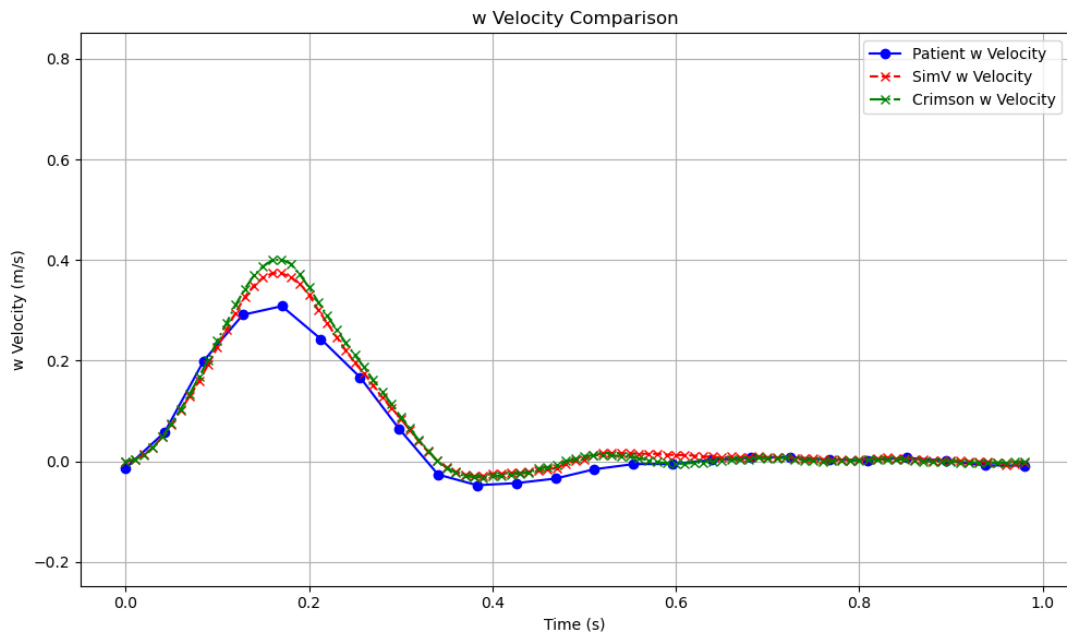


Figure 150: Graph comparing the w-velocity component before the brachiocephalic artery

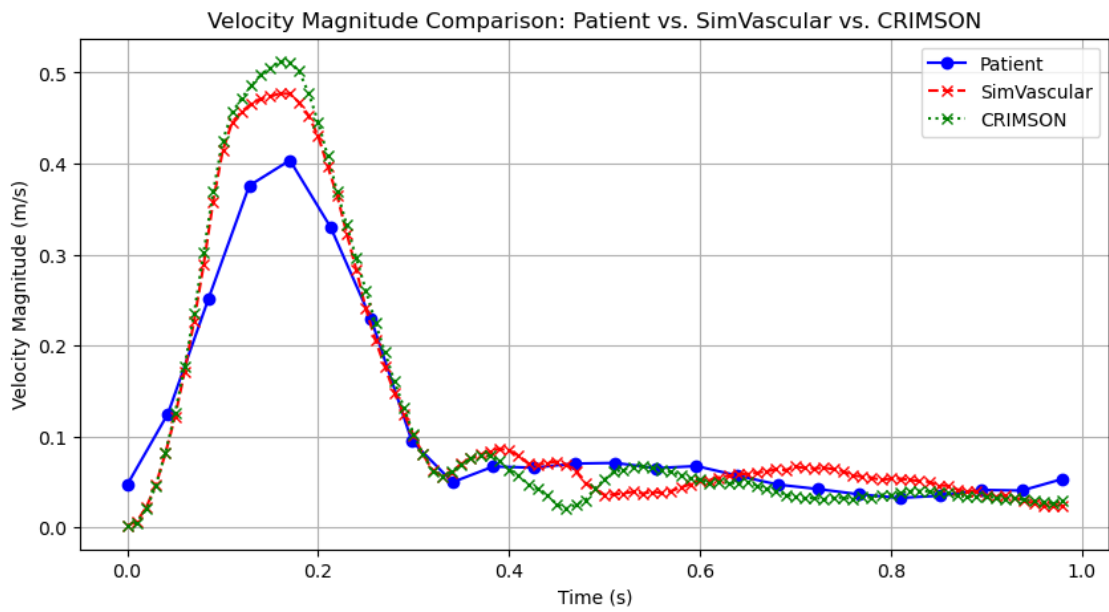


Figure 151: Graph comparing the velocity magnitude before the brachiocephalic artery

Before the LCC branch of the aortic arch. The next region analyzed is the aortic arch, just before its second branch, the left common carotid artery. Coronal slice 78 from the MRI data and coronal slice 39 from the CFD data were selected for examination (Figure 95).

For the u-velocity component (Figure 152), the MRI data consistently show small values throughout the cardiac cycle with no significant variations. However, both simulations overestimate the velocity around 0.2 s, with SimVascular predicting a higher peak and a sharper increase. Both simulations exhibit fluctuations before stabilizing, eventually converging to the same value. Despite the initial sharp increase and overestimation, SimVascular maintains values closer to the MRI data after the early systolic phase.

The graph in Figure 153 clearly shows that both simulations accurately capture the v-component velocity in this region, maintaining consistency throughout the cardiac cycle. The main difference is a slight overestimation of peak velocity by both software programs during the systolic phase. However, both simulations effectively capture the overall flow dynamics and predict key characteristics, such as backflow at the end of the systolic phase.

Similarly, as shown in Figure 154, both simulations effectively capture most aspects of the w-component, closely following its overall pattern. However, they overestimate velocity during the systolic phase and exhibit an unexpected trend where velocity initially decreases before increasing again—a behavior also observed in the previous region. During the diastolic phase, both simulations show minor velocity fluctuations, but these remain small and ultimately converge to the MRI data values. While the simulations tend to overestimate certain flow characteristics and display oscillatory patterns throughout the cardiac cycle, they ultimately align closely with the MRI data.

The graph in Figure 155 compares velocity magnitude over a cardiac cycle between patient MRI data, SimVascular, and CRIMSON simulations. Both simulations capture the general flow trends but show differences in key regions. During the systolic phase (~0.2s), the patient data exhibits a higher peak velocity, with CRIMSON overestimating the peak compared to SimVascular, which remains closer to the MRI data. In the post-systolic phase, the patient data follows a smooth decline, whereas CRIMSON and SimVascular display oscillatory patterns. During diastole (~0.4s – 0.98s), MRI data shows a steady, low velocity with minor fluctuations, a trend that SimVascular follows more closely, whereas CRIMSON exhibits noticeable oscillations before converging.

These discrepancies can be attributed to several factors. Firstly, both simulations use a parabolic velocity profile as an inlet condition instead of a patient-specific flow profile, which can lead to variations in velocity magnitude and distribution. Secondly, minor anatomical inaccuracies in the reconstructed patient model may influence local flow patterns, contributing to differences between the simulations and the MRI data. Lastly, the lack of Fluid-Structure Interaction (FSI) means the simulations assume rigid arterial walls, whereas in reality, arterial compliance affects flow dynamics, potentially explaining the underestimation of peak velocity and the deviations observed during diastole.

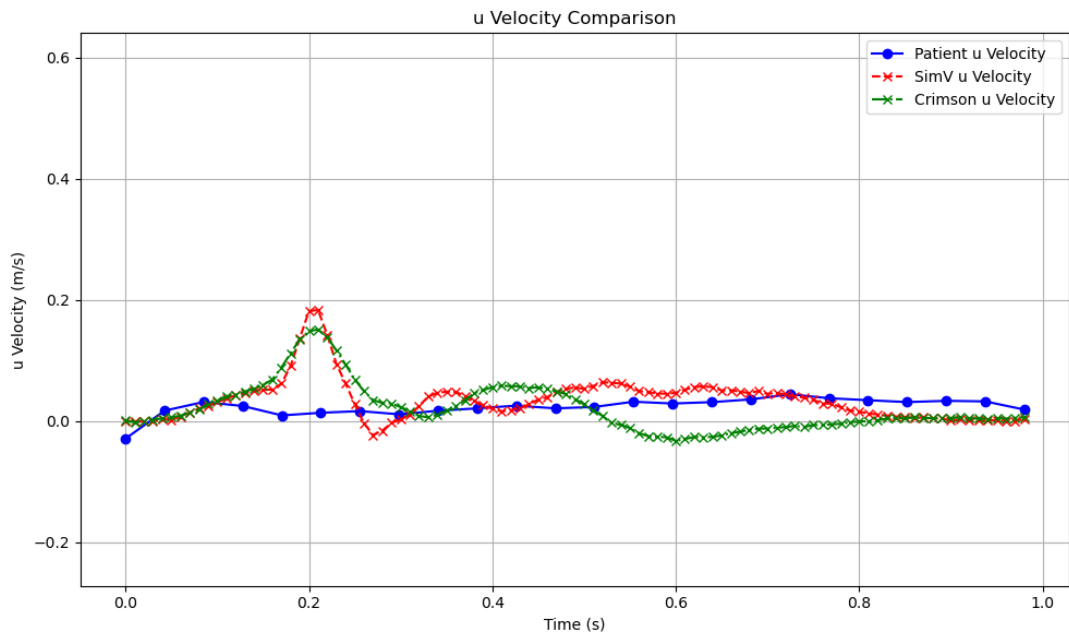


Figure 152: Graph comparing the u-velocity component before the LCC artery

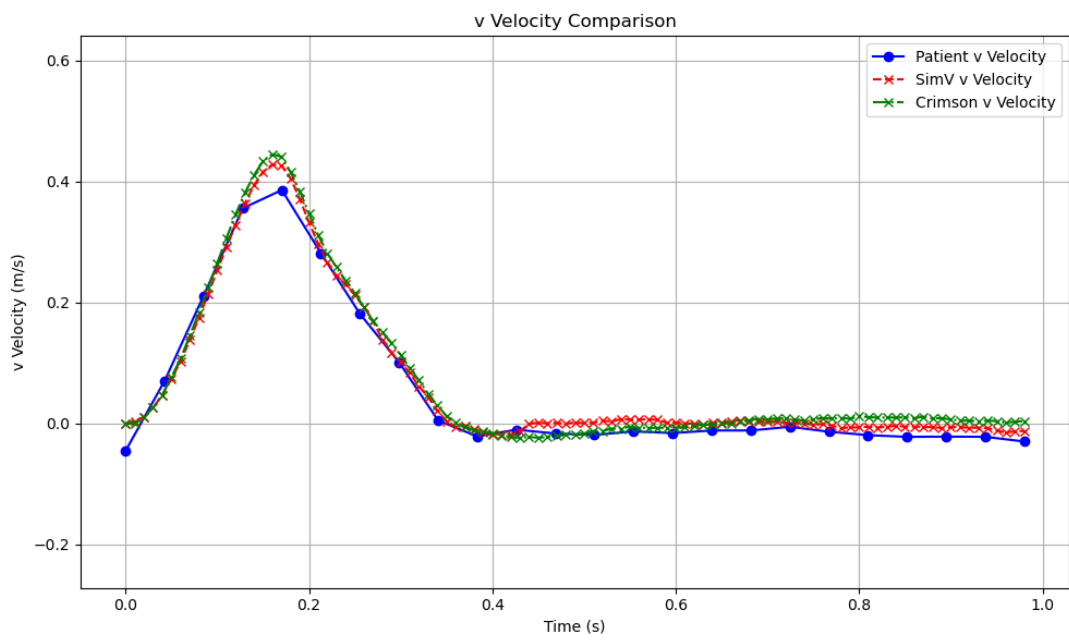


Figure 153: Graph comparing the v-velocity component before the LCC artery

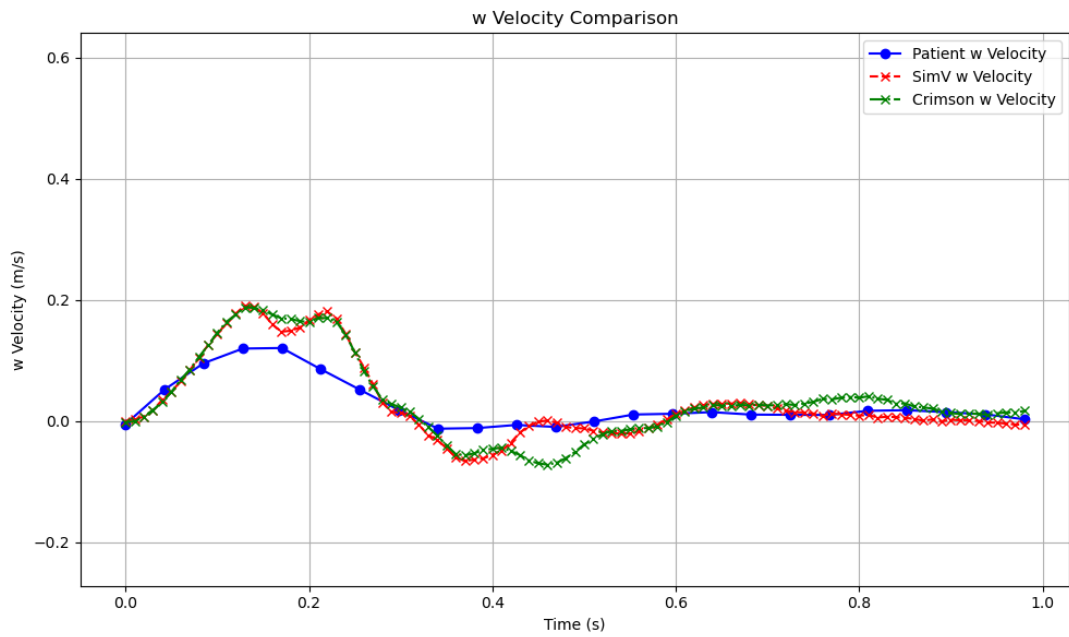


Figure 154: Graph comparing the w-velocity component before the LCC artery

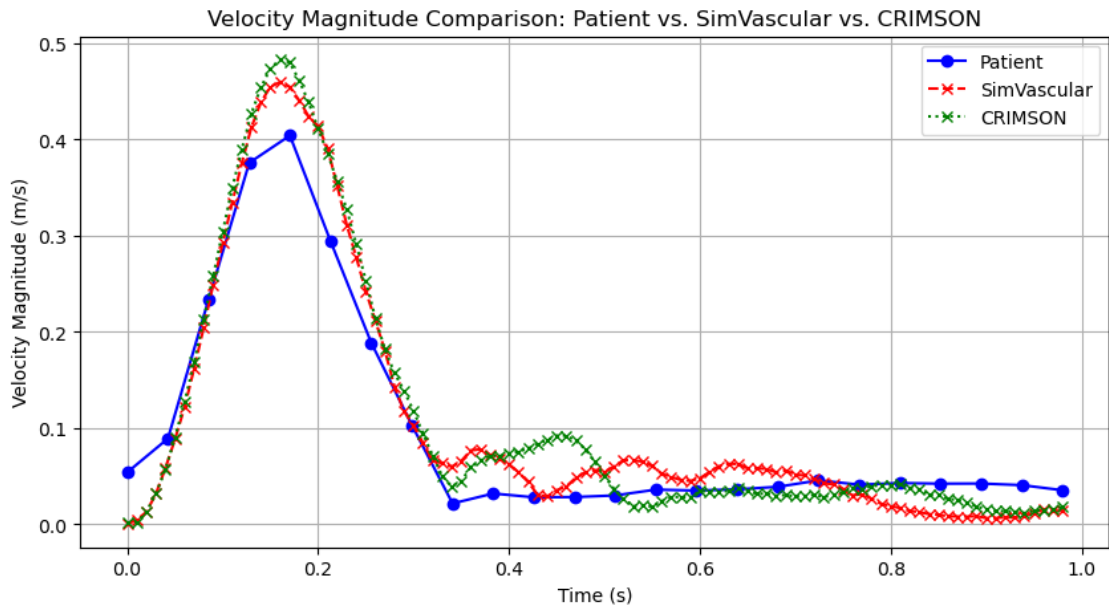


Figure 155: Graph comparing the velocity magnitude before the LCC artery

Before the LSA branch of the aortic arch. Another reference region has been selected for extracting velocity component graphs, located just before the flow enters the left subclavian artery (LSA), the final branch of the aortic arch (Figure 100). The graph in Figure 156 shows that both simulations accurately capture the flow pattern during diastole. However, during systole, both simulations display elevated values, overestimating the systolic phase and struggle to capture the flow behavior during this period, while the MRI data remains close to zero, with a slight increase occurring earlier than predicted, suggesting an almost non-existent u-velocity component in that region.

The results for the v-velocity component (Figure 157) demonstrate a strong agreement with the MRI data, with both simulations following the same pattern and producing similar values. They accurately predict key flow characteristics, such as the systolic phase and the subsequent backflow, though both overestimate the peak velocity during systole, a common trend observed in graphs of the parabolic profile. Throughout most of the diastolic phase, both simulations closely align with the MRI data. However, a slight discrepancy emerges around 0.75 s, where the simulation values begin to diverge from the MRI data.

For the w-component (Figure 158), the MRI data exhibit a clear trend, with velocity increasing to a peak during the systolic phase before stabilizing at relatively constant values near zero during diastole. In contrast, both simulations show irregular behavior for a significant portion of the cardiac cycle. While the velocity initially follows a similar pattern to the MRI data until approximately 0.18 s, the peak velocity occurs later, around 0.2 s. Beyond this point, both simulations display oscillations and abrupt velocity changes, with CRIMSON exhibiting larger deviations. However, around 0.53 s, both simulations begin to align more closely with the MRI data, and as time progresses, they gradually converge to the MRI values.

To provide a general overview of this region, the velocity magnitude graph in Figure 159 is analyzed. It demonstrates that both simulations capture the overall behavior of the MRI data relatively well during the systolic phase, though both tend to overestimate the peak velocity. Toward the end of systole and the early stages of diastole (~0.35–0.55 s), both simulations also overestimate the backflow in this region, resulting in higher velocity values. However, SimVascular maintains a smaller overestimation and remains closer to the MRI data. In contrast, CRIMSON predicts significantly higher backflow velocities, with the peak occurring around 0.45 s, whereas SimVascular predicts it at approximately 0.38 s, which aligns more closely with the MRI data. Around 0.55 s, both simulations report similar velocity values, and their patterns converge for the remainder of the cardiac cycle.

Although these patterns deviate from the MRI data, the velocity values remain within the same order of magnitude. These discrepancies can be attributed to several factors, similar to those identified in the previous region. Both simulations apply a parabolic velocity profile at the inlet rather than a patient-specific flow profile, which can lead to variations in velocity magnitude and distribution. Additionally, minor inaccuracies in the reconstructed patient model may influence local flow dynamics, contributing to differences between the simulations and MRI data. The absence of Fluid-Structure Interaction (FSI) results in the assumption of rigid arterial walls, whereas in reality, arterial compliance plays a role in flow behavior. This could explain the underestimation of peak velocity and the deviations observed during diastole.

Moreover, the analyzed region, located between the left common carotid artery (LCCA) and the left subclavian artery (LSA), is particularly sensitive to small disturbances due to the close proximity of these vessels. Flow separations in this area can significantly impact velocity due to the complex geometry. Both simulations appear to overinterpret these geometric complexities, generating more intricate flow patterns than the smoother velocity distribution observed in the MRI data.

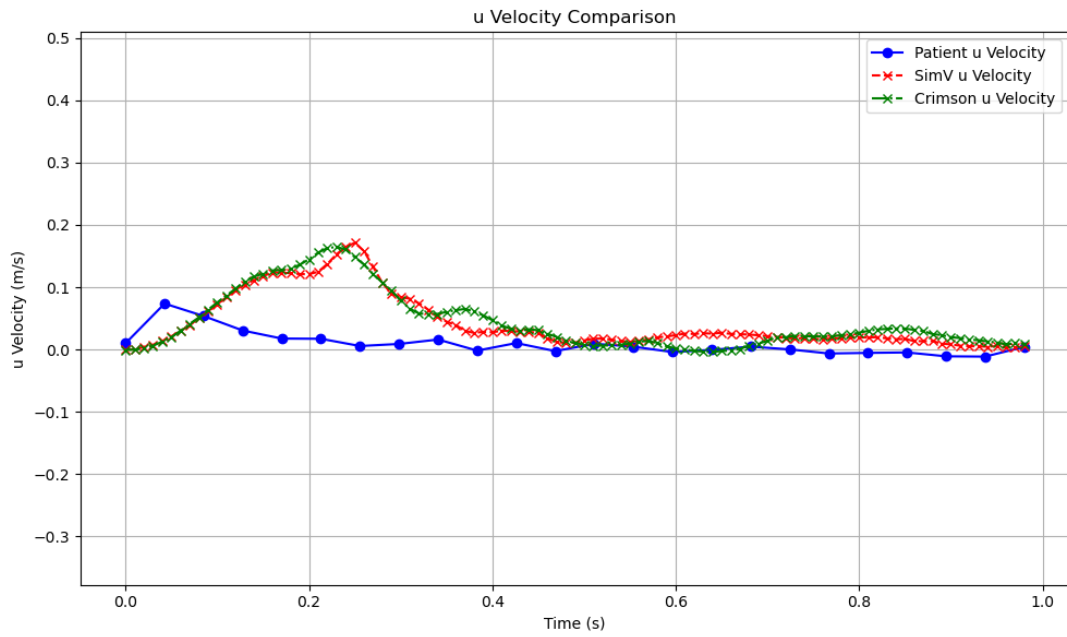


Figure 156: Graph comparing the u-velocity component before the LS artery

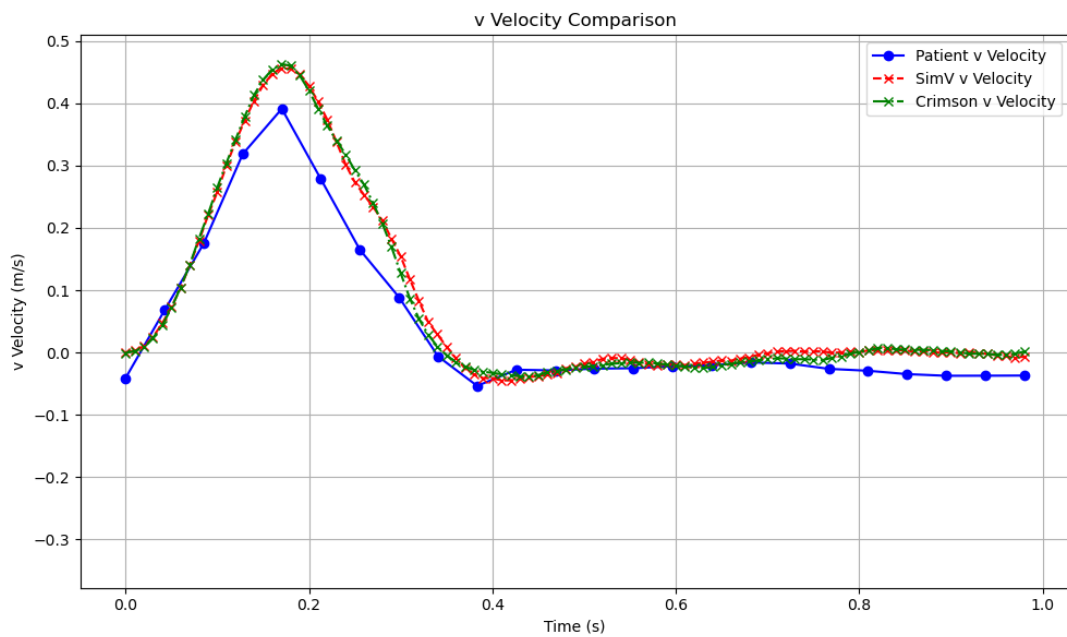


Figure 157: Graph comparing the v-velocity component before the LS artery

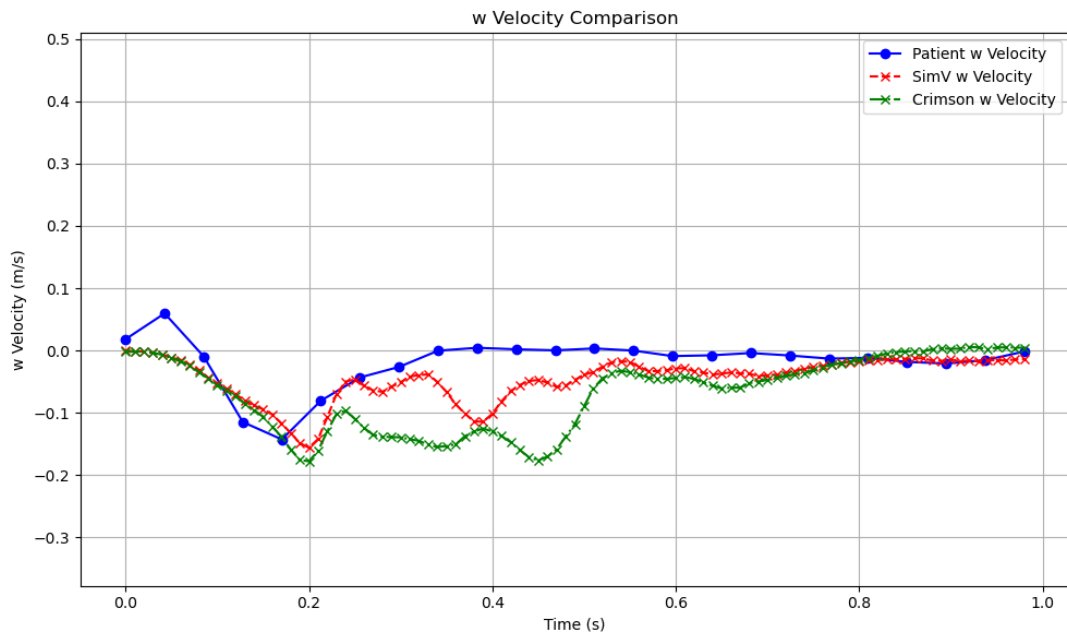


Figure 158: Graph comparing the w-velocity component before the LS artery

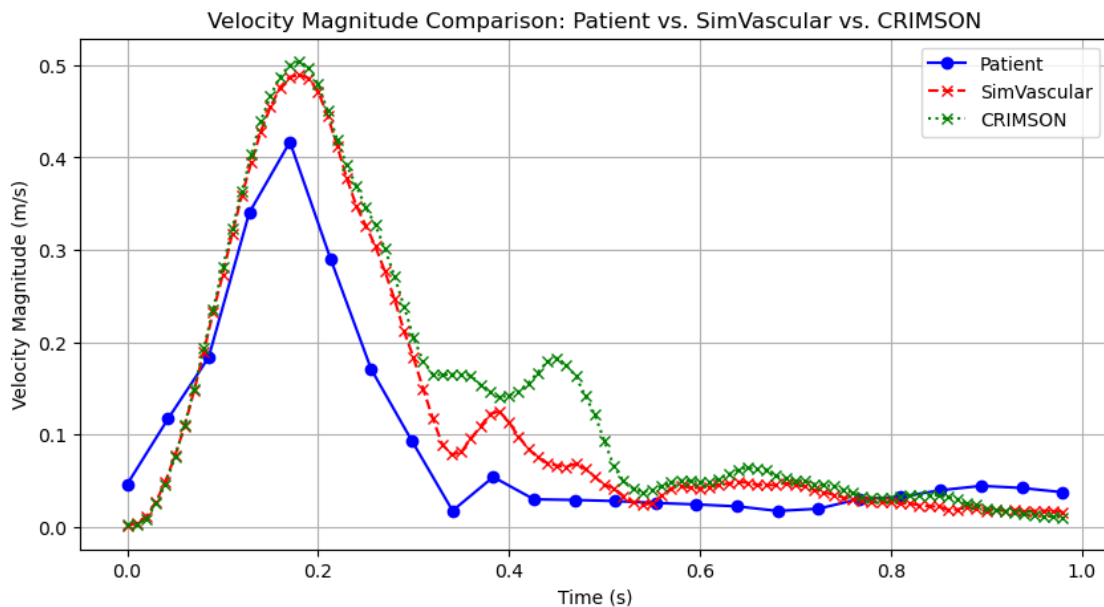


Figure 159: Graph comparing the velocity magnitude before the LS artery

Finally, across all studied regions, it was observed that the parabolic inlet velocity profile tends to overestimate velocity throughout the entire flow domain, particularly in the ascending aorta and the aortic arch. While both simulations effectively captured the primary velocity component in each region, they struggled to accurately represent the secondary velocity components. This suggests that using a parabolic or other idealized velocity profile may lead to inaccuracies in distributing secondary velocity components, which can propagate throughout the flow domain—especially in regions where flow separation and anatomical variations occur, such as the aortic arch.

Lastly, similar to the analysis with the patient-specific velocity profile, the Reynolds numbers for each cross-section at the peak of the systolic phase using the parabolic profile are summarized in Table 10.

Table 10: Reynolds numbers of each cross-section at the peak of the systolic phase (parabolic profile)

Cross-sections	Cross-section location (cm)	Cross-section area (cm ²)	Reynolds number (approx.)
Upper descending aorta	11.92 (z-axis)	7.556	4900
Ascending aorta	12.23 (z-axis)	22.361	4000
Before the LCC branch of the aortic arch	-5.67 (y-axis)	9.797	3700
Before the LSA branch of the aortic arch	-2.48 (y-axis)	9.09	3900

As expected, the Reynolds numbers derived from the parabolic velocity profile also indicate transitional flow at the peak of the systolic phase, similar to the patient-specific profile. The values are slightly higher, which aligns with the marginally elevated velocities observed in the parabolic case. However, this difference is considered negligible, and the same conclusions drawn from the Reynolds values in Table 9 also apply here.

3.3 Direct comparison between the patient-specific and parabolic velocity profile

In the final section of this study, velocity comparison graphs are presented for the previously selected slices. Unlike the previous analyses, these graphs now compare the patient-specific and parabolic velocity profiles within the studied region. This direct comparison helps evaluate their overall behavior, highlight differences, and identify potential causes of discrepancies. For the comparison of the two profiles, the results given from the simulations conducted using SimVascular were used.

Upper descending aorta. As in the previous analysis, the initial axial slice corresponds to slice 71 in the CFD data and slice 50 in the MRI data, located in the upper descending aorta (Figure 85). Graphs illustrating the three velocity components are provided for comparison between the patient-specific and parabolic velocity profiles.

For the u-velocity component (Figure 160), neither the patient-specific nor the parabolic profile accurately captures the velocity variations. The patient data show increase in velocity during systole, whereas the patient-specific profile remains relatively steady, and the parabolic profile exhibits some variation between approximately 0.48 s and 0.67 s. Consequently, the patient-specific profile tends to underestimate flow characteristics, while the parabolic profile tends to overestimate certain aspects of the flow. In this case, the patient-specific profile offers a more accurate representation of the u-component in this region, where the flow is more developed.

For the v-velocity component (Figure 161), both velocity profiles exhibit strong agreement throughout the cardiac cycle, effectively capturing the overall flow pattern and the peak velocity during systole. However, the patient-specific profile offers a more precise representation, closely aligning with the MRI data in both the systolic and diastolic phases. Notably, it also replicates the steeper decline in velocity at the end of systole, similar to the MRI data. From approximately 0.48 s onward, including the entire diastolic phase, both simulations accurately reflect the flow pattern. The same strong agreement between both profiles and the MRI data is also present in the w-velocity component (Figure 162), where the flow pattern is also well captured with the only discrepancy being that the peak velocity at the systolic phase is slightly underestimated from both velocity profiles.

The velocity magnitude graph in Figure 163 indicates that the overall simulated velocity behavior in this region is quite accurate. However, both profiles underestimate the peak velocity during the systolic phase. Additionally, the parabolic profile displays some oscillatory patterns during part of the diastolic phase, whereas the patient-specific profile follows a pattern much closer to that observed in the MRI data. Nevertheless, both simulations effectively capture the overall flow pattern in this region, with the parabolic profile overestimating some of its aspects.

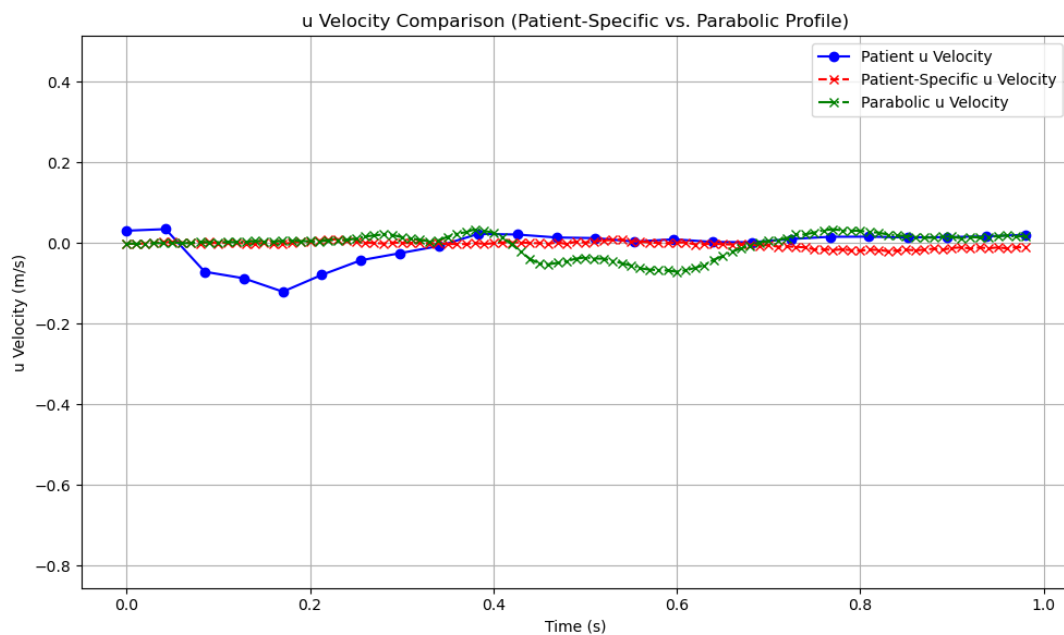


Figure 160: Graph comparing the u-velocity component at the upper descending aorta

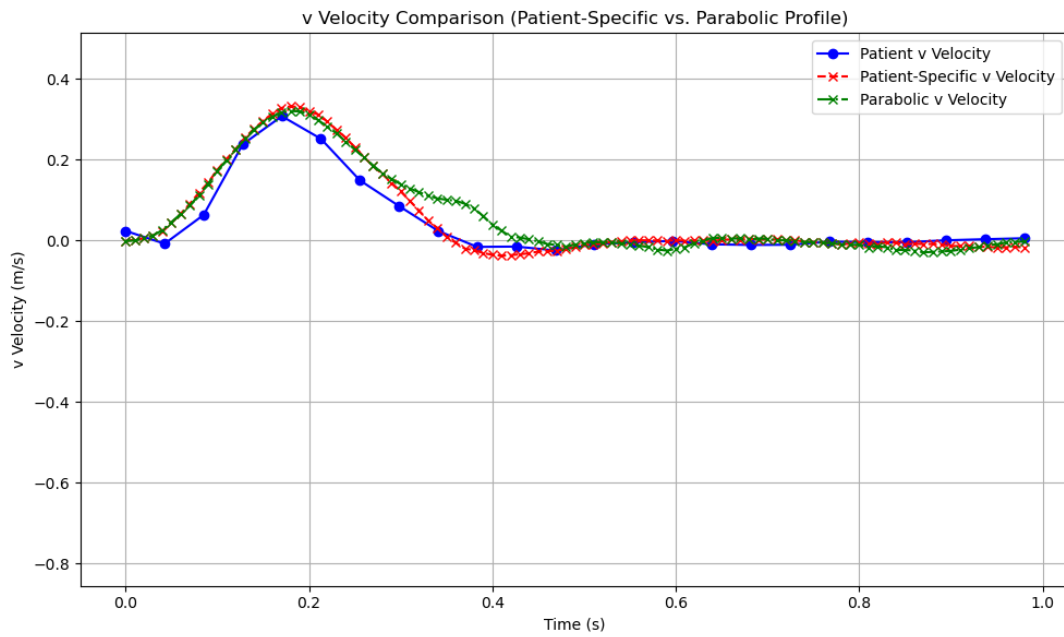


Figure 161: Graph comparing the v-velocity component at the upper descending aorta

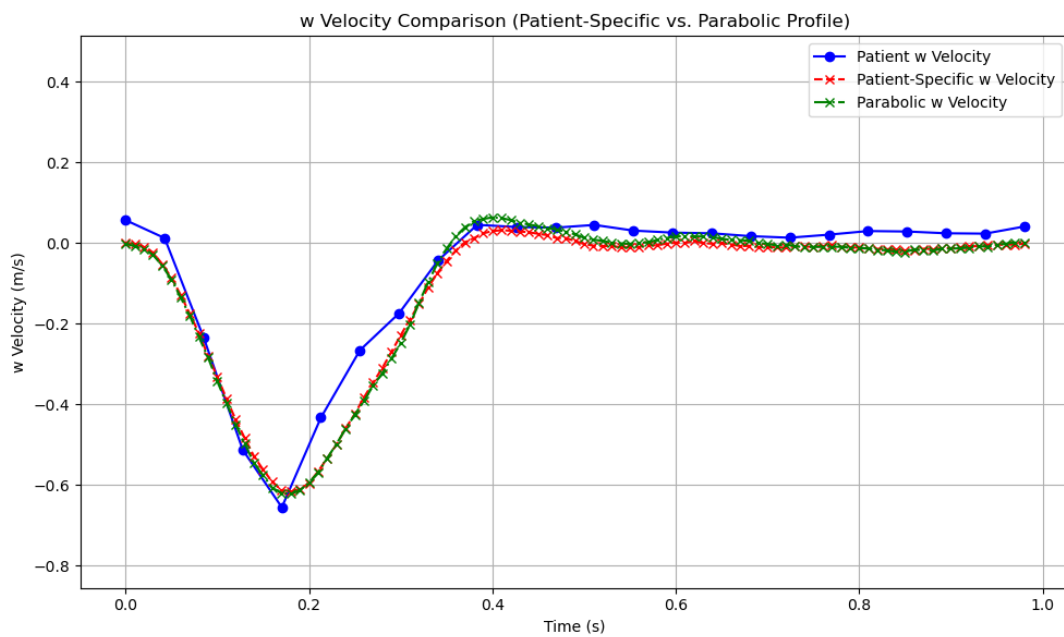


Figure 162: Graph comparing the w-velocity component at the upper descending aorta

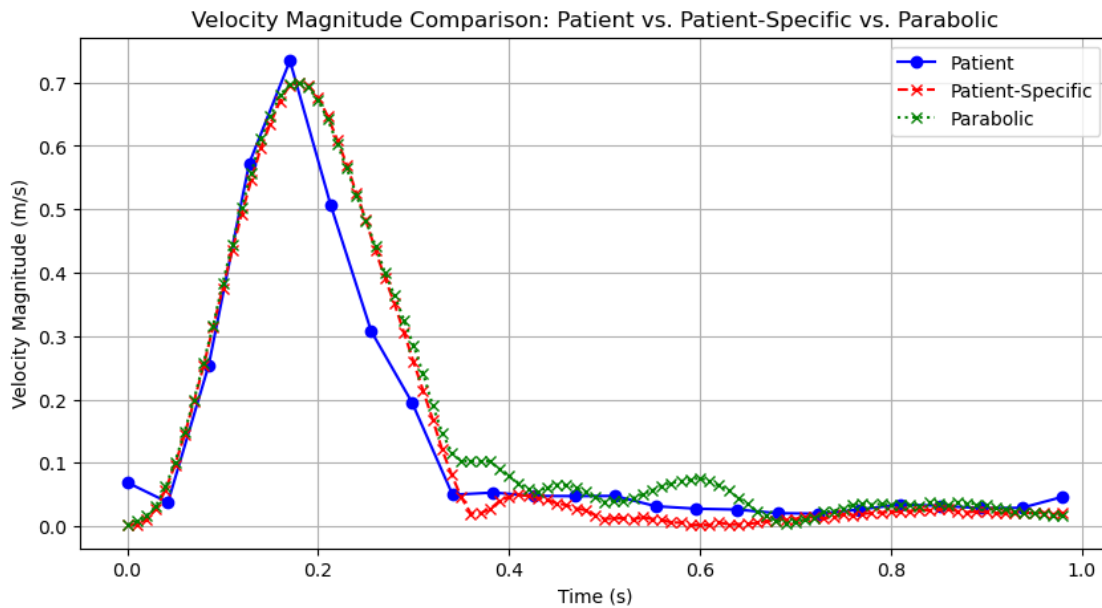


Figure 163: Graph comparing the velocity magnitude at the upper descending aorta

Ascending Aorta. The next region analyzed is where the flow enters the aortic arch in the ascending aorta region selected (Figure 90). In the u-component graph shown in Figure 164, both the parabolic and patient-specific velocity profiles capture the overall flow pattern, each with distinct strengths and limitations. The patient-specific profile demonstrates greater accuracy during the systolic phase, closely following the MRI data. It effectively captures both the systolic phase and most of the diastolic phase, though it struggles to replicate the steeper velocity change observed in the MRI data between 0.3 s and 0.5 s. Meanwhile, the parabolic profile maintains reasonable consistency with the MRI data, particularly during the diastolic phase, where it captures the flow pattern even more accurately than the patient-specific profile. However, it exhibits oscillatory behavior during systole, introducing some discrepancies.

For the v-component (Figure 165), the patient-specific profile demonstrates greater accuracy by capturing the key flow characteristics in this region and closely representing the actual velocity behavior. One notable difference is its steeper increase in velocity at the start of the systolic phase, whereas the MRI data show a more gradual rise. Despite minor overestimations, primarily during the diastolic phase, the overall velocity values remain consistent and eventually converge with the MRI data. In contrast, the parabolic profile exhibits more noticeable discrepancies, particularly in overestimating velocity values. The most significant difference is its struggle to capture the flow behavior during the systolic phase, instead of presenting a distinct flow pattern. It predicts a higher peak velocity during the systolic phase, occurring earlier than in the MRI data (~ 0.1 s vs. ~ 0.18 s), followed by a small decline and a steeper decrease around 0.18 s. Additionally, the parabolic profile overestimates peak systolic velocity and maintains higher velocity values throughout most of the diastolic phase, further highlighting its tendency to exaggerate certain flow characteristics.

Similar patterns between the two profiles are also observed in the w-velocity component, as shown in Figure 166. The patient-specific profile provides a highly accurate representation of the flow, correctly predicting the peak velocity during the systolic phase and capturing nearly all flow characteristics, including the backflow at the end of systole and the beginning of diastole. Additionally, it demonstrates good convergence with the MRI data. The parabolic profile also maintains consistency with the MRI data but retains certain distinct traits, such as overestimating peak velocity and slightly exaggerating some flow characteristics. However, these tendencies are less pronounced in this case, and overall, the parabolic profile captures the flow behavior well.

The velocity magnitude graph in Figure 167 suggests that the patient-specific profile closely aligns with the MRI data throughout the cardiac cycle, with some discrepancies, particularly during the diastolic phase. It accurately captures key flow characteristics, including backflow, peak systolic velocity, and the duration of systole. The parabolic profile effectively represents the overall flow pattern but tends to overestimate peak systolic velocity and other flow characteristics, as observed in previous analyses. It produces a higher peak velocity, which is reached more quickly than in patient-specific profile, and maintains a broader peak between approximately 0.15 s and 0.18 s. In contrast, the patient-specific profile provides a more precise representation of the systolic phase by capturing localized variations in flow. However, both profiles struggle to fully replicate the diastolic phase, exhibiting overestimations in certain regions and oscillatory patterns. The patient-specific profile converges more closely with the MRI data, offering a more accurate depiction of the flow behavior.

As previously discussed, these discrepancies are primarily attributed to the absence of Fluid-Structure Interaction (FSI), which would typically dampen oscillations due to vessel wall compliance. The higher velocity values seen in the parabolic profile likely stem from its velocity distribution, where the peak velocity is concentrated along the centerline rather than near the boundaries. In contrast, the patient-specific profile distributes velocity more realistically, potentially reducing its magnitude, particularly during the systolic phase.

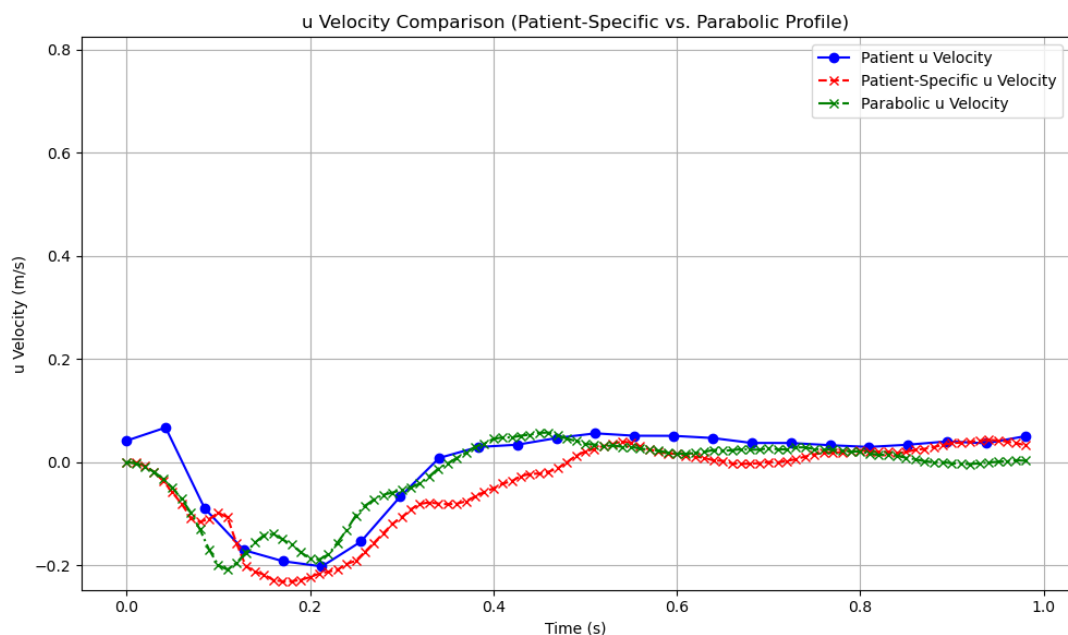


Figure 164: Graph comparing the u-velocity component before the aortic arch

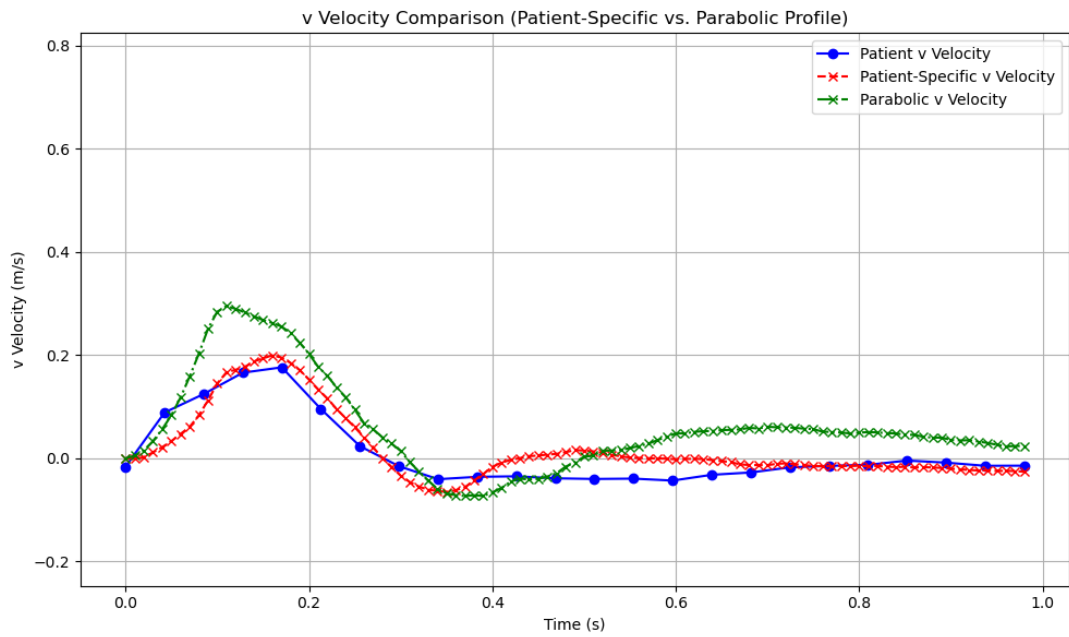


Figure 165: Graph comparing the v-velocity component before the aortic arch

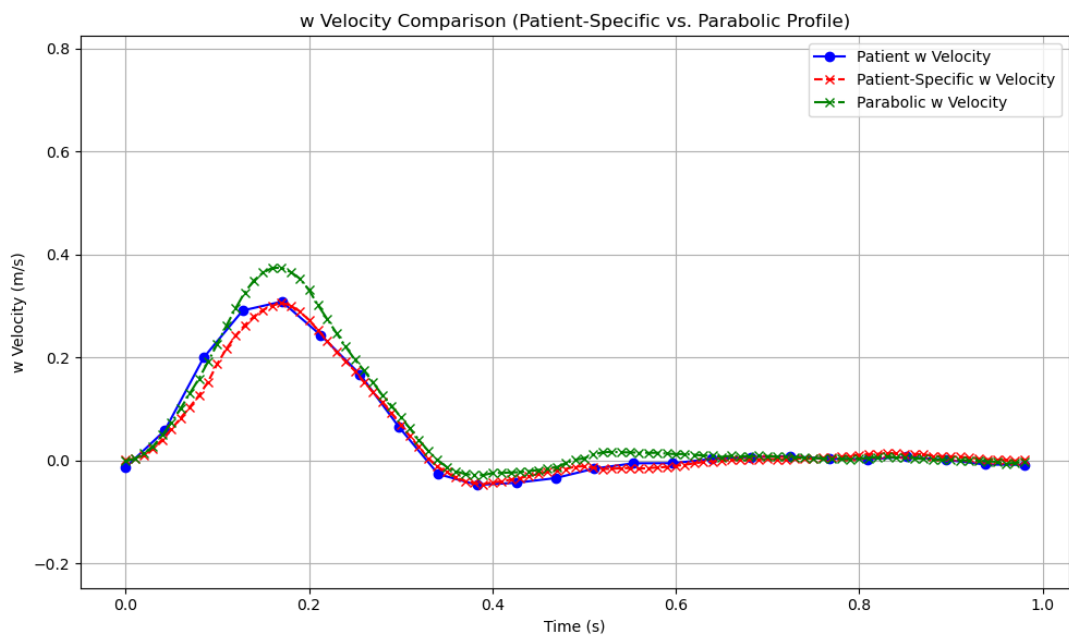


Figure 166: Graph comparing the w-velocity component before the aortic arch

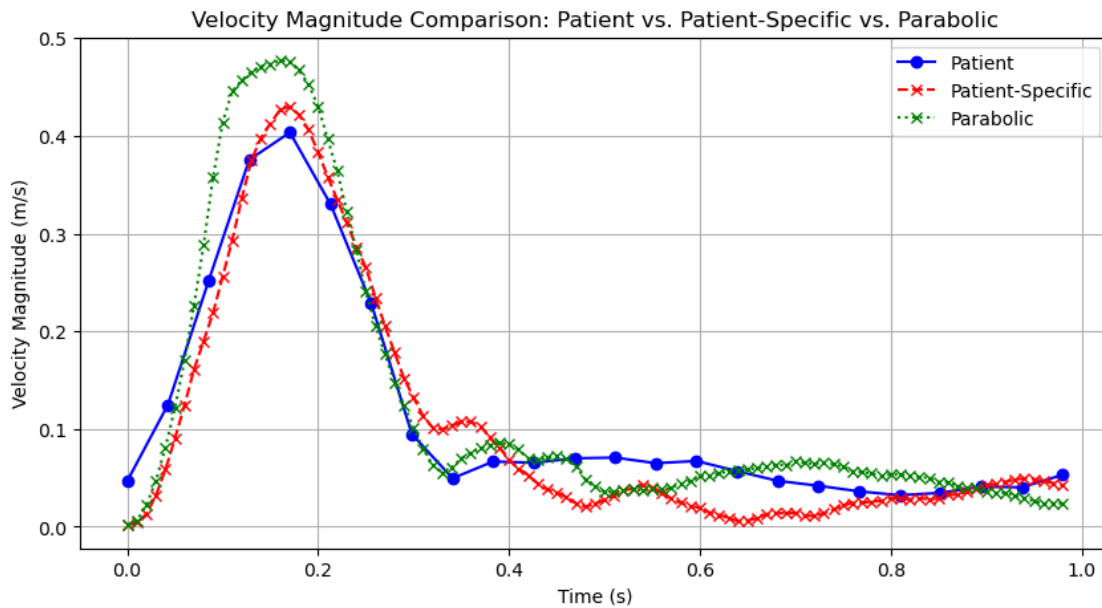


Figure 167: Graph comparing the velocity magnitude before the aortic arch

Before the LCC branch of the aortic arch. In the next region studied, just before the left common carotid artery (Figure 95), the velocity profiles display distinct patterns. The u-velocity component graph in Figure 168 shows that the MRI data maintains a relatively steady velocity near zero throughout the entire cardiac cycle. This trend is largely captured by the patient-specific profile, which exhibits a slight increase in velocity during the systolic phase along with minor oscillations throughout the cycle. The parabolic profile follows a similar general pattern but tends to overestimate velocity values during systole, showing a sharp velocity increase around 0.2 s and an exaggerated representation of flow characteristics, such as backflow, as previously observed.

For the v-velocity component, both velocity profiles (Figure 169) provide a highly accurate representation, capturing most of the flow characteristics throughout the entire cardiac cycle. Notably, although the parabolic profile produces a higher peak velocity during the systolic phase, it better captures the overall flow pattern, accurately predicting key features such as the systolic phase duration and small backflow. In contrast, the patient-specific profile estimates a longer systolic phase and does not predict any backflow. However, both profiles effectively capture the diastolic phase with high accuracy.

For the w-velocity component (Figure 170), somewhat unexpectedly, the parabolic profile offers a better representation of the flow. Both profiles tend to overestimate velocity values during the systolic phase, though the patient-specific profile provides slightly more consistent results. The parabolic profile exhibits more pronounced oscillations and overestimates certain flow characteristics, such as backflow following the systolic phase and velocity fluctuations during systole. However, it ultimately converges to the MRI values. In contrast, the patient-specific profile maintains greater accuracy for most of the cardiac cycle but eventually deviates from the MRI data.

By looking at the velocity magnitude graph in Figure 171 the overall velocity behavior of the velocity magnitude from MRI patient data, the patient-specific velocity profile, and the parabolic velocity profile over a complete cardiac cycle can be seen. During the systolic phase (~ 0 s - 0.35 s), both computational profiles closely follow the MRI data, capturing the peak systolic velocity around 0.18 s. However, the parabolic profile exhibits the highest peak velocity, overestimating the MRI data, while also predicting the peak velocity slightly earlier. The patient-specific profile also overestimates but follows the MRI pattern more accurately. In the diastolic phase (0.3 s – 0.98 s), both profiles show some oscillations, with the parabolic profile demonstrating more pronounced fluctuations. The patient-specific profile exhibits better convergence towards the MRI data, particularly in the latter part of the cycle, though both profiles struggle to capture diastolic velocity values. The parabolic profile's overestimation of the peak systolic velocity is likely due to its assumption of higher velocity values concentrated at the center, whereas the patient-specific profile distributes velocity more realistically. The oscillations during diastole may stem from the lack of Fluid-Structure Interaction (FSI), as vessel wall compliance could dampen fluctuations. Additionally, minor anatomical inaccuracies in model assumptions could contribute to small discrepancies in velocity trends.

Overall, the patient-specific profile provides a more accurate representation of the MRI data, particularly in the diastolic phase, while the parabolic profile tends to overestimate peak systolic velocity and introduce more oscillations. One notable observation is that the parabolic profile, despite overestimating peak systolic velocity, better captures the overall flow pattern of the systolic phase, including its duration and backflow, compared to the patient-specific profile, which predicts a longer systolic phase and lacks backflow.

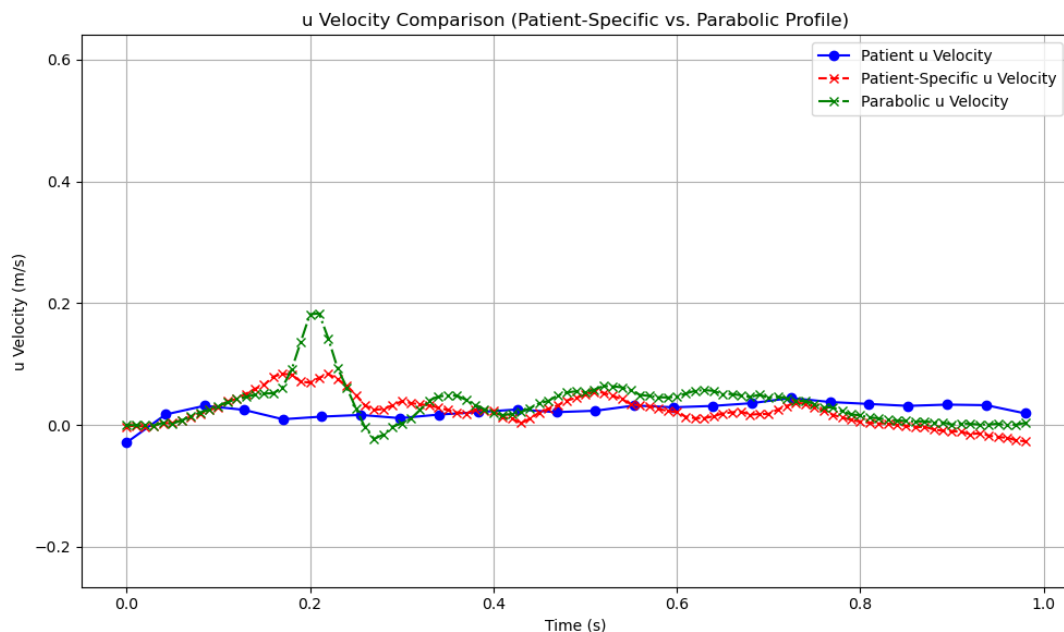


Figure 168: Graph comparing the u-velocity component before the LCCA

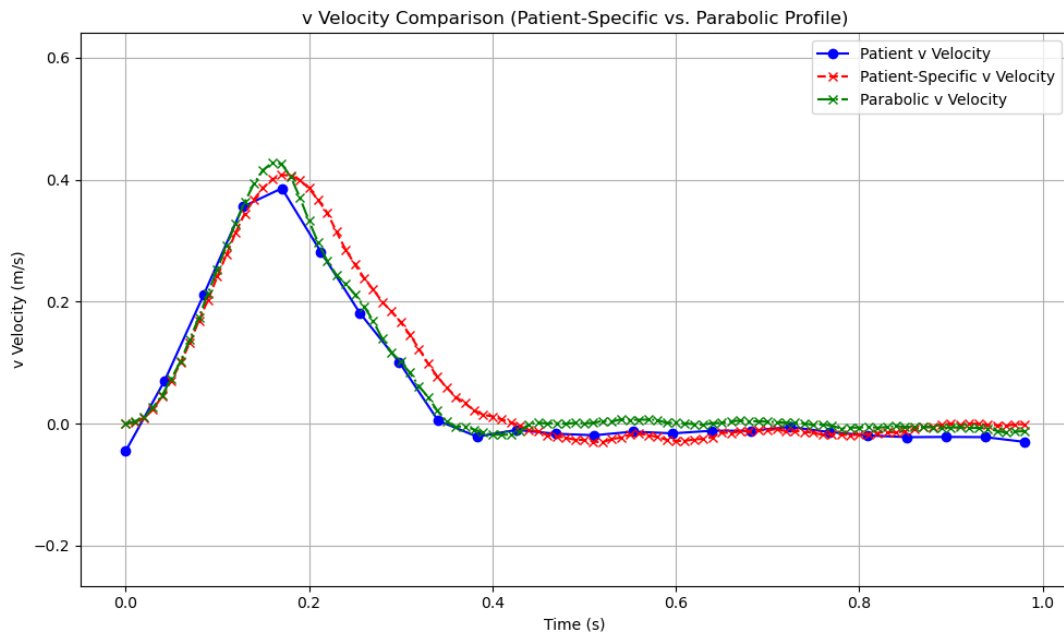


Figure 169: Graph comparing the v-velocity component before the LCCA

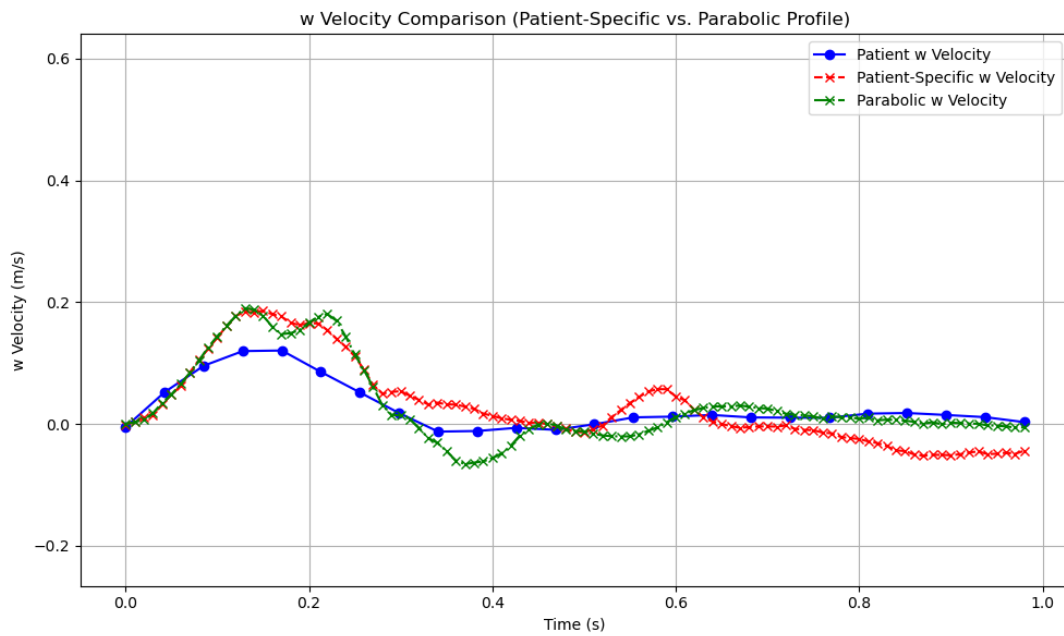


Figure 170: Graph comparing the w-velocity component before the LCCA

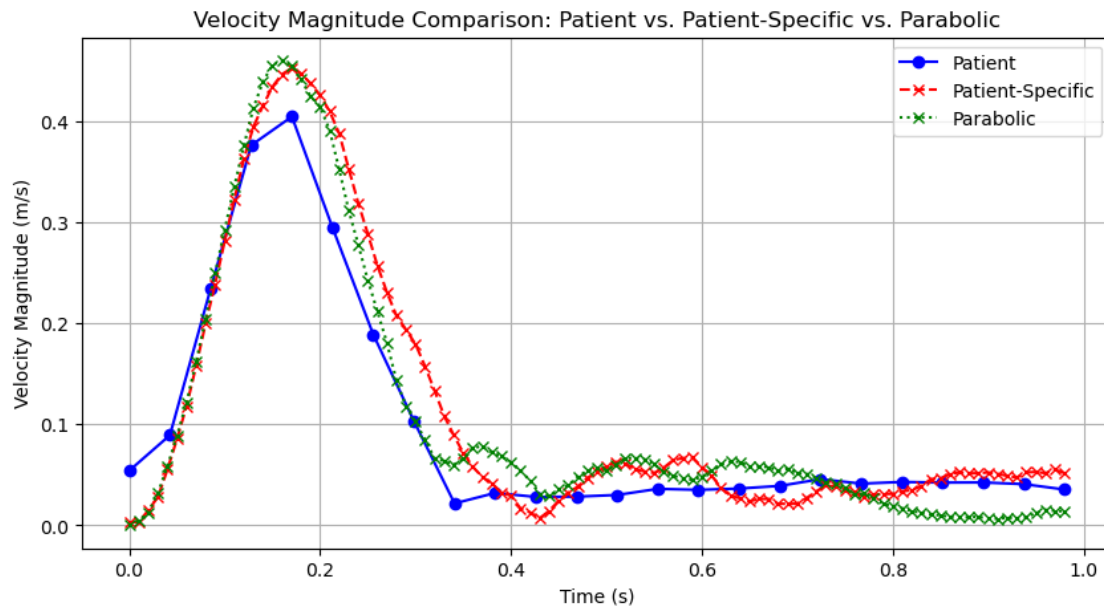


Figure 171: Graph comparing the velocity magnitude before the LCCA

Before the LSA branch of the aortic arch. Finally, the results for the last studied region (Figure 100) are presented. For the u-velocity component (Figure 172), both velocity profiles follow a similar pattern. However, the parabolic profile exhibits a sudden increase in velocity around 0.24 s, likely due to differences in velocity propagation. Throughout the systolic phase, both profiles show a comparable increase in velocity, though they tend to overestimate the MRI data, which exhibit a more gradual velocity rise occurring earlier in the cardiac cycle (around 0.5 s), compared to the simulations (around 0.2 s for the patient-specific profile and 0.28 s for the parabolic profile). For the remainder of the cardiac cycle, both profiles provide accurate results.

For the v-velocity component (Figure 173), both velocity profiles successfully capture the overall flow pattern, though some discrepancies remain. Both profiles overestimate the peak velocity during the systolic phase while maintaining the same duration for this phase. Like previous comparisons, the parabolic profile exhibits a slightly higher peak velocity than the patient-specific profile, though the difference is less pronounced in this case. During the diastolic phase, both profiles show high accuracy, with the parabolic profile performing slightly better due to its ability to capture the backflow at the end of systole.

For the w-velocity component (Figure 174), both profiles deviate from the MRI data during the systolic phase. While they capture the overall flow pattern relatively well throughout most of the diastolic phase, their behavior differs significantly during systole and up to ~ 0.6 s. Additionally, the two profiles not only diverge from the MRI data but also display differences from each other. The peak velocity during systole is captured by both profiles and is relatively close to the value observed in the MRI data, with the parabolic profile yielding a slightly higher value and the patient-specific profile a slightly lower one. However, both profiles estimate the peak velocity at 0.2 s, whereas the MRI data indicate it occurs slightly earlier (~ 0.17 s). Following this point, the patient-specific profile closely follows the MRI data, with the main discrepancy being a slight overestimation of the backflow. In contrast, the parabolic profile exhibits oscillatory behavior after the systolic peak, with fluctuations in velocity values persisting until approximately 0.6 s. These fluctuations likely result from how the parabolic

velocity distribution propagates within the studied anatomical region. Despite these differences, both profiles eventually converge with the MRI data later in the cardiac cycle.

The overall velocity behavior is summarized by the velocity magnitude graph in Figure 175. During peak systole, both simulated profiles overestimate velocity compared to the MRI data, with the parabolic profile reaching the highest peak and the patient-specific profile slightly lower. Between approximately 0.18 s and 0.35 s, all profiles show a rapid drop in velocity. However, the patient-specific profile closely follows the MRI data, while the parabolic profile remains slightly elevated—likely due to its assumption of fully developed flow, which may not hold in curved, branching arteries. The most notable discrepancies arise in the early diastolic phase, where the parabolic profile exhibits oscillatory behavior not observed in either the MRI data or the patient-specific profile. This suggests propagation issues stemming from enforcing an idealized parabolic flow in a complex arterial geometry.

Insights from the velocity component analysis further clarify these discrepancies, as previous findings indicated that the parabolic profile overestimated both u-velocity and v-velocity during systole, which aligns with its higher velocity magnitude in the graph. Additionally, fluctuations in the w-velocity component during early diastole correspond to the oscillatory behavior seen in the velocity magnitude graph, reinforcing the idea that the parabolic assumption struggles to replicate physiological flow conditions accurately. In contrast, the patient-specific profile more closely aligns with MRI data but does not fully capture the backflow observed in the MRI, possibly due to minor propagation errors in boundary conditions.

Overall, while both simulations effectively capture general flow trends, the parabolic profile, though able to represent key flow characteristics, introduces larger discrepancies, often predicting higher velocity values than expected and displaying oscillatory behavior, particularly in diastole, leading to greater instability. These traits make the patient-specific velocity profile the more suitable choice for simulations.

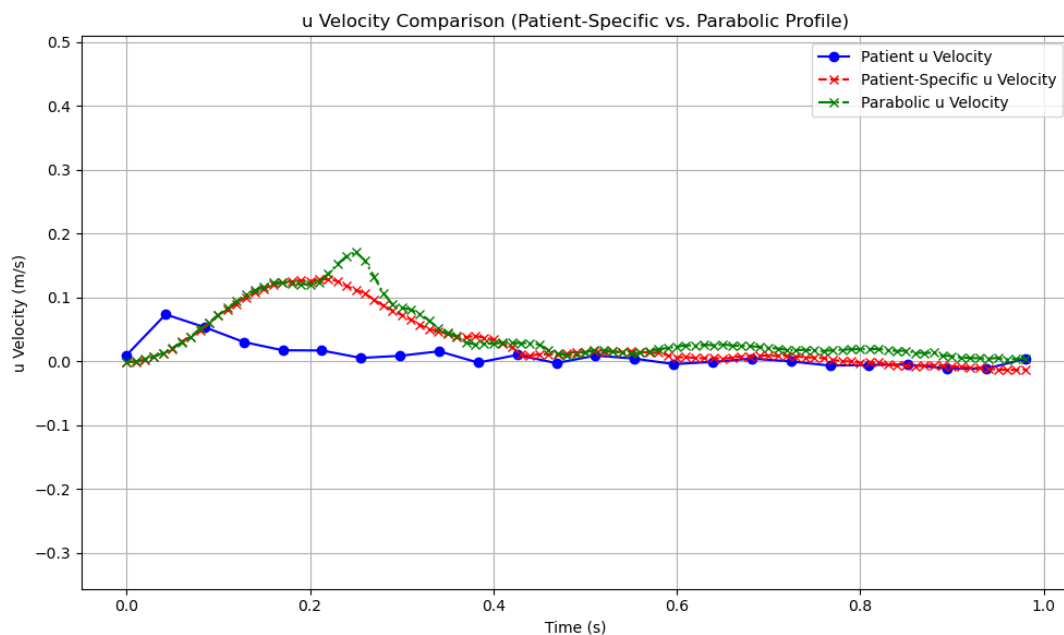


Figure 172: Graph comparing the u-velocity component before the LSA

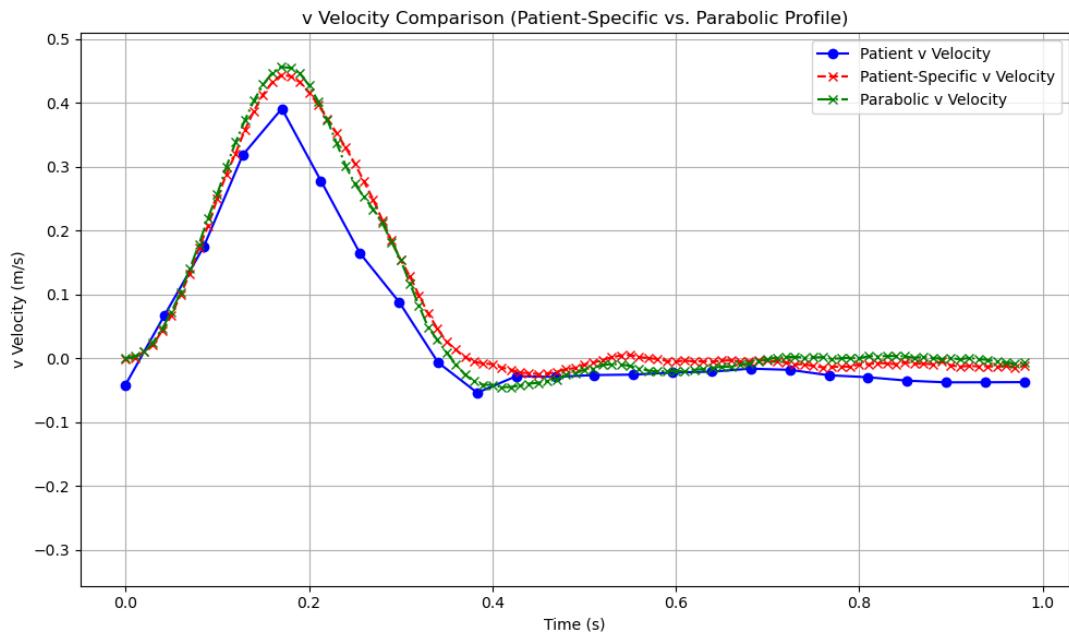


Figure 173: Graph comparing the v-velocity component before the LSA

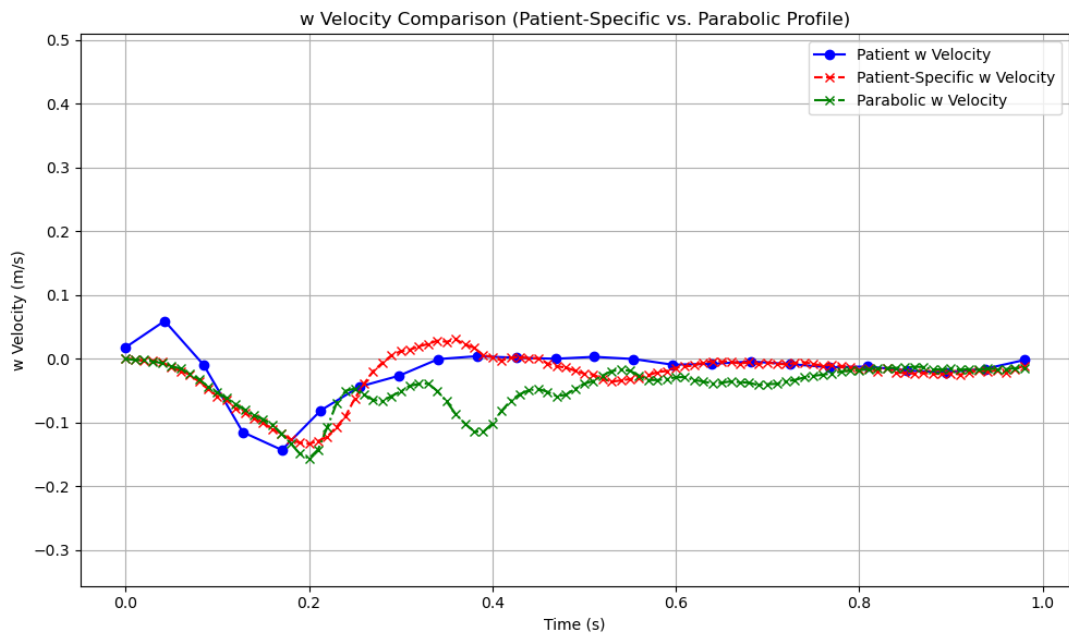


Figure 174: Graph comparing the w-velocity component before the LSA

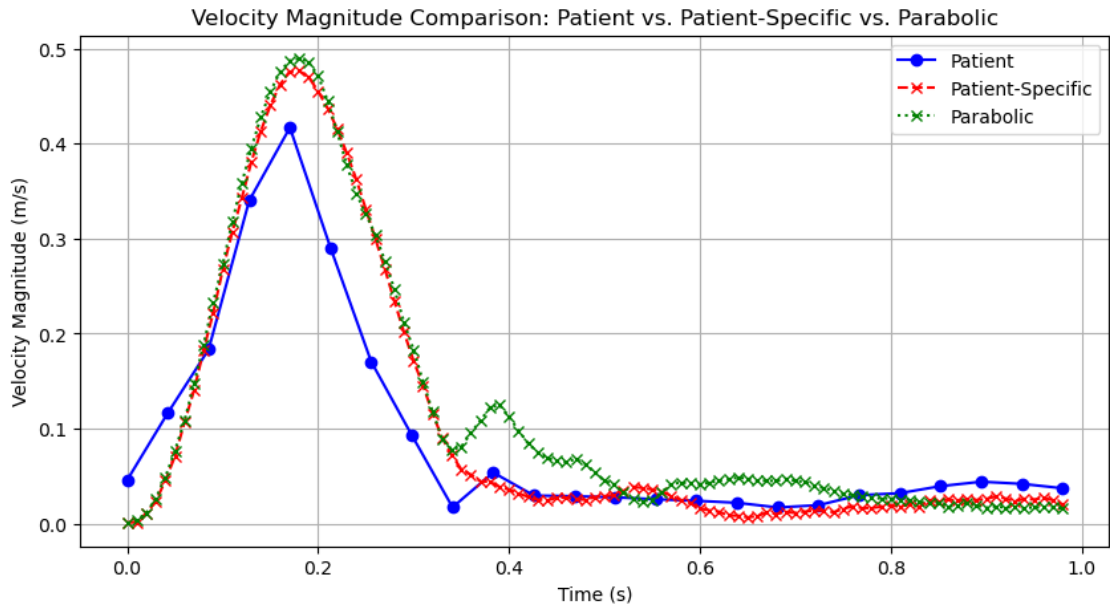


Figure 175: Graph comparing the velocity magnitude before the LSA

4. Conclusions

This study aims to create an *in silico* digital twin of the thoracic aorta, enabling the assessment of various mechanical characteristics using computational fluid dynamics (CFD). A significant portion of the workflow was developed from scratch to address the specific mechanical problem of the thoracic aorta. Through various simulations, physiologically relevant results were obtained that better align with patient-specific data, confirming the reliability of the workflow. By incorporating 4D flow MRI patient data, the anatomy was reconstructed as accurately as possible, and patient-specific inlet boundary conditions were derived, enhanced by the velocity profile of the patient. While the values for the other boundary conditions (RCR) were unknown, extensive testing and calibration were performed to match physiological conditions more accurately. The final simulation results indicated an elevated pressure of around 145 mmHg, which aligns with the clinical expectations for a 53-year-old male patient with high blood pressure.

The pressure distribution throughout the cardiac cycle follows expected physiological patterns. At the start of the systolic phase (acceleration), the pressure remains relatively uniform with a slight increase along the aorta. Higher pressures are observed in the descending aorta, influenced by gravity, while the ascending aorta exhibits slightly lower pressures due to the heart's relaxation prior to systole. The pressure difference between the ascending and descending aorta is minimal (~ 2 mmHg), indicating nearly uniform pressure at this stage. During the peak of the systolic phase, high pressure is seen in the ascending aorta, remaining elevated throughout the aortic arch. Pressure gradually decreases toward the descending aorta due to gravitational effects, peripheral resistance, vessel narrowing, and localized pressure changes from viscous friction. This demonstrates higher pressures near the heart and lower pressures in the descending aorta due to gravity-assisted flow. At the end of systolic phase (deceleration), pressure drops in the ascending aorta as the pumping force reduces, while pressure increases in the descending aorta due to residual momentum, vascular resistance, and vessel compliance. During the diastolic phase, low pressures dominate the aorta, with slight increases observed in the ascending aorta. However, the overall pressure distribution is nearly uniform across the entire flow domain (~ 97 mmHg). Both SimVascular and CRIMSON show consistent trends, with CRIMSON reporting slightly lower pressures. The use of both patient-specific and parabolic velocity profiles resulted in slightly higher-pressure values for the parabolic profiles, but with negligible differences overall.

This study also compares velocity profiles and vector fields for patient-specific and parabolic inlet profiles in SimVascular and CRIMSON. SimVascular produces a more diffused velocity distribution further along the flow domain, while CRIMSON exhibits more distinct high-velocity streaks in certain regions, likely due to differences in mesh resolution. CRIMSON also tends to predict slightly higher systolic velocities and a more pronounced low-velocity region near the boundary, due to the absence of boundary layers in the mesh. During diastole, both programs show low velocities, with SimVascular exhibiting slightly higher values, compared to the other cardiac cycle phases. For the parabolic profile, both programs maintain a uniform velocity distribution, with peak velocities at the center and no backflow at the onset of systole. Throughout the cycle, velocities remain elevated in the ascending aorta, aortic arch, and branches, with vorticity and localized disturbances emerging during diastole. Backflow develops at the end of systole, yet the parabolic profile remains more uniform across most of the flow domain, while the patient-specific profile demonstrates greater variability and

pronounced flow vorticity. During diastole, the parabolic profile retains an organized velocity pattern, whereas the patient-specific profile exhibits disorganized flow, with lingering high velocities due to geometry-induced vorticity. Overall, the parabolic profile tends to overestimate velocity, particularly in the aortic arch. Both profiles show an unexpected velocity increase in the lower descending aorta, likely due to the absence of Fluid-Structure Interaction (FSI), which would otherwise capture the velocity reduction caused by vessel expansion during systole. The key differences between the profiles are in flow structure: the parabolic profile generates more symmetrical, organized flow with higher velocities away from the walls, while the patient-specific profile produces a more complex physiological flow pattern, characterized by flow separation, recirculation, and secondary flow effects, with higher velocities near the walls and in some localized regions. Despite minor variations in velocity magnitude and flow structure, both SimVascular and CRIMSON exhibit consistent overall trends.

Wall Shear Stress (WSS) analysis showed that the patient-specific velocity profile resulted in the highest WSS values in the ascending aorta and near the aortic arch branches, reflecting elevated blood flow and vessel curvature. WSS was consistently high at flow direction changes, particularly at the aortic arch and bifurcations. During peak systole, WSS increased in the ascending aorta and branching points. Localized rises in WSS persisted due to backflow at the end of systole (deceleration). The descending aorta exhibited the lowest WSS throughout the entire cardiac cycle, except for a brief increase at peak systole. Time-Averaged Wall Shear Stress (TAWSS) showed high values in the ascending aorta, with a gradual decrease downstream, except for slight increases in the lower descending aorta. The parabolic profile showed higher WSS in the ascending aorta and early outer aortic arch regions and values like the patient-specific profile in the descending aorta region, due to the developed flow there. TAWSS was lower in the parabolic profile, with similar values in the descending aorta. The key difference was that the parabolic profile had more uniformly elevated values in the ascending aorta and early outer aortic arch, while the patient-specific profile had higher values at the start of the ascending aorta. The higher WSS in the patient-specific profile suggests velocity is concentrated near the aortic wall, while in the parabolic profile, it is distributed away. These findings highlight the importance of using patient-specific velocity profiles to accurately capture hemodynamic forces critical for vascular adaptation and disease progression.

This study compares velocity profiles from SimVascular and CRIMSON simulations with MRI data, offering insights into aortic flow dynamics. Both CFD programs effectively captured overall flow trends but showed regional variations. In the upper descending aorta, both closely matched MRI data, with SimVascular slightly underestimating and CRIMSON slightly overestimating systolic velocities. Before the aortic arch, systolic flow was well represented, but diastolic oscillations deviated from MRI data, likely due to the absence of fluid-structure interaction (FSI). Similar discrepancies appeared before the left common carotid artery (LCC), where CFD overestimated peak systolic velocity while MRI showed a smoother diastolic profile, with fluctuations and phase shifts linked to rigid-wall assumptions. Before the left subclavian artery (LSA), CFD models again overestimated systolic velocity and failed to capture MRI-observed backflow, likely due to boundary condition limitations and different flow propagation. Additionally, the parabolic inlet velocity profile consistently overestimated velocities, particularly in the ascending aorta and aortic arch, and struggled with secondary velocity distribution, highlighting its limitations in complex regions.

Overall, the descending aorta showed the highest accuracy due to fully developed flow and simpler anatomy, while the aortic arch had the greatest discrepancies due to flow division, curvature, and lack of FSI. Despite these differences, both models approximated general flow dynamics well and aligned more closely with MRI data as the cardiac cycle progressed. These findings emphasize the need for patient-specific conditions, including arterial wall motion and refined boundary conditions, to improve CFD accuracy in physiological flow simulations.

This study compares also patient-specific and parabolic velocity profiles across multiple regions of the arterial system, using SimVascular simulations and MRI data. In the upper descending aorta, neither profile accurately captured the u-velocity variations, but the patient-specific profile better represented the more developed flow region. Both profiles showed strong agreement in the v-velocity and w-velocity components, with the patient-specific profile closely matching the MRI data during both systole and diastole. In contrast, the parabolic profile exhibited oscillations during diastole. Before the aortic arch, the patient-specific profile provided better accuracy, particularly during the systolic and diastolic phases. The parabolic profile, however, overestimated systolic peak velocities and displayed oscillatory behavior. Near the left common carotid artery, the parabolic profile better captured the systolic peak, while the patient-specific profile overestimated the systolic duration and lacked backflow. Both profiles accurately represented the diastolic phase, but the patient-specific profile offered a more accurate overall flow pattern. In the final region before the left subclavian artery, the parabolic profile overestimated systolic peak velocity and showed fluctuating patterns during diastole. The patient-specific profile, though closer to the MRI data, slightly overestimated backflow. Across the entire study, the velocity magnitude graphs revealed that the parabolic profile tended to overestimate peak velocities during systole and exhibited oscillatory patterns. While the patient-specific profile was not perfect, it more closely reflected the MRI data and showed fewer oscillations, making it a more accurate representation of physiological flow, especially in diastole. In conclusion, both profiles captured general flow trends, but the parabolic profile introduced more discrepancies due to its idealized nature and inability to account for complex arterial geometries. As a result, patient-specific velocity profile is the more suitable choice for simulations.

In future studies, further calibration of the RCR values should be undertaken to ensure the accuracy of boundary conditions. This process requires careful evaluation of flow results at each outlet and the systematic selection of appropriate RCR values. Additionally, the implementation of Fluid-Structure Interaction (FSI) should be prioritized to capture the dynamic changes in vessel anatomy during the cardiac cycle, which significantly influence flow dynamics. FSI would help account for variations in vessel cross-sectional area during systole and diastole, reducing velocity overestimation and improving simulation accuracy. It would also dampen the oscillations observed in velocity profiles caused by rigid wall assumptions. Moreover, refining the selection of the Region of Interest (ROI) for velocity graph extraction would improve the precision of flow comparisons. Expanding the workflow by incorporating additional CFD software tools will allow for broader benchmarking and validation of results. Finally, optimizing the developed simulation codes through extensive testing will further enhance their precision and robustness, particularly when comparing specific regions of interest across platforms.

5. References

- Alfonso MR, Cymberknop LJ, Legnani W, Pessana F, Armentano RL (2014). Conceptual model of arterial tree based on solitons by compartments. *Annu Int Conf IEEE Eng Med Biol Soc.* 2014: 3224-3277. DOI: 10.1109/EMBC.2014.6944309.
- Anderson, JD (1995). *Computational Fluid Dynamics: The Basics with Applications*. McGraw-Hill. ISBN: 978-0-07-113210-7, 978-0-07-001685-9.
- AOBL (Online), Shear Stress VS Shear Rate in Fluid Mechanics updated Dec 15, 2023, <https://aoblpump.com/blogs/shear-stress-vs-shear-rate-in-fluid-mechanics/>, Accessed: Jan. 2025.
- Arthurs CJ, Khlebnikov R, Melville A, Marčan M, Gomez A, Dillon-Murphy D, et al. (2021), CRIMSON: An open-source software framework for cardiovascular integrated modelling and simulation. *PLoS Comput Biol* 17(5): e1008881. DOI: journal.pcbi.1008881
- Ashrafian H. (2007) Anatomically specific clinical examination of the carotid arterial tree. *Anat Sci Int.* 82(1):16-23. DOI: 10.1111/j.1447-073X.2006.00152.x.
- Azarine A, Garçon P, Stansal A, Canepa N, Angelopoulos G, Silvera S, Sidi D, Marteau V, Zins M. (2019). Four-dimensional Flow MRI: Principles and Cardiovascular Applications. *Radiographics* 39(3):632-648. DOI: 10.1148/rg.2019180091. PMID: 30901284.
- Bernstein MA, King KF, Zhou XJ (2004). *Handbook of MRI Pulse Sequences*. Elsevier. ISBN: 978-0-12-092861-3. DOI: 10.1016/B978-0-12-092861-3.X5000-6
- Betts-Gordon J, DeSaix P, Johnson E, Johnson JE, Korol O, Kruse D, Poe B, Wise JA, Womble M, Young KA (2022). *Anatomy and Physiology 2e*. https://assets.openstax.org/oscms-prodcms/media/documents/Anatomy_and_Physiology_2e_-_WEB_c9nD9QL.pdf. OpenStax, RICE. ISBN: 978-1-951693-42-8 (Digital version).
- Bissell MM, Raimondi F, Ait-Ali L, et al. (2023) 4D Flow cardiovascular magnetic resonance consensus statement: 2023 update. *J Cardiovasc Magn Reson* 25, 40. DOI: 10.1186/s12968-023-00942-z.
- Britannica (Online), Blood supply to the heart (M.F. Oliver, M.L Entman, Feb.7, 2025), <https://www.britannica.com/science/human-cardiovascular-system/Blood-supply-to-the-heart#/media/1/69887/141782>, Accessed Feb. 2025
- Brown RW, Cheng Y-CN, Haacke EM, Thompson MR, Venkatesan R (2014). *Magnetic Resonance Imaging: Physical Principles and Sequence Design*, 2nd Ed., John Wiley & Sons. DOI: 10.1002/9781118633953
- Çengel YA, Cimbala JM (2014). *Fluid mechanics: fundamentals and applications*, 3rd Ed. McGraw-Hill, ISBN 978-0-07-338032-2.
- Cleveland Clinic (Online), <https://my.clevelandclinic.org/health/body/17058-aorta-anatomy>, accessed Jan. 2025 (Aorta, 02/24/2022).

- Constantin, P., & Foias, C. (1988). Navier-stokes equations. University of Chicago Press. ISBN: 0-226-11548-8.
- CV Physiology (Online), Klabunde R.E., Cardiovascular Physiology Concepts, Laminar flow (11/05/2023), <https://cvphysiology.com/hemodynamics/h006>, Accessed: Jan. 2025.
- Damadian R (1971, Mar 19). Tumor Detection by Nuclear Magnetic Resonance. *Science* 171 (3976): 1151-1153. DOI: 10.1126/science.171.3976.1151.
- Day MA (1990). The no-slip condition of fluid dynamics. *Erkenntnis* 33(3), 285-296. DOI: 10.1007/BF00717588.
- Drake RL, Vogl WA, Mitchell AWM (2020). Gray's Anatomy for Students, 4th Ed., Elsevier. ISBN 978-0-323-39304-1, IE ISBN: 978-0-323-61104-6.
- Dugas BA, Samra NS (Updated 2023 Aug 7). Anatomy, Thorax, Brachiocephalic (Right Innominate) Arteries. In: StatPearls [Internet]. Treasure Island (FL): StatPearls Publishing; 2025 Jan-. Available from: <https://www.ncbi.nlm.nih.gov/books/NBK557678/>
- Eslahpazir M, Wittmann C, Krull R (2011). 2.75-Computational Fluid Dynamics, In: Comprehensive Biotechnology, 2nd Ed., M. Moo-Young Ed., Vol.2, pp. 1027-1038, Academic Press. DOI: 10.1016/B978-0-08-088504-9.00450-5
- Ferdian E, Suinesiaputra A, Dubowitz DJ, Zhao D, Wang A, Cowan B and Young AA (2020). 4DFlowNet: Super-Resolution 4D Flow MRI Using Deep Learning and Computational Fluid Dynamics. *Front. Phys.* 8: 138. DOI: 10.3389/fphy.2020.00138
- Frank O (1990). The basic shape of the arterial pulse. First treatise: mathematical analysis 1899. *J Mol Cell Cardiol.* 22 (3): 255–77. doi:10.1016/0022-2828(90)91460-O.
- Goldstein JS (1992). A Different Sort of Time: The Life of Jerrold R. Zacharias. The MIT Press. ISBN: 978-0-262-51909-0, 978-0-262-07138-3.
- GSU HyperPhysics (Online), Ohm's Law-Poiseuille's Law, <http://hyperphysics.phy-astr.gsu.edu/hbase/electric/watcir2.html>, Accessed: Dec. 2024
- Hahn EL (1950). Spin echoes. *Physical Review* 80 (4): 580-594. DOI: 10.1103/PhysRev.80.580.
- Hall JE (2011). Guyton and Hall Textbook of Medical Physiology, 12th Ed, Saunders Elsevier. ISBN: 978-1-4160-4574-8, 978-0-8089-2400-5 (IE).
- Hammer K (2009). High Resolution 3D-Imaging of the Physiology and Morphology of Isolated Adult Cardiac Myocytes from Rat and Mice, Doctoral Dissertation, Universität des Saarlandes, DOI: 10.22028/D291-21192.
- Herman IP (2016). Physics of the Human Body, 2nd Ed., Springer, DOI: 10.1007/978-3-319-23932-3.
- Mrimaster (Online), Phase-contrast (PC) flow MRI, <https://mrimaster.com/phase-contrast-pc-flow-mri/>, Accessed: Jan. 2025.

- NHLBI (Online), National Heart, Lung and Blood Institute (NHLBI), High Blood Pressure, <https://www.nhlbi.nih.gov/health/high-blood-pressure>, Accessed: Dec. 2025.
- Kokalari I, Karaja T, Guerrisi M (2013). Review on lumped parameter method for modeling the blood flow in systemic arteries. *J Biomedical Science and Engineering* 6: 92-99. DOI: 10.4236/jbise.2013.61012.
- Lauterbur PC (1973). Image Formation by Induced Local Interactions: Examples of Employing Nuclear Magnetic Resonance. *Nature* 242 (5394), 190–191. DOI: 10.1038/242190a0.
- LeVeque RJ (2002). Finite Volume Methods for Hyperbolic Problems, Cambridge: Cambridge University Press. ISBN 0-521-81087-6.
- Levitt MH (2002). Spin dynamics: basics of nuclear magnetic resonance. John Wiley & Sons, Chichester, UK, ISBN 0-471-48921-2, 2nd edition, ISBN 978-0-470-51117-6, 2008
- McGowan JC (2008). Basic principles of magnetic resonance imaging. *Neuroimaging Clin N Am.* 18(4): 623-636. DOI: 10.1016/j.nic.2008.06.004.
- Manning TS, Shykoff BE, Izzo JL Jr. (2002). Validity and Reliability of Diastolic Pulse Contour Analysis (Windkessel Model) in Humans. *Hypertension* 39(5): 963-968. DOI: 10.1161/01.HYP.0000016920.96457.7C
- Mansfield P (1977). Multi-planar image formation using NMR spin echoes. *J Phys C: Solid State Phys.* 10(3), L55-L58. DOI:10.1088/0022-3719/10/3/004.
- Markl M, Frydrychowicz A, Kozerke S, Hope M, Wieben O. 4D flow MRI. *J Magn Reson Imaging.* 2012 Nov;36(5):1015-36. doi: 10.1002/jmri.23632. PMID: 23090914.
- Maton A, Hopkins J, McLaughlin CW, Johnson S., Warner MQ, LaHart D, Wright JD (1993). Human Biology and Health. Prentice Hall, Englewood Cliffs. ISBN 978-0-13-981176-1.
- McRobbie DW, Moore EA, Graves MJ, Prince MR (2017). MRI from Picture to Proton, Cambridge University Press. DOI: 10.1017/9781107706958
- NCI (Online), National Cancer Institute (NCI), Magnetic Resonance Imaging <https://www.cancer.gov/publications/dictionaries/cancer-terms/def/magnetic-resonance-imaging>, Accessed Jan. 2025.
- Obligado, M.; Puy, M.; Bourgoïn, M. (2013). Bi-stability of a pendular disk in laminar and turbulent flows. *Journal of Fluid Mechanics*, 728. <https://doi.org/10.1017/jfm.2013.312>
- Orozco-Sevilla V, Coselli JS (2023). Management of the left subclavian artery during aortic arch replacement using a frozen elephant trunk approach: a review. *Cardiovasc Diagn Ther* 13 (4): 736-742. DOI: 10.21037/cdt-22-248.
- Pfützner J (1976). Poiseuille and his law. *Anaesthesia* 31 (2): 273–275. DOI: 10.1111/j.1365-2044.1976.tb11804.x.

- Pirola S, Cheng Z, Jarral OA, O'Regan DP, Pepper JR, Athanasiou T, Xu XY (2017). On the choice of outlet boundary conditions for patient-specific analysis of aortic flow using computational fluid dynamics. *J Biomech.* 60: 15-21. DOI: 10.1016/j.jbiomech.2017.06.005.
- Rinck PA (2024). Magnetic Resonance in Medicine. A critical introduction. The Basic Textbook of the European Magnetic Resonance Forum, e-Textbook 14th Ed., TRTF – The Round Table Foundation: TwinTree Media. Digital version 14.2 (www.magnetic-resonance.org).
- Ryan S, McNicholas M, Eustace SJ (2011). Anatomy for Diagnostic Imaging 3rd Ed., Saunders Elsevier, ISBN 978-0-7020-2971-4
- Sculpteo (Online), Meshmixer: 3D Modeling Software, <https://www.sculpteo.com/en/glossary/meshmixer-definition/>, Accessed Jan. 2025.
- SEER Training Website (Online), National Institute of Health, National Cancer Institute, SEER Training Modules, Introduction to the Cardiovascular System <https://training.seer.cancer.gov/anatomy/cardiovascular/>, Accessed Feb. 2025.
- Shan Y, Li J, Wang Y, Wu B, Barker AJ, Markl M, Wang C, Wang X, Shu X (2017). Aortic shear stress in patients with bicuspid aortic valve with stenosis and insufficiency. *J Thorac Cardiovasc Surg.* 153(6): 1263-1272.e1. DOI: 10.1016/j.jtcvs.2016.12.059.
- Shea MJ. "Blood Vessels – Heart and Blood Vessel Disorders". Merck Manuals Consumer Version. Merck Sharp & Dohme Corp. Archived from the original on April 24, 2015. Accessed Jan. 2025.
- Smith HW, Johnson L, Edwards DP (1981). First clinical applications of magnetic resonance imaging. *Radiology* 139(2), 333-340.
- Sohlman, M (Ed.) Nobel Foundation directory 2003. Vastervik, Sweden: AB CO Ekblad; 2003.
- Stankovic Z, Allen BD, Garcia J, Jarvis KB, Markl M (2014). 4D flow imaging with MRI. *Cardiovasc Diagn Ther.* 4(2): 173-192. DOI: 10.3978/j.issn.2223-3652.2014.01.02.
- Suleman M (2023) In Silico Approach Towards Magnetic Fluid Hyperthermia of Cancer Treatment: Modeling and Simulation, ISBN: 978-0-443-13286-5, DOI: 10.1016/C2022-0-02064-X
- UF Health (Online), Aorta anatomy, <https://ufhealth.org/conditions-and-treatments/aorta-anatomy>, Accessed: Dec. 2024.
- Updegrove A, Wilson NM, Merkow J, Lan H, Marsden AL, Shadden SC (2017). SimVascular: An Open Source Pipeline for Cardiovascular Simulation. *Ann Biomed Eng.* 45(3): 525-541. DOI: 10.1007/s10439-016-1762-8.
- Ursino M. (1998). Interaction between carotid baroregulation and the pulsating heart: a mathematical model. *Am. J Physiol.* 275(5):H1733-1747. DOI: 10.1152/ajpheart.1998.275.5.H1733.

Utkarsh Ayachit (January 22, 2015). The ParaView Guide: A Parallel Visualization Application (PDF). Kitware, Inc. ISBN 978-1930934306. Retrieved Jan, 2025.

Westerhof N, Lankhaar JW, Westerhof BE (2009). The arterial Windkessel. *Med Biol Eng Comput.* 47(2): 131-141. DOI: 10.1007/s11517-008-0359-2.

Woods S, (2010). Cardiac Nursing. New York: Lippincotts. p. 955. ISBN 9780781792806.

Woodward PJ, Griffith JF, Antonio GE, Ahuja AT. (Eds), Lower Cervical Level and Supraclavicular Fossa, *Imaging Anatomy: Ultrasound (Second Edition)*, Elsevier, pp. 124–129, DOI: 10.1016/B978-0-323-54800-7.50094-5.